University of Camerino

International School of Science and Technology

Doctorate Course in Materials Sciences (XXXVI cycle)

The use of physical methods for interdisciplinary materials investigation: from the characterization of natural waste for efficient upcycling to the analysis of cultural heritage

Doctorate Thesis

PhD Candidate

Sara Mattiello

Supervisor

Prof. Roberto Gunnella

Physics UNICAM

Academic Year (2020-2023)

Alle contraddizioni di tutti i percorsi.

Abstract

In a global context marked by increasingly urgent environmental, climatic and cultural challenges, it is essential to develop scientific approaches capable of combining innovation, sustainability and valorization of the past. Materials science is now a strategic discipline to address these challenges, offering tools for resource recovery and heritage conservation. This work explores the deep connection between the circular economy and the protection of historical artefacts, underlining how both processes imply an action of transformation and valorization of the material, aimed at revealing its "second nature". Case studies are presented regarding, on the one hand, the recovery and valorization of industrial waste (chicken feathers, wool and insects used for the treatment of organic waste) and, on the other, the analysis of archaeological finds in bronze. The investigations were conducted using advanced physical and chemical techniques (Raman, FT-IR, XPS, LIBS, XRF, SAXS, AFM, SEM), with the aim of defining key parameters for the characterization and recovery of materials, both in the technological and historical-artistic fields. The interdisciplinary approach adopted demonstrates how materials science can act as a bridge between innovation, sustainability and cultural memory.

Declaration

I am **Sara Mattiello**, hereby declare that the experimental thesis entitled,**"The use of physical methods for interdisciplinary materials investigation: from the upcycling of natural waste to the preservation of cultural heritage"** is my original research work which was done during my PhD tenure, 2020 - 2024, under the supervision of **Prof. Roberto Gunnella** at Physics Division, University of Camerino, Italy. I submit this thesis to fulfilment of the requirements for the award of Doctor of Philosophy in Material Sciences, to International School of Science and Technology (SAS), University of Camerino, Italy. This thesis work is a collaborative work mainly between University of Camerino and the Institute for Plasma Science and Technology (Bari Branch) of National Research Council (CNR). This work has not been previously submitted or published elsewhere for any form of degree, award, or professional qualification. Any text, illustrations, figures, tables, or other content utilized in this thesis from external sources have been appropriately cited and acknowledged.

Contents

List of Figures

Chapter1

Introduction

1.1 Bio-based and Traditional Materials: Synergies and Interdisciplinarity for addressing Circular Economy and Heritage Preservation issues.

The European Union (EU) has since long time recognized the importance to promote policies able to integrate environmental sustainability, public health, and preservation of cultural heritage. These fundamentals have been inserted in Maastricht treaty in 1992, in particular in those that are defined as the three pillars of European Union. Their institution has allowed dividing the policies adopted by the Union in three fundamental areas: the European Community (EC), the Common Foreign and Security Policy (CFSP) and Police and Judicial Co-operation in Criminal Matters (PJCCM)[1]. The pillars have been then implemented and integrated in the treaty of Lisbon in 2009. The first pillar concerns the European Common Market, the Monetary Union and a number of diverse competencies, such as education and culture, scientific research, and environmental protection. Lisbon treaty extends the competencies of the EU, by inserting among the objectives in its article 3 to protect and improve the quality of the environment, promoting the scientific and technological progress[2]. EU's environmental actions foster the circular economy, with the aim to minimize waste through the non-production of it, then promoting reuse, and getting to recycle only as the last and unavoidable option. The European Green Deal, package of policy initiatives, is central in this context, which poses the objective to reconcile the economical growth for the protection of ecosystem and the promotion of a better quality of life for all European citizens. Passing through the transformation of the models of production and consumption [3]. In an environment that is constantly evolving and threatened by pollution, urbanization, and climate change [4], the protection of material cultural heritage is of paramount importance. The protection of cultural heritage is not only a tangible act of preservation of historical memory but also an essential component of a sustainable development that looks ahead without forgetting or concealing the past. The European Framework for Action on Cultural Heritage (2018) highlights common action in this area, establishing five areas of permanent action with the aim of making heritage: participatory and accessible to all, sustainable, resilient through solutions that safeguard

heritage in danger, innovative for knowledge and research, promoting a stronger global partnership to strengthen international cooperation [5].

These initial considerations imply that a wider concept of sustainability does involve both the judicious exploitation of reuse to produce new value, and the protection of heritage materials and structures to accrue their inherent and historical importance by extending the knowledge upon them. In the specific context of materials science, this discipline is increasingly perceived as a bridge to create a culture of sensible and respectful use of materials according to their personality and potential. This includes characterization aimed at eliciting value, enhancing knowledge, and promoting preservation.

There is a clear link between these two aspects, those of the reuse and circular economy and that of the preservation of the cultural manufacts, and we do not mean the trivial fact that in both cases we are interested in "fixing" something existing, but that of digging the surface of the sample to expose a new phase, through a process of transformation i.e., the action of disveiling a second nature, in one case the original one after the time has strongly masked and sometimes compromised its nature, and in the other one transforming the otherwise useless waste to something still useful. In both cases the result is to discover a treasure, some added value for the society. Now if transpose the above concept in laboratory term it is not difficult to understand that physical and chemical tools must be deployed extensively and sinergetically as the process can be transformative and at the same time conservative from the point of view of the materials under study.

In particular, this work aims to treat, manipulate, and characterize different materials with various state-of-the-art techniques borrowed from physical and chemical practice. The current approach to materials science involves a wider consideration of materials developed by humans, hence anthropic, and natural, hence hierarchized, as a coherent whole.

Addressing the two above challenges requires a diversified and integrated approach, making interdisciplinary research increasingly relevant. Materials science, because of its interdisciplinary nature, allows following their transformation, from synthesis to application down to their performance over time. Reuse of waste materials is not a different process from the study of ancient manufacts, as the same attempt of giving a second life or unveiling the hidden real value of the environment or of the heritage is highly pursued.

In this thesis work, different techniques of analysis were used, chosen on the basis of the material and/or the information that was necessary to obtain.

In particular, physical spectroscopic fine analysis techniques were used, such as: Raman spectroscopy, Fourier-Transform Infrared Spectroscopy (FT-IR), X-Ray Photoelectron Spectroscopy (XPS), Laser-Induced Breakdown Spectroscopy (LIBS) and X-Ray Fluorescence (XRF), diffraction techniques such as Small Angle X-ray Scattering (SAXS) , microscopic techniques: Atomic Force Microscopy (AFM) and Scanning Electron Microscopy (SEM), all of them together, aim at establishing well defined key parameters to evaluate quality factors able to describe the best practice for recovery and characterization of the materials under study, i.e., molecular structure organization, novel physical properties (electric , optical and mechanical), or in the case of cultural heritage, the certain determination of the origin and of the specific manufact production process.

The case studies for the two segments of the work will be based respectively on one side on the study of recovery of keratin material from food industry waste i.e., keratin extracted from wool and chicken feathers (Section 2.1), and from the waste of soldier flies employed in the organic waste management (Section 2.2-2.3); on the other side, bronze archaeological artifacts have been chosen as an exemplary study (Section 3.1) of on fields application to heritage conservation.

References

[1] "Treaty on European Union". In: GU C 191 (29-07-1992), pp. 1–112.

[2] "Treaty of Lisbon amending the Treaty on European Union and the Treaty establishing the European Community". In: GU C 306 (13-10-2007), pp. 1–271.

[3] *The European Green Deal*. Available at: https://ec.europa.eu/commission/presscorner/detail/en/ip_19_6691 [Accessed: 21-10-2024]. 2019. URL: https://ec.europa.eu/commission/presscorner/detail/en/ip_19_6691.

[4] Intergovernmental Panel on Climate Change. *Climate Change 2021: The Physical Science Basis*. Available at: https://www.ipcc.ch/report/ar6/wg1/ [Accessed: 22-10-2024]. Intergovernmental Panel on Climate Change, 2021.

[5] European Commission, Sport Directorate-General for Education Youth, and Culture. *European framework for action on cultural heritage*. Publications Office, 2019. DOI: 10.2766/949707.

Chapter2

Biomaterial contribution to circular economy

2.1 Keratin extracted from wool and chicken feathers

Keratin is a group of structural, fibrous, and biopolymeric proteins that constitute the epithelial tissue of animals. It is found in various structures, such as human skin, hair, nails, wool, hooves, horns, beaks, and feathers of birds, among the most common examples [1]. Keratin contains numerous cysteine residues, characterized by the presence of a thiol groups (-SH). These groups form covalent disulfide bonds (S-S), which join the polypeptide chains together, allowing the formation of folded structures and the organization in increasingly complex hierarchical macrostructures [2]. Keratins can be classified into soft and hard based on their cysteine content. Soft keratin contains up to 3% cysteine and has less compact filaments, soft keratin tissues, namely the stratum corneum of the skin, are flexible and act as a barrier against external agents and also as camouflage from predators. Hard keratins are made up of filaments rich in cysteine (about 6-16% of the total amino acid residues), resulting in a higher degree of sulfur cross-linking than soft keratins. Tissues made of hard keratin, such as hair and wool, pig bristles, horns, nails and hooves, beaks, claws and feather shafts, are more resistant to heat, enzymes and both oxidizing and reducing agents than soft keratin [3]. In addition to the density of disulfide bonds, the organization of the secondary structure of keratin also plays an important role in the mechanical strength and flexibility of keratinous tissues (Figure 2.1). Alpha-helical keratins, typical of mammals, are more flexible proteins than beta-sheet keratins. In the case of feather keratins, they are mostly composed of beta-sheet structures [4] . The interest in using keratin as a basis for new materials arises from the need to dispose of a large amount of waste from industrial production. Keratin waste is generated by the meat industry (slaughterhouses) in the form of chicken feathers or by the wool textile industry. Keratin waste is degraded very slowly in nature and considered hazardous waste according to EU directives [6]. Conventional methods used for the disposal of keratin waste are not only expensive, but also very difficult. Decomposition methods such as incineration are used, but these procedures are polluting and pose a risk to the environment, especially if legal disposal procedures are not followed [7]. The best solution would therefore be to extract keratin using efficient and low environmental impact methods that fit perfectly into a circular economy perspective. The keratin used in

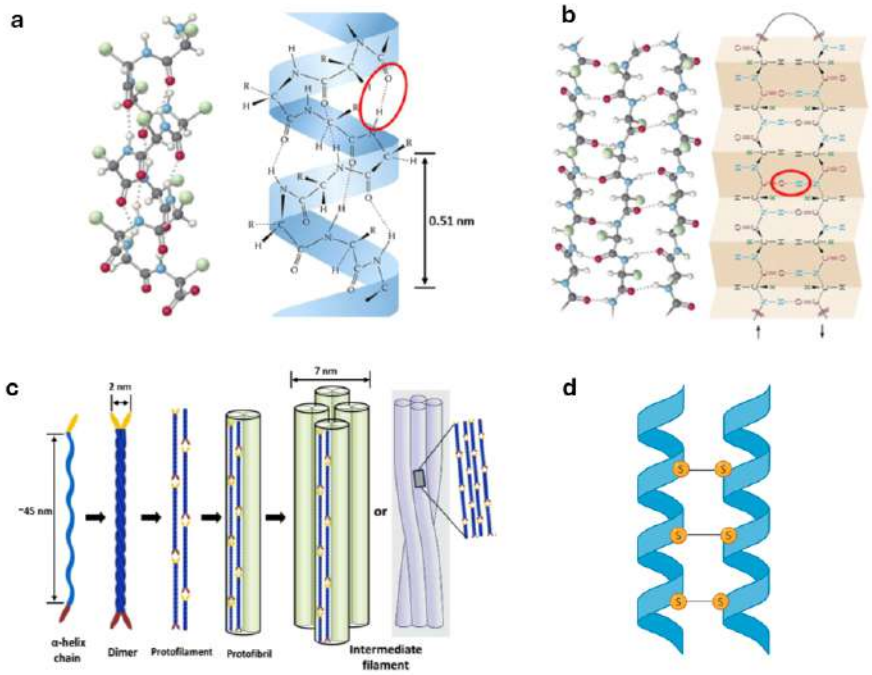

Figure 2.1: Keratin structure: (a) alpha keratin, represented as an alpha helical polypeptide chain highlighting the hydrogen bonds (red ellipse) that stabilize the helix; (b) beta keratin model of the polypeptide chain and as a beta pleated sheet (red ellipse highlight the hydrogen bond); (c) schematic illustration of intermediate filament formation as a hierarchical structure (Modified by [5]. (d) Model of disulfide bonds, where chains form covalent bonds between cysteine residues, generating keratin fibers.

this project was extracted from wool and feather fiber waste through different reduction processes, obtaining a protein that is more soluble in water in the case of sulfitolysis or, as in the case of feathers, with the ability to self-assemble into self-standing gel-like structures.

2.1.1 Paper I: *Physico-Chemical Characterization of Keratin from Wool and Chicken Feathers Extracted Using Refined Chemical Methods*

This work presents the study of the characteristics of the keratin structure extracted from wool and feathers. The method used for the extraction is sulfitolysis, i.e. a reduction that allows the preservation of the secondary structure of the protein [8]. The extracted keratin powders were analyzed with spectroscopic techniques such as Raman and FT-IR with the aim of verifying the preservation of the secondary structure. It was observed through the study of the deconvolutions of the IR and Raman spectra of the Amide I band that the keratin extracted from wool retains the alpha helix structure and that extracted from feathers preserves the beta sheet structure. With the SEM and AFM microscopy techniques they allowed the characterization of thin films obtained by solubilizing the keratins in water. The atomic force microscope showed how the organization of the particles is different for the two types of keratins, globular with an average radius of 45 nm for the wool keratin and elongated with an average length of 500 nm for the feather keratin. The SEM confirmed this organization, indicating how there is no preferential orientation. Subsequently, SAXS was used to study the size of the fibers extracted in aqueous solution,

leading to the suggestion of a model that defines their shape and size. In the liquid phase, the dimensions of the fibers fall within the range of the intermediate filament ($\leq 7nm$), therefore made up of smaller fibers that assemble laterally between them forming a cylinder and including a part of unfolded protein. The amorphous parts (unfolded protein) of the fiber and the medium-range structures are variously influenced by hydrogen bonds (reversible) and disulfide bonds (irreversible covalent), their presence plays a fundamental role in the structure of the keratin itself [5]. The complete chemical-physical analysis of the two different keratins extracted provides useful structural information for the definition of future applications of this type of waste. The preservation of the secondary structure of keratin offers the possibility of applying the protein by exploiting its properties to create novel materials providing also other characteristics, such as controlled water retention, elongation, and strength [9].

2.1.2 Paper II: *Synthesis and Properties of Biomimetic Self-Assembling Structures from Poultry Feather Keratin*

Chicken feathers are a large slaughter waste (8.5 billion tons annually, 2018 data) [10] and are an interesting source of keratin. In particular, the possibility of preserving the secondary protein structure seems to be a challenge. This review collects research works that through different chemical treatments have managed to preserve secondary structures capable of self-assembling into larger ones. A keratin extraction respectful of nature's intentions can be considered biomimetic. In particular, biomimetic extractions respect the very characteristics for which the protein was designed to serve in the specific environmental and mechanical situation in which it is inserted. The self-assembly of keratin extracted from chicken feathers, therefore intended for use in biomedical devices, such as scaffolds and wound dressings, has received some attention in recent studies. On the other hand, not many works that led to the regeneration of disulfide bonds have explicitly stated the potential for the self-assembly of obtained biomaterials, despite the fact that attention towards the synthesis of nanoparticles seems to gradually increase. The outcome of this review has indicated that reduction extraction processes are the most suitable for the purpose, including those using sodium sulfite or mercaptoethanol, or even those with ionic liquids and steam explosion extraction. A final comment would be that in the future, given the large availability of poultry feathers, investments will be made in higher value applications. In fact, the preservation of the secondary structure allows to obtain materials from the self-assembly of keratin in the form of nanoparticles, gels and mixtures with biopolymers.

2.1.3 Paper III: *Keratin Gel From Chicken Feathers Waste Obtained by Mercaptoethanol Extraction*

Protein gels obtained from chicken feather keratin offer interesting applications as engineered materials. Keratin derived from waste materials has gelling properties [11] that have not been sufficiently studied so far and are highly dependent on the extraction method used. This study aimed to explore the properties of gels obtained by mercaptoethanol extraction

followed by dialysis and to evaluate their structural characteristics. Keratin hydrogels were characterized by FT-IR and Raman spectroscopy, which allowed to identify the secondary structure of the protein in both hydrated and dry conditions. Furthermore, morphological analysis by SEM, together with rheological evaluations, showed that the gel consistency is stable over a wide range of loads and frequencies. The gel produced has a superior consistency compared to other biopolymer-based gels, such as cellulose-derived polymers [12], without the need for additional processing such as fiber reinforcement or chemical polymerization. The rheological moduli (G' and G") are comparable to other hydrogels obtained from feather keratin through different methodologies. The curcumin release analysis highlighted the potential use of this keratin gel as a vehicle for drugs and bioactive compounds, with the fastest release observed at pH 7.4, which corresponds to physiological conditions. The loading of curcumin, known for its anti-inflammatory and antioxidant properties [13], opens the way to the development of potential wound healing and scaffolding materials.

References

[1] Lawrence E. Murr. "Structures and Properties of Keratin-Based and Related Biological Materials". In: *Handbook of Materials Structures, Properties, Processing and Performance*. Cham: Springer International Publishing, 2015, pp. 483–510. ISBN: 978-3-319-01815-7. DOI: 10.1007/978-3-319-01815-7_28.

[2] Joanna McKittrick et al. "The structure, functions, and mechanical properties of keratin". In: *Jom* 64 (2012), pp. 449–468. DOI: 10.1007/s11837-012-0302-8.

[3] Shahin Banasaz and Vincenza Ferraro. "Keratin from animal by-products: structure, characterization, extraction and application—a review". In: *Polymers* 16.14 (2024), p. 1999. DOI: 10.3390/polym16141999.

[4] Wenwen Zhang and Yimin Fan. "Structure of keratin". In: *Fibrous Proteins: Design, Synthesis, and Assembly* (2021), pp. 41–53. DOI: https://doi.org/10.1007/978-1-0716-1574-4_5.

[5] Bin Wang et al. "Keratin: Structure, mechanical properties, occurrence in biological organisms, and efforts at bioinspiration". In: *Progress in materials science* 76 (2016), pp. 229–318. DOI: 10.1016/j.pmatsci.2015.06.001.

[6] Eric Deydier et al. "Physical and chemical characterisation of crude meat and bone meal combustion residue:"waste or raw material?"". In: *Journal of hazardous materials* 121.1-3 (2005), pp. 141–148. DOI: 10.1016/j.jhazmat.2005.02.003.

[7] Monica CM Parlato et al. "Livestock wastes sustainable use and management: Assessment of raw sheep wool reuse and valorization". In: *Energies* 15.9 (2022), p. 3008. DOI: 10.3390/en15093008.

[8] Amin Shavandi et al. "Keratin: dissolution, extraction and biomedical application". In: *Biomaterials science* 5.9 (2017), pp. 1699–1735. DOI: 10.1039/C7BM00411G.

[9] Xiang Mi et al. "From poultry wastes to quality protein products via restoration of the secondary structure with extended disulfide linkages". In: *ACS Sustainable Chemistry & Engineering* 8.3 (2020), pp. 1396–1405. DOI: 10.1021/acssuschemeng.9b05545.

[10] Tarun Kumar Kumawat et al. "Keratin Waste: The Biodegradable Polymers". In: *Keratin*. Ed. by Miroslav Blumenberg. Rijeka: IntechOpen, 2018. Chap. 9. DOI: 10.5772/intechopen.79502.

[11] Yussef Esparza, Aman Ullah, and Jianping Wu. "Molecular mechanism and characterization of self-assembly of feather keratin gelation". In: *International Journal of Biological Macromolecules* 107 (2018), pp. 290–296. ISSN: 0141-8130. DOI: 10.1016/j.ijbiomac.2017.08.168.

[12] M. Keshavarz and B. Kaffashi. "The ability of retention, drug release and rheological properties of nanogel bioadhesives based on cellulose derivatives". In: *Pharmaceutical Development and Technology* 19.8 (2014), pp. 952–959. DOI: 10.3109/10837450.2013.846371.

[13] Suchiwa Pan-On, Piyameth Dilokthornsakul, and Waree Tiyaboonchai. “Trends in advanced oral drug delivery system for curcumin: A systematic review”. In: *Journal of Controlled Release* 348 (2022), pp. 335–345. ISSN: 0168-3659. DOI: 10.1016/j.jconrel.2022.05.048.

I

polymers

MDPI

Article

Physico-Chemical Characterization of Keratin from Wool and Chicken Feathers Extracted Using Refined Chemical Methods

Sara Mattiello [1,*], Alessandro Guzzini [2,*], Alessandra Del Giudice [3], Carlo Santulli [4,*], Marco Antonini [5], Giulio Lupidi [2] and Roberto Gunnella [1]

[1] Physics Section, School of Science and Technology, Università di Camerino, via Madonna delle Carceri, 62032 Camerino, Italy
[2] School of Bioscience and Veterinary Medicine, Università di Camerino, via Gentile III da Varano, 62032 Camerino, Italy
[3] Department of Chemistry, Sapienza Università di Roma, Piazzale Aldo Moro 5, 00185 Rome, Italy
[4] Geology Section, School of Science and Technology, Università di Camerino, via Gentile III da Varano 7, 62032 Camerino, Italy
[5] ENEA—SSPT BIOAG PROBIO Via Gentile III da Varano, 62032 Camerino, Italy
* Correspondence: sara.mattiello@unicam.it (S.M.); alessandro.guzzini@unicam.it (A.G.); carlo.santulli@unicam.it (C.S.); Tel.: +39-380-652-2232 (C.S.)

Abstract: In this work, the characteristic structure of keratin extracted from two different kinds of industrial waste, namely sheep wool and chicken feathers, using the sulfitolysis method to allow film deposition, has been investigated. The structural and microscopic properties have been studied by means of scanning electron microscopy (SEM), Raman spectroscopy, atomic force microscopy (AFM), and infrared (IR) spectroscopy. Following this, small-angle X-ray scattering (SAXS) analysis for intermediate filaments has been performed. The results indicate that the assembly character of the fiber can be obtained by using the most suitable extraction method, to respond to hydration, thermal, and redox agents. The amorphous part of the fiber and medium range structure is variously affected by the competition between polar bonds (reversible hydrogen bonds) and disulfide bonds (DB), the covalent irreversible ones, and has been investigated by using fine structural methods such as Raman and SAXS, which have depicted in detail the intermediate filaments of keratin from the two different animal origins. The preservation of the secondary structure of the protein obtained does offer a potential for further application of the waste-obtained keratin in polymer films and, possibly, biocomposites.

Keywords: keratin; chicken feather waste; wool waste; metabisulfite extraction; Raman; SAXS

Citation: Mattiello, S.; Guzzini, A.; Del Giudice, A.; Santulli, C.; Antonini, M.; Lupidi, G.; Gunnella, R. Physico-Chemical Characterization of Keratin from Wool and Chicken Feathers Extracted Using Refined Chemical Methods. *Polymers* **2023**, *15*, 181. https://doi.org/10.3390/polym15010181

Academic Editor: Vincenzo Fiore

Received: 4 October 2022
Revised: 19 December 2022
Accepted: 27 December 2022
Published: 30 December 2022

1. Introduction

Keratin represents the most abundant structural protein in epithelial cells, and alongside with collagen, the most important biopolymer in animals. Its use in nature has an influence on its crystallinity and geometrical arrangement. This is connected in turn to its function, whether it serves, e.g., as thermal insulation and moisture control, such as in wool, or it absolves to more structural duties, such as in chicken feathers [1]. Keratin can be self-assembled to be employed for protective purposes, either explicitly as the main constituent of armors, or more implicitly in damage-tolerant structures, providing a shielding effect to the whole animal or to some critical parts of its body [2].

As a matter of fact, though, the function of protection is declined in different ways, which directly derive from the micro-assembly process developed in nature. For example, the cortical cells of animal hair, such as in wool keratin, constitute a microfibrillar composite, obtained with closely packed α-helical low-sulfur subunits [3]. In contrast, feather keratins, with their typical barbs–barbules network, also contain β-pleated sheets and are capable of forming filaments [4].

Large amounts of waste keratin are available from activities such as butchery and animal rearing. In particular, the poultry and wool industries generate huge amounts of keratin waste, estimated worldwide at 8.5 billion tons annually for the former (2018 data) [5] and 5 million tons produced yearly in the EU for the latter in 2019 [6]. The effective and profitable use of this waste would both reduce the amount of harmful material in the environment and the consumption of resources. Improving the extraction method for keratin from wool and feather waste can be a measure inspired by circular economy to reduce the environmental impact subsequent to the disposal of this waste, while providing indications for the "good practice" of its use as a secondary raw material. Landfilling, burying, and incinerating, which are still common procedures for this waste, represent environmental threats also in view of the limited significance, if any, of keratin structures for soil nutrition, due to the limited variety of micro-organisms able to feed on them [7].

Keratinous materials, formed by explicitly organized keratinized cells filled with mainly fibrous proteins (keratins), are natural polymer composites that exhibit a complex hierarchical structure ranging from nanoscale to centimeter scale (Figure 1). More specifically, the definition of "keratins" refers to a group of insoluble proteins and form the bulk of the stratum corneum of the epidermis and the epidermal appendages, such as hair, nails, horns, and feathers [8]. The basic macromolecules that form keratin are polypeptide chains constituted by amino acids. Keratin has a large amount of cysteine residues, which have a thiol group (-SH), producing a strong, covalent disulfide bond that cross-links both the polypeptide chains and the matrix molecules together [9]. Wool and feathers are characterized by two kinds of filament matrix structures at the nanoscale: alpha and beta keratin.

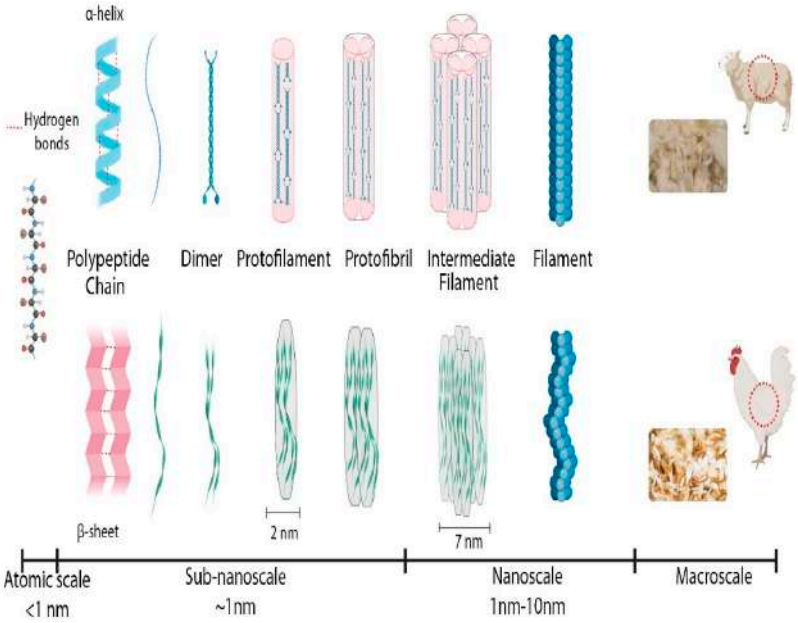

Figure 1. Schematic of the hierarchical structure of keratin from nanoscale to centimeter scale for wool and feathers (original drawing by S.M.).

In particular, the alpha keratin proteins are organized as spiral coils. The filament twists along its length in a right-handed coil; two chains formed by disulfide cross-link a left-handed coil, named as the dimer (45 nm long). Following this, dimers aggregate end-to-end and stagger side-by-side via disulfide bonds to form a protofilament (approximately 2 nm diameter); two protofilaments laterally associate into a protofibril; four protofibrils

combine into a circular or helical intermediate filament with a diameter of 7 nm [10]. In contrast, for beta keratin, the pleated sheet consists of laterally packed strands which can be parallel or antiparallel, forming chains that are held together by intermolecular hydrogen bonds. The pleated sheet structure is stabilized by two factors: the hydrogen bonds between beta strands contribute to form a sheet, while the peptide bond forces a beta-sheet to be pleated. The beta keratin filament is formed from the folded sheet that twists into a left-handed helix. Two pleated sheets overlap and wind in opposite directions, forming a filament with a diameter of 4 nm [11].

Keratins can be classified as soft keratin and hard keratin. The difference between the two kinds of keratin is the quantity of sulfur and the ability that proteins have to be bonded. Soft keratins, typically present in stratum corneum, have a lower amount of sulfur and are weakly consolidated, whilst hard keratins, found in hair, nails, and feathers, have a more coherent structure and a higher amount of sulfur [12].

The aim of the present work is to improve the knowledge of the process of extraction of the raw materials from wool and feathers. The complete chemical–physical analysis of the two different extracted keratins provides useful structural information for the definition of the future applications of this type of waste. These would possibly range from the introduction of keratin from different kinds of waste as filler in biodegradable films, to the production of films using extracted keratin.

2. Materials and Methods

2.1. Waste Materials

Keratin waste materials were obtained from chicken slaughtering and sheep shearing, without any treatment. The wool analyzed comes from flocks of merino and merinized sheep of the Apennine ridge, across the regions of Marche, Umbria, and Abruzzo (Italy). A sample of as-received waste is portrayed in Figure 2.

Figure 2. Waste as received: chicken feathers (**left**) and sheep wool (**right**).

The two types of as-received waste are widely recognized as containing a very high amount of pure keratin. In particular, as concerns chicken feathers, these are essentially constituted (>90%) by a structural keratin structure, rich in cysteine, and hydrophobic residues that enhance cross-linking by disulfide bonds, including a variety of other amino acids, such as lysine, serine, and proline [13,14]. On the other hand, wool was proven to contain up to 95% keratin by weight and all nine essential amino acids, so as to be considered a pure source of intermediate filament proteins [15]. The aforementioned evidence justified the selection of both sources for the extraction of keratin.

2.2. Extraction Method

A variety of chemical methods are potentially available for the extraction of keratin from industrial waste. For example, in the case of sheep wool, methods such as alkali hydrolysis, sulfitolysis, reduction, oxidation, and extraction using ionic liquid, were considered [16]. It is important to clarify that with sulfitolysis, reduction, and oxidation, only the cleavage of disulfide bonds takes place, whereas keratin hydrolysis leads to peptide bonds' breakage, which may be undesirable in view of the possible upcycling of waste in mechanically sound structures e.g., films [17]. However, it has been highlighted that, other than the yield of extraction, antioxidant properties of the extracted keratin from chicken poultry may vary e.g., using 2-mercaptoethanol, sodium sulfite, and sodium dodecyl sulfate [18]. The metabisulfite extraction method was selected as it provides sufficient yield, whilst also preserving the secondary structure of the protein [19]. In addition, the procedure is effective, being easily applicable to the raw material and requires lower amounts of chemicals and with lower toxicity compared to other methods such as the mercaptoethanol one [20,21]. The extraction of keratin from wool and chicken feathers involved a first wash with cold water and soap, followed by drying to constant weight at 60 °C in a forced-air oven. Dried sheep wool and chicken feathers were ground to pieces with maximal dimension not exceeding 5 mm. The dried wool and feathers were incubated with ethanol at 50 °C for 2 h to remove surface fats and waxes, which were then filtered out. All residues of ethanol on defatted wool or feathers were removed after incubation for 3 h in a forced-air oven at 60 °C. Subsequently, 3 4g of clean and defatted wool were added to 100 mL of a solution containing 48 g of urea (8 M), 1.8 g of sodium dodecyl sulfate (SDS), and 6.84 g of sodium metabisulphite. The reaction took place at 70 °C for 24 h under shaking, and after incubation, filtered for solids removal (partially digested residue). The filtered solution was dialyzed against ultrapure water for approximately 3 days at room temperature with several water changes using 12 kDa nominal low-molecular-weight cutoff membrane. After dialysis, the solution was centrifuged to separate the precipitated protein and the supernatant obtained was lyophilized to obtain a pure keratin powder. The process to obtain keratin from cleaned and defatted feathers was carried out with the following process: 4 g of clean feathers were immersed in 150 mL of a solution containing 47.7 g of urea, 7.5 g of SDS, 15 g of sodium metabisulfite, 195 mg of ethylenediaminetetraacetic acid (EDTA), and 4.84 g of tris(hydroxymethyl) aminomethane (Tris). The reaction took place at 70 °C for 24 h under shaking, as described above for wool. This method of extraction applied to wool and feathers allowed us to obtain keratin in powder form.

To determine the purity and an average molecular mass of the keratin hydrolysate samples, SDS-PAGE gel electrophoresis was performed according to the method of Laemmli [22]. The samples of freeze-dried lyophilized hydrolysate were mixed (at a ratio of 4:1) with a loading buffer 5x (containing 10% (v/v) SDS, 250 mM Tris−HCl buffer (pH 6.8), 50% (v/v) glycerol, 0.5 M dithiothreitol (DTT), 0.02% (w/v) bromophenol blue) and the solutions were heated in a dry bath heat block at 95 °C for 5 min. Denatured keratin samples from feather (F) and wool (W) were loaded onto each lane, resolved on a precast polyacrylamide separation gel 4–20%, and stained with 0.25% (w/v) Coomassie brilliant blue R250. Denatured protein markers, having a known molecular weight, were used as a standard. The different lyophilized keratins used in the experiments were not further purified by size exclusion chromatography.

2.3. Characterization of the Extracted Keratin

2.3.1. Keratin Film Preparation

Films were prepared by drop casting, to be subsequently characterized by scanning electron microscope (SEM) and atomic force microscope (AFM). For the deposition, 10 mg of keratin was dissolved in 1 mL of de-ionized water. Given the low solubility of keratin in water, dissolution was facilitated by using the sonicator for 10 min until a uniform suspension was obtained without precipitation for several days. A droplet of approximately 10 µL of the solution was deposited on glass forming a thin layer of keratin with a nominal

thickness of approximately 4.8 µm, as estimated from the density of the material and the subsequent volume obtained from measuring the film weight. This value is, of course, only approximated and is measured considering the density as constant throughout the keratin layer. The film was dried under fume hood at room temperature.

2.3.2. Microscopy Techniques

SEM analyses were carried out using a Field Emission Scanning Electron Microscopy (FE-SEM, Sigma Family, Zeiss, Jena, Germany), equipped with a backscattered detector (BSD) to obtain high-quality microphotographs.

AFM images were acquired in tapping mode by using CSI Nano-observer, Les Ulis, France, and P-doped n-type Si cantilever (resonance frequency = 75 kHz). The measurements were performed by using resonant mode.

2.3.3. Spectroscopy Techniques

Raman spectroscopy and FT-IR were used to investigate the secondary structure of keratin on powder samples.

Raman spectroscopy was performed with a HORIBA IHR320 micro-Raman Scattering system (Horiba, Palaiseau, France) equipped with an optical Microscope model Olympus BXF41 (with 5×, 20×, 50×, 100× objectives) (Münster, Germany). The Raman spectrometer was operated at 532 nm (diode laser).

IR spectra were recorded from 4000 to 600 cm^{-1} with a PerkinElmer Spectrum 100 FT-IR instrument (Waltham, MA, USA) by total reflectance on a CdSe crystal.

2.3.4. Small-Angle X-ray Scattering (SAXS)

Small-angle X-ray scattering experiments were performed using a Xeuss 2.0 Q Xoom system (Xenocs SA, Grenoble, France) equipped with a micro-focus Genix 3D X-ray Cu source (λ = 0.1542 nm), a two-dimensional Pilatus3 R 300 K detector placed at variable distance from the sample (Dectris Ltd., Baden, Switzerland).

Measurements were made on liquid solutions of keratin extracted from wool and feathers at different concentrations (0.5, 0.7, 1, 1.2 wt.%) obtained by dissolving weighted amounts of keratin powder with 1 mL of Tris-HCl 50 mM buffer (pH 8).

The keratin samples were loaded into disposable glass capillary cells with nominal thickness 1.5 mm and sealed with hot glue. Two capillaries, one loaded with the buffer used as dispersant and an empty one, were used for background subtraction.

The measurements were performed at room temperature (25 ± 1 °C) and at reduced pressure (∼0.2 mbar), with two different sample-detector distances, in order to overall access a scattering vector modulus (q) range between 0.045 and 13 nm^{-1}, where $q = 4\pi\sin(\theta)/\lambda$, and 2θ is the scattering angle. The two-dimensional scattering patterns were subtracted for the "dark" counts, and then masked, azimuthally averaged, and normalized for transmitted beam intensity, exposure time, and subtended solid angle per pixel, by using the FoxTrot software developed at SOLEIL. The one-dimensional intensity vs. q profiles were subtracted for the contributions of the solvent and empty capillary and measured in intensity units of macroscopic scattering cross-section (cm^{-1}) by dividing them for the capillary thickness estimated from the alignment scans. Pair distance distributions of the cross-section of elongated objects were obtained by indirect Fourier inversion of the I(q)·q profiles performed with the software BayesApp [23].

3. Results and Discussion

The sodium dodecyl sulfate polyacrylamide gel electrophoresis (SDS-PAGE) of keratins' preparations is reported in Figure 3.

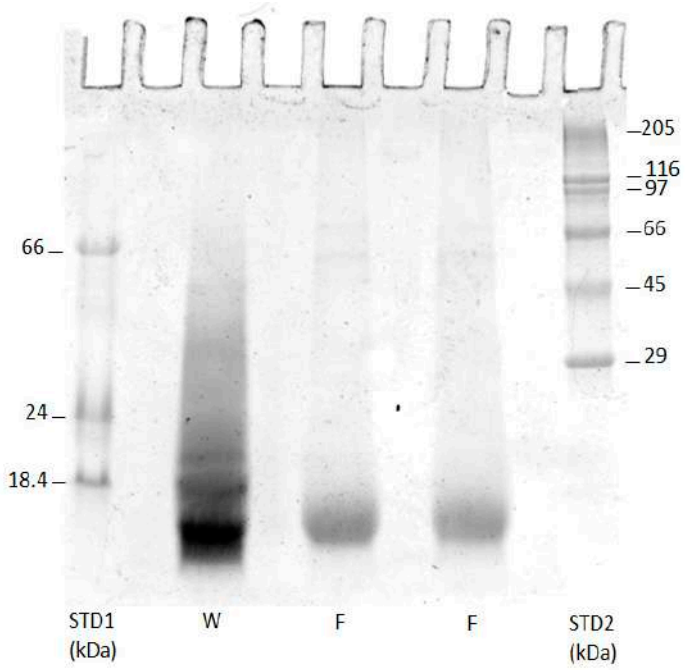

Figure 3. SDS-PAGE of keratin analysis. The first and last columns show the protein standard and keratin extracted from wool (W) and chicken feathers (F) using sodium metabisulfite as reducing agent.

The molecular weights of extracted protein fractions were in the range of 12–13 kDa for feathers (F), in the range of what was observed in [24], and the protein extracted seems to be relatively pure, near homogeneity. On the other hand, for wool (W) a large electrophoretic band with a similar MW to that reported for feathers is reported, in addition with another less intense band around 18 kD.

The yield of each extraction method (Y) was calculated in percent by the ratio between the weight of the freeze-dried sample (W′) and initial weight of the sample (W) using the following Equation (1):

$$Y\ (\%) = (W'/W) \times 100 \quad (1)$$

The yield of the extraction method, measured over three extractions for each waste, was 45 (±3)% for wool, whereas the yield obtained with feathers was 73 (±3)%. The data obtained for wool, although they might appear quite low, were even slightly higher than what was reported from sulfitolysis elsewhere, i.e., 41% [17]. The remainder is a partially digested residue that can be dried in the oven and mechanically reduced to powder.

Images of the extracted portion and the relevant residues are reported in Figure 4.

Optical micrographs of the residues of the keratin extraction are reported in Figure 5. Here, the needle-like structure with random orientation and very variable aspect ratios, with length mostly in the range between 10 and 20 microns, obtained from feather waste (Figure 5a) and the filamentous structure obtained from wool waste (Figure 5b), are respectively shown.

Figure 4. Result of keratin extraction: extracted keratin (**a**) and residue (**b**) from chicken feathers; extracted keratin (**c**) and residue (**d**) from sheep wool.

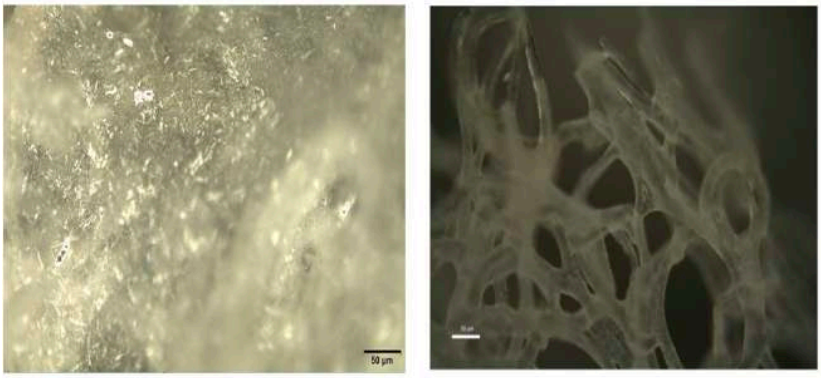

Figure 5. Optical micrographs of the residues of the keratin extraction process: (**a**) from chicken feathers; (**b**) from sheep wool. The scale bar indicates a 50 µm length.

Moreover, the microscopic characters of the films were analyzed with atomic force microscope and scanning electron microscope. Atomic force microscope images of keratin extracted from wool (Figure 6a) show the topography of the film at different dimensions. The structures are poorly defined and globular with a radius around 45 nm. In contrast, the images of keratin extracted from feathers (Figure 6b) show the topography of the film with elongated structures that have lengths of approximately 500 nm. This is confirmed by SEM images (Figure 7), where the image of the keratin extracted from wool (Figure 7a) is globular

and compact and does not show elongated structures. Otherwise, the keratin extracted from feathers (Figure 7b) has a uniform surface with elongated structures with a section of approximately 0.5 µm. No evidence of preferential orientation is clearly observable.

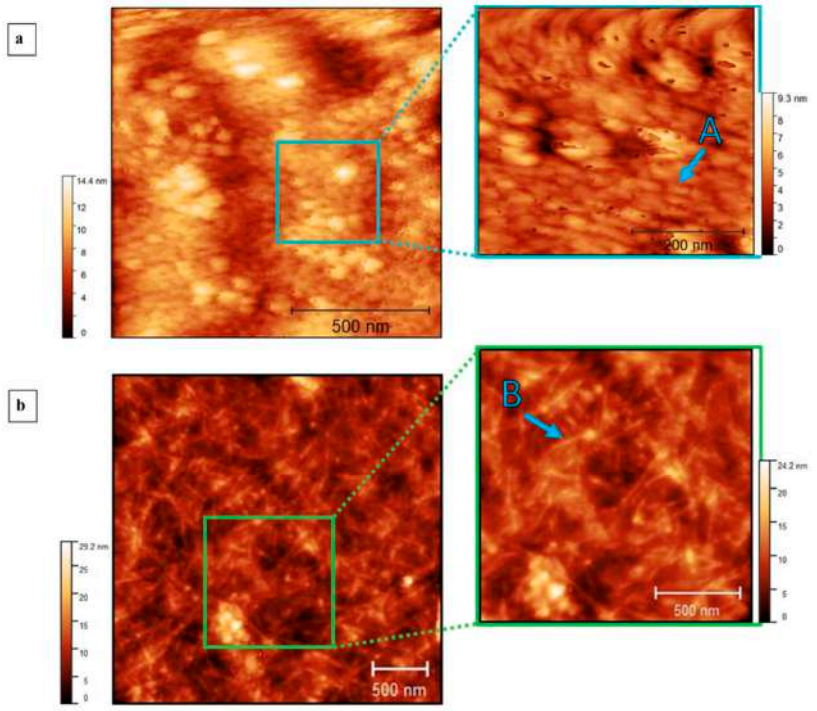

Figure 6. AFM images at different magnifications of keratin films obtained by drop-casting deposition, the color bar represents the variation of thickness of the materials on the substrate. (**a**) Images of keratin extracted from wool. Point A indicates the globular structure with a radius around 45 nm. (**b**) Images of keratin extracted from feathers. Point B indicates elongated structures that have lengths of approximately 500 nm.

Raman spectroscopy was also used to investigate the secondary structure of keratin on powder samples. Figure 8 shows spectra of keratin extracted from wool (in black) and feathers (in red) and the position of the main bands are 1200–1300 cm^{-1} for amide III band, 1600–1700 cm^{-1} for amide I band, and 1448 cm^{-1} for CH_2 group [25].

The spectra confirm that after the extraction, the keratin preserves its secondary protein structure, and it is possible to obtain further details about the structure by studying in more detail the different contributions that compose the amide I band. In particular, the position of two evident peaks have been identified at 1609 cm^{-1} for C = C double bond and between 1651 cm^{-1} and 1679 cm^{-1} for alpha and beta-sheet. Signals coming from the two latter contributions are partially superposed, yet a deconvolution operation (not shown) highlights the predominance of an alpha-helix structure (1651 cm^{-1}) in the case wool keratin and beta-sheet structure (1679 cm^{-1}) in the case of feather keratin.

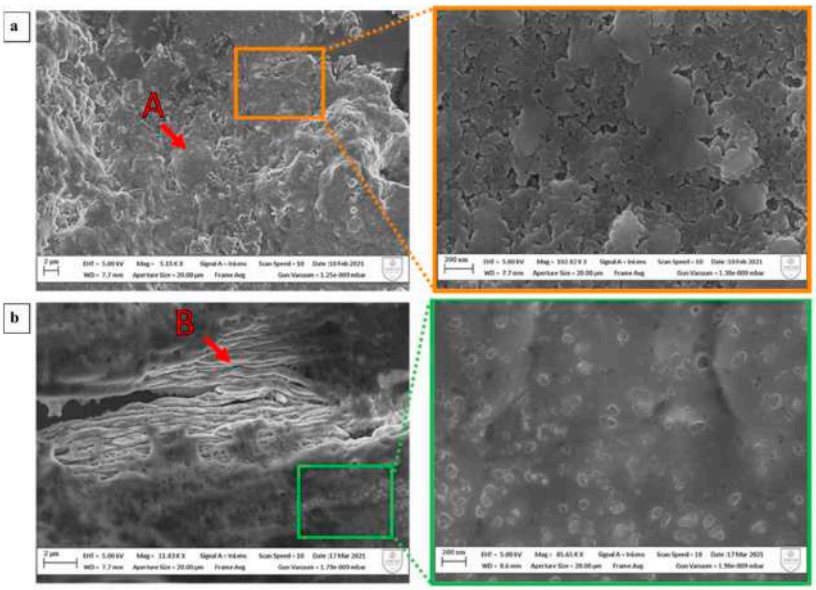

Figure 7. SEM images at different magnifications of keratin films obtained by drop-casting deposition. (**a**) The images of keratin extracted from wool. Point A indicates globular structure. (**b**) The images of keratin extracted from feathers. Point B indicates elongated structures, with a section of approximately 0.5 µm and a length in the order of 10 µm, hence with aspect ratio = ~20.

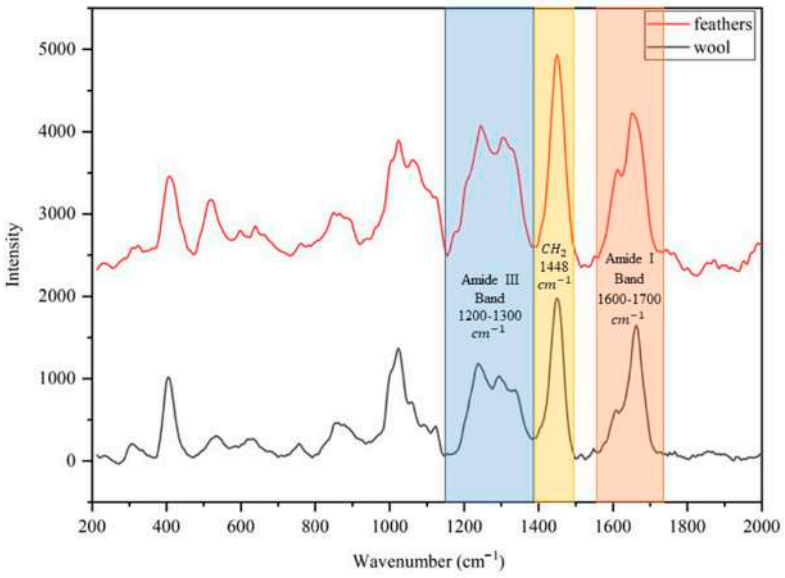

Figure 8. Comparison between the Raman spectrum of keratin extracted from wool (in black) and the spectrum of keratin extracted from feathers (in red).

The IR spectra of keratin powder extracted from wool and feathers are shown in Figure 9. Vibrations due to the characteristic bands of proteins are visible in both spectra.

The absorption band of stretching vibration of N-H and OH bonds at around 3300 cm^{-1} is related to amide A [26]. Stretching vibrations of C=O bonds appear from 1600 to 1700 cm^{-1} and they are typical of the amide I band, that contains information about the secondary structure of keratin [27]. At 1520 cm^{-1}, the bending vibration of N-H of amide II is visible [28]. The stretching vibrations of C-N and C–H and bending vibrations of N-H and C=O at around 1220–1300 cm^{-1} are related to amide III. Additionally, in this case, it is possible to obtain further information about the secondary structure by studying the contribution that constitutes the amide I band. In particular, the position of the amide I peak for wool keratin has been identified deconvoluted in one component at 1618 cm^{-1} for beta-sheet, one at 1645 cm^{-1} for alpha-helix, and one at 1675 cm^{-1} for disordered structure, while for feather keratin the peaks are in position 1625 cm^{-1} for beta-sheet, 1650 cm^{-1} for alpha-helix, and 1676 cm^{-1} for disordered structure.

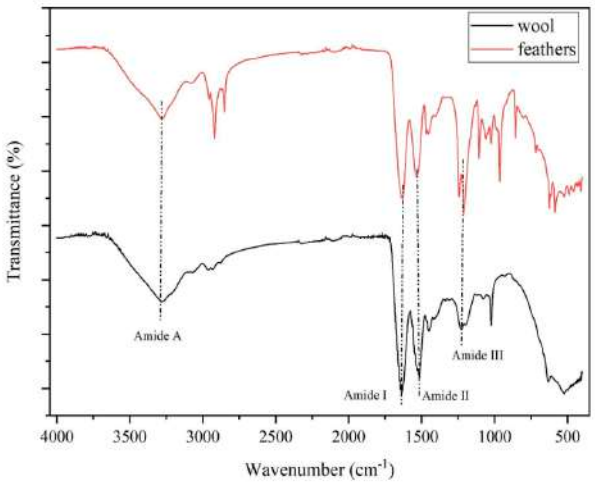

Figure 9. Comparison between the IR spectrum of keratin extracted from wool (in black) and the spectrum of keratin extracted from feathers (in red).

Since there is no water interference in the amide III region (1220–1300 cm^{-1}), it is possible to use this region to determine protein secondary structure, especially in the presence of pure proteins with a well-defined secondary structure, such as it is the case of feather keratin sample (beta-sheet structure) and wool (alpha keratin). As a matter of fact, the maximum absorbance wavenumber of pure protein containing only alpha-helix is around 1300 cm^{-1}, for beta-sheet proteins it is around 1235 cm^{-1}, beta-turn bands are located around 1260–1280 cm^{-1}, while the random coil is located around 1240–1260 cm^{-1} [29]. However, the presence of a non-homogeneous type of peptides (with different molecular weight derived from the type of extraction conditions) and the presence of oxidized sulfur derivatives such as sulfonic (RSO_3H) or sulfinic acid (RSO_2H) showed a more complicated pattern [30]. This could be further investigated in presence of homogeneous solution of the two keratins using the amide III region.

Furthermore, the area between 700 and 1100 cm^{-1} is strongly sensitive to the presence of sulfur-oxidized derivatives, which suggests an increasing number of disulfide bonds has been reduced to form cysteic acid [27]. As regards other peaks, in particular the one detected at 625 cm^{-1}, it is probably due to the vibration of the C-S bonds [31]. In contrast, there appears to be no interference due to SDS, even if it has bands in common with keratin: SDS shows intense peaks at 827 cm^{-1} and 1467 cm^{-1}, not visible in the spectrum of keratin extracted from feathers, yet due to the aliphatic CH_2 vibrations of SDS [32].

IR spectroscopy confirms what was detected with Raman spectroscopy, i.e., a greater presence of alpha-helix in the sample of keratin extracted from wool and beta-sheet in the keratin extracted from feathers. It also shows a contribution of disordered structure probably due to the extraction method. These unfolded protein parts are present in both samples.

The SAXS study was aimed at the characterization of the aggregation state of individual keratin filaments (namely intermediate filaments, with expected diameter of 7 nm [9]) when extracted from the raw materials by a sulfitolysis chemical digestion process and redispersed in aqueous solvent. Rather than describe the interaction of such filaments among themselves within a formed film, at this stage the structure of isolated filaments with a diameter in the range between 1 nm and 100 nm was characterized by means of SAXS, and information on the internal structure of the fiber was obtained [33].

For this reason, the choice was to study rather diluted samples (of the order of 10 mg/mL) to reduce the inter-particle interactions. The profiles collected for the two forms of keratin (Figure 10) show an initial power law in the low-q region ($q < 0.15$ nm^{-1}) close to q^{-1}, suggesting them to fall within the case of the rod-like particle model, for which the overall length lies above the size limit accessible within the available q-range (>100 nm): as the consequence, only information about their cross-section can be obtained. This was conducted by applying the indirect Fourier transform to the scattering intensity multiplied by q to obtain the pair distance distributions of the cross-section ($P_{CS}(r)$, inset of Figure 10). The skewed shape of these functions having intense peaks for small distances (<7 nm) and a slowly decaying profile at larger distances suggests that the average section of the fibrils is constituted by the lateral association of fundamental units with a smaller diameter.

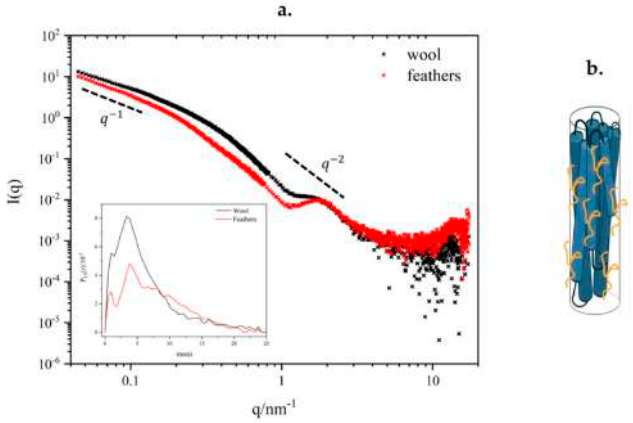

Figure 10. (**a**) Comparison between scattering curve of keratin extracted from wool (in black) and feathers (in red), in the inset figure, the Fourier transform of the scattering intensity; (**b**) sketch of the hypothesized fibers, which represents the possible aggregation of the smaller fibers in a bigger one; in yellow, the unfolded protein surfacing is reported.

In particular, maxima at approximately 1 nm and 3.5 nm could correspond to fundamental building blocks with diameters of 2 nm and 7 nm, potentially compatible with the size of a proto-filament and a proto-fibril up to the full intermediate filament. In the case of feather keratin, the first peak of the distribution function at approximately 1 nm is more pronounced and well resolved, confirming that keratin filaments in feathers have a higher degree of internal order than in the wool at this short range. From the value of r at which the $P_{CS}(r)$ fall to zero, an estimate of the maximum diameter of the section of the filaments present in solution is obtained: for the keratin extracted from wool, most of the filaments have diameters $\leq$7 nm (of the same order of an intermediate filament), and only a small fraction contribute with larger diameters; for the keratin extracted from feathers, more filaments with larger diameters are found, with a maximum size up to

20 nm, suggesting a higher degree of lateral association among intermediate filaments in the dispersed aggregates. Further studies on the *modeling* of these fibers are ongoing, involving core–shell cylinder form factors which also include the contribution of unfolded peptide chains in the shell, as suggested by the final slope observed in the SAXS data, following a power law closer to that expected for a coil (q^{-2}) rather than that predicted for a sharp interface according to the Porod law (q^{-4}) [34].

In general terms, the impact on the ambient of waste from feathers and wool derived from the important food supply chain poses the question of a possible engineered use of such materials for novel applications. It is widely recognized that keratin-based materials offered distinct properties, in particular coupling biodegradability, biocompatibility, and mechanical durability [35]. In addition, keratin-based biomaterials have an intrinsic ability to support cellular proliferation and can be used as sponges, films, and hydrogels for various biomedical applications. These are all possibilities that, to be explored, require a complete characterization of keratin waste, such as that performed on human hair keratin in [36]. Those applications should combine the well-known basic properties of the raw material into composites having the merit to offer sufficient mechanical and interface performance, needed for its industrial process. To this aim, the detailed knowledge of the material structure and its conversion, adaption, and transformation is necessary. The wool and feather keratins can be derived into water-soluble proteins with high molecular weight by means of simple chemical treatments and can be turned into films with plastic properties, which, in the past, was obtained from feathers, albeit by thermal treatments [37].

In the future, to make keratin the mainstream material for various bio-applications, the properties and structures of keratin must be investigated extensively at both the nanoscale and macroscale levels, as well as under chemical conditions for their dissolution and extraction, considering the filament–matrix structure for alpha and beta keratins of wool and feathers, respectively [38].

In this first step, the study on novel extraction methods described above outlined the properties of the pure fibers. In practice, the extraction of keratin from two different animal waste sources, namely sheep wool and chicken feathers, by the sulfitolysis method indicated some differences in extraction yield, in favor of feathers. However, in both cases, the extraction offered considerably higher yield than reported in the literature for other methods [39]. Metabisulfite is also preferable as a solvent due to its non-toxicity, which has been recognized to reduce the contamination effects, e.g., in cereals [40]. It is noteworthy, though, that both protein waste sources offered the possibility to obtain sufficiently sound and repeatable films from stir casting.

It is suggested, from both optical spectroscopies and X-ray scattering, that keratin from feathers would present a more oriented structure, evidenced by the beta-sheets contribution with respect to disordered coils (alpha-helices) and from the more intense small-angle scattering of x-rays, because of their more compact structure. It is suggested that the application of sulfitolysis did contribute to the preservation of compactness, which has not been accounted for when extracting keratin from poultry feathers using other methods, such as ionic liquids (sodium sulfate) [41]. In particular, the main absorption peaks are preserved in FTIR spectroscopy from both sources of keratin with no frequency shifts; therefore, no visible interaction has been detected with the extraction medium, which has been not the case in works using other methods [42]. As regards more specifically SAXS spectra, apart from the aforementioned higher degree of lateral aggregation for feather keratin, no significant changes in the broadness of peaks are observed between the two sources. This is promising for the production of composite films with other polymers (e.g., cellulose), where the structural variability these changes may imply do represent an issue [43]. As the result, a single model has been hypothesized as sufficiently representative for both keratins.

Though an exact model for the scattering object for the latter case is still unclear, such a more compact structure would possibly oppose higher tearing loads, though film plasticization. The choice of plasticizer does represent a crucial stage to improve these properties [44],

which is also related to the detailed object description and its chemical functionalization. The likely presence of unfolded proteins in keratin from feathers can be correlated with the higher viscoelastic properties of hydrogels they are able to form with respect to those synthesized using wool, as observed in [45]. As a matter of fact, in the literature, the production of blended films with wool–plasticizer combinations are less diffuse than with feather keratin, using typical plasticizers such as citric acid [46] or glycerol [47], where the lower properties might be compensated by a higher film translucency. In any case, these studies seldom posed the question of reducing the residue by optimizing keratin extraction for film production, and, in the long run, trying to hypothesize possible applications for it, in order to follow a circular economy-based approach [48].

4. Conclusions

In this study, metabisulfite was used for the extraction of keratin from wool and feather waste. The method guaranteed the high solubility of the keratin with respect to other procedures; in addition, it is highly efficient and preserves the secondary structure of the protein, allowing it to identify the presence of alpha and beta structures by using Raman spectroscopy and FTIR. While detailed information at a dimensional level between 1 and 100 nm has been obtained by SAXS and corroborated by microscopy analysis of the material, confirming the optimal preservation of the intermediate structure of the refined material was conducted with respect to other extraction methods. The dimension of fibers in the liquid phase seems to fall within the range of the intermediate filament that can be harnessed for further functionalization and composition with other biopolymers. Such a study is an advantageous starting point for future implementation of devices based on the functionalized material, to be proposed in applications for biosensors, biomedical, and other added-value applications.

Author Contributions: Methodology, G.L., R.G., A.D.G. and M.A.; validation, S.M., A.G., R.G. and G.L.; investigation, S.M., A.G. and A.D.G.; resources, M.A.; writing—original draft preparation, S.M. and A.G.; writing—review and editing, G.L., R.G. and C.S.; supervision, G.L., R.G. and C.S. All authors have read and agreed to the published version of the manuscript.

Funding: A.G.'s contribution to this research was funded by a biennial research contract from POR Marche FSE 2014–2020. S. M's contribution is part of her PhD work, under a EUREKA grant.

Acknowledgments: The authors are thankful to Marche Applied Research Laboratory for Innovative Composites (MARLIC) of Marche Region for laboratory instrumentation support. Fileni S.p.A. is also acknowledged for the supply of chicken feathers. A.D. acknowledges co-financing of Sapienza University of Rome and the European Union—FSE-REACT-EU, PON Research and Innovation 2014-2020 DM1062/2021 for the RTD-A contract. The Sapienza Research Infrastructure is acknowledged for the SAXS measurements at SAXSLab Sapienza, funded by the Large Equipment Project 2015-C26J15BX54.

Conflicts of Interest: The authors declare no conflict of interest.

References

1. Shah, A.; Tyagi, S.; Bharagava, R.N.; Belhaj, D.; Kumar, A.; Saxena, G.; Saratale, G.D.; Mulla, S.I. Keratin production and its applications: Current and future perspective. In *Keratin as a Protein Biopolymer*; Sharma, S., Kumar, A., Eds.; Springer: Cham, Switzerland, 2019; pp. 19–34.
2. Islam, M.K.; Hazell, P.J.; Escobedo, J.P.; Wang, H. Biomimetic armour design strategies for additive manufacturing: A review. *Mater. Des.* **2021**, *205*, 109730. [CrossRef]
3. Zahn, H.; Föhles, J.; Nlenhaus, M.; Schwan, A.; Spel, M. Wool as a biological composite structure. *Ind. Eng. Chem. Prod. Res. Dev.* **1980**, *19*, 496–501. [CrossRef]
4. Zoccola, M.; Aluigi, A.; Tonin, C. Characterisation of keratin biomass from butchery and wool industry wastes. *J. Mol. Struct.* **2009**, *938*, 35–40. [CrossRef]
5. Kumawat, T.K.; Sharma, A.; Sharma, V.; Chandra, S. Keratin Waste: The Biodegradable Polymers. In *Keratin*; Blumenberg, M., Ed.; IntechOpen: London, UK, 2018. [CrossRef]
6. Cataldi, P.; Condurache, O.; Spirito, D.; Krahne, R.; Bayer, I.S.; Athanassiou, A.; Perotto, G. Keratin-graphene nanocomposite: Transformation of waste wool in electronic devices. *ACS Sustain. Chem. Eng.* **2019**, *7*, 12544–12551. [CrossRef]

7. Dinu, R.; Cantarutti, C.; Mija, A. Design of sustainable materials by cross-linking a biobased epoxide with keratin and lignin. *ACS Sustain. Chem. Eng.* **2020**, *8*, 6844–6852. [CrossRef]
8. Karthikeyan, R.; Balaji, S.; Sehgal, P.K. Industrial applications of keratins—A review. *J. Sci. Ind. Res.* **2007**, *66*, 710–715.
9. Dale, B.A.; Holbrook, K.A.; Steinert, P.M. Assembly of stratum corneum basic protein and keratin filaments in macrofibrils. *Nature* **1978**, *276*, 729–731. [CrossRef]
10. McKittrick, J.; Chen, P.-Y.; Bodde, S.G.; Yang, W.; Novitskaya, E.E.; Meyers, M.A. The structure, functions, and mechanical properties of keratin. *J. Min. Met. Mater. Soc.* **2012**, *64*, 449–468. [CrossRef]
11. Wang, B.; Yang, W.; McKittrick, J.; Meyers, M.A. Keratin: Structure, mechanical properties, occurrence in biological organisms, and efforts at bioinspiration. *Prog. Mater. Sci.* **2016**, *76*, 229–318. [CrossRef]
12. Aebi, U.; Fowler, W.E.; Rew, P.; Sun, T.T. The fibrillar substructure of keratin filaments unraveled. *J. Cell. Biol.* **1983**, *97*, 1131–1143. [CrossRef]
13. Alashwal, B.Y.; Gupta, A.; Husain, M.S.B. Characterization of dehydrated keratin protein extracted from chicken feather. In *IOP Conference Series: Materials Science and Engineering*; IOP Publishing: Bristol, UK, 2019; Volume 702, p. 012033.
14. Reichl, S.; Borrelli, M.; Geerling, G. Keratin films for ocular surface reconstruction. *Biomaterials* **2011**, *32*, 3375–3386. [CrossRef] [PubMed]
15. Dias, G.J.; Haththotuwa, T.N.; Rowlands, D.S.; Gram, M.; Bekhit, A.E.D.A. Wool keratin—A novel dietary protein source: Nutritional value and toxicological assessment. *Food Chem.* **2022**, *383*, 132436. [CrossRef] [PubMed]
16. Gupta, A.; Kamarudin, N.B.; Kee, C.Y.G.; Yunus, R.B.M. Extraction of keratin protein from chicken feather. *J. Chem. Chem. Eng.* **2012**, *6*, 732–737.
17. Shavandi, A.; Bekhit, A.E.-D.A.; Carne, A.; Bekhit, A. Evaluation of keratin extraction from wool by chemical methods for bio-polymer application. *J. Bioact. Compatib. Polym.* **2017**, *32*, 163–177. [CrossRef]
18. Rajabinejad, H.; Zoccola, M.; Patrucco, A.; Montarsolo, A.; Rovero, G.; Tonin, C. Physicochemical properties of keratin extracted from wool by various methods. *Text. Res. J.* **2018**, *88*, 2415–2424. [CrossRef]
19. Alahyaribeik, S.; Ullah, A. Methods of keratin extraction from poultry feathers and their effects on antioxidant activity of extracted keratin. *Int. J. Biol. Macromol.* **2020**, *148*, 449–456. [CrossRef]
20. Sinkiewicz, I.; Śliwińska, A.; Staroszczyk, H.; Kołodziejska, I. Alternative methods of preparation of soluble keratin from chicken feathers. *Waste Biomass Valorization* **2017**, *8*, 1043–1048. [CrossRef]
21. Wang, K.; Li, R.; Ma, J.H.; Jian, Y.K.; Che, J.N. Extracting keratin from wool by using l-cysteine. *Green Chem.* **2016**, *18*, 476–481. [CrossRef]
22. Laemmli, U.K. Cleavage of structural proteins during the assembly of the head of bacteriophage T4. *Nature* **1970**, *227*, 680–685. [CrossRef]
23. Breßler, I.; Kohlbrecher, J.; Thünemann, A.F. SASfit: A tool for small-angle scattering data analysis using a library of analytical expressions. *J. Appl. Crystallogr.* **2015**, *48*, 1587–1598. [CrossRef]
24. Rad, Z.P.; Tavanai, H.; Moradi, A.R. Production of feather keratin nanopowder through electrospraying. *J. Aerosol Sci.* **2012**, *51*, 49–56.
25. Hansen, S. Bayesian estimation of hyperparameters for indirect Fourier transformation in small-angle scattering. *J. Appl. Crystallogr.* **2000**, *33*, 1415–1421. [CrossRef]
26. Skieresz-Szewczyk, K.; Jackowiak, H.; Buchwald, T.; Szybowicz, M. Localization of alpha-keratin and beta-keratin (Corneous Beta Protein) in the epithelium on the ventral surface of the lingual apex and its lingual nail in the domestic goose (*Anser Anser f. domestica*) by using immunohistochemistry and Raman microspectroscopy analysis. *Anat. Rec.* **2017**, *300*, 1361–1368.
27. Wang, X.; Shi, Z.; Zhao, Q.; Yun, Y. Study on the structure and properties of biofunctional keratin from rabbit hair. *Materials* **2021**, *14*, 379. [CrossRef]
28. Du, W.; Zhang, L.; Zhang, C.; Cao, J.; Wang, D.; Li, H.; Li, W.; Zeng, J. Green and highly efficient wool keratin extraction by microwave induction method. *Front. Mater.* **2022**, *8*, 789081. [CrossRef]
29. Cai, S.; Singh, B.R. A distinct utility of the amide III infrared band for secondary structure estimation of aqueous protein solutions using partial least squares methods. *Biochemistry* **2004**, *43*, 2541–2549. [CrossRef]
30. Fernández-d'Arlas, B. Tough and functional cross-linked bioplastics from sheep wool keratin. *Sci. Rep.* **2019**, *9*, 14810. [CrossRef] [PubMed]
31. Saravanan, S.; Sameera, D.K.; Moorthi, A.; Selvamurugan, N. Chitosan scaffolds containing chicken feather keratin nanoparticles for bone tissue engineering. *Int. J. Biological. Macromol.* **2013**, *62*, 481–486. [CrossRef]
32. Yildiz, H.B.; Kiralp, S.; Toppare, L.; Yilmaz, F.; Yagci, Y.; Ito, K.; Senyo, T. Conducting copolymers of 3-methylthienyl methacrylate and p-vinylbenzyloxy poly (ethyleneoxide) and their electrochromic properties. *Polym. Bull.* **2005**, *53*, 193–201. [CrossRef]
33. Pedersen, J.S. Form factors of block copolymer micelles with spherical, ellipsoidal and cylindrical cores. *J. Appl. Crystallogr.* **2000**, *33*, 637–640. [CrossRef]
34. Schnablegger, H.; Singh, Y. *The SAXS Guide: Getting Acquainted with the Principles*, 3rd ed.; Anton Paar GmbH: Graz, Austria, 2011.
35. Feroz, S.; Muhammad, N.; Ratnayake, J.; Dias, G. Keratin-Based materials for biomedical applications. *Bioact. Mater.* **2020**, *5*, 496–509. [CrossRef] [PubMed]
36. Lai, H.Y.; Setyawati, M.I.; Ferhan, A.R.; Divakarla, S.K.; Chua, H.M.; Cho, N.J.; Chrzanowski, W.; Ng, K.W. Self-assembly of solubilized human hair keratins. *ACS Biomater. Sci. Eng.* **2020**, *7*, 83–89. [CrossRef] [PubMed]

37. Barone, J.R.; Schmidt, W.F.; Liebner, C.F. Thermally processed keratin films. *J. Appl. Polym. Sci.* **2005**, *97*, 1644–1651. [CrossRef]
38. Hémonnot, C.Y.; Mauermann, M.; Herrmann, H.; Köster, S. Assembly of simple epithelial keratin filaments: Deciphering the ion dependence in filament organization. *Biomacromolecules* **2015**, *16*, 3313–3321. [CrossRef] [PubMed]
39. Ramya, K.R.; Thangam, R.; Madhan, B. Comparative analysis of the chemical treatments used in keratin extraction from red sheep's hair and the cell viability evaluations of this keratin for tissue engineering applications. *Process Biochem.* **2020**, *90*, 223–232. [CrossRef]
40. Dänicke, S.; Hegewald, A.K.; Kahlert, S.; Kluess, J.; Rothkötter, H.J.; Breves, G.; Döll, S. Studies on the toxicity of deoxynivalenol (DON), sodium metabisulfite, DON-sulfonate (DONS) and de-epoxy-DON for porcine peripheral blood mononuclear cells and the Intestinal Porcine Epithelial Cell lines IPEC-1 and IPEC-J2, and on effects of DON and DONS on piglets. *Food Chem. Toxicol.* **2010**, *48*, 2154–2162.
41. Ji, Y.; Chen, J.; Lv, J.; Li, Z.; Xing, L.; Ding, S. Extraction of keratin with ionic liquids from poultry feather. *Sep. Purif. Technol.* **2014**, *132*, 577–583. [CrossRef]
42. Feroz, S.; Muhammad, N.; Dias, G.; Alsaiari, M.A. Extraction of keratin from sheep wool fibres using aqueous ionic liquids assisted probe sonication technology. *J. Mol. Liq.* **2022**, *350*, 118595. [CrossRef]
43. Rybacki, K.; Love, S.A.; Blessing, B.; Morales, A.; McDermott, E.; Cai, K.; Hu, X.; Salas-de la Cruz, D. Structural and morphological properties of wool keratin and cellulose biocomposites fabricated using ionic liquids. *ACS Mater. Au* **2021**, *2*, 21–32. [CrossRef]
44. Reddy, C.C.; Khilji, I.A.; Gupta, A.; Bhuyar, P.; Mahmood, S.; AL-Japairai, K.A.S.; Chua, G.K. Valorization of keratin waste biomass and its potential applications. *J. Water Process. Eng.* **2021**, *40*, 101707. [CrossRef]
45. Esparza, Y.; Bandara, N.; Ullah, A.; Wu, J. Hydrogels from feather keratin show higher viscoelastic properties and cell proliferation than those from hair and wool keratins. *Mater. Sci. Eng. C* **2018**, *90*, 446–453. [CrossRef] [PubMed]
46. Ramirez, D.O.S.; Carletto, R.A.; Tonetti, C.; Giachet, F.T.; Varesano, A.; Vineis, C. Wool keratin film plasticized by citric acid for food packaging. *Food Packag. Shelf Life* **2017**, *12*, 100–106. [CrossRef]
47. Khodaei, D.; Álvarez, C.; Mullen, A.M. biodegradable packaging materials from animal processing co-products and wastes: An overview. *Polymers* **2021**, *13*, 2561. [CrossRef] [PubMed]
48. Chilakamarry, C.R.; Mahmood, S.; Saffe, S.N.B.M.; Arifin, M.A.B.; Gupta, A.; Sikkandar, M.Y.; Begum, S.S.; Narasaiah, B. Extraction and application of keratin from natural resources: A review. *3 Biotech* **2021**, *11*, 220. [CrossRef] [PubMed]

II

Journal of Renewable Materials

Tech Science Press

DOI: 10.32604/jrm.2024.056251 Published Online: 09 October 2024

REVIEW

Synthesis and Properties of Biomimetic Self-Assembling Structures from Poultry Feather Keratin

Sara Mattiello and Carlo Santulli*

School of Science and Technology, Università di Camerino, via Gentile III da Varano 7, Camerino, 62032, Italy

*Corresponding Author: Carlo Santulli. Email: carlo.santulli@unicam.it

Received: 17 July 2024 Accepted: 19 September 2024

ABSTRACT

Taking a widely contaminated yet abundant waste, such as poultry feathers, and extracting keratin from this structure appears to be a real challenge whenever the preservation of the secondary structure of the protein is desired. This process would allow exploiting it in ways (e.g., in the biomedical field) that are inspired by a structure that is primarily designed for flight, therefore capable specifically of withstanding flexure and lateral buckling, also with very low thicknesses. The preservation of the structure is based on disulfide crosslinks, and it is offered with preference by some chemical treatments, mainly those based on ionic liquid and on a reduction process. However, the degree of preservation cannot always be precisely assessed; however, beyond chemical characterization, the formation of homogeneous gels can also suggest that the process was successful in this sense. An extraction respectful of nature's intentions, considering that the secondary structure builds up according to the very function of the feathers in the animal, can be deemed to be biomimetic. In particular, biomimetic extractions comply with the very characteristics the protein was designed for to serve in the specific environmental and mechanical situation in which it is inserted. This review tries to elucidate in which cases this aim is achieved and for which specific applications a chicken feather keratin that has preserved its secondary structure can be suited.

KEYWORDS

Keratin extraction; secondary structure; self-assembly; chicken feathers

Nomenclature

[Amim]Cl	1-Allyl-3-methyl-1H-imidazol-3-ium chloride
[Bmim]Br	1-Butyl-3-methylimidazolium bromide
[Bmim]Cl	1-Butyl-3-methylimidazolium chloride
[HOEMIm]	1-hydroxyethyl-3-methylimidazolium bis(trifluoromethanesulfonyl)amide
FTIR	Fourier transform infrared spectroscopy
ILs	Ionic Liquids
[NTf_2]	1-Butyl-3-methylimidazolium bis(trifluoromethylsulfonyl)imide
PBAT	Poly(butylene adipate-co-terephtalate)
PCL	Polycaprolactone
PVA	Poly(vinylalcohol)
SAXS	Small angle X-ray scattering

1 Introduction

A biomimetic approach to materials would regard the possibility of promoting their self-assembly in a way that allows the growth of autonomous structures to be used for functional purposes [1,2]: this procedure is particularly sought in the case of peptides and proteins [3]. More specifically, the typical structures of proteins, such as collagen, elastin, and keratin, all include some degree of α-helices arrangements [4]. The most recent novelty, however, is constituted by the possibility of obtaining these structures out of the material extracted from animal waste, which enables the establishment of correlations between their aspect and the route by which self-assembly has been realized [5]. As far as protein extraction is concerned, extracted material takes the form of hydrolysates and small peptides [6]. These nanomaterials can have a role in acquiring a biomimetic function towards appropriate training exerted on non-natural protein backbones [7]. In other words, some extraction methods confer to the material a higher capability to resist proteolysis than others and can be regarded as adapted to its biomimicking [8].

In practice, keratin-based waste from different origins/biological structures can be used for the purpose: these include, among others, sheep wool in the form of hydrolyzed peptides [9], or in more structured form for direct blending with biopolymers [10], where a biomimetic approach might reduce the final risk of generating other hazardous material difficult to dispose of [11]. Other keratin residues in search of sustainable routes for disposal are human hair [12], epidermal waste [13], nails [14] or claws [15], and poultry feathers [16], on which this review specifically focuses.

Chicken feathers can be considered dense shells with a porous core, which provides lightness and is able to be compressed or even locally torqued without being buckled [17]. Their application as fibers (chicken feather fibers, CFF) in composites, purposely separated from the rachis [18], though proposed in many cases, does reduce this structural complexity to the bare tensile support of a polymer resin [19]. On the other hand, keratin extraction may result in the destruction of the composite structure, which is the scope of the biomimetic process to avoid. The main issue is unlocking the protein by extracting it without damaging its secondary structure and, therefore, promoting the self-assembly of the keratin structure in another geometry from the original one [20]. The secondary structure is mainly influenced by the position of the side chains and hence the degree of close packing in the protein, which for keratin is controlled by the presence of a number of different motifs [21], namely α-helical, β sheets, β-turn, and random coil structures [22].

In practice, the organization of chicken feathers includes, as the effect of the judicious combination of α and β forms, the combined presence of crossed-lamellar structure (300–600 nm thick) in lateral walls of rachis and barbs, arranged into alternate layers of crossed-fibers [23]. A significant grade of preservation of this structure out of keratin extraction is particularly beneficial in terms of toughness, which also allows its blending with other proteins isolated, e.g., from soy, for the formation of composite films [24].

The isolation of keratin from poultry feathers has been demonstrated of interest in the last few decades, especially, but not exclusively, in the food-related and the cosmetics sector [25]. Here, the preservation of secondary structure is not always considered essential [26], while rather preventive purification processes, based, e.g., on ethanol, ozone, and sodium chlorite, are given larger significance [27]. Another possibility, which is specific to poultry-originated keratin is the capability to absorb some metals, e.g., in soil treatment, such as cadmium, nickel, chromium, and zinc [28]. In some cases, nonetheless, the use of keratin from poultry feathers can be considered biomimetic, more explicitly whenever the architecture of the folding structure is considered and used to achieve specific functionalities. This has been, e.g., recently performed in the case of carbonized feathers therefore used as biochar [29], where the preservation of keratin structure did result in the possible application to the removal of the residues of drugs, such as amoxicillin, from aqueous solutions [30]. Keratin biochar is also particularly adapted to be possibly blended with other similarly abundant biomass waste, such as is the case for sugarcane bagasse,

which suggests synergistic effects to be obtained from adapted doping strategies between the two feedstocks [31]. However, the energy-intensive character of these processes based on carbonization has also suggested that to use chicken feathers with a biorefinery approach, biodegradation/metabolism by the action of bacteria would represent a more suitable route towards the extraction of free amino-acids and soluble proteins [32].

To allow the potential use of keratin extracted, hence solubilized, from chicken feathers, a possible approach is based on the fabrication of autogenous cross-linked gels, e.g., serving as plant growth media [33]. On the one hand, this route can provide some mechanical performance that might ease application and compete, at least as blends, with other categories of gel structures, such as those obtained from polysaccharides, e.g., starch [34], alginates [35], or guar gum [36]. On the other hand, restoring secondary structure, hence protein cross-linking, starting from disulfide links, but not limiting to them, would represent a more natural application of keratin, therefore providing also other characteristics, such as controlled water retention, elongation, and strength [37]. These properties were exploited for some uses, such as wound healing, using a blended film with polysaccharides [38], or in a more general sense, in the biomedical engineering sector, including, e.g., also applications for drug delivery [39].

This review concentrates on chicken feathers since they constitute a very large waste of the food-related production sector, and therefore, their functional use would possibly result in a circular economy approach, offering a larger value to waste. Using poultry feathers in a biomimetic way for the production of engineered structures does involve preserving as much as possible their features during extraction, in the understanding that keratin-based structures do present a number of fundamental biomimetic properties in a thermal insulation and low-density context, which include reversible adhesion, structural coloration and the possibility to offer super-hydrophobic surfaces [40]. To achieve this potential, it is important, though, to preserve as much as possible the secondary structure of feather keratin, which will be described in Section 2. A number of methods exist for the extraction of keratin from feathers, which are reported in Section 3.

Following this, the discussion does particularly concentrate on those works where keratin is extracted with the preservation of its secondary structure, which can be suggested to represent a biomimetic application of poultry feathers' keratin. With this aim, bio-inspired materials based on poultry feather keratin are discussed, after general considerations of the keratin role in these materials (Section 4.1), being either exclusively based on keratin or as a significant component of a blend with another biopolymer (Section 4.2). Finally, applications with particular reference to the bio-inspired potential, therefore with evidence of self-assembly, are discussed (Section 4.3). Conclusions and potential for future research are offered in Section 5.

2 Structure of Keratin in Feathers

The design of a chicken feather is constituted on hierarchical levels, depicted in Fig. 1 [41], namely the basal calamus, the main structure of the rachis, from which barbs, and then barbules irradiate. Recent studies also emphasized the variable characteristics of feather design between broiler chicken, reared for meat production, and layer chicken, which are intended at egg production instead [42]. This occurs since the feathers have specialized functions, in particular, contour feathers are dedicated to flight, down feathers serve for insulation, and small ornamental ones are aimed at signaling for social activity. The different dimensional levels represented are deemed to constitute the base for the engineering of feathers' functionality, comprising flight ability and thermal insulation properties [43]. In other words, they are able to transform through a controlled and tailored spiraliform arrangement, a unidimensional appendage into a volumetric body capable of actively sustaining the flight action [44]. In particular, the section of the rachis comprises epicortex, with crossed-fiber architecture, made of β keratin, which offers a trabeculae-like support [45], then cortex and the medullary pith with its foam-like structure [46]. The latter has recently been proposed as to offer some bio-inspired action of thermal insulation due to its

cellular geometry [47]. Keratin fibers are arranged in a cross-like architecture being coated with amorphous protein: this disposition is connected to the need to withstand specific forces during flight, mainly by flexural and shear loads, maintaining a sufficient flexibility notwithstanding the required stiffness offered by the protein structure [48]. In particular, an uninterrupted structural connection appears to be formed between the cortex of the rachis and the barbs [49]. The idea is that the rooting of barbs within the rachis is helpful in withstanding the aerodynamic forces during flight [50]. As a matter of fact, the whole structure of the feather optimizes bending stiffness to sustain loading in flight: in that respect, the heavily deformed structure is then recovered by immersion in water, aimed at simulating air moisture effect [51].

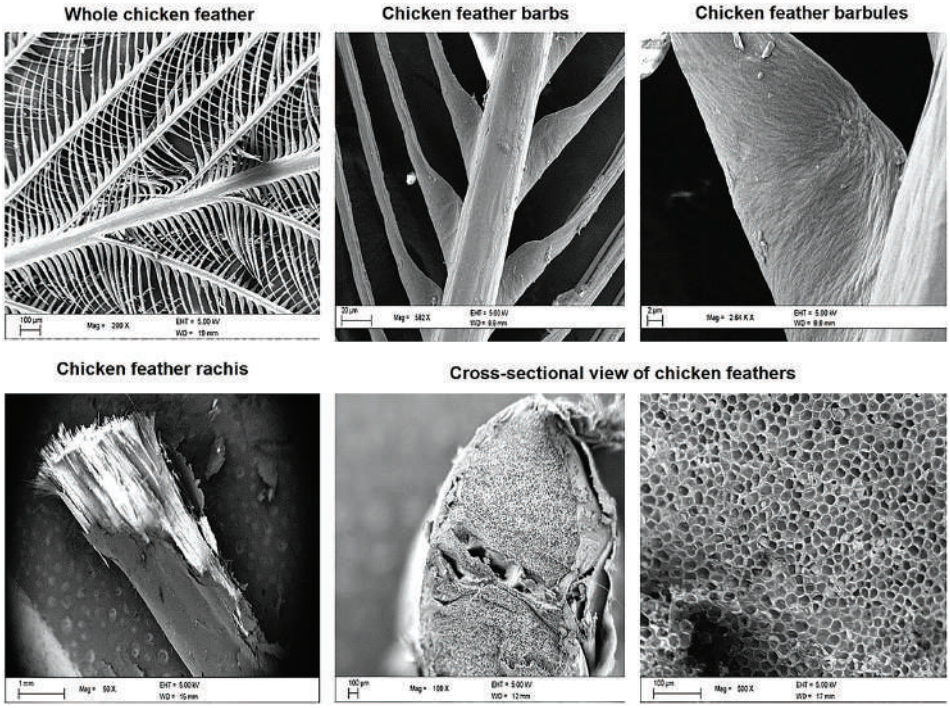

Figure 1: Different parts of keratin feathers, showing hierarchical structure (Reproduced with permission from Reference [43], © Elsevier 2017)

At a microscopical level, though, the structure of feather keratin takes the form of microfibrils, less ordered with respect to alpha-keratin, yet still following a composite arrangement such as fiber + matrix [52]. It has been also suggested that the natural model followed during feather development, and that has therefore to be accounted for in the self-assembly process, is that of a simple twisted β-sheet [53], as indicated in Fig. 2, which details the different dimensional levels. Investigations carried out by small angle X-ray scattering (SAXS) have demonstrated the more compact short-range organization of feather keratins with respect to wool keratin [54].

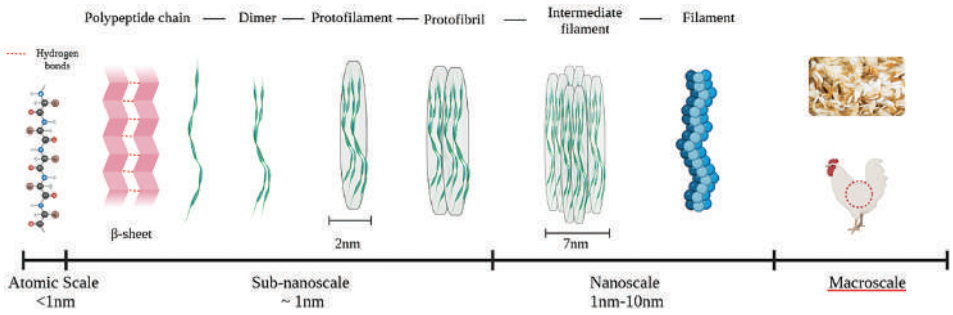

Figure 2: Schematic representation of keratin structure ranging from the atomic scale to the macroscale (Adapted from Reference [20] © Elsevier 2022)

Going more into detail, into the molecular level, keratin is generally rich in cysteine, which creates a strong covalent disulfide bond, which results in crosslinking, promoting therefore an increased hardness of the structures [55]. This ultimately contributes to cornification, hence conversion into a horn structure, of epithelial cells of feathers [56].

3 Methods for the Extraction of Keratin from Feathers and Preservation of the Secondary Structure

Different methods are available to extract keratin from feathers (a summary of the various techniques adopted is offered in Fig. 3), among which this review gives preference to those that are able to preserve its secondary structure, which results also in maintaining its antioxidant potency [57]. A number of chemical methods like reduction [58], ionic liquid [59] and alkaline hydrolysis [60], are used for keratin extraction, but not all of them preserve the secondary structure. The completeness of the secondary structure preservation is difficult to assess, even for recent studies that concentrate on the morphological characteristics of the keratin extracted from feathers the amount of β sheets crosslinked by disulfide bonds was not easily measurable from microscopical observation [61]. More reliable measurements can be offered by quantitative Raman spectroscopy, especially by comparing the intensity of the peaks representing S-S disulfide bridges and β sheets, typically around 521 and 1662 cm^{-1}, respectively [62]. Apart from the extraction process, it is also worth noting that the application of tensile stress on the keratin structure might lead to a more reduced preservation of disulfide bonds, due to their stretching, which might also be ascribed to the agitation process during chemical action [63].

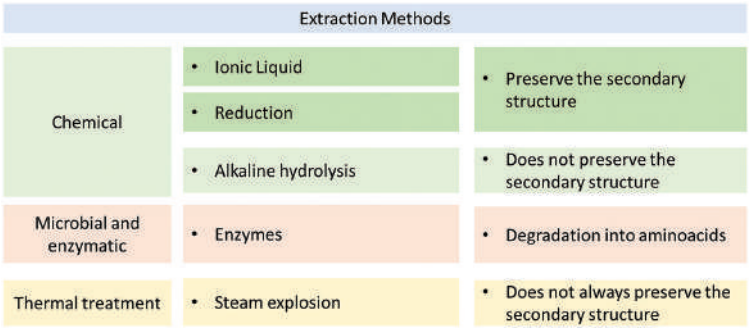

Figure 3: Summary of extraction methods used for feathers keratin

In particular, alkaline hydrolysis, also facilitated by cetrimonium bromide, resulted in a significant disruption of the hydrogen links and in the virtual absence of peptides at 200°C [64]. Often alkaline methods are assisted by microbial and enzymatic ones [65] using keratinases [66]. These can operate autonomously in a biorefinery concept, involving diversification of products and full use of waste resources [67]. This contributes to the complete use of the whole of feather residues, in a circular economy approach, as reported in Fig. 4. Further assistance can be provided by ultrasound irradiation [68], or by microwave treatment [69], where the texture and morphology of extracted material can be controlled by the time and energy of irradiation [70]. In all these cases, the final product yielded are functional protein + hydrolysates of interest for the food industry [71]. Another important factor, which in particular influenced the preservation of the secondary structure, while not directly related with the adopted method, is the retention time in the alkaline solution, since keratin is typically soluble in variable amounts depending on the pH of the relevant environment [72].

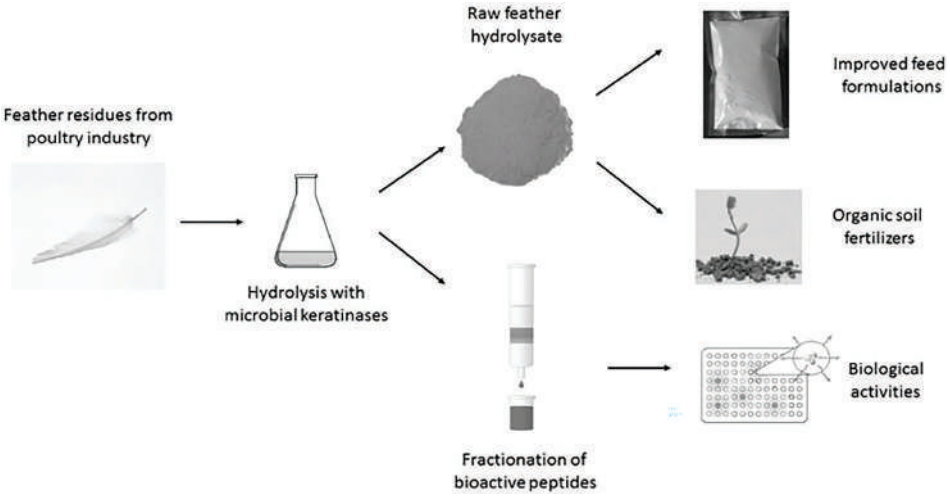

Figure 4: Different destinations of poultry feathers by a microbial enzymatic extraction (Reproduced with permission from Reference [67], © Elsevier 2015)

Ionic liquids (ILs) method for the extraction preserves the structure of the keratin, at least partially, with yields as high as 45% in turkey feathers [73]. In particular, on chicken feathers, the use of ILs [Amim]Cl, [Bmim]Cl and [Bmim]Br have been studied by Ji et al. [74], demonstrating that the imidazole liquid [Bmim]Cl can extract keratin from feathers, the solvent of IL is non-volatile and easy recyclable. Other hydrophobic IL have been used, such as [HOEMIm] [NTf_2], which offers molecular weights for extracted keratin in the order of 10,000 [75]. Moreover, with extraction using ionic liquids, there is no discharge of pollutants, which goes in agreement with circular economy and eco-friendliness, since the ionic liquid is easily separated from keratin, and it benefits the recycling of the salt, being not detrimental to the quality of extracted keratin [76].

The reduction method that uses mercaptoethanol has a high yield, and preserves the secondary structure of the keratin, yet being harmful for the possible non-preservation of mercaptan in the final product, hence its possible discharge [77]. The reduction with sulfitolysis method, using sodium sulfate or sodium

metabisulfite, is the most extensively used for the extraction of keratin due the good yield, low toxicity, and the likely preservation of the secondary structure of the protein [78]. Treatment with thiourea leads also to sufficient self-assembly properties, which are deemed to depend on the preservation of cysteine residues, with possible re-oxidation of free cysteine thiols, specifically responsible for the possible recoiling of the protein: this method has been widely applied on wool keratin [79]. A symptom of the degree of potential self-assembly of extracted keratin is described by the formation of homogeneous gels, normally at rather neutral pH. As a consequence, methods based on sulfitolysis treatment offer larger availability due to the larger presence of sulfato-kerateines, for biomedical applications [80].

Thermal treatments for the extraction of keratin appear to be quicker and are therefore prevalently used in the industrial sector. The steam flash explosion is a process based on a hydrolysis in high temperature and pressure, the exposure of keratin to these conditions allows obtaining the disintegration of the proteins [81], and a significant modification of the secondary structure with an increase of the disorder domains [82]. Furthermore, it can even assist alkaline hydrolysis into increasing the extraction rate of keratin from feathers up to over 65% [83]. However, although β sheets are comparatively more diffuse than α-helical, β-turn, and random coil structures, steam explosion does maintain on the other side a tertiary structure of partially coiled proteins in a generally more polar environment [84]. In this context, the use of supercritical water does also induce an extensive depolymerization of keratin into aliphatic chains [85]: in other contexts, this process appears particularly suitable for the production of bio-hydrogen [86].

4 Bio-Inspired Materials Obtained from Poultry Feathers with Preservation of Secondary Protein Structure

4.1 General Considerations

In this section, the structures that have been obtained using keratin extracted from chicken feathers with preservation of protein secondary structure, further down defined as “conservative methods”, therefore with the possibility of self-assembly, are presented and discussed. As from the above considerations, the preservation of secondary structure is allowed by extracting keratin through chemical processes (ionic liquids, and reduction) and all the works that will be mentioned in this section will involve the use of the aforementioned methods. Possibly the most suitable demonstration that the secondary structure has been preserved is linked to Fourier transform infrared spectroscopy (FTIR), finding out that cysteine-S-sulfonated residues are still present in the sample, which are able to promote self-assembly [87]. This is usually correlated with a 1024 cm^{-1} sharp peak observed in the FTIR results [88].

To recognize the function of keratin and its self-assembly, it is sometimes complicated. This was noticed in early studies on avian feathers, in particular, due to the fact that the fit-for-purpose alternance of α and β structures with specific monomers, defined as φ keratins, leads to a non-obvious relation between the subunits and the tissue morphology [89]. In other words, the macroscopic geometry does not immediately recall the function, such as it occurs instead in other cases, for example ligno-cellulosic fibers, which are clearly designed for structures intended for tension and possibly torque [90]. Provided the preservation of the secondary structure is adequately achieved, feather keratin arranged in the β form suggests the prevalence of the resistance to defect propagation, described as toughness, rather than the bare mechanical strength [91]. This exceptional toughness is achieved by incorporating matrix and filaments into an only protein, whose structural preservation is therefore of paramount importance [92].

It has been elsewhere recognized that the characteristics of crosslinked gels formed from keratin obtained from chicken feathers are different from those from other sources, such as hair and wool, namely as for viscoelastic properties and in particular a higher cell proliferation [93]. In terms of blending, poultry keratin can be associated with a large variety of biodegradable and conventional polymers, as reported in [94,95]. The already mentioned autogenous cross-linking of poultry feather keratin gels has also potential to offer bio-based cross-linking agents in other contexts, such as rubber,

avoiding on one hand the use of carbon black as hardener, while on the other side the high nitrogen content of feathers would delay the thermal degradation of rubber up to 400°C [96]. However, this is not the kind of operation that would provide any bio-inspired sense to the keratin structure, which is used as just the replacement of the synthetic counterpart, trying to match as much as possible its performance. The same concept applies when using keratin as a bare filler for lignin and bio-epoxy to increase possibly to 100% the bio-based content of a composite [97].

4.2 Development and Function of Keratin Materials and Blends Extracted with Conservative Methods

The preservation of the secondary structure in chicken keratin can serve to various purposes, which enhance the characteristics of the material beyond its bare properties of hardness and toughness, enabling applications that span from the biomedical field to the production of biodegradable materials to other technical applications, such as water treatment. This potential has particularly been demonstrated in connection with the large availability of keratin waste products to be reprocessed, which offer large amounts of material for study [98]. Typically, to grow beyond the nanometric level, the material needs to be added with some plasticizers/biopolymers, a large variety of which was demonstrated effective to the purpose. The use of keratin feather fibers by bare alkali treatment, therefore at a micrometric dimensional level, taking the example of lignocellulosic fillers, while it allows introducing large amounts of fibers (up to 60 wt.% in [99] using PLA and PBAT), on the other hand it penalizes tensile strength in polymers, suggesting rather their use for acoustic panels, or similar applications, generally as bio-insulation [100]. It is also noteworthy that preservation of secondary structure is not particularly sought for when extracted feather fibers are only exploited in terms of their compressive densification in a sponge-like geometry, such as in [101], where enzymatic extraction was preferred [102]. In this sense, other applications are not in need of any particular efficiency for keratin extraction, such as it is the case for oil spill absorption [103], use as natural flocculants for the treatment of potato starch wastewater [104], or heavy metal ions (e.g., hexavalent chromium) removal from wastewater [105], as an alternative to the use of polysaccharide absorbers, such as chitosan [106]. However, also for this application, an extraction of keratin with reduction by sodium sulfite and sodium hydroxide showed effectiveness over a larger spectrum of metals [107].

The same applies when keratin fibers are supposed to be employed as fillers possibly with considerable tensile elongation and in small tenors in biopolymer blends, such as for PLA/PHB in [108], where strain at break was brought as high as to 140%. Here, it can be suggested that protein hydrolysates would do their job better in terms of low-quantity fillers for tensile elongation, with no need for preservation of the secondary structure. Conversely, the extraction of keratin capable of potential self-assembly opens the field to further sectors, which require smaller film thicknesses and more controllable mechanical properties, especially in shear, as desirable in applications such as biomedical and bioplastics. The quality of self-assembly through preservation of the secondary structure offers keratin with higher shear properties, which enable molding of structure for wound healing and tissue regeneration [109].

To avoid including chicken keratin in other polymers, which is likely to be a suitable approach for keratin with self-assembling properties, a possible solution is its plasticization through polyols, such as glycerol. An amount of glycerol between 2% and 10% was used in [110], processing bioplastics at 60°C, from feathers extracted using sodium sulfide. Another work on sodium sulfide extraction from chicken feathers used glycerol in an amount of 3.5%, adding then a smaller amount of microcrystalline cellulose (0.2%) in a sodium hydroxide solution for 48 h again at 60°C, to offer improved mechanical properties [111]. The idea was to offer a bioplastic film, which could be aimed at various applications, including biomedical, pharmaceutical and generally biopolymer development. Other films with chicken keratin extracted by sulfitolysis, yet with plasticization enhanced by citric acid, did include 25% glycerol [112]. Adding more glycerol gradually affects tensile strength and solubility, whilst increasing elongation at

break up to 35% glycerol content, where still swelling is below 17% for a urea-sodium sulfide high yield (73%) extraction [113]. A possible alternative polyol plasticizer for chicken keratin is sorbitol, which offered good performance in a 2-mercaptoethanol extraction with concentrated urea solution using sodium dodecyl sulfate (SDS) [114].

Passing to the blends of conservatively extracted keratin with chicken feathers with biopolymers, the variety of solutions attempted appear considerable and would especially depend on the application that was proposed for the keratin-based structure. It is also noteworthy that some polymers, such as poly (ethylene oxide) (PEO), are able to hinder the self-assembly of cysteine residues, and therefore keratin blending with them might not always be desirable for the production of biomaterials, though it eases electrospinning of fibers [115].

In particular, in the biomedical field, keratin nanoparticles are particularly effective in producing drug delivery systems, where their distinct advantages are their generous surface area, and encapsulation efficiency, which results in a controlled drug release [116]. Successful examples have been provided using poly(vinyl alcohol) (PVA) in crosslinked films with dialdehyde starch [117,118]. In other uses, the objective might also be orienting the specific polymer towards more focused properties through its blending with potentially self-assembling keratin [119]. This occurred for example with polycaprolactone (PCL)-human hair keratin blend coated with hydroxyapatite particles, when the objective is to fabricate scaffolds for human bone regeneration [120].

The capability of keratin to contribute to faster regeneration and to promote hydration in tissue engineering is well recognized [121]. More recently, also the combination of an adapted reduction process and the capability to regenerate natural tissue has received a considerable deal of attention [122–124]. In the case of the use of keratin from chicken feathers, a limited number of studies, summarized in Table 1, do possibly represent combinations with polymers that do not exclude in principle a self-assembly process, because of keratin extraction performed through reduction processes.

Table 1: Studies on biopolymer composites with keratin from chicken feathers obtained with reduction processes

Biopolymer	Keratin extraction method	Amount of keratin	Application	Reference
Chitosan	Dialysis precipitated by HCl	0.5% w/v nanoparticles	Bone tissue regeneration	[125]
Chitosan/PLA	Feather fibers	Up to 4%	Bone tissue regeneration	[126]
PVA/PVP/ starch	NaOH	56% w/v	Biomedical hydrogel	[127]
PHB	Sodium sulfide-L-cysteine	20% w/v	Scaffolds	[128]
PVA	0.1 M Na_2S and 5% NaOH	20% w/v	Neural repair scaffold	[129]

A conclusion can be that most studies on keratin from poultry feathers do not effectively preserve the secondary structure of the protein, though in general this would appear to be necessary to improve the application profile of the material, especially in terms of upcycling, whenever this is obtained from industrial waste. As a consequence, the following section does concentrate on those studies where explicitly this characteristic leading to self-assembly is declared or evident and possibly the extraction method for keratin is tailored to obtain this result.

4.3 Self-Assembled Structures: Nanoparticles and Nanofibers

To summarize what has been exposed previously, when maintained in a natural system and at adapted conditions of pH, temperature, etc. Keratin has the tendency to self-assemble into functional structures (e.g., hair, nails, feathers…) due to their specific amino acid sequences and interactions.

A natural example of self-assembly of beta keratin fibers is the photonic system that is created inside the feathers of some birds which generates the structural color of the feather itself [130,131].

In general, self-assembly is an intrinsic property of keratin proteins that is favored by environmental conditions during the experimental process. In particular, the self-assembly potential does depend on the chemical action performed, including nature of the chemical involved pH, temperature, and retention time, yet also may be affected by the mechanical action, such as in the case of vapor pressure for steam explosion, which hinders the preservation of cysteine residues [132]. Cysteine residues present in keratin proteins form the S-S bonds, which are responsible for the structural stability and self-assembly. At the same time the hydrophobic and hydrophilic regions of the proteins allow it to interact with itself and other molecules in aqueous environments, promoting self-assembly [133]. This suggested the potential use of keratin waste-based materials also in the field of biomedical scaffolding [134].

Self-assembling properties are found in the formation of keratin nanoparticles. Keratin nanoparticles have a high tendency to create interparticle bonds, leading to the creation of larger structures such as nanofibrils or nanolayers. The reconstruction of disulfide bonds during dialysis, used during the extraction method, is crucial for the structural integrity and stability of the keratin nanoparticles. These bonds help maintain the folded structure of the proteins and promote aggregation. Hydrogen bonds between the backbone and side chains of keratin molecules stabilize the secondary and tertiary structures, facilitating the formation of beta-sheets and subsequent self-assembly into nanoparticles [135]. Hydrophobic regions of keratin molecules tend to aggregate to minimize exposure to the aqueous environment, driving the self-assembly process. By modifying the incubation time, the temperature, together with pH and concentration of keratin in solution, the dimensions and characteristics of the nanostructures can be controlled, offering various building blocks that allow a tailored and effective design of the nanostructure passing from 1-D to 3-D geometries at the nano-level, as detailed in Fig. 5. This suggests to better orient the envisaged application in the biomedical field offering further advantages are low immunogenicity, colloidal stability and biodegradability [136].

Dialysis process can also influence the mechanism of self-assembly creating a gel. The mechanism called “gelation” is due to the intermolecular interactions and the reformation of disulfide bonds. Viscoelastic properties of this kind of gels can be controlled by manipulating disulfide bond reoxidation and cross-link density during the dialysis process. Keratin gels are primarily stabilized by disulfide bonds, though complete dissolution is only possible by disrupting hydrophobic interactions and hydrogen bonds as well. As suggested above, the appearance and viscoelastic properties of the gels are also influenced by pH and temperature.

The self-assembly of keratin fibers plays a crucial role in determining their mechanical properties and performance; this characteristic was also observed in the wet spinning process. To start from an extraction by chemical process, using mercaptoethanol, helps manipulating disulfide bonds, essential for building the keratin fibers. In particular, the self-assembly of keratin fibers via controlled disulfide bond formation involves the gradual recovery of secondary structures and the creation of ordered protein configurations. This process ultimately improves the mechanical properties of the fibers, including their toughness and durability. For instance, the regenerated keratin fibers exhibit breaking strain and toughness that were much higher than those of cotton and linen. Their toughness was nearly equivalent to that of viscose fibers. These results indicate that keratin fibers, which retain their secondary structures through continuous production, are well-suited for practical applications.

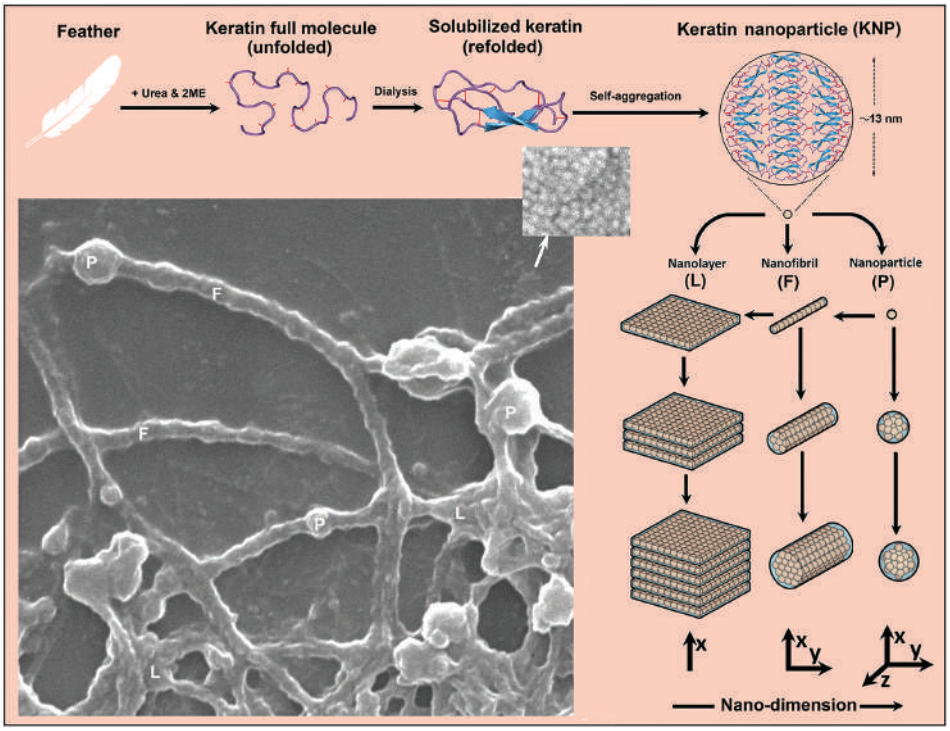

Figure 5: A schematic diagram demonstrating how keratin nanoparticles can be formed and served as the building blocks for higher nanostructures. Letters P, F and L indicate nanoparticles, nanofibrils and nanolayers, respectively (Reproduced with permission from Reference [133], © Elsevier 2020)

The ability to control and utilize this natural self-assembly process opens possibilities for creating advanced materials for biomedical applications, such as wound dressings, drug delivery systems, and tissue engineering scaffolds. In Wang et al. [137], for the production of hydrogel, it was used as an extraction method, a reduction and then an oxidation, that preserve the secondary structure of keratin. The hydrogel formation was favored by the use of H_2O_2 which promotes the formation of disulfide bonds, finally the hydrogel was used as an effective base for the formation of scaffolds useful for cell proliferation in wound healing. Similar applications have been tested by Polesca et al. [76], starting from the extraction process based on ionic liquids, they create a film of pure keratin. The formation of the film is favored by using temperatures between 50°C and 60°C. They also demonstrated non-toxicity to cells and the *in vitro* wound healing study demonstrates that this type of film improves the proliferation of keratinocytes and fibroblasts, accelerating wound healing up to 16 h.

5 Conclusions

Self-assembly of chicken feather extracted keratin, therefore intended as use in biomedical devices, such as for scaffolds and wound dressing, received some degree of attention in recent studies. On the other hand, not many works that resulted in regenerating the disulfide bonds explicitly declared the potential for

prospective self-assembly of obtained biomaterials, despite the fact that the attention towards the synthesis of nanoparticles does appear to be gradually increasing. The outcome of this review indicated the reduction extraction processes as the most suitable for the purpose, including those with use of sodium sulfite or mercaptoethanol, or also those with ionic liquids, and even more surprisingly, the extraction of keratin through steam explosion.

A final comment would concern the fact that future developments in this field, also given the very large availability of poultry feather would also be likely to invest in larger value applications for extracted keratin, which will necessarily involve the preservation of secondary structure to enable its self-assembly process in the form of nanoparticles, gels, and blends with biopolymers.

Acknowledgement: None.

Funding Statement: The authors received no specific funding for this study.

Author Contributions: Study conception and design: Carlo Santulli; data collection: Sara Mattiello, and Carlo Santulli; draft manuscript preparation: Sara Mattiello, and Carlo Santulli. All authors reviewed the results and approved the final version of the manuscript.

Availability of Data and Materials: No new data were generated.

Ethics Approval: Not applicable.

Conflicts of Interest: The authors declare that they have no conflicts of interest to report regarding the present study.

References

1. Aliprandi A, Mauro M, De Cola L. Controlling and imaging biomimetic self-assembly. Nat Chem. 2016;8(1):10. doi:10.1038/nchem.2383.
2. Levin A, Hakala TA, Schnaider L, Bernardes GJ, Gazit E, Knowles TP. Biomimetic peptide self-assembly for functional materials. Nat Rev Chem. 2020;4(1):615–34.
3. Pizzi A, Pigliacelli C, Bergamaschi G, Gori A, Metrangolo P. Biomimetic engineering of the molecular recognition and self-assembly of peptides and proteins via halogenation. Coord Chem Rev. 2020;411:213242. doi:10.1016/j.ccr.2020.213242.
4. Kumawat TK, Sharma A, Sharma V, Chandra S. Keratin waste: the biodegradable polymers. In: Blumenberg M, editor. Keratin. London: IntechOpen; 2018. doi:10.5772/intechopen.79502.
5. Piras S, Salathia S, Guzzini A, Zovi A, Jackson S, Smirnov A, et al. Biomimetic use of food-waste sources of calcium carbonate and phosphate for sustainable materials—a review. Materials. 2024;17(4):843. doi:10.3390/ma17040843.
6. Ferraro V, Anton M, Santé-Lhoutellier V. The "sisters" α-helices of collagen, elastin and keratin recovered from animal by-products: Functionality, bioactivity and trends of application. Trends Food Sci Technol. 2016;51:65–75. doi:10.1016/j.tifs.2016.03.006.
7. Czyzewski AM, Barron AE. Protein and peptide biomimicry: gold-mining inspiration from nature's ingenuity. AIChE J. 2008;54:2–8. doi:10.1002/aic.v54:1.
8. Hasan A, Saxena V, Castelletto V, Zimbitas G, Seitsonen J, Ruokolainen J, et al. Chain-end modifications and sequence arrangements of antimicrobial peptoids for mediating activity and nano-assembly. Front Chem. 2020;8:416. doi:10.3389/fchem.2020.00416.
9. Barba C, Méndez S, Roddick-Lanzilotta A, Kelly R, Parra JL, Coderch L. Cosmetic effectiveness of topically applied hydrolysed keratin peptides and lipids derived from wool. Skin Res Technol. 2008;14:243–8. doi:10.1111/srt.2008.14.issue-2.

10. Shavandi A, Bekhit AEDA, Carne A, Bekhit A. Evaluation of keratin extraction from wool by chemical methods for bio-polymer application. J Bioact Compat Polym. 2017;32:163–77. doi:10.1177/0883911516662069.
11. Ali MA, Gould M. Untapped potentials of hazardous nanoarchitectural biopolymers. J Hazard Mater. 2021;411:124740. doi:10.1016/j.jhazmat.2020.124740.
12. Havryliak V, Mykhaliuk V. The comparative analysis of the methods for keratin extraction from sheep wool and human hair. Bìol Tvarin. 2020;22(4):9–12. doi:10.15407/animbiol22.04.009.
13. Holkar CR, Jain SS, Jadhav AJ, Pinjari DV. Valorization of keratin based waste. Proc Saf Environ Protect. 2018;115:85–98. doi:10.1016/j.psep.2017.08.045.
14. Timorshina S, Popova E, Osmolovskiy A. Sustainable applications of animal waste proteins. Polymers. 2022;14(8):1601. doi:10.3390/polym14081601.
15. Petrucci R, Dominici F, Santulli C, Puglia D, Kenny J. Mechanical and thermal characterisation of poly(ethylene) and thermoplastic starch filled with keratin horn powder from bovine claws. Mater Sci Eng Adv Res. 2015;1(1):1–4. doi:10.24218/msear.2015.06.
16. Shih JC. Recent development in poultry waste digestion and feather utilization—a review. Poultry Sci. 1993;72(9):1617–20. doi:10.3382/ps.0721617.
17. McKittrick J, Chen PY, Bodde SG, Yang W, Novitskaya EE, Meyers MA. The structure, functions, and mechanical properties of keratin. JOM. 2012;64(4):449–68. doi:10.1007/s11837-012-0302-8.
18. Paşayev N, Tekoğlu O, Kocatepe S, Erol M, Maraş N. The machine method for processing chicken feathers by splitting them into fibers and rachis. Tekstil ve Mühendis. 2021;28(124):248–60. doi:10.7216/1300759920212812401.
19. Kurien RA, Biju A, Raj KA, Chacko A, Joseph B, Koshy CP. Chicken feather fiber reinforced composites for sustainable applications. Mater Today Proc. 2022;58(1):862–6. doi:10.1016/j.matpr.2021.10.400.
20. Hussain FS, Memon N. Recent developments in extraction of keratin from industrial wastes. In: Bhawani SA, Khan A, Ahmad FB, editors. Extraction of natural Products from agro-industrial wastes. Amsterdam: Elsevier; 2022. p. 281–302.
21. Zhu J, Avakyan N, Kakkis A, Hoffnagle AM, Han K, Li Y, et al. Protein assembly by design. Chem Rev. 2021;121(22):13701–96. doi:10.1021/acs.chemrev.1c00308.
22. Mason TO, Shimanovich U. Fibrous protein self-assembly in biomimetic materials. Adv Mater. 2018;30(41):1706462. doi:10.1002/adma.201706462.
23. Wang B, Yang W, McKittrick J, Meyers MA. Keratin: structure, mechanical properties, occurrence in biological organisms, and efforts at bioinspiration. Progr Mater Sci. 2016;76:229–318. doi:10.1016/j.pmatsci.2015.06.001.
24. Li X, Wei Y, Jiang S, Zhou Y, Li J, Li K, et al. Full bio-based soy protein isolate film enhanced by chicken feather keratin. Macromol Mater Eng. 2021;306:2100004. doi:10.1002/mame.v306.5.
25. Maurya SD, Singh A. Application and future perspectives of keratin protein extracted from waste chicken feather: a review. Sustain Chem Eng. 2024;5:31–45.
26. Cherry JP, Young CT, Shewfelt AL. Characterization of protein isolates from keratinous material of poultry feathers. J Food Sci. 1975;40:331–5. doi:10.1111/jfds.1975.40.issue-2.
27. Li H, Hu J, Wang X, An L. Development of a bio-inspired photo-recyclable feather carbon adsorbent towards removal of amoxicillin residue in aqueous solutions. Chem Eng J. 2019;373:1380–8. doi:10.1016/j.cej.2019.03.160.
28. Pourjavaheri F, Mohaddes F, Shanks RA, Czajka M, Gupta A. Effects of different purification methods on chicken feather keratin. Adv Mater Res. 2014;941:1184–7.
29. Adil S, Tariq S. Study of traditional and modern applications of feathers—a review. J Wild Ecol. 2020;4:141–50.
30. Chilakamarry CR, Mahmood S, Saffe SNBM, Arifin MAB, Gupta A, Sikkandar MY. Extraction and application of keratin from natural resources: a review. 3 Biotech. 2021;11:1–12.
31. Emenike EC, Amusa VT, Iwuozor KO, Ojeyemi T, Micheal TT, Micheal KT, et al. Enhancing biochar properties through doping: a comparative study of sugarcane bagasse and chicken feather. Biofuels. 2024;15:627–34. doi:10.1080/17597269.2023.2274694.

32. Chaturvedi V, Agrawal K, Verma P. Chicken feathers: a treasure cove of useful metabolites and value-added products. Environ Sustain. 2021;4:231–43. doi:10.1007/s42398-021-00160-2.
33. Brenner M, Weichold O. Autogenous cross-linking of recycled keratin from poultry-feather waste to hydrogels for plant-growth media. Polym. 2021;13:3581. doi:10.3390/polym13203581.
34. Oluba OM, Obi CF, Akpor OB, Ojeaburu SI, Ogunrotimi FD, Adediran AA, et al. Fabrication and characterization of keratin starch biocomposite film from chicken feather waste and ginger starch. Sci Rep. 2021;11(1):8768. doi:10.1038/s41598-021-88002-3.
35. Gupta P, Nayak KK. Compatibility study of alginate/keratin blend for biopolymer development. J Appl Biomater Funct Mater. 2015;13(4):332–9. doi:10.5301/jabfm.5000242.
36. Das A, Das A, Basu A, Datta P, Gupta M, Mukherjee A. Newer guar gum ester/chicken feather keratin interact films for tissue engineering. Int J Biol Macromol. 2021;180:339–54. doi:10.1016/j.ijbiomac.2021.03.034.
37. Mi X, Mu B, Li W, Xu H, Yang Y. From poultry wastes to quality protein products via restoration of the secondary structure with extended disulfide linkages. ACS Sustain Chem Eng. 2020;8(3):1396–405. doi:10.1021/acssuschemeng.9b05545.
38. Shanmugasundaram OL, Ahmed KSZ, Sujatha K, Ponnmurugan P, Srivastava A, Ramesh R, et al. Fabrication and characterization of chicken feather keratin/polysaccharides blended polymer coated nonwoven dressing materials for wound healing applications. Mater Sci Eng C. 2018;92(3):26–33. doi:10.1016/j.msec.2018.06.020.
39. Sharma S, Rostamabadi H, Gupta S, Nadda AK, Kharazmi MS, Jafari SM. Nano/micro-formulations of keratin in biocomposites, wound healing and drug delivery systems; recent advances in biomedical applications. Eur Polym J. 2022;180:111614. doi:10.1016/j.eurpolymj.2022.111614.
40. Tesfaye T, Sithole B, Ramjugernath D, Mokhothu T. Valorisation of chicken feathers: characterisation of thermal, mechanical and electrical properties. Sustain Chem Pharm. 2018;9:27–34. doi:10.1016/j.scp.2018.05.003.
41. Lazarus BS, Chadha C, Velasco-Hogan A, Barbosa JD, Jasiuk I, Meyers MA. Engineering with keratin: a functional material and a source of bioinspiration. iScience. 2021;24:102798. doi:10.1016/j.isci.2021.102798.
42. Chitnis S, Gaikwad SA, Lambate SB, Ingole SD, Zende RJ. Comparative morphological study of feathers of broiler and layer chicken. Ind J Vet Anat. 2024;35(2):113–6.
43. Tesfaye T, Sithole B, Ramjugernath D, Chunilall V. Valorisation of chicken feathers: characterisation of physical properties and morphological structure. J Clean Prod. 2017;149:349–65. doi:10.1016/j.jclepro.2017.02.112.
44. Chang WL, Wu H, Chiu YK, Wang S, Jiang TX, Luo ZL, et al. The making of a flight feather: bio-architectural principles and adaptation. Cell. 2019;179:1409–23. doi:10.1016/j.cell.2019.11.008.
45. Ritchison G. Integument. In: In a class of their own: a detailed examination of avian forms and functions. Cham: Springer International Publishing; 2023. p. 319–477.
46. Schmidt RE, Struthers JD, Phalen DN. Pathology of pet and aviary birds. New York: John Wiley & Sons; 2024.
47. Metwally S, Comesaña SM, Zarzyka M, Szewczyk PK, Karbowniczek JE, Stachewicz U. Thermal insulation design bioinspired by microstructure study of penguin feather and polar bear hair. Acta Biomater. 2019;91:270–83. doi:10.1016/j.actbio.2019.04.031.
48. Lingham-Soliar T. Feather structure, biomechanics and biomimetics: the incredible lightness of being. J Ornithol. 2014;155(2):323–36. doi:10.1007/s10336-013-1038-0.
49. Lingham-Soliar T, Murugan N. A new helical crossed-fibre structure of β-keratin in flight feathers and its biomechanical implications. PLoS One. 2013;8(6):e65849. doi:10.1371/journal.pone.0065849.
50. Lingham-Soliar T. Microstructural tissue-engineering in the rachis and barbs of bird feathers. Sci Rep. 2017;7(1):45162. doi:10.1038/srep45162.
51. Sullivan TN, Zhang Y, Zavattieri PD, Meyers MA. Hydration-induced shape and strength recovery of the feather. Adv Funct Mater. 2018;28(30):1801250. doi:10.1002/adfm.201801250.
52. Filshie BK, Rogers GE. An electron microscope study of the fine structure of feather keratin. J Cell Biol. 1962;13(1):1–12. doi:10.1083/jcb.13.1.1.
53. Fraser RB, Parry DA. Molecular packing in the feather keratin filament. J Struct Biol. 2008;162(1):1–13. doi:10.1016/j.jsb.2008.01.011.

54. Mattiello S, Guzzini A, Del Giudice A, Santulli C, Antonini M, Lupidi G, et al. Physico-chemical characterization of keratin from wool and chicken feathers extracted using refined chemical methods. Polymers. 2022;15(1):181. doi:10.3390/polym15010181.
55. Dale BA, Lonsdale-Eccles JD, Holbrook KA. Stratum corneum basic protein: an interfilamentous matrix protein of epidermal keratin. In: Mali JWH, editor. Biochemistry of normal and abnormal epidermal differentiation. Basel: Karger Publishers; 1981. vol. 10, p. 311–25.
56. Ehrlich F, Lachner J, Hermann M, Tschachler E, Eckhart L. Convergent evolution of cysteine-rich keratins in hard skin appendages of terrestrial vertebrates. Mol Biol Evol. 2020;37(4):982–93. doi:10.1093/molbev/msz279.
57. Alahyaribeik S, Ullah A. Methods of keratin extraction from poultry feathers and their effects on antioxidant activity of extracted keratin. Int J Biol Macromol. 2020;148(4):449–56. doi:10.1016/j.ijbiomac.2020.01.144.
58. IIsarankura Na Ayutthaya S, Tanpichai S, Wootthikanokkhan J. Keratin extracted from chicken feather waste: extraction, preparation, and structural characterization of the keratin and keratin/biopolymer films and electrospuns. J Polym Environ. 2015;23(4):506–16. doi:10.1007/s10924-015-0725-8.
59. Polesca C, Passos H, Neves BM, Coutinho JA, Freire MG. Valorization of chicken feathers using aqueous solutions of ionic liquids. Green Chem. 2023;25(4):1424–34. doi:10.1039/D2GC04477C.
60. Nagai Y, Nishikawa T. Alkali solubilization of chicken feather keratin. Agric Biol Chem. 1970;34(1):16–22. doi:10.1080/00021369.1970.10859572.
61. Wang Z, Lu B, Xiao N, Guo S, Liu C, Ai M. Structural and functional assessment of keratin extracted from chicken feathers using microwave-assisted l-cysteine method. Food Biosci. 2024;61(5):104712. doi:10.1016/j.fbio.2024.104712.
62. Windt X, Scott EL, Seeger T, Schneider O, Asadi Tashvigh A, Bitter JH. Fourier transform infrared spectroscopy for assessing structural and enzymatic reactivity changes induced during feather hydrolysis. ACS Omega. 2022;7(44):39924–30. doi:10.1021/acsomega.2c04216.
63. Harland DP, Popescu C, Richena M, Deb-Choudhury S, Wichlatz C, Lee E, et al. The susceptibility of disulfide bonds to modification in keratin fibers undergoing tensile stress. Biophys J. 2022;121(11):2168–79. doi:10.1016/j.bpj.2022.04.029.
64. Qiu J, Wilkens C, Barrett K, Meyer AS. Microbial enzymes catalyzing keratin degradation: classification, structure, fuction. Biotechnol Adv. 2020;44:107607. doi:10.1016/j.biotechadv.2020.107607.
65. Faraon VA, Mihăilă EG, Tritean N, Trică B, Capră L, Roman MB, et al. Keratin extraction from chicken feathers in aqueous solutions. Sci Bull Ser F. Biotechnol. 2023;27:106–12.
66. Nurkhasanah U, Susanti E, Idris AM, Suharti S. Keratin biofilm from chicken feathers. IOP Conf Ser: Earth Environ Sci. 2020;475:012073. doi:10.1088/1755-1315/475/1/012073.
67. Brandelli A, Sala L, Kalil SJ. Microbial enzymes for bioconversion of poultry waste into added-value products. Food Res Int. 2015;73:3–12. doi:10.1016/j.foodres.2015.01.015.
68. Qin X, Yang C, Guo Y, Liu J, Bitter JH, Scott EL, et al. Effect of ultrasound on keratin valorization from chicken feather waste: process optimization and keratin characterization. Ultrason Sonochem. 2023;93:106297. doi:10.1016/j.ultsonch.2023.106297.
69. Feroz S, Muhammad N, Ratnayake J, Dias G. Keratin-Based materials for biomedical applications. Bioact Mater. 2020;5(3):496–509. doi:10.1016/j.bioactmat.2020.04.007.
70. Rodríguez-Clavel IS, Paredes-Carrera SP, Flores-Valle SO, Paz-García EJ, Sánchez-Ochoa JC, Pérez-Gutiérrez RM. Effect of microwave or ultrasound irradiation in the extraction from feather keratin. J Chem. 2019;2019:1326063.
71. Alahyaribeik S, Sharifi SD, Tabandeh F, Honarbakhsh S, Ghazanfari S. Bioconversion of chicken feather wastes by keratinolytic bacteria. Proc Saf Environ Protect. 2020;135(4):171–8. doi:10.1016/j.psep.2020.01.014.
72. Meko OA, Eraga SO, Arhewoh MI. Effect of extraction parameters on some properties of keratin obtained from waste chicken feathers. Trop J Nat Prod Res. 2024;8:7423.
73. Idris A, Vijayaraghavan R, Rana UA, Fredericks D, Patti AF, Macfarlane DR. Dissolution of feather keratin in ionic liquids. Green Chem. 2013;15(2):525–34. doi:10.1039/c2gc36556a.

74. Ji Y, Chen J, Lv J, Li Z, Xing L, Ding S. Extraction of keratin with ionic liquids from poultry feather. Separ Purif Technol. 2014;132:577–83. doi:10.1016/j.seppur.2014.05.049.
75. Wang YX, Cao XJ. Extracting keratin from chicken feathers by using a hydrophobic ionic liquid. Process Biochem. 2012;47(5):896–9. doi:10.1016/j.procbio.2012.02.013.
76. Polesca C, Al Ghatta A, Passos H, Coutinho JA, Hallett JP, Freire MG. Sustainable keratin recovery process using a bio-based ionic liquid aqueous solution and its techno-economic assessment. Green Chem. 2023;25(10):3995–4003. doi:10.1039/D3GC00850A.
77. Sinkiewicz I, Śliwińska A, Staroszczyk H, Kołodziejska I. Alternative methods of preparation of soluble keratin from chicken feathers. Waste Biomass Valorization. 2017;8(4):1043–8. doi:10.1007/s12649-016-9678-y.
78. Shavandi A, Silva TH, Bekhit AA, Bekhit AEDA. Keratin: dissolution, extraction and biomedical application. Biomater Sci. 2017;5(9):1699–1735. doi:10.1039/C7BM00411G.
79. Buchacher M, Bechtold T, Pham T. Characterisation of reduction state of cystine linkages on wool fibre surface under heterogeneous reaction conditions. Polym Test. 2022;106:107438. doi:10.1016/j.polymertesting.2021.107438.
80. Reddy CC, Khilji IA, Gupta A, Bhuyar P, Mahmood S, AL-Japairai KAS, et al. Valorization of keratin waste biomass and its potential applications. J Water Proc Eng. 2021;40:101707. doi:10.1016/j.jwpe.2020.101707.
81. Vadillo J, Montes S, Grande HJ, Verstichel S, Almqvist J, Wrześniewska-Tosik K. Enhanced biodegradability in soil of chicken feather by steam explosion for potential application in agricultural biodegradable plastics. Polymers. 2023;15:3701. doi:10.3390/polym15183701.
82. Shen Q, Ma Y, Qin X, Guo Y, Zhang C. Steam explosion as a green method to treat animal waste: a mini-review. Proc Saf Environ Protect. 2024;181:43–52. doi:10.1016/j.psep.2023.11.012.
83. Zhang Y, Zhao W, Yang R. Steam flash explosion assisted dissolution of keratin from feathers. ACS Sustain Chem Eng. 2015;3:2036–42. doi:10.1021/acssuschemeng.5b00310.
84. Rigueto CVT, Rosseto M, Alessandretti I, Krein DDC, Emer CD, Loss RA, et al. Extraction and improvement of protein functionality using steam explosion pretreatment: advances, challenges, and perspectives. J Food Sci Technol. 2024;61:1215–37. doi:10.1007/s13197-023-05817-w.
85. Wei N, Xu D, Hao B, Guo S, Guo Y, Wang S. Chemical reactions of organic compounds in supercritical water gasification and oxidation. Water Res. 2021;190(1):116634. doi:10.1016/j.watres.2020.116634.
86. Škerget M, Čolnik M, Zemljič LF, Gradišnik L, Semren TŽ, Lovaković BT, et al. Efficient and green isolation of keratin from poultry feathers by subcritical water. Polymers. 2023;15(12):2658. doi:10.3390/polym15122658.
87. Poole AJ, Lyons RE, Church JS. Dissolving feather keratin using sodium sulfide for bio-polymer applications. J Polym Environ. 2011;19(4):995–1004. doi:10.1007/s10924-011-0365-6.
88. Erra P, Gomez NDLM, Dolcet LM, Juliá MR, Lewis DM, Willoughby JH. FTIR analysis to study chemical changes in wool following a sulfitolysis treatment. Text Res J. 1997;67(6):397–401. doi:10.1177/004051759706700602.
89. Brush AH. Self-assembly of avian φ-keratins. J Protein Chem. 1983;2(1):63–75. doi:10.1007/BF01025168.
90. Badrulzaman SZS, Aminan AW, Ramli ANM, Che Man R, Wan Azelee NI. Extraction and characterization of keratin from chicken and swiftlet feather. In: Materials science forum. Zurich: Trans Tech Publications Ltd; 2021. vol. 1025, p. 157–62. doi:10.4028/www.scientific.net/MSF.
91. Esparza Y, Ullah A, Wu J. Molecular mechanism and characterization of self-assembly of feather keratin gelation. Int J Biol Macromol. 2018;107:290–6. doi:10.1016/j.ijbiomac.2017.08.168.
92. Perţa-Crişan S, Ursachi CŞ, Gavrilaş S, Oancea F, Munteanu FD. Closing the loop with keratin-rich fibrous materials. Polymers. 2021;13:1896. doi:10.3390/polym13111896.
93. Esparza Y, Bandara N, Ullah A, Wu J. Hydrogels from feather keratin show higher viscoelastic properties and cell proliferation than those from hair and wool keratins. Mater Sci Eng C. 2018;90:446–53. doi:10.1016/j.msec.2018.04.067.
94. Donato RK, Mija A. Keratin associations with synthetic, biosynthetic and natural polymers: an extensive review. Polymers. 2019;12:32. doi:10.3390/polym12010032.

95. Mi X, Li W, Xu H, Mu B, Chang Y, Yang Y. Transferring feather wastes to ductile keratin filaments towards a sustainable poultry industry. Waste Manage. 2020;115:65–73. doi:10.1016/j.wasman.2020.07.022.
96. Brenner M, Weichold O. Poultry feather waste as bio-based cross-linking additive for ethylene propylene diene rubber. Polymers. 2020;13:3908.
97. Dinu R, Cantarutti C, Mija A. Design of sustainable materials by cross-linking a biobased epoxide with keratin and lignin. ACS Sustain Chem Eng. 2020;8:6844–52. doi:10.1021/acssuschemeng.0c01759.
98. Banasaz S, Ferraro V. Keratin from animal by-products: structure, characterization, extraction and application—a review. Polymers. 2024;16:1999. doi:10.3390/polym16141999.
99. Aranberri I, Montes S, Azcune I, Rekondo A, Grande HJ. Fully biodegradable biocomposites with high chicken feather content. Polymers. 2017;9:593. doi:10.3390/polym9110593.
100. Fedorik F, Zach J, Lehto M, Kymäläinen HR, Kuisma R, Jallinoja M, et al. Hygrothermal properties of advanced bio-based insulation materials. Energy Build. 2021;253:111528. doi:10.1016/j.enbuild.2021.111528.
101. Ramakrishnan N, Sharma S, Gupta A, Alashwal BY. Keratin based bioplastic film from chicken feathers and its characterization. Int J Biol Macromol. 2018;111:352–8. doi:10.1016/j.ijbiomac.2018.01.037.
102. Sadeghi S, Dadashian F, Eslahi N. Recycling chicken feathers to produce adsorbent porous keratin-based sponge. Int J Environ Sci Technol. 2019;16:1119–28. doi:10.1007/s13762-018-1669-z.
103. Strnad S, Jug A, Peršin Fratnik Z. Composite materials based on waste chicken feather fibers for oil-spill management. J Nat Fib. 2024;21:2346803. doi:10.1080/15440478.2024.2346803.
104. Wang RM, Li FY, Wang XJ, Li QF, He YF, Wang YB. The application of feather keratin and its derivatives in treatment of potato starch wastewater. Funct Mater Lett. 2010;3:213–6. doi:10.1142/S1793604710001275.
105. Chakraborty R, Asthana A, Singh AK, Verma R, Sankarasubramanian S, Yadav S, et al. Chicken feathers derived materials for the removal of chromium from aqueous solutions: kinetics, isotherms, thermodynamics and regeneration studies. J Dispers Sci Technol. 2022;43:446–60. doi:10.1080/01932691.2020.1842760.
106. Saha S, Zubair M, Khosa MA, Song S, Ullah A. Keratin and chitosan biosorbents for wastewater treatment: a review. J Polym Environ. 2019;27(7):1389–403. doi:10.1007/s10924-019-01439-6.
107. Donner MW, Arshad M, Ullah A, Siddique T. Unravelled keratin-derived biopolymers as novel biosorbents for the simultaneous removal of multiple trace metals from industrial wastewater. Sci Total Environ. 2019;647(9):1539–46. doi:10.1016/j.scitotenv.2018.08.085.
108. Mosnáčková K, Opálková Šišková A, Kleinová A, Danko M, Mosnáček J. Properties and degradation of novel fully biodegradable PLA/PHB blends filled with keratin. Int J Molec Sci. 2020;21(24):9678. doi:10.3390/ijms21249678.
109. Yan RR, Gong JS, Su C, Liu YL, Qian JY, Xu ZH, et al. Preparation and applications of keratin biomaterials from natural keratin wastes. Appl Microbiol Biotechnol. 2022;106(7):2349–66. doi:10.1007/s00253-022-11882-6.
110. Sharma S, Gupta A, Kumar A, Kee CG, Kamyab H, Saufi SM. An efficient conversion of waste feather keratin into ecofriendly bioplastic film. Clean Technol Environ Pol. 2018;20(10):2157–67. doi:10.1007/s10098-018-1498-2.
111. Athwal S, Sharma S, Gupta S, Nadda AK, Gupta A, Husain MSB. Sustainable biodegradation and extraction of keratin with its applications. In: Thomas S, Ajitha AR, Chirayil CJ, Thomas B, editors. Handbook of Biopolymers. Singapore: Springer Nature Singapore; 2023. p. 713–47.
112. Vanderlei RM, Novo-Mansur MT, Mattoso LH, Moreira FK. Effect of precipitation methods on physicochemical properties of keratin films produced from chicken feather waste. J Appl Polym Sci. 2024;141(34):e55863. doi:10.1002/app.55863.
113. Dou Y, Zhang B, He M, Yin G, Cui Y. The structure, tensile properties and water resistance of hydrolyzed feather keratin-based bioplastics. Chin J Chem Eng. 2016;24(3):415–20. doi:10.1016/j.cjche.2015.11.007.
114. Martelli SM, Moore GRP, Laurindo JB. Mechanical properties, water vapor permeability and water affinity of feather keratin films plasticized with sorbitol. J Polym Environ. 2006;14(3):215–22. doi:10.1007/s10924-006-0017-4.

115. Aluigi A, Varesano A, Montarsolo A, Vineis C, Ferrero F, Mazzuchetti G, et al. Electrospinning of keratin/poly (ethylene oxide) blend nanofibers. J Appl Polym Sci. 2007;104(2):863–70. doi:10.1002/app.25623.
116. Srinivasan V, Palanisamy P. A state-of-the-art review on keratin biomaterial as eminent nanocarriers for drug delivery applications. Lett Drug Des Discov. 2023;20(3):245–63. doi:10.2174/1570180819666220620094943.
117. Khumalo M, Tesfaye T, Sithole B, Ramjugernath D. Possible beneficiation of waste chicken feathers via conversion into biomedical applications. Int J Chem Sci Rev. 2019;17:1–20.
118. Dou Y, Zhang B, He M, Yin G, Cui Y. Preparation and physicochemical properties of dialdehyde starch crosslinked feather keratin/PVA composite films. J Macromol Sci A. 2014;51:1009–15. doi:10.1080/10601325.2014.967108.
119. Dou Y, Zhang B, He M, Yin G, Cui Y, Savina IN. Keratin/polyvinyl alcohol blend films crosslinked by dialdehyde starch and their potential application for drug release. Polymers. 2015;7(3):580–91. doi:10.3390/polym7030580.
120. Zhao X, Lui YS, Choo CKC, Sow WT, Huang CL, Ng KW, et al. Calcium phosphate coated Keratin-PCL scaffolds for potential bone tissue regeneration. Mater Sci Eng C. 2015;49:746–53. doi:10.1016/j.msec.2015.01.084.
121. Zamri MFMA, Bahru R, Amin R, Khan MUA, Abd Razak SI, Hassan SA, et al. Waste to health: a review of waste derived materials for tissue engineering. J Clean Prod. 2021;290:125792. doi:10.1016/j.jclepro.2021.125792.
122. Salleh KM, Abd Rashid NF. Keratin-based biomaterials for biomedical applications. In: Sapuan SM, Azhari CH, Nurazzi NM, editors. Polymer composites derived from animal sources. Sawston, UK: Woodhead Publishing; 2024. p. 219–42.
123. Abrar S, Kiran S, Ashraf A, Ghaffar A, Farooq T, Rahmat M. Chemical modifications of keratin. In: Handbook of Natural Polymers. Amsterdam: Elsevier; 2024. vol. 2, p. 155–76.
124. Soleymani Eil Bakhtiari S, Karbasi S. Keratin-containing scaffolds for tissue engineering applications: a review. J Biomater Sci, Polym Ed. 2024;35:916–65. doi:10.1080/09205063.2024.2311450.
125. Saravanan S, Sameera DK, Moorthi A, Selvamurugan N. Chitosan scaffolds containing chicken feather keratin nanoparticles for bone tissue engineering. Int J Biol Macromol. 2013;62:481–6. doi:10.1016/j.ijbiomac.2013.09.034.
126. Tanase CE, Spiridon I. PLA/chitosan/keratin composites for biomedical applications. Mater Sci Eng C. 2014;40:242–7. doi:10.1016/j.msec.2014.03.054.
127. Husain MSB, Gupta A, Alashwal BY. Development of keratin based hydrogels for biomedical applications. In: IOP Conference Series: Materials Science and Engineering, 2019; Bristol, UK: IOP Publishing, vol. 702, no. 1.
128. Zarei M, Tanideh N, Zare S, Aslani FS, Koohi-Hosseinabadi O, Rowshanghias A, et al. Electrospun poly (3-hydroxybutyrate)/chicken feather-derived keratin scaffolds: fabrication, *in vitro* and *in vivo* biocompatibility evaluation. J Biomater Appl. 2020;34:741–52. doi:10.1177/0885328219873090.
129. Mahanta B, Mary SA, Bhaduri A, Giridev VR. Electrospun PVA/keratin nanofibrous scaffold and its application in neural repair. Trends Biomater Artif Organs. 2014;28:188–96.
130. Dufresne ER, Noh H, Saranathan V, Mochrie SG, Cao H, Prum RO. Self-assembly of amorphous biophotonic nanostructures by phase separation. Soft Matt. 2009;5(9):1792–5. doi:10.1039/b902775k.
131. D'Alba L, Saranathan V, Clarke JA, Vinther JA, Prum RO, Shawkey MD. Colour-producing β-keratin nanofibres in blue penguin (*Eudyptula minor*) feathers. Biology Lett. 2011;7(4):543–6. doi:10.1098/rsbl.2010.1163.
132. Nepal D, Kang S, Adstedt KM, Kanhaiya K, Bockstaller MR, Brinson LC, et al. Hierarchically structured bioinspired nanocomposites. Nat Mater. 2023;22(1):18–35. doi:10.1038/s41563-022-01384-1.
133. Pakdel M, Moosavi-Nejad Z, Kermanshahi RK, Hosano H. Self-assembled uniform keratin nanoparticles as building blocks for nanofibrils and nanolayers derived from industrial feather waste. J Clean Prod. 2020;335(4):130331. doi:10.1016/j.jclepro.2021.130331.
134. Woodin AM. Molecular size, shape and aggregation of soluble feather keratin. Biochem J. 1954;57(1):99–109. doi:10.1042/bj0570099.

135. Mu B, Hassan F, Yang Y. Controlled assembly of secondary keratin structures for continuous and scalable production of tough fibers from chicken feathers. Green Chem. 2020;22:1726–34. doi:10.1039/C9GC03896E.
136. Diwan H, Sah MK. Exploring the potential of keratin-based biomaterials in orthopedic tissue engineering: a comprehensive review. Emergent Mater. 2023;6(5):1441–60. doi:10.1007/s42247-023-00545-5.
137. Wang J, Hao S, Luo T, Cheng Z, Li W, Gao F, et al. Feather keratin hydrogel for wound repair: preparation, healing effect and biocompatibility evaluation. Coll Surf B: Biointerfaces. 2017;149(6):341–50. doi:10.1016/j.colsurfb.2016.10.038.

III

Polymers for Advanced Technologies

WILEY

polymers advanced technologies

RESEARCH ARTICLE

Keratin Gel From Chicken Feathers Waste Obtained by Mercaptoethanol Extraction

Sara Mattiello[1] | Alessandro Guzzini[1] | Diego Romano Perinelli[2] | Giulia Bonacucina[2] | Roberto Gunnella[1] | Giulio Lupidi[2] | Carlo Santulli[1]

[1]School of Science and Technology, University of Camerino, Camerino, Italy | [2]School of Pharmacy, University of Camerino, Camerino, Italy

Correspondence: Sara Mattiello (sara.mattiello@unicam.it)

Received: 19 July 2024 | **Revised:** 24 September 2024 | **Accepted:** 30 September 2024

Keywords: chicken feathers | curcumin | drug delivery system | keratin gel | mercaptoethanol extraction

ABSTRACT

Protein gels prepared by keratin extracted from chicken feathers show potential applications as engineered materials. Feathers are an abundant waste material, whose principal component is keratin, which may have gelling properties not yet sufficiently studied so far which are strongly dependent on the extraction method adopted. The aim of the study is to explore the properties of gels obtained through mercaptoethanol extraction and dialysis process and to evaluate their structural characteristics. The keratin hydrogels were characterized with Fourier transform infrared spectroscopy (FTIR) and Raman spectroscopy through which it was possible to identify the secondary structure of the protein on hydrated and dry gel. Moreover, the morphological analysis by scanning electron microscopy (SEM) combined with the rheological analysis showed how the consistency of the gels is maintained on a wide range of loads and frequencies. Furthermore, the biocompatibility of the gels was investigated for the release of subcutaneous drugs using curcumin, an antioxidant polyphenol compound. The fastest release was obtained at pH 7.4, corresponding to physiological conditions.

1 | Introduction

The extraction of keratin, the most diffuse biopolymer, from various types of waste, has recently become a diffuse practice for upcycling byproduct materials. The principal sources of keratin are human hair [1], wool [2], and chicken feathers [3]. Chicken feathers from slaughtering do represent a very large waste source, in particular due to the fact that poultry meat consumption did present a fivefold increase in half a century, reaching the amount of 17.2 kg/capita in 2015 [4]. Applications suggested for chicken feather waste have been various, spanning from the production of organic fertilizers [5], the traditional use in textiles or related fillers [6], to geotextiles [7], or polymer composites [8]. However, in most cases, keratin extraction from feathers has been aimed at the production of biomaterials, for example for cosmetic and pharmaceutical studies [9], although in some cases in the form of protein hydrolysates [10]. The process to serve a more practicable and reliable drug release would conversely require the preservation of the secondary structure of the protein [11]. This appears less difficult to obtain in the case of chicken feathers, provided an adapted extraction procedure is applied to this aim [12] and also paves the way toward their blending with other biopolymers, such as Poly (hydroxybutyrate) (PHB) [13].

A peculiar characteristic that offered much value to this extraction process is the various geometries in which chicken feather keratin can be processed, including films, sponges, fibers, and hydrogels [14]. The latter has shown some promising evidence with respect to the other forms of keratin, namely regarding the prospective mechanical performance of the structure [15]. This is connected with the degree of preservation of the protein's secondary structure which results in a possible self-assembly process [16].

More specifically, a variety of chemical methods based on a reduction for the extraction of keratin from chicken feathers have been experimented with, such as sodium sulfite, sodium dodecyl sulfate, and 2-mercaptoethanol [17]. 2-mercaptoethanol keratin extraction offers a high yield, such as 84%, after a time of 2 h [18]. A slightly inferior yield was obtained in [19], in the order, though confirming the experimental outcome of extensive protein aggregation, even with the diffuse presence of oligomers. The study was specifically oriented to the production of glycerol-plasticized films, which indicated optimal mechanical performance at approximately 50% cysteine carboxymethylation [20].

To the best of our knowledge, keratin gels have never been obtained using 2-mercaptoethanol extraction. However, hydrogels obtained from extracted keratin have proven their potential for example, in terms of wound healing in a blend with genistein [21]. An essential characteristic that is also sought in biopolymer hydrogels, among which those based on keratin are very popular in various fields, is mechanical durability over time [14]. It is required therefore that the extraction method would provide long-lasting and resistant materials.

This study derives from previous investigations on metabisulfite extraction on wool and chicken feathers waste, which led to evaluations of the effectiveness of the process to obtain, after dialysis, material geometries suitable for further application in the biomedical field [22]. It was noticed during these studies that also 2-mercaptoethanol extraction, namely on chicken feathers, might be likely to provide some merits as for yield and preservation of the chemical structure of keratin obtained. Further analysis of the characteristics of this keratinous extract constitutes the core of this work, which is then focused on potential use for drug delivery. With this aim, preliminary tests for drug delivery from the obtained gel have been performed, more specifically studying the release of curcumin in different pH conditions. Curcumin is a well-known naturally occurring anti-cancer compound [23], which has a long history of applications in drug release from biopolymers [24].

2 | Materials and Methods

2.1 | Waste Materials

The keratin-based waste materials, in the form of white feathers from chicken, were obtained during the process of slaughtering and have been supplied by Fileni S.p.A. (Cingoli, MC, Italy).

2.2 | Extraction Method

According to the literature, the 2-mercaptoethanol method of the extraction of keratin from feathers has been used [25]. First, the feathers were washed with cold water and soap, followed by grinding and a second wash with ethanol at 50°C for 2 h to remove surface fats and waxes.

The extraction was performed using the following proportions for a quantity of 4 g of feathers: Urea = 31.8 g, Mercaptoethanol = 1.2 mL (14.2 M), EDTA = 130 mg, Tris (hydroxymethyl) aminomethane = 3.23 g, and the total volume of the solution was 100 mL. The reagents' temperature was kept at 70°C for 24 h, and the solution was then filtered to remove the partially digested residue. Following this, the solution was dialyzed using a membrane with a diameter of 28.6 mm and a molecular weight cut-off (MWCO) of 12–14 kDa in water for about 3 days at room temperature changing the water once a day.

2.3 | Characterization of the Keratin Gel

2.3.1 | Microscopy Techniques

SEM analyses were carried out using a field emission scanning electron microscope (FE-SEM, Sigma Family, Zeiss, Jena, Germany), equipped with a Backscattered Detector (BSD) to obtain high-quality microphotographs. Before being analyzed, a slice of keratin gel was dehydrated by evaporation of water at room temperature under a hood.

2.3.2 | Spectroscopy Techniques

Raman spectroscopy was performed with a HORIBA IHR320 micro-Raman Scattering system (Horiba; Palaiseau, France) equipped with an optical Microscope model Olympus BXF41 (with 5, 20, 50, 100 objectives) (Münster, Germany). The Raman spectrometer was operated at 532 nm (diode laser) with a power of 40 mW. Raman spectra are collected on gel dehydrated by evaporation of water at room temperature under the chemical hood for 12/14 h and on wet gel.

IR spectra were recorded from 4000 to 400 cm^{-1} with a PerkinElmer Spectrum 100 FT-IR instrument (Waltham, MA, USA) by total reflectance on a cadmium selenide (CdSe) crystal. For IR spectra the gel samples were dehydrated in the same way as the samples for Raman.

To obtain information about the secondary structure of the protein, the spectra were fitted into a set of Gaussian functions using Fityk (version 1.3.1).

2.3.3 | Rheological Characterization

Rheological analyses were carried out using a stress-controlled rotational rheometer (Kinexus lab+; Malvern, UK) equipped with a C40/4 cone-plate geometry. The gel was analyzed by stress sweep and frequency sweep tests at 25°C. Stress sweep analysis was performed in the range of 0.5–100 Pa and at a frequency of 1 Hz. For the frequency sweep tests, an increasing frequency in the range of 0.01–10 Hz was applied to the samples at a constant stress (1 Pa). The measured rheological parameters were the elastic modulus (G'), the viscous modulus (G''), and the complex modulus (G^*). Analyses were performed on thin disks with a thickness of 5 mm and a diameter of 28.6 mm.

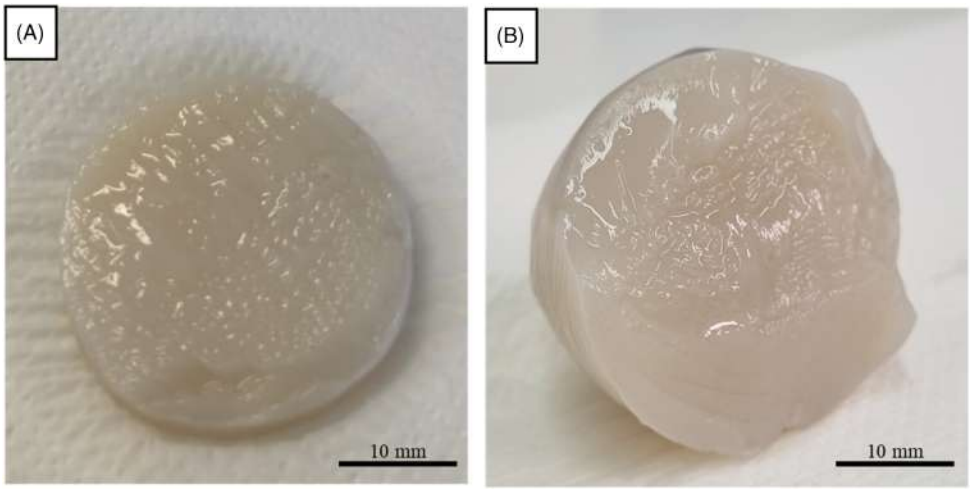

FIGURE 1 | (A) Sample of fresh keratin gel after extraction; (B) Sample of keratin gel 2 years after its extraction.

2.4 | Preparation of Gel With Curcumin and Evaluation of Curcumin Release

Pure keratin gel was cut into small cylinders with a thickness of 10 mm and the same diameter of membrane dialysis (28.6 mm) and was tested to evaluate the possible absorption of hydrophobic drugs using a solution of curcumin (Cayman Chemical, CAS registry n 458-37-7), dissolved in alcohol. Curcumin solutions for the experiment were prepared as follows: 5 mg of curcumin was dissolved in 40 mL of an 80/20 vol.% ethanol/water solution. For absorption by the gel, 16 mL of this solution was placed in contact with a cut cylinder of gel in a beaker. The beaker was placed in a shaker (Stuart SI20H Scientific Hybridization Oven/Shaker, Cole Parmer) with an oscillation of 15 strokes/min for 60 min at ambient temperature. After absorption, excess curcumin was washed away using distilled water. Curcumin release tests were done in triplicate using a solution of 10×PBS (phosphate buffer saline) diluted five times with the addition of 2% TWEEN 80 polysorbate. Then, three solutions at different pHs (7.4/5.8/1.2) with the use of hydrochloric acid (HCl) for acidification were prepared, and the curcumin release at different pHs was calculated. During the release time (72 h at ambient temperature), several samplings were carried out by taking 1 mL of solution, and the relative absorbance was measured at 450 nm using a Varian Cary 1 spectrophotometer. Subsequently, the 1 mL sample was reinserted into the initial solution so as not to change the release medium volume.

Release profiles were compared to each other using model-independent parameters such as dissolution efficiency (DE, %) and mean dissolution time (MDT). DE represents the area under the total release profile referred to as the percentage of the rectangle area, describing 100% of the release at the same time point according to the following equation:

$$\mathrm{DE} = \frac{\int_0^t y dt}{y_{100} t}$$

where y is the drug released at the time point t and y_{100} is the maximum amount of the drug released.

MDT represents the mean value of the distribution time relative to the release and it can be calculated from the following equation:

$$\mathrm{MDT} = \frac{\mathrm{ABC}}{W_\infty}$$

where W_∞ is the asymptote relative to the dissolved drug and ABC is the area between the dissolution curve and W_∞.

Release data were also fitted using the following models: zero-order (cumulative amount of drug released vs. time), first-order (log percentage of drug unreleased vs. time), Higuchi's (cumulative percentage of drug released vs. square root of time), and Korsmeyer's equation (Log cumulative amount of drug release vs. Log time) to investigate the release mechanism.

3 | Results and Discussion

Unexpectedly and repeatedly (a number of 12 experiments were performed), the extraction led to the formation of a very consistent pure keratin gel after dialysis without any further manipulation, which appears as self-standing and composed of approximately 98% water in weight. In Figure 1, images of the gel at different moments are depicted. In particular, Figure 1A shows the gel just after production. Figure 1B shows a cut piece of the gel, stored in distilled water, 2 years after its extraction, which does not show any significant change in appearance, consistency, and color. Such effective preservation has been elsewhere related to the intactness of the integument (e.g., feather supporting structure), which is based on β-keratin: it might be suggested that the method applied for extraction does particularly foster that process [26]. The recovered keratin gel from dialysis was stored in distilled water in a refrigerator, at a

temperature of 4(±1)°C, to avoid desiccation, which would normally occur in around 12 h. After the introduction of curcumin, the gels treated with curcumin appeared with an intense orange color (Figure 2). The uniformity of the color obtained throughout the sample suggested that the curcumin had solidly and uniformly bound to it, a sign of effective dispersion, which is often applied on curcumin-loaded films [27], which is deemed even more significant on thicker structures. This would need to be quantitatively assessed in further investigations.

3.1 | IR Spectroscopy

The keratin gel was analyzed using IR spectroscopy and the spectrum in Figure 3 shows the absorption bands of stretching vibration of N—H and OH bonds at around 3300 cm^{-1}, which are related to amide A [28]. Stretching vibrations of C═O bonds appear from 1600 to 1700 cm^{-1} and they are typical of the amide I band, which contains information about the secondary structure of keratin [29]. At 1520 cm^{-1}, the bending vibration of N—H of amide II is visible [30]. The stretching vibrations of C—N and C—H and bending vibrations of N—H and C═O at around 1220–1300 cm^{-1} are related to amide III. We also performed an analysis on the gel after the curcumin absorption and on pure curcumin for comparison, the spectra are reported in Figure 3. The curcumin spectrum is consistent with the one reported and extensively analyzed by Fugita et al. [31]. In the spectrum of the gel containing curcumin, the contributions of curcumin peaks at 1282 and 960 cm^{-1} were respectively attributed to the symmetric C—O—C stretch methoxy group [32] and to the trans-CH vibration of the benzoate [33].

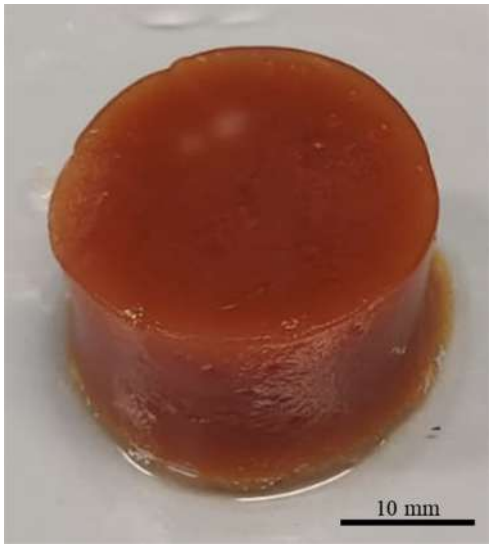

FIGURE 2 | Cylindrical piece of keratin gel after curcumin absorption.

Additionally, it was possible to obtain information about the composition of the secondary protein structure of the keratin gel by studying the deconvolution of the amide I band. Figure 4A reports the contribution of three peaks at 1625 cm^{-1} for the beta sheet, at 1650 cm^{-1} for the alpha helix, and at 1676 cm^{-1} for the disordered structure, respectively [34]. After 2 years of storage, the FTIR spectrum of the gel offered again the same peaks, as shown in Figure 4B, which is a sign of the secondary structure being preserved.

3.2 | Raman Spectroscopy

The Raman spectra of keratin gel water-saturated and dry are depicted in Figure 5. The data show the characteristic bands of the proteins in position: 1200–1300 cm^{-1} for Amide III, 1600–1700 cm^{-1} for Amide I band, and 1448 cm^{-1} for CH_2. The assignment of the vibration bands was done using previous literature as a reference (see Table 1). The obtained spectra were similar in terms of the position of the peaks and did not exhibit distinct features, with the only difference in the noise of the signal that increases with the presence of water.

To study the secondary structure of proteins, the Amide I band was deconvoluted into its components. The deconvolution of

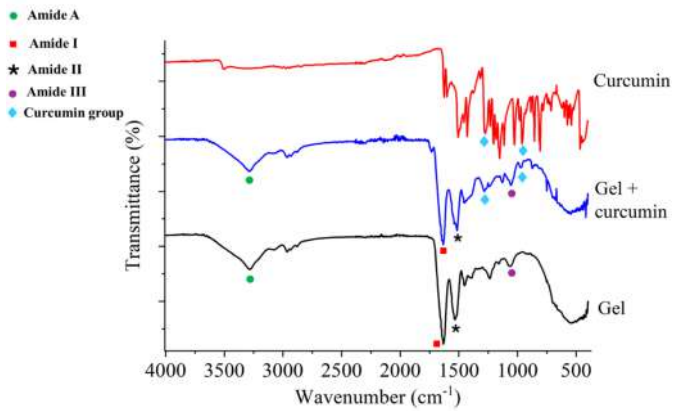

FIGURE 3 | FTIR spectrum of pure keratin gel, curcumin, and keratin gel after curcumin absorption.

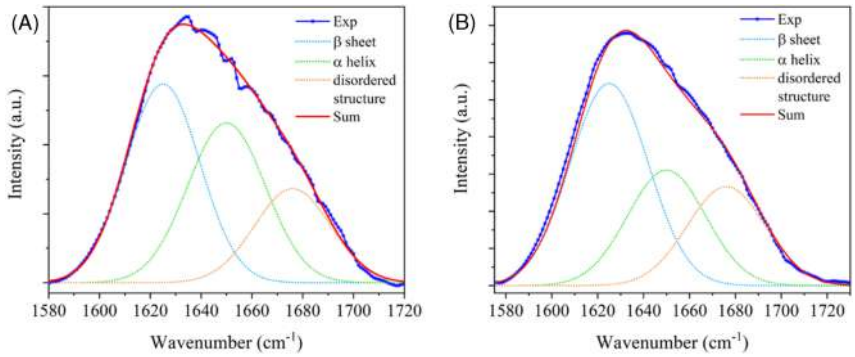

FIGURE 4 | Peaks deconvolution from FTIR spectra of amide I band for (A) fresh dry keratin gel and (B) dry keratin gel after 2 years of storage. The dashed lines indicate the fitted peaks for increasing wavenumber: Beta sheet, alpha helix, and disordered structure, respectively.

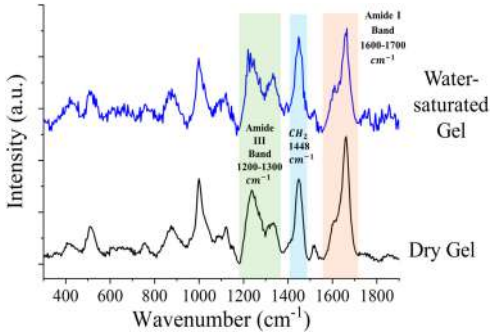

FIGURE 5 | Raman spectra of dry (in black) and water-saturated (in blue) keratin gel with the main characteristic bands of the proteins underlined with colored squares.

the Amide I band is shown in Figure 6, where the contributions are given by four components for dry (Figure 6A) and water-saturated gel (Figure 6B): 1576 cm^{-1} for guanine, 1601–1602 cm^{-1} for C═C (carbon–carbon double bond), 1623–1626 cm^{-1} for Tryptophan or β-sheet, 1658–1660 cm^{-1} for β-sheet structure and 1688 cm^{-1} for unordered coil. No particular differences have been noticed between the spectra, only the signal contribution of guanine, C═C, and unordered structure increase in the presence of water (Figure 6B).

Protein aggregation is frequently associated with changes in the secondary and/or tertiary structures of proteins [39]. The analysis of secondary structures through nondestructive spectroscopic techniques, such as FTIR and Raman, can provide valuable insights into the role of chemical agents in bond extraction and reformation. These techniques are essential for understanding the process of keratin gel formation, whose secondary structure significantly influences the properties of the gel itself. Keratin gel presents a structure composed mainly of beta sheets and a portion of disorder that appears to increase with the presence of water, as detected in the Raman spectra. The ordered and rigid β-sheet structures cannot be further stretched, resulting in mechanically robust hydrogels. The reduction of keratin with mercaptoethanol produces free cysteine residues. Cysteine-containing derivatives are less polar and more stable in acidic and alkaline solutions compared to their oxidized counterparts, and they contain amino acid residues capable of re-crosslinking [27]. In Raman spectra, the peak related to S—S bonds at 521 cm^{-1} suggests the presence of disulfide bridge formation. Moreover, cysteine groups are located at the ends of keratin chains, acting as anchor points in the self-assembly of these chains (Figure 7). The strength and stability of keratin gels are primarily due to the formation of multiple covalent disulfide bonds between cysteine residues, enhancing the gel's mechanical properties as suggested also by [40].

3.3 | SEM

The analyses performed using SEM showed the structural features of the gels. Pure keratin gel (Figure 8A,B) showed a wound-up structure due to dehydration, and the surface does not present voids which suggests a quasi-uniform rehydration of the structure. Bundles were also visible which suggests the preservation of the secondary structure of the protein (Figure 8B).

SEM analysis was performed also on keratin gel after curcumin absorption. Figure 9 shows a surface composed of bundles that form a lattice on which aggregates are visible, which can be identified by the presence of curcumin.

3.4 | Rheological Analysis

The keratin extracted using mercaptoethanol formed a jellified system that was easy to handle and cut into the shape of disks. A rheological analysis has been performed to characterize the gel in terms of consistency and viscoelastic properties.

A stress sweep test at 25°C was first carried out (results are reported in Figure 10) to determine the consistency and linear viscoelastic region. In a stress interval up to 5 Pa, the values of the rheological moduli G' and G'' (both in the order of 10^3 Pa) and tan δ were quasi-constant as typical for structured gels, such as crosslinked poly(methyl methacrylate) (PMMA) [41]. Only a

TABLE 1 | Raman wavenumbers (cm^{-1}) and attribution of the vibrational modes according to the literature references.

Peak position Raman (cm^{-1})	Current assignment	References
521	SS (disulfide bridges)	Akhtar [35], Wang [36]
761	(CH_2) in-phase	Akthar [35]
866	CCH aromatic ring	Akthar [35]
1007	CC aromatic ring	Akthar [35], Wang [36]
1120	(CC) skeletal	Akthar [35]
1153	(CC); (COH)	Akthar [35]
1238	Amide III	Talari [37]
1337	Amide III and CH_2 wagging vibrations from glycine backbone and proline sidechain	Talari [37]
1448	CH_2	Akthar [35], Wang [36]
1511	C═C	Akthar [35]
1612	C═C tryptophan	Akthar [35], Skieresz-Szewczyk [38]
1662	β-sheet	Akthar [35], Skieresz-Szewczyk [38]

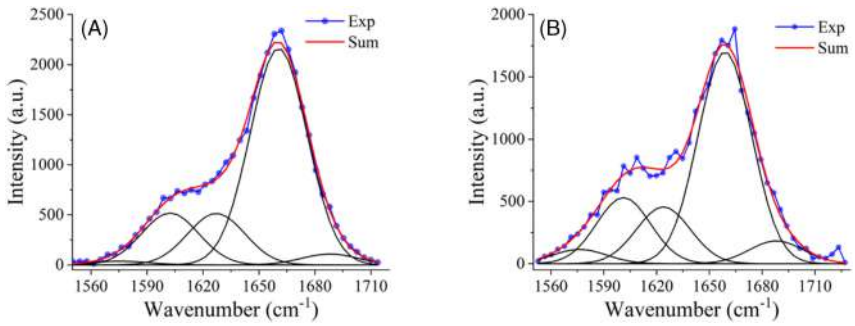

FIGURE 6 | Peaks deconvolution from Raman spectra of Amide I band of dry (A) and water-saturated gel (B): The black lines indicate fitted peaks.

slight decrease of the G' modulus occurred at higher stresses applied, confirming the resistance of the gel to mechanical solicitations.

A frequency sweep test at 25°C was also performed to confirm the solid-like behavior of the gel (Figure 11). Indeed, for pure keratin gel, the value of the storage modulus (G', 12–14 kPa) was considerably higher than that of the loss modulus (G'') in the range of frequencies analyzed. Compared with other biopolymer-based gels already employed for drug release, this novel keratin-based gel appeared to be considerably more structural and sound. This applies, for example, to liposome gels [42], cellulose derivatives [43], and pullulan [44] gels, as well as to silk (fibroin and sericin) or other protein-based hydrogels with a low content of beta sheet structures [45]. With regard to the comparison with other keratin-based hydrogels, this hydrogel, prepared using keratin extracted from feathers, has rheological properties and G' and G'' moduli values similar to those reported in the literature for hydrogels using keratin from the same source. This can be explained by the

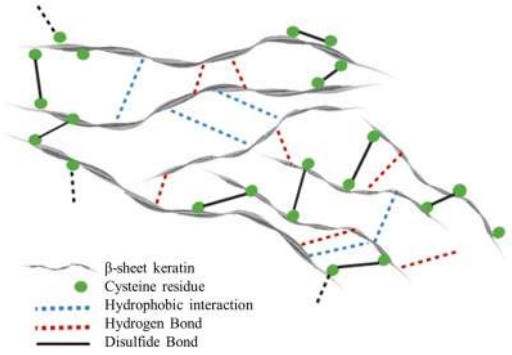

FIGURE 7 | Illustration of the hypothesized self-assembly process of keratin hydrogels, highlighting key intermolecular forces: Disulfide bonds, hydrophobic interactions, and hydrogen bonds. These forces drive the formation of stable molecular networks essential for hydrogel structure and function.

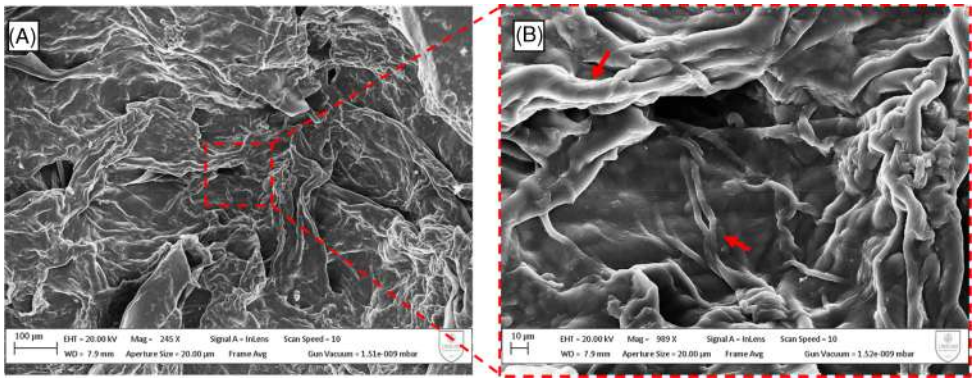

FIGURE 8 | SEM images of (A) and (B) pure keratin gel at different magnifications. The arrows indicate the protein fiber bundles.

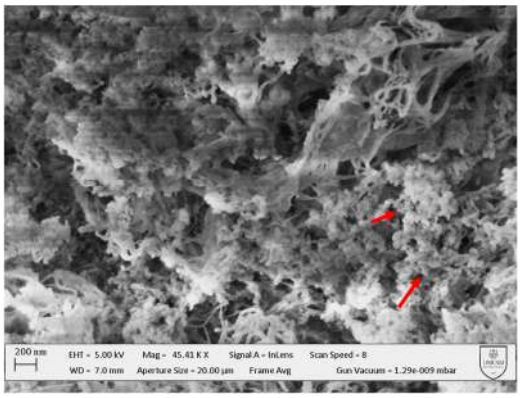

FIGURE 9 | SEM images of keratin gel after curcumin absorption. The arrows indicate the curcumin aggregates.

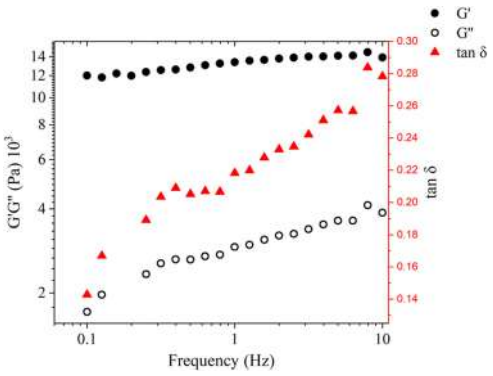

FIGURE 11 | Frequency sweep test of pure keratin gel. Black points indicate the values of G', white points indicate the values of G'' and red triangles indicate the tan δ related to the frequency.

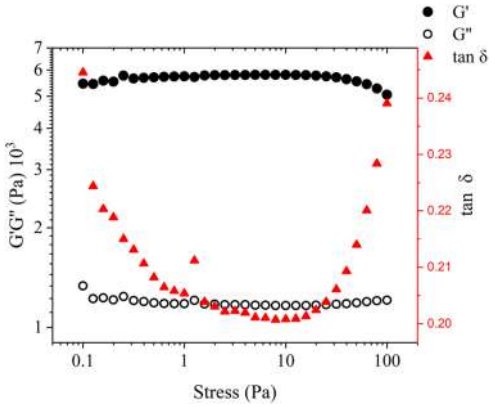

FIGURE 10 | Stress sweep test of pure keratin gel. Black points indicate the values of G', white points indicate the values of G'' and red triangles indicate the tan δ related to the stress.

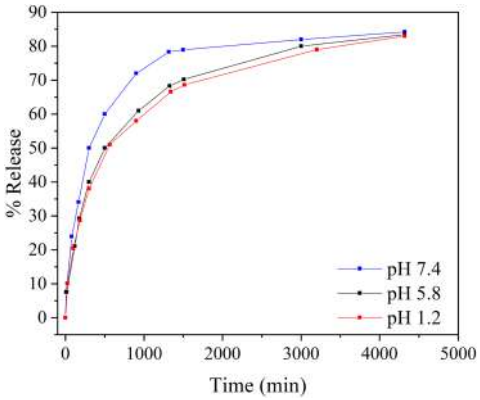

FIGURE 12 | Release of curcumin from keratin gel at various pHs.

TABLE 2 | Kinetic values (K_0, K_1, K_h, and n) were obtained by fitting the curcumin release profiles using the zero-order, first-order, Higuchi, and Korsmeyer models.

	Zero order		First order		Higuchi		Korsmeyer	
	K_0	R^2	K_1	R^2	K_h	R^2	n	R^2
pH 1.2	0.017	0.700	−0.0002	0.896	1.289	0.917	0.414	0.967
pH 5.8	0.017	0.675	−0.0002	0.876	1.313	0.904	0.441	0.954
pH 7.4	0.016	0.549	−0.0002	0.711	1.331	0.812	0.404	0.932

ordered β-sheet structures, which improve the elasticity and resistance of the hydrogel when stress is applied This can be explained by the ordered β-sheet structures, which improve the elasticity and resistance of the hydrogel when stress is applied [17, 46]. This relative stiffness, on the one hand, does not allow easy injectability of the gels, but conversely does not necessarily require the addition of nanoparticles for higher compaction and hardening. A higher storage modulus (G') is related to the ability of a material to store energy and return to its original shape after being subjected to stress. The substantial independence of tan δ from frequency identifies an elastic behavior during shearing [47], which indicates that the gel may be particularly suitable for film casting at ambient temperature.

3.5 | Drug Delivery System

The release kinetics of curcumin at various pH was then investigated to evaluate any differences in the release rate related to pH in particular environments or conditions. For example, the pH of a typical mucous membrane, such as the colonic one (5.8) [48], physiological pH that is, referred to the blood and interstitial fluids (7.4) [49] or the lower end of the stomach environment (1.2) [50]. For this purpose, similar sections of the curcumin-containing gels were incubated in PBS solution, containing 2% polysorbate 80 as a surfactant at various pH and the results are shown in Figure 12.

Data on the release of curcumin from the gel with time indicate that it reaches a plateau around 1700 min, therefore having continuous release over a total of 24–28 h. After 72 h the maximum release point for the various pH is 84.22% for pH 7.4, 83.45% for pH 5.8, and 83.01% for pH 1.2. The total release is in the region of 80% and it is definitely more evident in quasi-neutral conditions. The strength and elasticity of the gel obtained also indicate that there is no need for further blending of the gel with other biopolymers (e.g., cellulose-based ones), which has been revealed to considerably reduce the curcumin release [51].

The comparison between the curcumin release profile was performed by calculating DE (%) and MDT parameters. The obtained values were for DE (%), 67.42%, 69.07%, and 74.73%, and for MDT 811 min, 744 min, and 486 min for curcumin release at pH 1.2, 5.8, and 7.4, respectively. These results highlight that the release profile at pH 7.4 is different from those at pH 5.8 and pH 1.2, despite for all formulations the cumulative curcumin release is ~84% at the end of the experiment. Specifically, the MDT value for curcumin release at pH 7.4 is nearly half with respect to that at the other pHs, highlighting the faster release of the drug at shorter times promoted in a neutral environment.

Among all model equations used to fit the experimental data from the release study (Table 2), the Korsmeyer-Peppas equation is the more descriptive (higher R^2) for all three profiles. The calculated exponents ($n < 0.45$) from the Korsmeyer equation suggest a Fickian diffusion mechanism of curcumin release from keratin hydrogels.

4 | Conclusions

This work demonstrated that a keratin-based hydrogel can be obtained from chicken feathers through mercaptoethanol extraction, followed by dialysis. The gel has a superior consistency compared to other biopolymer-based gel (e.g., cellulose-derived polymers), without further processing as fiber-reinforcement or chemical polymerization. The chemical–physical characterization of the hydrogel using IR and Raman spectroscopy highlighted the preservation of the beta sheet secondary protein structure and the viscoelastic properties found were typical of those from structured hydrogels. Particularly, the rheological moduli (G' and G'') were comparable to those from other hydrogels prepared using keratin extracted from feathers through other methodologies. The release of curcumin suggested the possible use of this keratin gel as a carrier for drugs and bioactive compounds. Specifically, the loading with curcumin, having anti-inflammatory and antioxidant activities, can lead to the formulation of potential dressing materials for wound healing and scaffolds.

Conflicts of Interest

The authors declare no conflicts of interest.

Data Availability Statement

The data that support the findings of this study are available from the corresponding author upon reasonable request.

References

1. H. Lee, K. Noh, S. C. Lee, et al., "Human Hair Keratin and Its-Based Biomaterials for Biomedical Applications," *Tissue Engineering and Regenerative Medicine* 11 (2014): 255–265.

2. H. Rajabinejad, M. Zoccola, A. Patrucco, A. Montarsolo, G. Rovero, and C. Tonin, "Physicochemical Properties of Keratin Extracted From Wool by Various Methods," *Textile Research Journal* 88, no. 21 (2018): 2415–2424.

3. E. M. Brown, K. Pandya, M. M. Taylor, and C. K. Liu, "Comparison of Methods for Extraction of Keratin From Waste Wool," *Agricultural Sciences* 7, no. 10 (2016): 670–679.

4. P. R. Josephson, *Chicken: A History From Farmyard to Factory* (Hoboken, NJ: John Wiley & Sons, 2020).

5. M. H. Abu, G. P. Okolo, and S. Eboh, "Nutritional and Industrial Applications of Broiler Chickens Feather–A Review," *Nigerian Journal of Animal Science* 24, no. 2 (2022): 163–174.

6. N. Pasayev and O. Tekoglu, "The Use of Chicken Feather Fibers as Filling Material in Winter Clothes for Heat Insulation Purposes," *International Journal of Clothing Science and Technology* 31, no. 2 (2019): 259–271.

7. V. Buragadda and M. P. Kompala, "Effect of Novel Chicken Feather-Jute Geotextile Composite Reinforcement on Sand Load Bearing Capacity: An Experimental Study," *International Journal of Geosynthetics and Ground Engineering* 8, no. 3 (2022): 42.

8. R. A. Kurien, A. Biju, K. A. Raj, A. Chacko, B. Joseph, and C. P. Koshy, "Chicken Feather Fiber Reinforced Composites for Sustainable Applications," *Materials Today Proceedings* 58 (2022): 862–866.

9. S. Sharma, A. Gupta, S. M. S. T. Chik, et al., "Extraction and Characterization of Keratin From Chicken Feather Waste Biomass: A Study," in *Proceedings of the National Conference for Postgraduate Research* (*NCON-PGR 2016*), *Universiti Malaysia Pahang* (*UMP*), *Pekan* (2016), 693–699.

10. P. Mokrejš, M. Huťťa, J. Pavlačková, and P. Egner, "Preparation of Keratin Hydrolysate From Chicken Feathers and Its Application in Cosmetics," *JoVE (Journal of Visualized Experiments)* 129 (2017): e56254.

11. X. C. Yin, F. Y. Li, Y. F. He, Y. Wang, and R. M. Wang, "Study on Effective Extraction of Chicken Feather Keratins and Their Films for Controlling Drug Release," *Biomaterials Science* 1, no. 5 (2013): 528–536.

12. Y. Esparza, A. Ullah, and J. Wu, "Molecular Mechanism and Characterization of Self-Assembly of Feather Keratin Gelation," *International Journal of Biological Macromolecules* 107 (2018): 290–296, https://doi.org/10.1016/j.ijbiomac.2017.08.168.

13. M. Zarei, N. Tanideh, S. Zare, et al., "Electrospun Poly (3-Hydroxybutyrate)/chicken Feather-Derived Keratin Scaffolds: Fabrication, In Vitro and In Vivo Biocompatibility Evaluation," *Journal of Biomaterials Applications* 34, no. 6 (2020): 741–752.

14. C. R. Chilakamarry, S. Mahmood, S. N. B. M. Saffe, et al., "Extraction and Application of Keratin From Natural Resources: A Review," *3 Biotech* 11 (2021): 1–12.

15. S. Alahyaribeik and A. Ullah, "Methods of Keratin Extraction From Poultry Feathers and Their Effects on Antioxidant Activity of Extracted Keratin," *International Journal of Biological Macromolecules* 148 (2020): 449–456, https://doi.org/10.1016/j.ijbiomac.2020.01.144.

16. S. Mattiello and C. Santulli, "Synthesis and Properties of Biomimetic Self-Assembling Structures From Poultry Feather Keratin, Accepted for Publication in the Journal of Renewable Materials, September 2024," 2024.

17. Y. Esparza, N. Bandara, A. Ullah, and J. Wu, "Hydrogels From Feather Keratin Show Higher Viscoelastic Properties and Cell Proliferation Than Those From Hair and Wool Keratins," *Materials Science and Engineering: C* 90 (2018): 446–453, https://doi.org/10.1016/j.msec.2018.04.067.

18. I. Sinkiewicz, A. Śliwińska, H. Staroszczyk, and I. Kołodziejska, "Alternative Methods of Preparation of Soluble Keratin From Chicken Feathers," *Waste and Biomass Valorization* 8 (2017): 1043–1048.

19. P. M. Schrooyen, P. J. Dijkstra, R. C. Oberthür, A. Bantjes, and J. Feijen, "Partially Carboxymethylated Feather Keratins. 1. Properties in Aqueous Systems," *Journal of Agricultural and Food Chemistry* 48, no. 9 (2000): 4326–4334.

20. P. M. Schrooyen, P. J. Dijkstra, R. C. Oberthür, A. Bantjes, and J. Feijen, "Partially Carboxymethylated Feather Keratins. 2. Thermal and Mechanical Properties of Films," *Journal of Agricultural and Food Chemistry* 49, no. 1 (2001): 221–230.

21. N. M. Mahajan, K. Wanaskar, N. Ali, et al., "Innovative Wound Healing Hydrogel Containing Chicken Feather Keratin and Soy Isoflavone Genistein: In Vivo Studies," *Gels* 9, no. 6 (2023): 462.

22. S. Mattiello, A. Guzzini, A. Del Giudice, et al., "Physico-Chemical Characterization of Keratin From Wool and Chicken Feathers Extracted Using Refined Chemical Methods," *Polymers* 15, no. 1 (2022): 181.

23. R. Patwa, N. Soundararajan, N. Mulchandani, et al., "Silk Nano-Discs: A Natural Material for Cancer Therapy," *Biopolymers* 109, no. 11 (2018): e23231.

24. S. Pan-On, P. Dilokthornsakul, and W. Tiyaboonchai, "Trends in Advanced Oral Drug Delivery System for Curcumin: A Systematic Review," *Journal of Controlled Release* 348 (2022): 335–345.

25. M. H. Schweitzer, W. Zheng, A. E. Moyer, P. Sjövall, and J. Lindgren, "Preservation Potential of Keratin in Deep Time," *PLoS One* 13, no. 11 (2018): e0206569.

26. P. Rachtanapun, W. Klunklin, P. Jantrawut, et al., "Characterization of Chitosan Film Incorporated With Curcumin Extract," *Polymers* 13, no. 6 (2021): 963.

27. A. Shavandi, A. E.-D. A. Bekhit, A. Carne, and A. Bekhit, "Evaluation of Keratin Extraction From Wool by Chemical Methods for Bio-Polymer Application," *Journal of Bioactive and Compatible Polymers* 32, no. 2 (2017): 163–177, https://doi.org/10.1177/0883911516662069.

28. S. Sharma, A. Gupta, A. Kumar, C. G. Kee, H. Kamyab, and S. M. Saufi, "An Efficient Conversion of Waste Feather Keratin Into Ecofriendly Bioplastic Film," *Clean Technologies and Environmental Policy* 20 (2018): 2157–2167.

29. X. Wang, Z. Shi, Q. Zhao, and Y. Yun, "Study on the Structure and Properties of Biofunctional Keratin From Rabbit Hair," *Materials* 14 (2021): 379.

30. W. Du, L. Zhang, C. Zhang, et al., "Green and Highly Efficient Wool Keratin Extraction by Microwave Induction Method," *Frontiers in Materials* 8 (2022): 789081.

31. R. A. Fugita, D. A. Gálico, R. B. Guerra, et al., "Thermal Behaviour of Curcumin," *Brazilian Journal of Thermal Analysis* 1, no. 1 (2012): 19–23.

32. P. K. Singh, K. Wani, R. Kaul-Ghanekar, A. Prabhune, and S. Ogale, "From Micron to Nano-Curcumin by Sophorolipid Co-Processing: Highly Enhanced Bioavailability, Fluorescence, and Anti-Cancer Efficacy," *RSC Advances* 4, no. 104 (2014): 60334–60341.

33. R. Joshi, B. K. Cho, S. Lohumi, et al., "Evaluation of Benzene Residue in Edible Oils Using Fourier Transform Infrared (FTIR) Spectroscopy," *Korean Journal of Agricultural Science* 46, no. 2 (2019): 257–271.

34. X. Hu, D. Kaplan, and P. Cebe, "Determining Beta-Sheet Crystallinity in Fibrous Proteins by Thermal Analysis and Infrared Spectroscopy," *Macromolecules* 39, no. 18 (2006): 6161–6170.

35. W. Akhtar and H. G. M. Edwards, "Fourier-Transform Raman Spectroscopy of Mammalian and Avian Keratotic Biopolymers," *Spectrochimica Acta Part A* 53 (1997): 81–90, https://doi.org/10.1016/s1386-1425(97)83011-9.

36. K. Wang, R. Li, J. H. Ma, Y. K. Jian, and J. N. Che, "Extracting Keratin From Wool by Using l-Cysteine," *Green Chemistry* 18 (2016): 476–481, https://doi.org/10.1039/C5GC01254F.

37. A. C. S. Talari, Z. Movasaghi, S. Rehman, and I. Rehman, "Raman Spectroscopy of Biological Tissues," *Applied Spectroscopy Reviews* 50, no. 1 (2015): 46–111, https://doi.org/10.1080/05704928.2014.923902.

38. K. Skieresz-Szewczyk, H. Jackowiak, T. Buchwald, and M. Szybowicz, "Localization of Alpha-Keratin and Beta-Keratin (Corneous Beta Protein) in the Epithelium on the Ventral Surface of the Lingual Apex and Its Lingual Nail in the Domestic Goose (Anser Anser f. Domestica) by Using Immunohistochemistry and Raman Microspectros," *Anatomical Record* 300 (2017): 1361–1368, https://doi.org/10.1002/ar.23591.

39. A. L. Fink, "Protein Aggregation: Folding Aggregates, Inclusion Bodies and Amyloid," *Folding and Design* 3, no. 1 (1998): R9–R23.

40. L. Wang, Y. Shang, J. Zhang, J. Yuan, and J. Shen, "Recent Advances in Keratin for Biomedical Applications," *Advances in Colloid and Interface Science* 321 (2023): 103012.

41. K. Ogura and M. H. Wagner, "Rheological Characterization of Cross-Linked Poly (Methyl Methacrylate)," *Rheologica Acta* 52 (2013): 753–765.

42. J. H. Lee, H. Oh, U. Baxa, S. R. Raghavan, and R. Blumenthal, "Biopolymer-Connected Liposome Networks as Injectable Biomaterials Capable of Sustained Local Drug Delivery," *Biomacromolecules* 13, no. 10 (2012): 3388–3394.

43. M. Keshavarz and B. Kaffashi, "The Ability of Retention, Drug Release and Rheological Properties of Nanogel Bioadhesives Based on Cellulose Derivatives," *Pharmaceutical Development and Technology* 19, no. 8 (2014): 952–959.

44. E. Santamaría, L. Anjinho de Barros, C. González, and A. Maestro, "Rheological Study of the Formation of Pullulan Hydrogels and Their Use as Carvacrol-Loaded Nanoemulsion Delivery Systems," *Gels* 9, no. 8 (2023): 644.

45. D. Yao, M. Li, T. Wang, F. Sun, C. Su, and T. Shi, "Viscoelastic Silk Fibroin Hydrogels With Tunable Strength," *ACS Biomaterials Science & Engineering* 7, no. 2 (2021): 636–647.

46. J. Wang, S. Hao, T. Luo, et al., "Feather Keratin Hydrogel for Wound Repair: Preparation, Healing Effect and Biocompatibility Evaluation," *Colloids and Surfaces B: Biointerfaces* 149 (2017): 341–350.

47. L. Tan, D. Pan, and N. Pan, "Water Effect on the Rheologic Behavior of PAN Solution During Thermal-Induced Gelation Process," *Polymers for Advanced Technologies* 22, no. 12 (2011): 2279–2284.

48. B. Tirosh, N. Khatib, Y. Barenholz, A. Nissan, and A. Rubinstein, "Transferrin as a Luminal Target for Negatively Charged Liposomes in the Inflamed Colonic Mucosa," *Molecular Pharmaceutics* 6, no. 4 (2009): 1083–1091.

49. E. Proksch, "pH in Nature, Humans and Skin," *Journal of Dermatology* 45, no. 9 (2018): 1044–1052.

50. E. M. M. Quigley and L. A. Turnberg, "pH of the Microclimate Lining Human Gastric and Duodenal Mucosa In Vivo: Studies in Control Subjects and in Duodenal Ulcer Patients," *Gastroenterology* 92, no. 6 (1987): 1876–1884.

51. S. K. Bajpai, N. Chand, and S. Ahuja, "Investigation of Curcumin Release From Chitosan/Cellulose Micro Crystals (CMC) Antimicrobial Films," *International Journal of Biological Macromolecules* 79 (2015): 440–448.

2.2 Melanin extracted from soldier flies

Melanins are a class of compounds defined as pigments, characterized by a heterogeneous structure and origin. They derive from the oxidation and polymerization of tyrosine in animals or from phenolic compounds in lower organisms [1]. In general, this class includes three main types of compounds, which can be extended to five if nitrogen-free systems are considered [2]. According to the most traditional classification, which includes only nitrogen-containing materials, the first compound is eumelanin, generally associated with the term melanin. It is an insoluble black-brown pigment, which can be obtained by oxidative polymerization of 5,6-dihydroxyindole (DHI) and 5,6-dihydroxyindole-2-carboxylic acid (DHICA) as shown in Figure 2.2. Another type of melanin is pheomelanin, a sulfur-containing pigment with shades ranging from yellow to red-brown. It is derived from the oxidation of cysteinyldopa precursors by benzothiazine and benzothiazole intermediates and is typically responsible for red hair color [3]. Finally, neuromelanin is a dark pigment produced in neurons through the oxidation of dopamine and other catecholamine precursors [1]. This compound is found in the substantia nigra of the brainstem and has been shown to have a structure with a pheomelanin core and an external eumelanin shell [4].

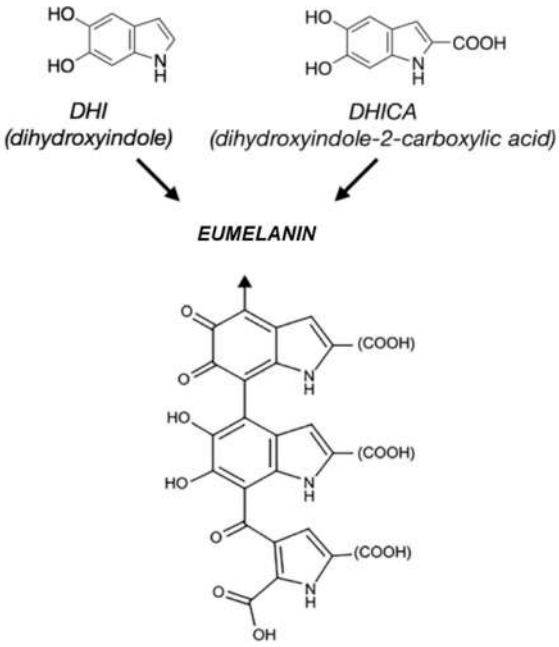

Figure 2.2: Schematic overview of eumelanin production starting from DHI and DHICA units (from [5]).

In particular, eumelanin provides photoprotection and pigmentation in mammals, insects and invertebrates [6]. Due to its unique physical and chemical properties and biocompatibility, eumelanin is a promising biomaterial for applications in energy storage, biomedicine and sensing [7]. However, poor water solubility [3] and the lack of sustainable and low-cost sources of eumelanin have so far limited the full exploitation of this biomaterial. New types of melanin are on the horizon to replace the use of synthetic melanin (very expensive) and cuttlefish melanin (widely studied). Inseccta, an industry from Singapore,

produces soldier flies by breeding them for the purpose of using them for the disposal of urban organic waste. The development and life process of the fly generates the exuviae from which chitosan and melanin are extracted. The entire process is part of a circular economy circuit without producing waste.

2.2.1 Paper IV: *Exploring the chemistry and composition of black soldier fly eumelanin, a material for a circular economy*

Insect farming as an alternative source of melanin is emerging due to its low environmental impact for production [8]. Unlike other types of eumelanin, black soldier fly eumelanin (BSF-mel) from Insectta Pte. Ltd, is extracted from the exoskeleton of larvae (*Hermetia Illucens*) and is water dispersible [9]. The following work reports a comprehensive characterization of this type of melanin using different techniques that shed light on its composition and the presence of DHI and DHICA groups, in contrast to the previous belief that insect eumelanin does not have DHICA. This inconsistency raises intriguing questions about melanogenesis in black soldier flies. Furthermore, the presence of DHICA in BSF eumelanin has implications for its material applications. The extensive characterization addressed and then reported in the article was the result of the work of multiple research groups. Specifically, I worked on the characterization of the melanin particles size in the form of films by AFM, identifying a surface with spherical particles with an average size of $140nm(\pm 40nm)$, similar to previous reports on natural eumelanin obtained from Sepia ink [10] [11]. Furthermore, the type of melanin was identified by FTIR and Raman spectroscopies, classifying it as eumelanin, in support of the data obtained with XPS and the identification of the presence of DHICA groups.

Additional details are provided in the Supplementary Information (see Appendix A.1).

References

[1] Marco d'Ischia et al. "Melanins and melanogenesis: methods, standards, protocols". In: *Pigment cell & melanoma research* 26.5 (2013), pp. 616–633. DOI: 10.1111/pcmr.12121.

[2] Wei Cao et al. "Unraveling the structure and function of melanin through synthesis". In: *Journal of the American Chemical Society* 143.7 (2021), pp. 2622–2637. DOI: 10.1021/jacs.0c12322.

[3] A Bernardus Mostert. "Melanin, the what, the why and the how: An introductory review for materials scientists interested in flexible and versatile polymers". In: *Polymers* 13.10 (2021), p. 1670. DOI: 10.3390/polym13101670.

[4] William D Bush et al. "The surface oxidation potential of human neuromelanin reveals a spherical architecture with a pheomelanin core and a eumelanin surface". In: *Proceedings of the National Academy of Sciences* 103.40 (2006), pp. 14785–14789. DOI: 10.1073/pnas.0604010103.

[5] Maria Letizia Terranova. "Physiological Roles of Eumelanin-and Melanogenesis-Associated Diseases: A Look at the Potentialities of Engineered and Microbial Eumelanin in Clinical Practice". In: *Bioengineering* 11.8 (2024), p. 756. DOI: 10.3390/bioengineering11080756.

[6] Paul Meredith and Tadeusz Sarna. "The physical and chemical properties of eumelanin". In: *Pigment cell research* 19.6 (2006), pp. 572–594. DOI: 10.1111/j.1600-0749.2006.00345.x.

[7] Konstantin Motovilov and Albertus Bernardus Mostert. "Melanin: Nature's 4th bioorganic polymer". In: *Soft Matter* (2024). DOI: 10.1039/D4SM00491D.

[8] Yu-Shiang Wang and Matan Shelomi. "Review of black soldier fly (Hermetia illucens) as animal feed and human food". In: *Foods* 6.10 (2017), p. 91. DOI: 10.3390/foods6100091.

[9] Nina Ushakova et al. "Antioxidative properties of melanins and ommochromes from black soldier fly Hermetia illucens". In: *Biomolecules* 9.9 (2019), p. 408. DOI: 10.3390/biom9090408.

[10] Dieudonné Niyonkuru et al. "A nanoscale study of the structure and electrical response of Sepia eumelanin". In: *Nanoscale Advances* 5.19 (2023), pp. 5295–5300. DOI: 10.1039/D3NA00355H.

[11] Agnes Mbonyiryivuze et al. "Morphological and chemical composition characterization of commercial sepia melanin". In: *American Journal of Nanomaterials* (2015). DOI: 10.12691/ajn-3-1-3.

IV

Materials Advances

ROYAL SOCIETY OF CHEMISTRY

PAPER

View Article Online
View Journal

Cite this: DOI: 10.1039/d4ma00825a

Exploring the chemistry and composition of black soldier fly eumelanin, a material for a circular economy†

A. B. Mostert, *[a] S. Mattiello, [bc] S. Li, [d] G. Perna, [e] M. Lasalvia, [e] P. F. Ambrico, [b] J. V. Paulin, [f] J. V. M. Lima, [f] C. F. O. Graeff, [f] J. W. Phua, [g] M. Matta, [d] A. J. Surman, [d] R. Gunnella *[c] and M. Ambrico [b]

Received 14th August 2024,
Accepted 18th October 2024

DOI: 10.1039/d4ma00825a

rsc.li/materials-advances

Eumelanin is a black-brown biopigment that provides photoprotection and pigmentation in mammals, insects, and invertebrates. It can be obtained by oxidative polymerisation of 5,6-dihydroxyindole (DHI) and its 2-carboxylic acid (DHICA). Due to its unique physical and chemical properties and its biocompatibility, eumelanin is a promising biomaterial for applications in energy storage, biomedicine, and sensing. However, poor solubility in water and lack of sustainable and low-cost sources of eumelanin have so far limited the full exploitation of this biomaterial. Insect farming is rapidly emerging as an alternative source of eumelanin. Unlike other types of eumelanin, BSF eumelanin, which is extracted from the exoskeleton of the black soldier fly (BSF, *Hermetia illucens*), is water-dispersible; however, its fundamental chemical properties are not completely understood. Here, we report the characterisation of BSF eumelanin using various spectroscopy techniques. Contrary to what is known about other insect eumelanins, which are believed to contain exclusively DHI, our results indicate that BSF eumelanin may contain both DHI and DHICA moieties. We discuss the potential reasons for this discrepancy.

1. Introduction

Eumelanin is a black-brown biopigment that plays a crucial role as a protector from UV radiation damage and as a radical scavenger, and is also responsible for the dark pigmentation found in mammals, insects, and invertebrates. Eumelanin can be produced by oxidative polymerisation of two monomers, 5,6-dihydroxyindole (DHI) and 5,6-dihydroxyindole-2-carboxylic acid (DHICA) and their various redox and tautomeric states (Fig. 1).[1–4] While its structure is poorly understood, the material is considered a disordered oligomer system, with a hierarchical supramolecular structure characterised by π-stacking and hydrogen bonding interactions. The stacking distance can vary from ~3.2–4.0 Å depending on hydration and type of eumelanin.[5]

The ratio of DHI to DHICA determines the material's morphology and solubility, as well as its redox and radical scavenging activity.[6] For example, DHI-heavy eumelanin is more insoluble, likely as a consequence of a lower polarity and more efficient π-stacking, which prevents water from penetrating the aggregate structure.[7] In contrast, the presence of carboxylic acid

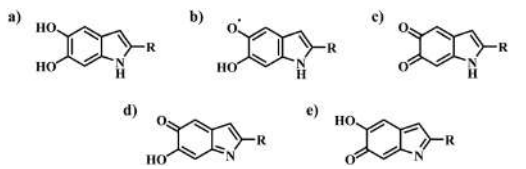

Fig. 1 The monomer building blocks of eumelanin. (a) 5,6-Dihydroxyindole (DHI) for R═H or 5,6-dihydroxyindole-2-carboxylic acid (DHICA) for R═COOH. (b) Protonated semiquinone. (c) Quinone. (d) Quinone imine tautomer. (e) Quinone methide tautomer.

[a] Department of Physics and Centre for Integrative Semiconductor Materials, Swansea University Bay Campus, Fabian Way, Swansea, SA1 8EN, UK. E-mail: a.b.mostert@swansea.ac.uk
[b] CNR-Institute for Plasma Science and Technology, Bari Branch, Via Amendola 122/D, I-70125 Bari, Italy
[c] School of Science and Technology University of Camerino, Via Madonna delle Carceri 9, I-62032, Camerino, Italy. E-mail: roberto.gunnella@unicam.it
[d] Department of Chemistry, King's College London, Britannia House, 7 Trinity Street, SE1 1DB London, UK
[e] Department of Clinical and Experimental Medicine, Università degli Studi di Foggia Via Napoli 20, I-71122 Foggia, Italy
[f] São Paulo State University (UNESP), School of Sciences, Department of Physics and Meteorology, Bauru/SP, Brazil
[g] Insectta Pte. Ltd., 8 Cleantech Loop, S637145, Singapore
† Electronic supplementary information (ESI) available. See DOI: https://doi.org/10.1039/d4ma00825a

groups in DHICA prevents the tight π-stacking of aggregates, making the material more accessible to water permeation.[6] Notably, naturally sourced eumelanin tends to be more DHICA-rich compared to its synthetically made variants.[3]

Eumelanin is of great interest due to its unique physical and chemical properties,[1,2,8] which are uncommon in bioderived, and potentially biocompatible, materials. For example, eumelanin has a broad-band optical absorbance,[9,10] can chelate metal ions in large quantities,[11–18] exhibits paramagnetism,[12,17,19–24] serves as radiation protection,[25,26] binds pharmacological products,[27–29] presents photoconductivity,[30–32] has redox activity,[33–36] and has humidity dependent conductivity,[10,11,18,31,32,37–44] to name just a few key properties. A number of applications exploiting these properties have been reported, *e.g.*, pH sensing,[45–47] transistor devices,[11,45,48,49] capacitors,[50] battery components,[33,51–53] water filtration,[54] and optical coatings.[55]

Even though eumelanin has had the potential to be a "work horse" biomaterial, it has historically had four major drawbacks:

(1) It is not readily sourced at large scale

Eumelanin extracted from cuttlefish (*Sepia officinalis*) ink sacs has been characterised extensively and incorporated in proof of-concept applications.[56,57] However, this sourcing approach is neither scalable nor sustainable. The synthesis of eumelanin by oxidative polymerisation of its precursors[1] is another common strategy; however, it is not cost-effective; synthetic eumelanin and its building blocks (DHI and DHICA) are prohibitively expensive. Overall, neither approach abides by the ideals of a circular economy.

(2) It is not readily processed

Eumelanin is notoriously insoluble in water and common solvents.[1–3] To enhance solubility, or at least obtain a fine dispersion, it is possible to use DMSO as a solvent during synthesis,[58] or alternatively to synthesize under O_2 pressure.[59] Alternatively, eumelanin can be synthetically modified post-synthesis to increase solubility.[60] However, these examples run counter to a circular economy framework due to the solvent or reagent requirements.

(3) It is not chemically/morphologically well-defined

Eumelanin is a heterogeneous 'polymer' that lacks a well-defined chemical structure (the lack of solubility, and crystallinity is an important contributing factor in this). Eumelanin from different organisms or obtained *via* different synthesis methods/precursors have different properties,[3] which are expected to impact its processability, functionalisation and application.[1] This lack of "standardisation", and means to standardise, present a challenge.

(4) Its research community is fragmented

The melanin research community is very diverse, but fragmented across research 'silos': medicine, biology/biotechnology, paleontology, materials science, chemistry.[61] Furthermore, the interests of these groups often do not intersect, with research focused either on melanin nanoparticles and their applications or on melanogenesis and small oligomeric precursors.[61]

Due to the issues above, eumelanin has not received widespread attention and remains a niche material. This is perhaps set to change: the growing industry of insect farming is emerging as a source of sustainable, abundant and low-cost eumelanin, offering a solution to points (1) and (2).

Insect farming is on the rise as a solution to the issues of protein scarcity and food security; by manufacturing an alternative animal feed while valorising food waste, it fulfils a circular economy framework.[62,63] The black soldier fly (BSF, *Hermetia illucens*) is the most popular insect for this endeavour due to its rapid reproduction cycle and low carbon footprint.[64–68] From BSF farming, high-value products, such as chitin and eumelanin, can be extracted; the latter will be referred to as BSF eumelanin henceforth.[69–71] BSF eumelanin offers unique properties that set it aside from other types of eumelanin, most notably that it is *water-dispersible*.[65,69–71] Furthermore, given that only a single species is involved, one may expect a material with consistent properties. In this work, we set out to explore the chemical composition of BSF eumelanin in more detail; we hope our study will spur further research and future device applications for this 'new' kind of eumelanin.

2. Materials and methods

2.1. Eumelanin extraction

BSF eumelanin powders were provided by the manufacturer Insectta Pte. Ltd for research purposes. The material is produced *via* a patented targeted extraction process from the black soldier fly (*Hermetia illucens*).[69,70]

In brief, pupal exuviae were homogenised into ~0.5 mm pieces and demineralised with 10% (w/w) lactic acid for 3 h at 25 °C. The solid fraction was deproteinated with 1 M sodium hydroxide for 3 h at 50 °C. Following this, BSF eumelanin was liberated from the solid fraction by heating with 2 M sodium hydroxide for 3 h at 90 °C. The pH of the supernatant was corrected to 1 with 37% (v/v) hydrochloric acid to precipitate BSF eumelanin, which was collected by centrifugation and further subjected to a series of proprietary steps in order to derive a lyophilised, salt-free, water-dispersible powder (Note: we refer to stable dispersions of these particles here as 'solution' for clarity). The latter property is achieved at pH 7.3, lower than a standard synthesis pH of 8.[3]

Generally, as part of the preparation of the material, the manufacturer recommends filtering, to ensure that any minor insoluble fraction is removed. This study predominantly applies this approach, but some important experimental results will be highlighted where the unfiltered material is also tested for contrast.

2.2. Thin film deposition

Solutions of BSF eumelanin were prepared by stirring in deionized water at a concentration of 20 mg mL^{-1}. Thin films

were prepared from approximately 10 μL of the solution *via* drop casting deposition and left to dry in a fume hood at room temperature for several hours.

For atomic force microscopy (AFM) and Raman measurement, drop casting was done on an FTO glass substrate (Sigma-Aldrich). For X-ray Photoelectron Spectroscopy (XPS), a Si(001) substrate after 0.1% HF solution etching of the oxide was used, and subsequently metallized by 5 nm Cr deposition. BSF eumelanin 10 mg mL^{-1} solution was filtered by a 0.45 μm filter (Millipore) to remove possible residues.

For UV-Vis, both filtered and unfiltered solutions, were drop cast onto UV-ozone treated (Ossila Ltd, 5 min) and untreated glass substrates.

2.3. UV-Visible techniques

Absorbance spectra (100 nm to 3500 nm) for solutions of filtered (0.2 μm and 0.45 μm filters, Millipore) and unfiltered material were performed with a Lambda 40 PerkinElmer UV-Vis spectrophotometer (Waltham, MA, USA). Solutions contained 2 mg mL^{-1} BSF eumelanin dispersed in distilled water. The samples were examined in quartz cuvettes with an optical path of 1 cm.

For thin films of material, transmission and reflectance spectra were obtained using a 150 mm diameter integrating sphere coupled to a Lambda 950 UV-Vis-NIR spectrometer (PerkinElmer). We employed a wavelength λ range between 2000 and 350 nm with a wavelength step of 10 nm and used an InGaAs detector. An individual slide was measured four times, with each measurement being taken at a 90-degree rotation of the slide to the previous measurement. Data was then averaged to obtain a representative spectrum for the slide. Absorbance spectra was obtained *via* the relation $A = 100\% - T - R$ where A is the absorbance, T is the transmission and R is the reflectance. The transmission data was then further analysed using NKFinder from which the attenuation coefficient k was obtained and then the absorption coefficient $\alpha = \frac{4\pi k}{\lambda}$ calculated.[72] We note that for the modelling we derived a function for R derived from the transmission in the Cauchy regime as inputting the reflection data gave unphysical results.

2.4. Morphological analyses

Atomic force microscopy (AFM) images were acquired in tapping mode by using a CSI Nano-observer and P-doped n-type Si cantilever (resonance frequency = 75 kHz). The measurements were performed by using resonant mode. Gwyddion software was used for the processing of the images.[73] The calculation of the average particles size was carried out using ImageJ software by measuring the length and determining the average size.[74]

2.5. DLS and zeta potential for particle size and surface charge analysis

Dynamic light scattering (DLS) and zeta potential measurements of BSF eumelanin particles in H_2O solution were performed using a Litesizer DLS 500, DLS particle size and zeta potential analyzer (Anton Paar Ltd, UK) for the determination of the particle size distributions and zeta potential of dispersed BSF eumelanin particles in water, at room temperature (*ca.* 25 °C). For measurements, the automatic angle selection setting (Anton Paar Kalliope) was used. Fisherbrand™ disposable cuvettes (Fisher Scientific, UK) were used to perform DLS measurements. Measurement cuvettes (Omega Mat. No. 225288, Anton Paar Ltd, UK) were used to perform zeta potential measurements. Briefly, 0.5 mg mL^{-1} of BSF eumelanin solution was prepared and filtered using Fisherbrand™ PTFE Syringe Filter 0.2 μm pore size, the sample was measured in quadruplicate for DLS scattering and a single time for zeta potential. Zeta potential distributions were normalised and fit to Gaussian functions using Origin 2020.

2.6. FTIR and Raman techniques

Attenuated total reflection Fourier-transform infrared spectroscopy (ATR-FTIR) was recorded on BSF eumelanin powder from 4000 to 600 cm^{-1} with a PerkinElmer Spectrum 100 FT-IR instrument (Waltham, MA, USA) by total reflectance on a CdSe crystal. To obtain more information about vibration modes we performed an analysis using Voigt functions (convolution of Gaussian and Lorentzian functions in a ratio of 20% of Lorentzian and 80% of Gaussian) with Fityk (version 1.3.1).

Additional Raman analyses were performed on a BSF eumelanin thin film on a FTO glass substrate using a HORIBA IHR320 micro-Raman Scattering system (Horiba, Palaiseau, France) equipped with an optical Microscope model Olympus BXF41 (with 5×, 20×, 50×, 100× objectives) (Münster, Germany). The Raman spectrometer was operated at 532 nm (diode laser). To obtain information about the melanin components, the spectrum was fitted into a set of Gaussian functions using Fityk (version 1.3.1).

2.7. XPS measurements

The X-ray photoelectron spectroscopy (XPS) measurements were performed using Al-Kα un-monochromatised sources) (PSP Vacuum Technology) and hemispherical analyser VG-Clam 4.

The modelling of the data was performed using Fityk (version 1.3.1) using a subtraction of a linear background and a pseudo-Voigt profile for the peaks utilising mixed Gaussian/Lorentzian with 20% Lorentzian weighting.

The sensitivity factor library used from theoretical photoelectron cross-section specific for Mg/Al-Kα sources used CASA-XPS code.[75]

Surface scans on eumelanin like materials are generally good enough to give indications of the bulk elemental composition. For thin film morphologies the exact chemical nature of the surface and the bulk can be considered equivalent.[76]

2.8. HPLC measurements

An alkaline hydrogen peroxide oxidation (AHPO) analysis was performed to enable observation of the distribution of oxidation products from eumelanin materials, following procedures reported by Ito *et al.*[77,78] Briefly, the samples were 'digested' using AHPO and high performance liquid chromatography

(HPLC) analysis was used to determine the concentration of ''markers'' of oxidised eumelanin products.

Any filtration was performed using Fisherbrand™ PTFE Syringe Filter 0.2 μm pore size. 2.5 mg of extracted eumelanin was dispersed in 1 mL of H_2O; the solution was slowly filtered through the 0.2 μm syringe filter described above. After filtration the syringe filter was purged with an additional 1 mL of H_2O; the combined 2 mL solution was subjected to lyophilization to obtain a filtered BSF eumelanin solid.

AHPO. In a 2 mL Eppendorf tube, 2.5 mg of eumelanin was subjected to 100 μL of water and 375 μL 1M K_2CO_3 (Fisher Scientific, UK) and 25 μL 30% H_2O_2 (Sigma Aldrich, UK) were added. The Eppendorf tube was stirred at room temperature using an SciQuip rotator for 20 hours. The remaining H_2O_2 was quenched with 50 μL Na_2SO_3 (Fisher Scientific, UK) and acidified to pH 1 using 150 μL 6 M H_3PO_4 (Thermo Scientific, UK). The reaction mixture was centrifuged, and 30 μL of supernatant was directly analysed by HPLC. Acid hydrolysis of BSF eumelanin was performed as described in Ito *et al.*[77] with a minor modification. Briefly, acid hydrolysis was performed on 2.5 mg BSF eumelanin suspended in 1 mL 6 M HCl in a vial and heated at 110 °C for 16 h. The solution was then diluted with 1 mL of water and centrifuged. The suspension was collected and subjected to the AHPO process. Each digestion was performed in duplicate, with each sample measured in duplicate.

Synthesis of ''markers''. Pyrrole-2,3-dicarboxylic acid (PDCA) and pyrrole-2,3,5-tricarboxylic acid (PTCA) were synthesised according to reported methods by Ito and Wakamatsu with minor modifications.[79] ^{1}H NMR of PDCA: (400 MHz, MeOD) δ 7.05 (s, 1H), 6.81 (s, 1H). ^{1}H NMR of PTCA: (400 MHz, MeOD) δ 7.34 (s, 1H). Thiazole-2,4,5-tricarboxylic acid (TTCA) was synthesised according to reported methods by M. d'Ischia *et al.* with minor modifications.[3] ^{13}C NMR of TTCA: (101 MHz, D_2O) δ 171.31, 167.55, 165.78, 165.14, 153.32, 136.12. See ESI† for further spectra, demonstrating purity.

HPLC. HPLC measurements were performed using the Agilent 1100 series HPLC. A reversed phase C18 column (Poroshell 120 EC-C18; 4 μm; 4.6 × 250 mm) from Agilent technologies, with a Diode Array detector measuring absorbance at 288 nm. The mobile phase was 0.1 M potassium phosphate buffer (Sigma Aldrich, UK), pH 2.8, containing 1 mM TBA^+Br^- (Fluorochem, UK): methanol at 83 : 17 (v/v) and a flow rate of 0.5 mL min^{-1} and analyses were performed at 45 °C. The markers were used to calibrate measurements of marker concentration in eumelanin samples (see ESI† for calibration curves), with peaks identified by comparing retention times. All solvents were purchased from Sigma Aldrich, UK (HPLC grade).

2.9. NMR measurements

^{13}C CP/MAS analyses were performed on a Bruker Avance III 400 MHz spectrometer equipped with a 4 mm CP/MAS probe, operating at 100.5 MHz for ^{13}C. The ^{13}C CP/MAS spectra of the solid eumelanins were obtained by means of the cross-polarization technique (Cross-Polarization Magic Angle Spinning – CPMAS) with contact time of 3 ms, repetition time of 2 s and MAS rotation frequency of 5 kHz. Two pulse phase Modulation (tppm) proton decoupling was used.

Two eumelanin materials were employed for comparison. The first was an unfiltered BSF eumelanin, and the other for control, was a synthetic eumelanin. The latter was synthesized from 1 g of 3,4-dihydroxy-phenyl-DL-alanine (DL-DOPA; Sigma-Aldrich, ≥98%), which was dissolved in 200 mL of MiliQ water (18 MΩ cm). The mixture's pH was adjusted to be between 8 and 10 by the addition of 1.4 mL of ammonium hydroxide (NH_4OH; synth, 28–30%). The solution was stirred at room temperature (27 °C) and oxygenated using an air pump for three days. For extraction and purification, a 3500 MWCO dialysis membrane was used with MiliQ water as a dialysate medium, which was changed for six days until no further colour change was observed. Finally, drying the aggregated solution was done in an oven at 90 °C for two days.

2.10. Elemental analysis

CHNS analyses were performed by the Elemental Analysis Laboratory, Department of Chemistry, Faculty of Science, National University of Singapore using a ThermoFisher Scientific FlashSmart Elemental Analyser, which operates with dynamic flash combustion of the sample. The instrument is calibrated for CHNS with sulfanilamide standard, using the *K* factor as the calibration method. Samples were weighed into tin containers and introduced into the combustion reactor *via* an autosampler with oxygen. After the combustion, the analyte gases are carried along a helium flow to a layer containing copper, then swept through a GC column, which provides the separation of the combustion gases and are detected by a thermal conductivity detector. The limit of detection for the instrument is 100 ppm or 0.01% w/w.

3. Results and discussions

3.1. UV-Visible spectroscopy

The broad-spectrum absorbance of eumelanins is its most defining feature. Fig. 2 shows the UV-Vis spectra for a BSF eumelanin suspension (filtered with a 0.45 μm filter, a 0.22 μm filter). The spectra exhibit a broad-band, exponential decay, expected of eumelanin, though with a peak at around 280 nm (*vide infra*).[2,9,80] Overall, the solution spectra indicates that the BSF eumelanin optical response is typical of eumelanins.

In previous reports, several attempts were made to interrogate the absorbance spectra to give quantitative insight into eumelanin compositions (an approach also adopted for insect eumelanins).[85] In particular, the ratio of absorbance at 650 nm and 500 nm (A_{650}/A_{500}) has been considered to estimate eumelanin/pheomelanin content,[86–88] and in the absence of pheomelanin, as a value enabling the estimate of the DHI/DHICA content (for example in human hair).[89] Given that our elemental analysis (see ESI†) and elemental XPS (*vide infra*) detect no sulfur present, and we do not observe significant amounts of the TTCA marker on AHPO-HPLC analysis (see ESI†) or pheomelanin-related peaks in FTIR & Raman spectroscopy (*vide infra*), we

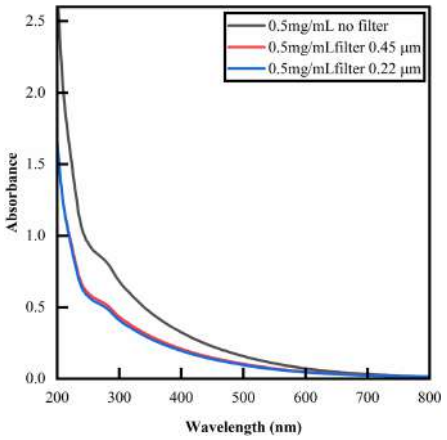

Fig. 2 UV-Vis absorbance of BSF eumelanin suspensions at 0.5 mg mL^{-1} in deionised water. The spectrum is that of an exponential decay, commonly observed for eumelanins,[9] but exhibiting a peak at 280 nm that is likely due to additional proteins in the material.[81–84] Filtration state indicated in the figure.

discount significant presence of pheomelanin. Thus, in principle, A_{650}/A_{500} ratio analysis could be pertinent to a DHI/DHICA analysis. However, the A_{650}/A_{500} ratios reported in the literature (see Fig. S7, ESI†) do not provide a sufficient basis for estimation. Considering this, we refrain from drawing quantitative conclusions, but report A_{650}/A_{500} ratios for BSF eumelanin (0.3, unfiltered; 0.33 filtered), noting that these values fall into the range reported for mixed DHI/DHICA eumelanins.[82–84,90,91]

Turning to thin films, we observe a representative set of transmission, reflectance, and absorbance optical data, as well as the corresponding absorption coefficient spectrum, in Fig. 3. The overall absorbance profile shows the same behaviour as observed in solution: decaying exponential behaviour with increasing wavelength, consistent with other eumelanin thin films.[10] An attempt was made at an A_{650}/A_{500} ratio analysis for this thin film data (see ESI†); however, the A_{650}/A_{500} ratio fall outside the ranges observed in solution, and we conclude performing this analysis in the solid state is not comparable.

3.2. Morphology

The morphology of BSF eumelanin thin film presents a surface characterized by spherical particles with an average diameter of 140 ± 40 nm (Fig. 4a and c), similar to previous reports on natural eumelanin obtained from *Sepia* ink.[92,93] The surface profile suggests roughness, as estimated by the range of about 10 nm (Fig. 4b).

DLS analysis of a BSF eumelanin dispersion observed very similar particle diameters as seen in AFM, ranging from 130–159 nm, with an average measurement of *ca.* 145 nm (Fig. 5a).

Using the same instrument, the surface (zeta) potential of BSF eumelanin particles was measured as *ca.* −66 mV (Fig. 5b). This is a significantly negative charge and is consistent with the presence of carboxylate groups at the particle surface, providing some explanation for BSF eumelanin particles being readily dispersed in water.

3.3. Raman and ATR-FTIR results

The Raman spectrum of BSF eumelanin is depicted in Fig. 6a. The data show two wide bands centred around 1350 cm^{-1} and 1550 cm^{-1}. These two dominant bands are similar to other reports on eumelanin elsewhere, where the two peaks tend to show a range of values (1335–1415 cm^{-1} and 1528–1600 cm^{-1}), with exact values depending on the laser excitation wavelength, the broadness of the peaks and the origin of the sample.[94–98] The blue curve shows the spectrum of the FTO substrate analysed with the same laser wavelength as the BSF eumelanin thin film. Spectra were fitted by using Gaussian functions, with the assignment of the Raman bands done with the use of previous literature (see Table 1).

The ATR-FTIR spectrum of BSF eumelanin is shown in Fig. 6b. The fitting analysis of the spectra used Voight functions

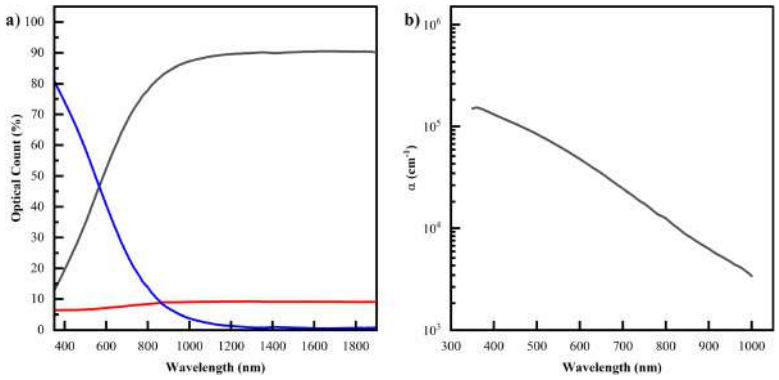

Fig. 3 (a) The optical data for samples of a filtered solution drop cast on UV-ozone treated glass. (b) The corresponding modelled absorption coefficient. Datasets for the other permutations of (un)filtered and (un)treated films can be seen in the ESI.†

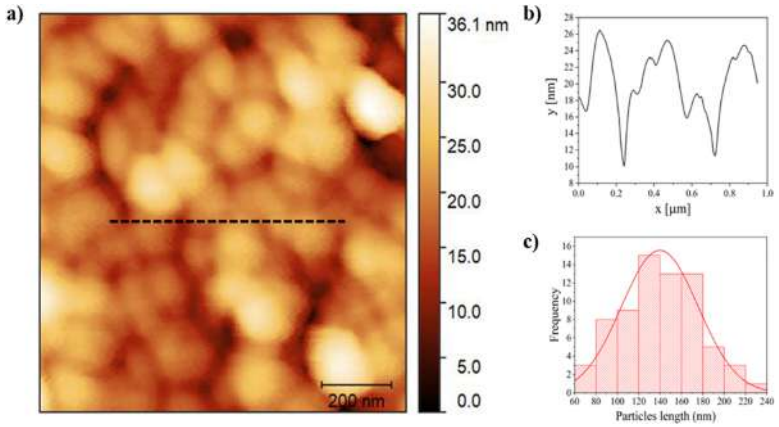

Fig. 4 (a) AFM image of a BSF eumelanin film. The black line indicates the line position of the profile capture depicted in (b). (b) A 1D AFM profile scan of the film surface. (c) A histogram of particle dimensions with an associated distribution curve.

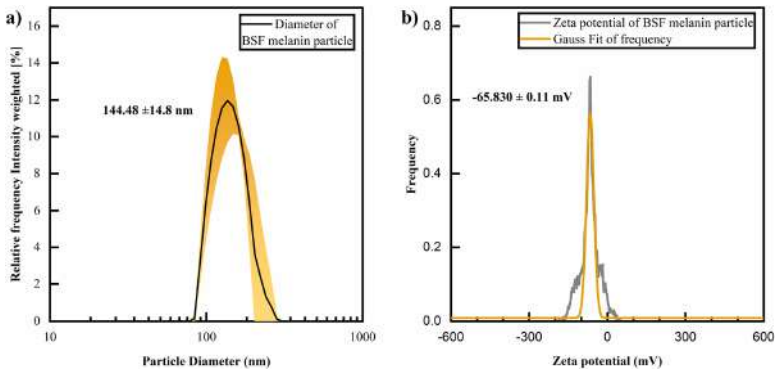

Fig. 5 (a) Size distribution of dispersed BSF eumelanin particles determined by measuring diameters in dynamic light scattering (DLS). The standard deviation of 4 measurements determined the confidence region. (b) Zeta potential analysis of BSF eumelanin particle.

(grey lines, Fig. 6b), with assignments of the vibrational peaks/modes based on previous works, and recorded in Table 1.

Both the Raman and FTIR spectra for BSF eumelanin are consistent with a typical eumelanin polymer. Of specific interest are the vibrational modes at 1714 cm^{-1} (Raman) and 1214 cm^{-1} (FTIR) as these modes are typical of DHICA group vibrations and support our observations of the presence of DHICA. However, since the relationship between FTIR and Raman line strengths and DHI/DHICA concentrations are not established, we can only conclude that DHICA is present.

Furthermore, the FTIR and Raman spectra do not show peaks related to the presence of pheomelanin. In particular, the FTIR signal of pheomelanin presents a peak related to the vibration of the S–O bond at 1172 cm^{-1},[99] which is absent in the spectra acquired on eumelanin from black soldier flies. At the same time, the Raman spectrum (Fig. S8, ESI†) also does not present the peaks related to pheomelanin at 500 cm^{-1} and the single band at 1490 cm^{-1}.[100] The data therefore support the absence of pheomelanin.

3.4. XPS analysis

XPS has been established to obtain the elemental composition of eumelanins, with literature demonstrating that elemental analysis by surface scans of the material is equivalent to the bulk elemental composition.[76] Fig. 7a depicts an example of a wide survey XPS spectrum of a filtered BSF eumelanin film and indicates the presence of C, O, N and Na 1s core levels. The presence of Na at 1080 eV is likely due to the precipitation method used during the material extraction process. Also, minimal traces of Cr are visible while S traces are not visible within the sensitivity of the XPS spectrometer.

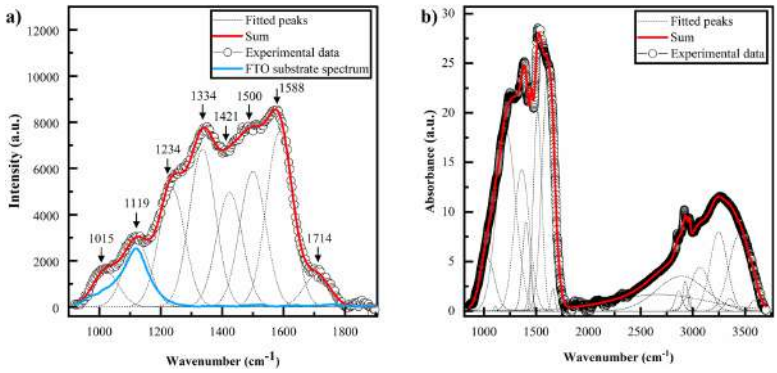

Fig. 6 (a) Raman spectra of a drop cast film of BSF eumelanin deposited on a FTO substrate. Grey lines indicate the fitted peaks and the blue curve the FTO substrate spectrum. (b) FTIR spectrum of BSF eumelanin powder sample. The assignments of the fitted peaks are listed in Table 1.

Table 1 Peak assignment of FTIR and Raman spectra for BSF eumelanin and the literature used

Peak position in fit, IR (cm^{-1})	Peak position in fit, Raman (cm^{-1})	Current assignment	Ref.
	1015	C–H plane deformation	Centeno *et al.*[94]
1033		δ(CH) + δ(NH) + ν(C–O)	Bedran *et al.*[98]
1111		δ(CH) + δ(NH) + ν(C–O)	Bedran *et al.*[98]
	1119	-FTO substrate	Measured (Fig. 6)
1214		δ(OH) + δ(CH) + ν(C(O)–OH in carboxyls) + ν(C–OH inconjugated cycles)	Bedran *et al.*[98]
	1234	ν(CO) + δ(CH) + δ ring	Roldan *et al.*[95]
	1334	ν(CN) + δ(OH) + ν ring	Roldan *et al.*[95]
1363		ν(CN) + δ(OH) + ν(ring)	Bedran *et al.*[98]
1404		Cycle semiquinone C$\cdots$O stretching	Bedran *et al.*[98]
	1421	δ(OH) + ν ring or C–C, C–N in-plane vibration in pyrrole	Roldan *et al.*[95] & Perna *et al.*[97]
1454		semiquinone C$\cdots$O stretching	Beldran *et al.*[98]
	1500	C=N in semiquinone/NH bending	Centeno *et al.*[94]
1514		ν(ring) + δ(NH) + δ(CH) or Semiquinone anion C$\cdots$O stretching	Bedran *et al.*[98]
	1588	Indole ring vibration	Perna *et al.*[97]
1614		ν(ring) + ν(C=O)	Bedran *et al.*[98]
	1714	C=O stretching in COOH	Perna *et al.*[97] & Perna *et al.*[96]
2675		Enol H-bonded OH stretching	Bedran *et al.*[98]
2866		Aliphatic C–H stretching	Bedran *et al.*[98]
2929		Aliphatic C–H stretching	Bedran *et al.*[98]
2968		Aliphatic C–H stretching	Bedran *et al.*[98]
3070		Aromatic C–H stretching	Bedran *et al.*[98]
3247		ν(NH) in aromatic system	Bedran *et al.*[98]
3354		ν(C(O)O–H) hydrogen bonded	Bedran *et al.*[98]
3444		OH H-bonded stretching in water	Bedran *et al.*[98]
3588		OH stretching in water	Bedran *et al.*[98]

To understand the chemical structure of the BSF eumelanin in greater detail, we performed additional fitting of the high-resolution scans to the C1s core level data (Fig. 7b). A fit was obtained using Voigt functions of 0.80 eV and 0.15 eV, respectively, for Gaussian and Lorentzian HWHM. The C1s spectrum can be decomposed into four chemically shifted components with characteristic binding energy values: at 284.6 eV consistent with a C=C/C–C bond (58%); at 286.0 eV consistent with a C–N and/or C–O bond (24%), at 287.8 eV consistent with C=O/C–O bonds (16%); which is in line with other systematic XPS work on synthetic eumelanin systems.[76,101] Finally, a minor component related to COOH group is found at 289.5 eV (2%). The ratio of C–C : C–O(N) : C=O is 58 : 40 : 2, intermediate between that of DHI (67 : 33 : 0) and DHICA (60 : 33 : 7).

An important aspect of the XPS data is the elemental analysis. By comparing the peak areas of C, N and O 1s, core levels, after the subtraction of the background, and adjusting for the sensitivity factors, it is possible to estimate the ratio between the elements composing the samples. In Table 2, the atomic composition (%) that is obtained for the BSF eumelanin film can be compared to theoretical values for DHI and DHICA. As can be seen, the atomic percentages are intermediate between expected DHI and DHICA, indicating a probable DHICA component.

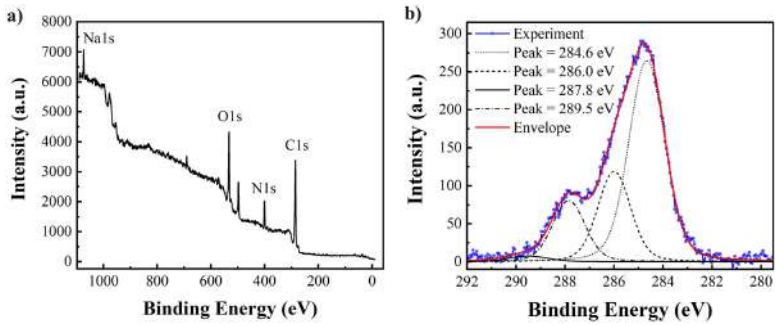

Fig. 7 (a) The XPS wide survey scan. (b) High-resolution C1s core level spectrum of thin film BSF eumelanin with fitting.

Overall, the high-resolution fitting and elemental analysis indicates a material consistent with the composition of DHI and DHICA.

3.5. HPLC

While eumelanin is not typically soluble, the oxidation of eumelanin materials (using hydrogen peroxide) to observe oxidation products (''markers'') by HPLC has been established over many years.[77,79] The balance between the PDCA and PTCA markers is thought to reflect the balance between DHI and DHICA content in eumelanin materials.[102] We produced the requisite markers and implemented this method, as reported by Ito *et al.* (see Methods and ESI†).[79]

Performing AHPO on BSF eumelanin, we observe product chromatograms like those previously reported for eumelanin samples (Fig. 8). For native BSF eumelanin, a PDCA/PTCA (w/w) ratio in of *ca.* 0.22 is observed (see Fig. 9, and ESI† for data). This ratio is not altered dramatically either by filtration or HCl-treatment. The latter is expected to remove proteins and low molecular weight components from eumelanin samples, suggesting this reflects the bulk structure of the material, rather than surface contamination (indeed the ratio drops slightly following this treatment, consistent with a higher % DHICA). This PDCA/PTCA ratio is somewhat smaller than other insect eumelanins reported by Ito *et al.*,[102] consistent with the presence of DHICA in BSF eumelanin (this would be estimated around 20%, using published AHPO calibration data, though we note that scant data in this range precludes confident quantification.[89,103]

Ratios between PDCA and TTCA can be used to estimate pheomelanin content.[104] We note that comparison with TTCA standards shows no/negligible TTCA detected in BSF eumelanin (see ESI,† Fig. S12–S15 for the data). This further supports the conclusions we draw from elemental analyses and FTIR/Raman spectroscopies on the absence of detectable levels of pheomelanin.

Table 2 Atomic concentration in samples BSF eumelanin film as determined from XPS and the respective theoretical values of DHI and DHICA

Element	% AT BSF melanin	DHI	DHICA
C	0.66 (2)	0.73	0.64
N	0.11(2)	0.09	0.07
O	0.23(2)	0.18	0.29

3.6. NMR results

Fig. 10 shows the ^{13}C CP/MAS NMR of BSF eumelanin in comparison to synthetic eumelanin. As expected, the spectra have broad resonances due to the heterogeneous nature of eumelanin. These signals can be divided into three central resonance regions: (I) 0–90 ppm, designated to aliphatic groups; (II) 95–155 ppm, due to aromatics carbons from pyrrole and indole carbons; and (III) 160–200 ppm, related to carboxyl and quinone groups.

Synthetic eumelanin gives a weaker region I signal due to the uncyclized precursor DL-DOPA, which can imply that the intense signals found in the aliphatic region of BSF eumelanin are primarily due to residual protein components and environmental impurities from the biological medium. Such behavior is compatible with other examples of natural melanin.[105–108] We note that S. Ghiani *et al.* attributed a combination of eumelanin and protein to the highly intense signal of the carboxyl region.[106]

A theoretical prediction using the incremental method of the ChemDraw Ultra (version 12.0.2) software package for each peak assignment is shown in the ESI† (Fig. S16).[109] Based on the predictions, the main contribution of eumelanin should be the aromatic signal, and we can try a qualitative comparison between BSF eumelanin and the DL-DOPA synthetic eumelanin, the latter of which is well known to be relatively poor in DHICA content (~5–10%).[3]

The CP/MAS experiment can differ between samples due to proton concentration and relaxation rates. Assuming that the amount of ^{13}C nuclei is equal in both samples, we could expect BSF eumelanin to have an extensive cross-linking between the DHI/DHICA units and DHI/DHICA and protein. This would reduce the proton concentration and yield the low intensity of the aromatic region.

The aromatic-to-carboxyl signal area ratio is usually employed to compare eumelanin content in a given sample.

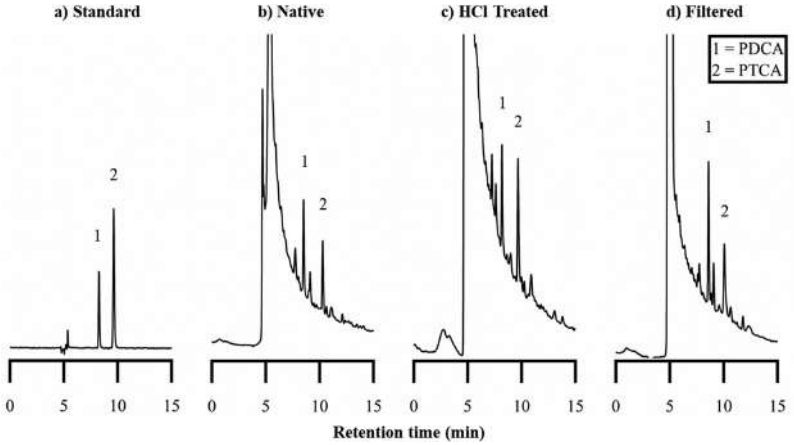

Fig. 8 High-performance liquid chromatography (HPLC) chromatograms of (a) standard eumelanin markers, and AHPO mixtures from (b) original native BSF eumelanin, (c) HCl–AHPO mixtures from BSF eumelanin and (d) AHPO mixtures from 0.2 μm filtered BSF eumelanin.

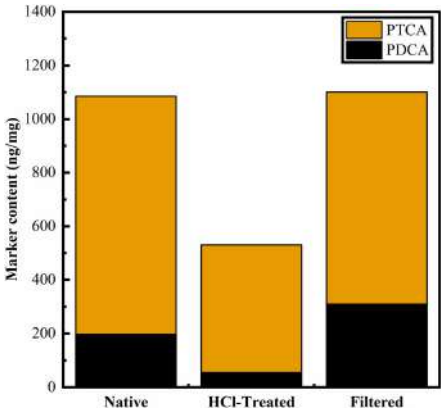

Fig. 9 Marker content observed in AHPO mixture of BSF-Mel (ng mg^{-1}).

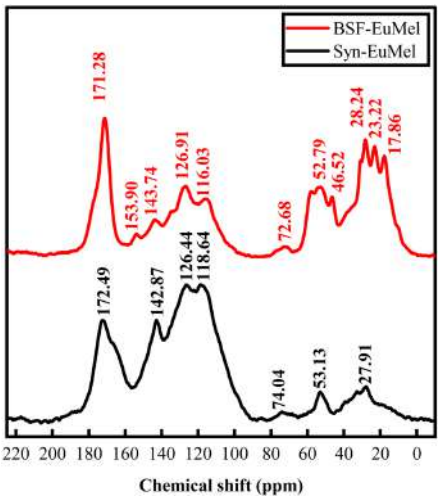

Fig. 10 ^{13}C CP/Mas NMR spectra of BSF eumelanin (top, BSF-EuMel) and synthetic eumelanin (bottom, Syn-EuMel).

Thus, one would expect a low concentration of eumelanin in BSF eumelanin compared to synthetic eumelanin by a factor of approximately 2, as indicated by Table 3 (see R-II/R-III). Indeed, the abundance in BSF eumelanin of the protein matrix is such that the signal around 154 ppm is seen in Fig. 10[106,108] and is aligned with purity ranging from 40 to 80%.[69]

To compare the DHI/DHICA units between BSF eumelanin and synthetic eumelanin, we normalise the aromatic and carboxyl region area to the eumelanin content. The data is reported in Table 4. The BSF eumelanin has a decrease in the aromatic region and an increase in the carboxyl region. This behavior has been linked to the rise in the DHICA ratio and to the oxidation of phenolic carbons.[59,105] Interestingly, the increase in oxidation is compatible with previous reports on BSF eumelanin.[70]

3.7. Discussion

The synthesis of eumelanin in higher animals is quite well understood. Briefly, both tyrosine and L-3,4-dihydroxyphenylalanine (L-DOPA) are oxidised *via* catalysis by the enzyme tyrosinase into dopaquinone. After catalysis, non-enzymatic intramolecular cyclization occurs leading to dopachrome, which in turn is then converted to DHICA by tyrosinase-related protein or dopachrome isomerase. In contrast, DHI is formed non-enzymatically.[77,102,110,111] However, work by Barek *et al.* investigated a number of insects and found that the

Table 3 Normalised signal (to total signal) areas in ^{13}C CP/MAS NMR spectra

Sample	Aliphatic (0–85 ppm)	Aromatic A (95–140 ppm)	Aromatic B (140–155 ppm)	Carboxyl (160–190 ppm)	R-II/R-III ratio
BSF eumelanin	0.49	0.23	0.06	0.19	1.53
Synthetic eumelanin	0.12	0.52	0.16	0.21	3.24

eumelanin formed was based on DHI only, formed from dopamine.[102] It is noted that thus far no DHICA-producing enzyme has been characterised in insects.[112] This led Sugumaran and Barek, in their extensive overview, to suggest that the question "*Do insects and other arthropods make significant amounts of pheomelanin and DHICA melanin?*" is unresolved, and note: "*. . .in insect systems the presence or absence of DHICA melanin should be unequivocally assessed*".[112] Given this background, the presumption coming into the present study was that BSF eumelanin would be a solely DHI-based eumelanin.

However:

(1) We see no evidence of significant pheomelanin fractions, based on the absence of sulfur in bulk and XPS-based elemental analyses, absence of pheomelanin-related features in FTIR & Raman spectra, and the absence of TTCA is AHPO-HPLC analysis of BSF eumelanin.

(2) The solution-based UV-Vis spectra appears consistent with eumelanin, and the A_{650}/A_{500} ratio analysis is consistent with eumelanin containing DHICA.

(3) Both Raman and FTIR peak analysis include COOH moieties, consistent with DHICA monomers being present.

(4) The AFM exhibits a morphology consistent with other natural eumelanins known to contain DHICA. The AFM is also consistent with the DLS measurements, and the zeta potential obtained is consistent with carboxylic groups, which are present in DHICA.

(5) The XPS high-resolution C1s fit indicates some COOH content and the elemental analysis indicates a material intermediate between DHI and DHICA, *i.e.*, BSF eumelanin is consistent in exhibiting probable DHICA content.

(6) The AHPO-HPLC analysis, designed to decompose eumelanin into marker molecules associated with DHI and DHICA (PDCA and PTCA), shows results that are consistent with a material containing both DHI and DHICA when the ratio of these markers are compared. This ratio does not show diminished evidence of DHICA on washing with HCl (designed to remove residual protein).

(7) The NMR data indicates a material system with a higher signal ratio in the carboxyl region *vs.* aromatic region when compared to a synthetic material, the latter of which is well known to be DHICA poor (~5–10%). Therefore, the NMR suggests that BSF eumelanin has DHICA present, potentially in greater quantity than synthetic analogues.

Table 4 Re-normalized signal areas in ^{13}C CP/MAS NMR spectra. The signal area normalized to the eumelanin content in each sample

Sample	Aromatic A (95–140 ppm)	Aromatic B (140–155 ppm)	Carboxyl (160–190 ppm)
BSF eumelanin	0.48	0.13	0.39
Synthetic eumelanin	0.59	0.19	0.22

Overall, these data are consistent with the presence of DHICA in BSF eumelanin. We note the use of a different extraction protocol to that of Barek *et al.* However, our use of NaOH is common, and we find no published precedent suggesting our unexpected observations may arise from our approach. The unexpected result of DHICA presence raises questions about its potential origin. One possibility is that BSF eumelanin is produced initially as a poly-DHI system, which through the various refinement processes has oxidized to yield a material with the above properties. Ring fission is possible,[3] but would be inconsistent with the observed AHPO results. Alternatively, BSF eumelanin may be produced by a pathway including DHICA, differing from what is thought to be known of other fly species.[102] These results may vindicate the caution expressed by Sugumaran & Barek.

If BSF eumelanin biosynthesis differs from that in other species, this raises some interesting biological questions, particularly on whether the enzyme needed to produce DHICA within the synthesis pathway is present within the black soldier fly. Furthermore, if the black soldier fly does lack the usual enzyme for producing DHICA, then there may be another, unexplored mechanism producing DHICA-containing eumelanins. Answering these questions may have more general implications for the synthesis and biosynthesis of DHICA-containing eumelanin materials, beyond the black soldier fly.

The presence of DHICA within BSF eumelanin has significant material implications. As has been shown by others, the presence of DHICA within a eumelanin polymer changes not only its morphology, but also its redox properties, making DHICA-rich eumelanin polymers excellent radical scavengers.[6] Furthermore, the DHI-only materials are expected to be more tightly stacked, and thus able to exclude water more efficiently from their internal structures.[6,7,113–115] We therefore infer that this black soldier fly eumelanin would be a promising candidate to exploit the hydration-dependent properties for material applications for which eumelanin is known. In fact, recent papers investigated the hydration/dependent BSF eumelanin electrical properties and found the material very sensitive to hydration changes, in a fashion similar to that observed in synthetic eumelanin.[116] Also, BSF eumelanin was implemented as the active material in fast, responsive humidity sensors[117] and capacitors,[118] which makes BSF eumelanin a competitive and sustainable alternative to other similar materials.

4. Conclusion

Eumelanin research – and potential applications – have historically been limited by its high cost, low availability and poor

solubility. BSF farming offers a new, sustainable, potentially low-cost and abundant supply of water-processable eumelanin. Here, we have presented a wide range of characterisations of BSF eumelanin. Our data is consistent with the presence of both DHI and DHICA in this material, in contrast to the previous belief that insect eumelanin lacks DHICA. This inconsistency raises intriguing questions about melanogenesis in black soldier flies. In addition, the presence of DHICA in BSF eumelanin has implications for its material applications.

Author contributions

A. B. M.: conceptualization; formal analysis (solid state UV-Vis); investigation (solid state UV-Vis); validation (XPS); writing – original draft preparation; writing – review and editing. S. M.: investigation (AFM, Raman, FT-IR, XPS); formal analysis (AFM, Raman, FT-IR, XPS); writing – original draft preparation (AFM, Raman, FT-IR, XPS); writing – review and editing. S. L.: investigation (synthesis, AHPO, HPLC, DLS); formal analysis (synthesis, AHPO, HPLC, DLS); visualisation; writing – review and editing. G. P.: investigation (solution UV-Vis); formal analysis (solution UV-Vis). M. L.: investigation (solution UV-Vis); formal analysis (solution UV-Vis). P. F. A.: writing – review and editing; supervision. J. V. P.: formal analysis (solid-state NMR); investigation (solid-state NMR); writing – review and editing. J. V. M. L.: formal analysis (NMR); investigation (NMR); writing – original draft preparation (NMR). C. G. O. G.: writing – review and editing; formal analysis (NMR); investigation (NMR); funding acquisition; supervision. J. W. P.: conceptualization; resources (eumelanin extraction); writing – review and editing. M. M.: writing – review and editing; funding acquisition; supervision. A. J. S.: writing – review and editing; funding acquisition; supervision. R. G.: conceptualization; investigation (AFM, Raman, FT-IR, XPS); formal analysis (AFM, Raman, FT-IR, XPS); writing – original draft preparation (AFM, Raman, FT-IR, XPS); writing – review and editing; funding acquisition; supervision. M. A.: conceptualization; methodology (solid state UV-Vis); supervision; resources.

Data availability

The data supporting this article have been included as part of the ESI.†

Conflicts of interest

There are no conflicts of interest to declare.

Acknowledgements

M. A. acknowledges the CNR-Short Term Mobility program 2021 Prot.0052594/230721. M. A. and P. F. A. acknowledges the Italian Ministry of University and Research (MUR) PONa3_00369 SISTEMA. R. G. and S. M. thanks European Union – NextGenerationEU under the Italian Ministry of University and Research (MUR) National Innovation Ecosystem grant ECS00000041 – VITALITY – Spoke 9. M. M. gratefully acknowledges financial support from the European Union's Horizon 2020 research and innovation programme under the Marie Skłodowska-Curie grant agreement No. 843554. A. J. S. is grateful to The Royal Society for research funding (Research Grant RGS\R2\222385). S. L. has been supported by a studentship from the King's China Scholarship Council. S. L., A. J. S., and M. M. are grateful to King's College, Chemistry, for research facilities. A. B. M. acknowledges this work was supported by the UKRI Research Partnerships Investment Fund through the Centre for Integrative Semiconductor Materials. J. V. P., J. V. M. L. & C. F. O. G. acknowledges that this work was financially supported by São Paulo Research Foundation, FAPESP (grant 2013/07296-2 and 2021/03379-7). J. V. P. acknowledges the support of the São Paulo State University research office (PROPe) postdoctoral fellowship (grant 05/2024). We acknowledge Ms Wei Ling Tan from the Elemental Analysis Laboratory, Department of Chemistry, Faculty of Science, National University of Singapore for the elemental analysis.

References

1 A. B. Mostert, *Polymers*, 2021, **13**, 1670.
2 P. Meredith and T. Sarna, *Pigm. Cell Res.*, 2006, **19**, 572–594.
3 M. d'Ischia, K. Wakamatsu, A. Napolitano, S. Briganti, J. C. Garcia-Borron, D. Kovacs, P. Meredith, A. Pezzella, M. Picardo, T. Sarna, J. D. Simon and S. Ito, *Pigm. Cell Res.*, 2013, **26**, 616–633.
4 S. Ito, K. Wakamatsu, M. d'Ischia, A. Napolitano and A. Pezzella, in *Melanins and Melanosomes*, ed. J. Borovanský and P. A. Riley, Wiley-VCH Verlag GmbH & Co., 2011, ch. 6, pp. 167–185.
5 C.-T. Chen, V. Ball, J. J. de Almeida Gracio, M. K. Singh, V. Toniazzo, D. Ruch and M. J. Buehler, *ACS Nano*, 2013, **7**, 1524–1532.
6 L. Panzella, G. Gentile, G. D'Errico, N. F. Della Vecchia, M. E. Errico, A. Napolitano, C. Carfagna and M. d'Ischia, *Angew. Chem., Int. Ed.*, 2013, **52**, 12684–12687.
7 S. Soltani, S. Sowlati-Hashjin, C. G. Tetsassi Feugmo and M. Karttunen, *J. Phys. Chem. B*, 2022, **126**, 1805–1818.
8 P. Meredith, C. J. Bettinger, M. Irimia-Vladu, A. B. Mostert and P. E. Schwenn, *Rep. Prog. Phys.*, 2013, **76**, 034501.
9 P. Meredith, B. J. Powell, J. Riesz, S. P. Nighswander-Rempel, M. R. Pederson and E. G. Moore, *Soft Matter*, 2006, **2**, 37–44.
10 J. V. Paulin, A. P. Coleone, A. Batagin-Neto, G. Burwell, P. Meredith, C. F. O. Graeff and A. B. Mostert, *J. Mater. Chem. C*, 2021, **9**, 8345–8358.
11 A. B. Mostert, S. Rienecker, M. Sheliakina, P. Zierep, G. R. Hanson, J. R. Harmer, G. Schenk and P. Meredith, *J. Mater. Chem. B*, 2020, **8**, 8050–8060.
12 C. C. Felix, J. S. Hyde, T. Sarna and R. C. Sealy, *J. Am. Chem. Soc.*, 1978, **100**, 3922–3926.
13 M. M. Jastrzebska, H. Isotalo, J. Paloheimo, H. Stubb and B. Pilawa, *J. Biomater. Sci., Polym. Ed.*, 1996, **7**, 781–793.

14 B. Szpoganicz, S. Gidanian, P. Kong and P. Farmer, *J. Inorg. Biochem.*, 2002, **89**, 45–53.
15 Y. Liu, L. Hong, V. R. Kempf, K. Wakamatsu, S. Ito and J. D. Simon, *Pigm. Cell Res.*, 2004, **17**, 262–269.
16 J. D. Hong and J. D. Simon, *Photochem. Photobiol.*, 2006, **82**, 1265–1269.
17 T. Sarna, J. S. Hyde and H. M. Swartz, *Science*, 1976, **192**, 1132–1134.
18 P. A. Abramov, S. S. Zhukov, M. Savinov, A. B. Mostert and K. A. Motovilov, *Phys. Chem. Chem. Phys.*, 2023, **25**, 11601–11612.
19 S. Chio, J. S. Hyde and R. C. Sealy, *Arch. Biochem. Biophys.*, 1980, **199**, 133–139.
20 S. Chio, J. S. Hyde and R. C. Sealy, *Arch. Biochem. Biophys.*, 1982, **215**, 100–106.
21 A. B. Mostert, G. R. Hanson, T. Sarna, I. R. Gentle, B. J. Powell and P. Meredith, *J. Phys. Chem. B*, 2013, **117**, 4965–4972.
22 J. V. Paulin, A. Batagin-Neto, P. Meredith, C. F. O. Graeff and A. B. Mostert, *J. Phys. Chem. B*, 2020, **124**, 10365–10373.
23 J. V. Paulin, A. Batagin-Neto and C. F. O. Graeff, *J. Phys. Chem. B*, 2019, **123**, 1248–1255.
24 M. Al Khatib, J. Costa, M. C. Baratto, R. Basosi and R. Pogni, *J. Phys. Chem. B*, 2020, **124**, 2110–2115.
25 T. Vasileiou and L. Summerer, *PLoS One*, 2021, **16**, e0257068.
26 E. Dadachova, R. A. Bryan, X. Huang, T. Moadel, A. D. Schweitzer, P. Aisen, J. D. Nosanchuk and A. Casadevall, *PLoS One*, 2007, **2**, e457.
27 L. Lyttkens, B. Larsson, H. Göller, S. Englesson and J. Stahle, *Acta Oto-Laryngol.*, 1979, **88**, 61–73.
28 R. M. J. Ings, *Drug Metab. Rev.*, 1984, **15**, 1183–1212.
29 P. Jakubiak, F. Lack, J. Thun, A. Urtti and R. Alvarez-Sánchez, *Mol. Pharmaceutics*, 2019, **16**, 2549–2556.
30 M. M. Jastrzebska, A. Kocot and L. Tajber, *J. Photochem. Photobiol., B*, 2002, **66**, 201–206.
31 A. B. Mostert, B. J. Powell, I. R. Gentle and P. Meredith, *Appl. Phys. Lett.*, 2012, **100**, 093701.
32 A. B. Mostert, S. B. Rienecker, C. Noble, G. R. Hanson and P. Meredith, *Sci. Adv.*, 2018, **4**, eaaq1293.
33 Y. J. Kim, W. Wu, S.-E. Chun, J. F. Whitacre and C. J. Bettinger, *Adv. Mater.*, 2014, **26**, 6572–6579.
34 Y. J. Kim, A. Khetan, W. Wu, S.-E. Chun, V. Viswanathan, J. F. Whitacre and C. J. Bettinger, *Adv. Mater.*, 2016, **28**, 3173–3180.
35 I. S. Kwon, Y. J. Kim, L. Klosterman, M. Forssell, G. K. Fedder and C. J. Bettinger, *J. Mater. Chem. B*, 2016, **4**, 3031–3036.
36 H.-A. Park, Y. J. Kim, I. S. Kwon, L. Klosterman and C. J. Bettinger, *Polym. Int.*, 2016, **65**, 1331–1338.
37 M. R. Powell and B. Rosenberg, *Bioenergetics*, 1970, **1**, 493–509.
38 M. Jastrzebska, H. Isotalo, J. Paloheimo and H. Stubb, *J. Biomater. Sci., Polym. Ed.*, 1995, **7**, 577–586.
39 A. B. Mostert, B. J. Powell, F. L. Pratt, G. R. Hanson, T. Sarna, I. R. Gentle and P. Meredith, *Proc. Natl. Acad. Sci. U. S. A.*, 2012, **109**, 8943–8947.
40 S. B. Rienecker, A. B. Mostert, G. Schenk, G. R. Hanson and P. Meredith, *J. Phys. Chem. B*, 2015, **119**, 14994–15000.
41 A. B. Mostert, *J. Mater. Chem. B*, 2022, **10**, 7108–7121.
42 M. Reali, A. Gouda, J. Bellemare, D. Ménard, J.-M. Nunzi, F. Soavi and C. Santato, *ACS Appl. Bio Mater.*, 2020, **3**, 5244–5252.
43 M. Sheliakina, A. B. Mostert and P. Meredith, *Adv. Funct. Mater.*, 2018, **28**, 1805514.
44 J. V. Paulin, S. Bayram, C. F. O. Graeff and C. C. B. Bufon, *ACS Appl. Bio Mater.*, 2023, **6**, 3633–3637.
45 M. P. da Silva, J. C. Fernandes, N. B. de Figueredo, M. Mulato and C. F. O. Graeff, *AIP Adv.*, 2014, **4**, 037120.
46 Z. Tehrani, S. P. Whelan, B. Mostert, J. V. Paulin, M. M. Ali, E. D. Ahmadi, C. F. O. Graeff, O. J. Guy and D. T. Gethin, *2D Mater.*, 2020, **7**, 024008.
47 J. V. Paulin, L. G. S. Albano, D. H. S. Camargo, M. P. Pereira, B. A. Bregadiolli, C. F. O. Graeff and C. C. B. Bufon, *Appl. Mater. Today*, 2022, **28**, 101525.
48 N. L. Nozella, J. V. M. Lima, R. F. de Oliveira and C. F. D. O. Graeff, *Mater. Adv.*, 2023, **4**, 4732–4743.
49 M. Sheliakina, A. B. Mostert and P. Meredith, *Mater. Horiz.*, 2018, **5**, 256–263.
50 P. Kumar, E. Di Mauro, S. Zhang, A. Pezzella, F. Soavi, C. Santato and F. Cicoira, *J. Mater. Chem. C*, 2016, **4**, 9516–9525.
51 C. J. Bettinger and J. Whitacre, *US Pat.*, 9985320, 2018.
52 Y. J. Kim, W. Wu, S. Chun, J. F. Whitacre and C. J. Bettinger, *Proc. Natl. Acad. Sci. U. S. A.*, 2013, **110**, 20912–20917.
53 M. Muskovich and C. J. Bettinger, *Adv. Healthcare Mater.*, 2012, **1**, 248–266.
54 A. N. Tran-Ly, K. J. De France, P. Rupper, F. W. M. R. Schwarze, C. Reyes, G. Nyström, G. Siqueira and J. Ribera, *Biomacromolecules*, 2021, **22**, 4681–4690.
55 J. M. Gallas, *US Pat.*, 4698374, 1987.
56 J. Dong, J. Sun, W. Cai, C. Guo, Q. Wang, X. Zhao and R. Zhang, *Nanomedicine*, 2022, **41**, 102510.
57 A. Camus, M. Reali, M. Rozel, M. Zhuldybina, F. Soavi and C. Santato, *Proc. Natl. Acad. Sci. U. S. A.*, 2022, **119**, e2200058119.
58 E. S. Bronze-Uhle, A. Batagin-Neto, P. H. P. Xavier, N. I. Fernandes, E. R. de Azevedo and C. F. O. Graeff, *J. Mol. Struct.*, 2013, **1047**, 102–108.
59 E. S. Bronze-Uhle, J. V. Paulin, M. Piacenti-Silva, C. Battocchio, M. L. M. Rocco and C. F. D. O. Graeff, *Polym. Int.*, 2016, **65**, 1339–1346.
60 L. Gao, L. Yang, L. Guo, H. Wang, Y. Zhao, J. Xie and N. Shi, *J. Appl. Biomater. Biomech.*, 2022, **20**, 22808000221124418.
61 The Royal Society, *Theo Murphy Meetings*, 2024, From melanogenesis to melanin technologies, Eastbourne, UK.
62 A. van Huis, *Annu. Rev. Entomol.*, 2013, **58**, 563–583.
63 International Platform of Insects for Food and Feed, The European Insect Sector Today: Challenges, Opportunities and Regulatory Landscape, 2019, IPIFF vision paper on the future of the insect sector towards 2030.

64 Y.-S. Wang and M. Shelomi, *Foods*, 2017, **6**, 91.
65 K. C. Surendra, J. K. Tomberlin, A. van Huis, J. A. Cammack, L.-H. L. Heckmann and S. K. Khanal, *Waste Manage.*, 2020, **117**, 58–80.
66 A. Müller, D. Wolf and H. O. Gutzeit, *Z. Naturforsch., C: J. Biosci.*, 2017, **72**, 351–363.
67 C.-H. Kim, J. Ryu, J. Lee, K. Ko, J.-Y. Lee, K. Y. Park and H. Chung, *Processes*, 2021, **9**, 161.
68 A. Mertenat, S. Diener and C. Zurbrügg, *Waste Manage.*, 2019, **84**, 173–181.
69 J. W. Phua and C. J. H. Ottenheim, *US Pat.*, 11981818, 2024.
70 U. D'Amora, A. Soriente, A. Ronca, S. Scialla, M. Perrella, P. Manini, J. W. Phua, C. Ottenheim, R. Di Girolamo, A. Pezzella, M. G. Raucci and L. Ambrosio, *Biomedicines*, 2022, **10**, 2945.
71 N. Ushakova, A. Dontsov, N. Sakina, A. Bastrakov and M. Ostrovsky, *Biomolecules*, 2019, **9**, 408.
72 R. Kerremans, C. Kaiser, W. Li, N. Zarrabi, P. Meredith and A. Armin, *Adv. Opt. Mater.*, 2020, **8**, 2000319.
73 D. Nečas and P. Klapetek, *Open Phys.*, 2012, **10**, 181–188.
74 C. A. Schneider, W. S. Rasband and K. W. Eliceiri, *Nat. Methods*, 2012, **9**, 671–675.
75 N. Fairley, V. Fernandez, M. Richard-Plouet, C. Guillot-Deudon, J. Walton, E. Smith, D. Flahaut, M. Greiner, M. Biesinger, S. Tougaard, D. Morgan and J. Baltrusaitis, *Appl. Surf. Sci. Adv.*, 2021, **5**, 100112.
76 J. V. Paulin, J. D. McGettrick, C. F. O. Graeff and A. B. Mostert, *Surf. Interfaces*, 2021, **24**, 101053.
77 K. Wakamatsu and S. Ito, *Int. J. Mol. Sci.*, 2023, **24**, 8305.
78 S. Ito and K. Fujita, *Anal. Biochem.*, 1985, **144**, 527–536.
79 S. Ito and K. Wakamatsu, *Pigm. Cell Res.*, 1998, **11**, 120–126.
80 P. Meredith and J. Riesz, *Photochem. Photobiol.*, 2004, **79**, 211–216.
81 M. Al Khatib, M. Harir, J. Costa, M. C. Baratto, I. Schiavo, L. Trabalzini, S. Pollini, G. M. Rossolini, R. Basosi and R. Pogni, *Molecules*, 2018, **23**, 1916.
82 N. Madkhali, H. R. Alqahtani, S. Al-Terary, A. Laref and A. Hassib, *Opt. Quantum Electron.*, 2019, **51**, 227.
83 V. Capozzi, G. Perna, P. Carmone, A. Gallone, M. Lastella, E. Mezzenga, G. Quartucci, M. Ambrico, V. Augelli, P. F. Biagi, T. Ligonzo, A. Minafra, L. Schiavulli, M. Pallara and R. Cicero, *Thin Solid Films*, 2006, **511–512**, 362–366.
84 T. Ligonzo, M. Ambrico, V. Augelli, G. Perna, L. Schiavulli, M. A. Tamma, P. F. Biagi, A. Minafra and V. Capozzi, *J. Non-Cryst. Solids*, 2009, **355**, 1221–1226.
85 C. Xin, J.-h Ma, C.-j Tan, Z. Yang, F. Ye, C. Long, S. Ye and D.-b Hou, *J. Biosci. Bioeng.*, 2015, **119**, 446–454.
86 H. Ozeki, S. Ito, K. Wakamatsu and A. J. Thody, *Pigm. Cell Res.*, 1996, **9**, 265–270.
87 K. Wakamatsu and S. Ito, *Pigm. Cell Res.*, 2002, **15**, 174–183.
88 I.-E. Pralea, R.-C. Moldovan, A.-M. Petrache, M. Ilies, S.-C. Heghes, I. Ielciu, R. Nicoara, M. Moldovan, M. Ene, M. Radu, A. Uifalean and C.-A. Iuga, *Int. J. Mol. Sci.*, 2019, **20**, 3943.
89 T. Itou, S. Ito and K. Wakamatsu, *Int. J. Mol. Sci.*, 2019, **20**, 3739.
90 A. Pezzella, M. d'Ischia, A. Napolitano, A. Palumbo and G. Prota, *Tetrahedron*, 1997, **53**, 8281–8286.
91 S. Ito, A. Pilat, W. Gerwat, C. M. B. Skumatz, M. Ito, A. Kiyono, A. Zadlo, Y. Nakanishi, L. Kolbe, J. M. Burke, T. Sarna and K. Wakamatsu, *Pigm. Cell Melanoma Res.*, 2013, **26**, 357–366.
92 D. Niyonkuru, A. Camus, M. Reali, Z. Gao, D. M. Shadrack, O. Butyaev, M. Surtchev and C. Santato, *Nanoscale Adv.*, 2023, **5**, 5295–5300.
93 A. Mbonyiryivuze, Z. Y. Nuru, B. D. Ngom, B. Mwakikunga, S. M. Dhlamini, E. Park and M. Maaza, *Am. J. Nanomater.*, 2015, **3**, 22–27.
94 S. A. Centeno and J. Shamir, *J. Mol. Struct.*, 2008, **873**, 149–159.
95 M. L. Roldán, S. A. Centeno and A. Rizzo, *J. Raman Spectrosc.*, 2014, **45**, 1160–1171.
96 G. Perna, M. Lasalvia, C. Gallo, G. Quartucci and V. Capozzi, *Open Surf. Sci. J.*, 2013, **5**, 1–8.
97 G. Perna, M. Lasalvia and V. Capozzi, *Polym. Int.*, 2016, **65**, 1323–1330.
98 Z. V. Bedran, S. S. Zhukov, P. A. Abramov, I. O. Tyurenkov, B. P. Gorshunov, A. B. Mostert and K. A. Motovilov, *Polymers*, 2021, **13**, 4403.
99 V. Stanic, F. C. B. Maia, R. D. O. Freitas, F. E. Montoro and K. Evans-Lutterodt, *Nanoscale*, 2018, **10**, 14245–14253.
100 I. Galván, A. Jorge, K. Ito, K. Tabuchi, F. Solano and K. Wakamatsu, *Pigm. Cell Melanoma Res.*, 2013, **26**, 917–923.
101 M. Abbas, F. D'Amico, L. Morresi, N. Pinto, M. Ficcadenti, R. Natali, L. Ottaviano, M. Passacantando, M. Cuccioloni, M. Angeletti and R. Gunnella, *Eur. Phys. J. E: Soft Matter Biol. Phys.*, 2009, **28**, 285–291.
102 H. Barek, M. Sugumaran, S. Ito and K. Wakamatsu, *Pigm. Cell Melanoma Res.*, 2018, **31**, 384–392.
103 S. Ito, S. Miyake, S. Maruyama, I. Suzuki, S. Commo, Y. Nakanishi and K. Wakamatsu, *Pigm. Cell Melanoma Res.*, 2018, **31**, 393–403.
104 S. Ito, Y. Nakanishi, R. K. Valenzuela, M. H. Brilliant, L. Kolbe and K. Wakamatsu, *Pigm. Cell Melanoma Res.*, 2011, **24**, 605–613.
105 Y. Liu, L. Hong, K. Wakamatsu, S. Ito, B. Adhyaru, C.-Y. Cheng, C. R. Bowers and J. D. Simon, *Photochem. Photobiol.*, 2005, **81**, 135–144.
106 S. Ghiani, S. Baroni, D. Burgio, G. Digilio, M. Fukuhara, P. Martino, K. Monda, C. Nervi, A. Kiyomine and S. Aime, *Magn. Reson. Chem.*, 2008, **46**, 471–479.
107 B. B. Adhyaru, N. G. Akhmedov, A. R. Katritzky and C. R. Bowers, *Magn. Reson. Chem.*, 2003, **41**, 466–474.
108 P. Thureau, F. Ziarelli, A. Thévand, R. W. Martin, P. J. Farmer, S. Viel and G. Mollica, *Chem. – Eur. J.*, 2012, **18**, 10689–10700.
109 Chem Draw Ultra 12.0.2, *Cambridge Soft Corporation*, 1986-2010.
110 S. Ito and K. Wakamatsu, *Photochem. Photobiol.*, 2008, **84**, 582–592.

111 S. Ito, *Pigm. Cell Res.*, 2003, **16**, 230–236.
112 M. Sugumaran and H. Barek, *Int. J. Mol. Sci.*, 2016, **17**, 1753.
113 M. d'Ischia, A. Napolitano, V. Ball, C. T. Chen and M. J. Buehler, *Acc. Chem. Res.*, 2014, **47**, 3541–3550.
114 P. A. Abramov, O. I. Ivankov, A. B. Mostert and K. A. Motovilov, *Phys. Chem. Chem. Phys.*, 2023, **25**, 16212–16216.
115 S. Soltani, A. Roy, A. Urtti and M. Karttunen, *Mater. Adv.*, 2024, **5**, 5494–5513.
116 M. Ambrico, A. B. Mostert, P. F. Ambrico, J. Phua, S. Mattiello and R. Gunnella, *J. Phys. D: Appl. Phys.*, 2024, **57**, 265303.
117 P. Krebsbach, M. Rincón-Iglesias, M. Pietsch, C. Henel, S. Lanceros-Mendez, J. W. Phua, M. Ambrico and G. Hernandez-Sosa, *ACS Appl. Mater. Interfaces*, 2024, **16**, 42555–42565.
118 N. Al-Shamery, X. Gong, C. Dosche, A. Gupta, M. W. M. Tan, J. W. Phua and P. S. Lee, *Commun. Mater.*, 2024, **5**, 156.

2.3 Functionalization of Melanin: From Structure to Applications

Hybrid materials inspired by nature represent the future of technology, especially in the biomedical sector [1], where the pharmaceutical industry is increasingly engaged in the development of "electroceutical" devices, i.e. instruments that exploit electrical signals for therapeutic purposes [2]. As a consequence, research in the field of bioelectronics is experiencing a rapid expansion. This interdisciplinary field, which lies between physical, chemical and life sciences, is focused on the design of new medical sensors [3]. In parallel, the growing need for low-cost sensors to monitor parameters such as pressure, temperature and humidity [4] is fostering greater environmental and air quality control. However, this diffusion brings with it an increase in electronic waste, including environmentally harmful materials. To address this challenge, a circular economy approach is being adopted, in which waste management and recycling play a key role [5]. In this context, eumelanin, a water-soluble pigment extracted from the pupal exuviae of the black soldier fly (BSF-mel) and from keratin derived from the poultry industry, presents itself as an alternative biomaterial of great interest. Figure 2.3 schematically represents the circular economy cycles resulting from two different waste production systems. On the one hand, butchery and textile activities generate waste such as wool and feathers; on the other, the breeding of soldier flies used for urban waste recycling produces exuviae resulting from the life cycle of the insects. Both of these flows fall into the general category of waste, which can be subjected to extraction processes to recover molecules of interest. These compounds, recovered as secondary raw materials, can be reused in new technological and industrial applications, thus contributing to the valorization of waste and the promotion of a sustainable circular economy model.

The study of this combination is the focus of the work described in the following chapter, in particular in Article V. In parallel, several projects are underway aimed at functionalizing eumelanin to improve its performance. In particular, the compatibility between eumelanin and graphene oxide (GOX) has been studied by mixing the two materials. GOX offers the advantage of presenting numerous functional groups, distributed both on the basal planes and on the edges of the flakes, including hydroxyl (-OH), epoxy (-O-) and carboxylic (-COOH) groups. These groups enhance the hydrophilicity of GOX, hence making it more easily dispersible in water compared to pure graphene. The interaction between the functional groups of eumelanin and GOX occurs without compromising their structures, due to the presence of residual oxygen in the hydroxyl, epoxy, carbonyl and carboxyl groups of GOX, which reacts with melanin [6]. Raman spectroscopy measurements were acquired for both eumelanin (Bsf-Mel) and micronized graphene oxide and the combination of these two organic-inorganic hybrid materials, showing their strong mutual interactions in Figure 2.4. Bright-field TEM images show morpho-micrometric objects of the studied compounds on which the corresponding experimental micro-Raman spectra were acquired (Figure 2.4). Barely micronized GOX (GOXm) indicates disordered sheet arrangements creating bending, curving and wrinkling formations with maximum electronic transparency even compared to

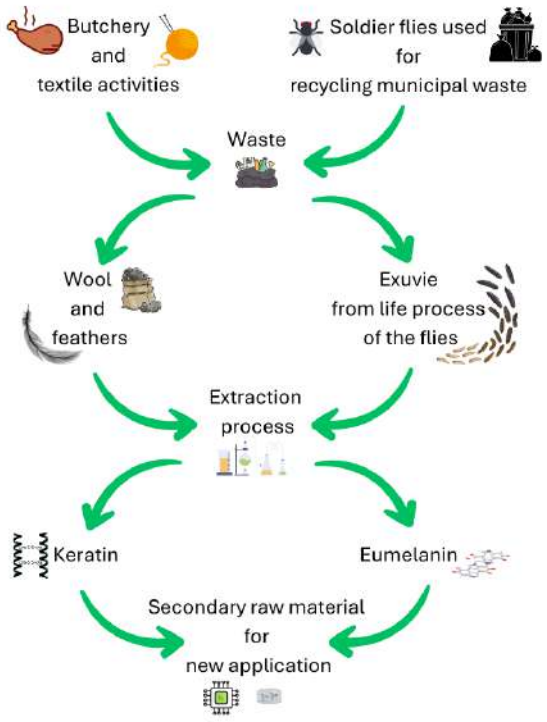

Figure 2.3: Summary diagram of the entire process involved in the reuse of waste with the aim of creating a secondary raw material for new sustainable applications.

the thin-film carbon support depicted in Figure 2.4a.

The structural interaction, technically not visible by HR-TEM, with the surface edge of GOXm is mainly validated by the evolution of the sensitive resonant bands G and D' (Figure 2.4c-RI). Thus, the high-resolution TEM observation of GOXm-BSF-mel provides direct imaging evidence of a linear self-aggregation of BSF-mel nanoparticles interacting with the defective disordered layers of GOXm at the nanoscale (Figure 2.5c).

The aim of this study is to optimize the binding of melanin to GOXm through different graphite sources and functionalization methods, with potential applications in devices such as hygrometers, gas sensors, thermoelectrics, and biophotonics.

2.3.1 Paper V: *Eumelanin & Keratin sourced from waste: unravelling criss-cross functionalities for green electronic applications*

The high solubility of BSF-mel and chicken feather keratin allowed the creation of suspensions in water with the two biopolymers. Keratin was obtained by two different sustainable extraction procedures: reduction by metabisulfite [7] and steam explosion [8]. Colloidal-type suspensions were produced in water as a single-component system or as a mixture of both in selected ratios. The suspensions were examined using a comprehensive set of chemical, structural and dielectric techniques to gather information on their properties. SAXS results provided information on the size and organization of the structures in water, while TEM images indicated that keratin is the component that drives the shape of the aggregation structure in a colloidal environment and, in some cases, showed the internalization of

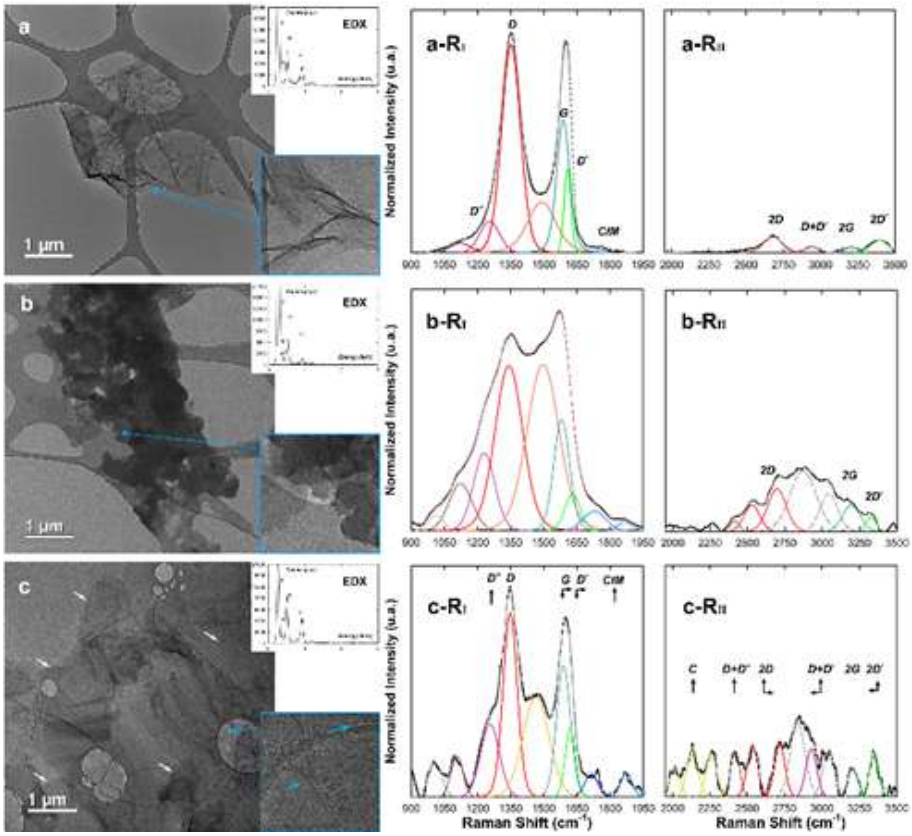

Figure 2.4: Morpho-vibrational microscopy of GOXm, BSF-mel and its GOXm- BSF-mel interactions. a-c Low magnification BF-TEM images of a) GOXm, b) BSF-mel and c) GOXm-BSF-mel. Inset: EDX spectroscopy and magnified image of the corresponding compounds. a-c-RI First-order resonance Raman spectra showing the experimental, fitting and deconvolution profiles. a-c-RII Second-order resonance Raman spectra displaying the experimental, fitting and deconvolution profiles.

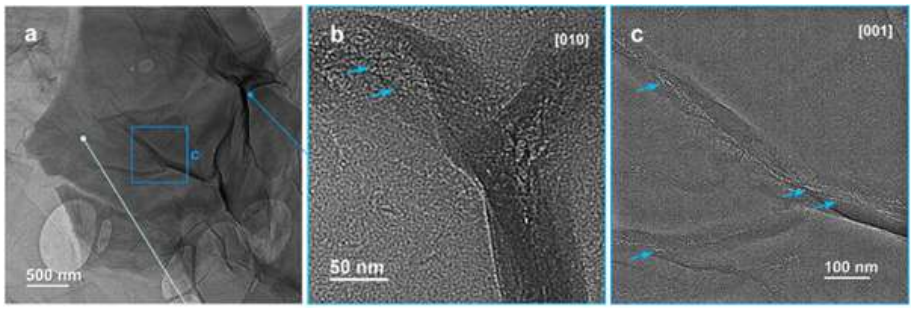

Figure 2.5: Morpho-structural observations of eumelanin interacting with graphene oxide sheets. a) BF-TEM image of the graphene oxide sheet. b) High-resolution image of the bright nanoscale eumelanin aggregates (blue arrow), interacting with the vertical multilayer graphene. c) High magnification of the nanoarea of a (blue line) showing the bright nanoscale eumelanin aggregates aligned along the defective GOXm sheets (blue arrow).

BSF-mel. In particular, SAXS modeling confirmed that the BSF-mel aggregation exhibits a flat disk-like structure with a diameter of 4 nm, similar to that observed in synthetic melanin [9] [10] confirming the π–π/pancake structure [11]. SAXS modeling of steam-exploded keratin (KerST) and metabisulfite keratin (KerBS) reveals a different structure due to the extraction methods. In the case of KerST the model that best fits the data is a particle with a pronounced prolate spheroidal shape, probably due to the mechanical action of the extraction process and to the fragmentation into elementary sections and unfolded peptide chains. In the case of KerBS the best model is a core-shell cylinder, whose overall length extends beyond the limit imposed by the minimum detected scattering moment (100 nm). For the mixed sample with KerBS the scattering profile closely resembles the signal observed for KerBS, indicating that the fibrillar structure of keratin is substantially preserved after the interaction with eumelanin. For the mixed sample involving KerST no major structural transition of eumelanin is detected. The TEM results were found to be in line with the SAXS ones, with aggregation of BSF-mel nanoparticles showing a star-shaped planar structure in KerST and a linear one in KerBS. The structural information was correlated to on the dielectric properties using Broadband Dielectric Spectroscopy (BDS). The BDS spectra highlight cooperative effects through a substantially different behavior with respect to one component, which is more expressed when increasing the eumelanin content. The DC conductivities suggest a plasticizing effect carried out by keratin. Finally, the production of disposable or medium-long term operating devices by adopting deposition techniques from such suspensions in aqueous liquid phase is already underway, with promising results that will be the subject of our future research papers.

Additional details are provided in the Supplementary Information (see Appendix A.2).

References

[1] Taesik Eom et al. "Multifunctional Natural and Synthetic Melanin for Bioelectronic Applications: A Review". In: *Biomacromolecules* 25.9 (2024), pp. 5489–5511. DOI: 10.1021/acs.biomac.4c00494.

[2] Geoffrey Ling and Corinna E. Lathan. "Electroceuticals". In: *SA special* 28.3s (2019), p. 76. DOI: 10.1038/scientificamericanwildideas0619-76.

[3] Nadav Amdursky, Eric Daniel Głowacki, and Paul Meredith. "Macroscale biomolecular electronics and ionics". In: *Advanced Materials* 31.3 (2019), p. 1802221. DOI: 10.1002/adma.201802221.

[4] Daniele Puccinelli and Martin Haenggi. "Wireless sensor networks: applications and challenges of ubiquitous sensing". In: *IEEE Circuits and systems magazine* 5.3 (2005), pp. 19–31. DOI: 10.1109/MCAS.2005.1507522.

[5] Aldo Alvarez-Risco, Shyla Del-Aguila-Arcentales, and Marc A. Rosen. "Waste Management and the Circular Economy". In: *Towards a Circular Economy*. Ed. by Aldo Alvarez-Risco, Marc A. Rosen, and Shyla Del-Aguila-Arcentales. CSR, Sustainability, Ethics & Governance. Springer, Mar. 2022. Chap. 0, pp. 119–131. DOI: 10.1007/978-3-030-94293-9.

[6] Min-Chien Hsiao et al. "Preparation of covalently functionalized graphene using residual oxygen-containing functional groups". In: *ACS applied materials & interfaces* 2.11 (2010), pp. 3092–3099. DOI: 10.1021/am100597d.

[7] Sara Mattiello et al. "Physico-chemical characterization of keratin from wool and chicken feathers extracted using refined chemical methods". In: *Polymers* 15.1 (2022), p. 181. DOI: 10.3390/polym15010181.

[8] Qingshan Shen et al. "Steam explosion as a green method to treat animal waste: a mini-review". In: *Process Safety and Environmental Protection* 181 (2024), pp. 43–52. DOI: 10.1016/j.psep.2023.11.012.

[9] JM Gallas et al. "Solution structure of copper ion-induced molecular aggregates of tyrosine melanin". In: *Biophysical journal* 77.2 (1999), pp. 1135–1142. DOI: 10.1016/S0006-3495(99)76964-X.

[10] Kenneth C Littrell et al. "Structural Studies of Bleached Melanin by Synchrotron Small-angle X-ray Scattering". In: *Photochemistry and photobiology* 77.2 (2003), pp. 115–120. DOI: 10.1562/0031-8655(2003)0770115SSOBMB2.0.CO2.

[11] PA Abramov et al. "Signatures of pancake bonding in hydrated eumelanin". In: *Physical Chemistry Chemical Physics* 25.24 (2023), pp. 16212–16216. DOI: 10.1039/D3CP01773G.

OPEN ACCESS
IOP Publishing
Journal of Physics D: Applied Physics
J. Phys. D: Appl. Phys. **58** (2025) 125302 (21pp)
https://doi.org/10.1088/1361-6463/ada44d

Eumelanin & keratin sourced from waste: unraveling criss-cross functionalities for green electronic applications

Marianna Ambrico[1,*], Sara Mattiello[2], Albertus Bernardus Mostert[3], Jun Wei Phua[4], Domenico Aceto[1], Paolo F Ambrico[1], Alessandro Guzzini[2], Angelo De Stradis[5], Federico Liuzzi[6], Carlo Santulli[2], Giulio Lupidi[7], Alessandra Del Giudice[8] and Roberto Gunnella[2]

[1] CNR-Institute for Plasma Science and Technology, Bari Branch, Via Amendola 122/D, I-70125 Bari, Italy
[2] School of Science and Technology University of Camerino, Via Madonna delle Carceri 9, I-62032 Camerino, MC, Italy
[3] Centre for Integrative Semiconductor Materials, Department of Physics, Swansea University Bay Campus, Fabian Way, Swansea SA1 8EN, United Kingdom
[4] INSECTTA Pte. Ltd, 8 Cleantech Loop, Singapore 637145, Singapore
[5] CNR-Institute for Sustainable Plant Protection, Bari Branch, Via Amendola 165/A, I-70126 Bari, Italy
[6] ENEA-Centro Ricerche Trisaia, S.S. 106 Ionica 301-75026 Rotondella, MT, Italy
[7] School of Pharmaceutical Sciences and Health Products, University of Camerino, Via Madonna delle Carceri 9 I-62032 Camerino, MC, Italy
[8] Department of Chemistry, Università 'La Sapienza' di Roma, Piazzale Aldo Moro, 5, 00185 Rome, Italy

E-mail: marianna.ambrico@istp.cnr.it

Received 17 October 2024, revised 5 December 2024
Accepted for publication 30 December 2024
Published 23 January 2025

Abstract

In the framework of the Circular Economy this study provides a detailed analysis of water-based suspensions of two biopolymers derived by sustainable processes: eumelanin from insect farming and keratin from chicken feathers. The latter material was obtained via two different extraction procedures. Colloidal-like suspensions were produced in water either as a single component system or a mixture of both in selected ratios, taking advantage of their high solubility. The suspensions were examined using a comprehensive set of chemical, structural and dielectric techniques to gather information on their properties. Small-Angle x-ray Scattering results provided insights into the elemental polymer sections within the suspension, while Transmission Electron Microscopy images indicate that keratin is the component driving the shape of the aggregation structure in a colloidal environment, and, in some cases, eumelanin internalization. Furthermore, the co-presence of both polymers in water determines the aggregation dimensions and shapes. The discussion focuses on the influence of the aggregation on the dielectric proper-ties by comparing the former to the AC dynamic response returned by

* Author to whom any correspondence should be addressed.

Broadband Dielectric Spectroscopy (BDS). Within the BDS framework various items are highlighted including dielectric relaxations, screening effects, counterion condensation and ionic charge transport. The results shown in this work let to foresee the adoption of water or biofriendly aqueous BSF-EuM:Keratin suspensions in the production of devices and sensors with low environmental impact.

Supplementary material for this article is available online

Keywords: circular economy, organic waste, eumelanin, keratin, TEM, SAXS, dielectric spectroscopy

1. Introduction

A key objective of the Circular Economic (CE) is 'to minimize waste and promote a sustainable use of natural resources, through smarter product design, longer use, recycling and more, as well as regenerate nature' [1]. In this framework, one of the CE challenge is to reduce the waste production and/or the adoption of effective solutions in waste management.

One example of applying CE thinking to a major source of waste is to the organic fraction from municipal waste. Based on the most recent 2022 European Compost Network (ECN) report, '[2] an estimated 71 million metric tons per annum (tpa) of separately collected biowaste were treated through composting and anaerobic digestion (60 million tpa in the EU27 and 11 million in CH, NO and UK)'. These estimates included both municipal and commercial/industrial biowastes. Composting accounted for 42 million tpa (59%), while anaerobic digestion (AD) accounted for 29 million tpa (41%) [2].

A parallel problem has also emerged due to the increase in the use of electronics. The large variety of electronic devices, from the simplest ones such as disposable sensors, to the most complex ones such as batteries, PCs, mobile phones etc are all rapidly subjected to hardware updates. As a result, a significant amount of electronic waste (e-waste) is produced (>45 megatons per year), adding strain to the environment [3, 4]. Therefore, e-waste management constitutes a new challenge for a CE approach. One partial solution can be found in the introduction of biodegradable electronics, whose products coming from decomposition or disintegration will lessen the impact on the environment [3].

However, other major activities produce organic waste, for which effective CE solutions are still to be found. Among the others, wool and poultry industries, which contribute large amounts of waste [5].

Recently, two categories of organic waste have become an unexpected resource that could potentially address the e-waste and wool/poultry farming waste problems: eumelanin, obtained via processing of black soldier fly larvae shed skins (BSF-EuM) and keratin obtained from wool and feathers via industrial processes. This has been the result of companies and start-ups investing in innovative processes trying to push them more and more towards low or zero environmental impact. A specific aim is the extraction of biomaterials with unique functionalities, making them spendable on the market in diverse areas of manufacturing, packaging, environmental technologies, medicine, and agriculture [6].

These two classes of materials, eumelanin and keratin, are the focus of this work, and are in general of great interest as many research groups worldwide have investigated them for their useful properties [7–19].

The eumelanin materials can be classified into three main compounds that are associated to the more traditional, nitrogen containing materials, with the primary compound called eumelanin (commonly termed melanin) and is a black-brown pigment derived at least in part from the oxidative polymerization of L-dopa via 5,6-dihydroxyindole intermediates; the second main compound is pheoeumelanin, a yellow-to-reddish brown sulfur containing pigment derived from the oxidation of cysteinyldopa precursors via benzothiazine and benzothiazole intermediates. The third main compound is neuroeumelanin, found in the substantia nigra of the brain stem and is a dark pigment produced within neurons by the oxidation of dopamine and other catecholamine precursors that has been shown to contain a pheoeumelanin core and a eumelanin outer shell [20–22].

Eumelanin, the melanin investigated herein, is of technological interest due to its properties and demonstration of use in devices. Properties include broad band optical absorbance [23–25], metal ion chelation [26], paramagnetism [27], radiation protection [28, 29], and humidity dependent conductivity [25, 30–32], to name a few. For devices, several examples include electrochemical transistors [31, 33, 34], energy storage [35–38], memory [39, 40], optoelectronic skins [41], phototransistors [42], coloring films [43], and sensors [7, 44–47]. Eumelanin has the additional advantage of demonstrating biodegradability with reduced phytotoxic effects, thus paving the way for its use as a potential green electronics material [48].

Keratin represents the most abundant structural protein in epithelial cells and, together with collagen, the most important biopolymer in animals [49]. Given its biological origin, it is remarkable to see its toughness and wide range of functions. For instance, scales provide body armor, horns are used for combat, hagfish slime acts as a defense against predators, nails and claws enhance prehension, and hair and fur protect against environmental elements. These inspiring examples can offer valuable insights for designing new structural and functional

materials. Different forms of keratin can be obtained with different phases of purification, appropriately modulated and depending on the origin (e.g. wool or feathers), yielding differentiation in structure, which allows for example, the production from membranes to gels [10, 13]. The various properties of these keratin substances make them interesting from an application point of view for microelectronics, applied medicine, and energy storage [13, 14, 50].

Eumelanin contains both amino and catechol groups that are well known for metal ion chelation [51], which we anticipate being an anchoring mechanism for eumelanin internalization into keratin biopolymers, as suggested by the removal of eumelanin from melanocytes into keratinocytes [52]. Thus, we envisage new multifunctional materials of eumelanin/keratin for exploitation.

With the above background, we were stimulated towards a deeper understanding of the chemical, structural and electrical transport properties of eumelanin-keratin materials. Especially given that the properties of the elicited biopolymers and their combination can significantly alter their properties and enabling interfacing with both biological and inorganic systems. For melanic materials, the advantage they confer is they can carry both ionic and electronic current compatible with the demands of bio-electronic devices [53]. The multiplicity of final morphological structures of keratin, together with their strength and adhesiveness makes them suitable for supporting appropriate functionalization steps.

Notably, the high solubility/dispersibility in water for both materials allow studying them in a peculiar environment at a neutral pH, without altering the chemistry of either biopolymer. Also, this peculiarity makes them of particularly interest in transient electronic devices and specifically in those adopted in biology or medicine, where sensors are mainly working once in water-exposed conditions, and where the biodegradability and high performance are requirements [54].

An additional side benefit is that exploring the electrical transport properties in an only water-based suspension, one can investigate and isolate redox processes that is between H_2O and the unaltered chemical structure of these materials, whether a single component or a mixture.

With the above in mind, this work will develop through the investigation firstly water-based suspensions of each component, and then their mixtures. We will first present the chemical and structural aspects of these systems, with experimental data from FTIR on powders then from TEM and SAXS. From this data set we will infer the resulting functionality and modification of the mixtures from the baseline materials.

Once the chemical and structural data has been presented, we will show in the second part of this work the electrical responses via broadband dielectric spectroscopy (BDS) of these materials in water suspensions. The resemblance between these suspensions (both single-component and mixed) and those involving hydrated proteins (as discussed by the first relevant paper of Schwan and recently by Nakanishi [55, 56]) prompts us to focus on analyzing the BDS spectra. In our study, we will extensively analyze the BDS data within the framework of the Havriliak-Negami (HN) dielectric modeling. This approach is like a recent study we have conducted on solid state eumelanin samples [57].

Insights gained will then be correlated back to the chemical and structural work.

2. Materials and methods

2.1. BSF-EuMelanin and Keratin extraction methods

The eumelanin investigated in this paper is extracted by the start-up Insectta Pte. Ltd from the pupal exuviae of the black soldier fly larvae. This company occupies a circular economic position within Singapore, in which the flies are used to valorize food waste, and the black soldier fly eumelanin (BSF-EuMelanin, from now on labeled as BSF-EuM for sake of conciness, whenever needed) is a value-added product currently co-extracted during the process of chitin production. The production cost is therefore low, while the yield is approximately 1% by weight from pupal exuviae. Thus, the BSF-EuM appears to be a competitive product, critically being based upon a circular economic approach. The expectation is that price will continue to decrease and volume increase as the product becomes more widely recognizable, and applications are found for it.

BSF-EuM was isolated from the black soldier fly (Hermetia illucens) according to a patented protocol released by Insectta [58]. The process in brief is as follows: Hermetia Illucens pupal exuviae were minced into approximately 0.5 mm pieces using a blender (Robot Coupe Blixer 4, France). The pupal exuviae were then demineralized with 10% (w/w) lactic acid at room temperature for 3 h. To reduce protein contamination in the eumelanin fraction, deproteination of the pupal exuviae was performed with 1 M NaOH for 3 h at 50 °C. Subsequently, eumelanin was liberated by heating the mixture with 3 M NaOH, for 2 h at 90 °C. Thorough washing of the mixture was performed in between steps. The eumelanin-containing supernatant was filtered through a 500 mm mesh nylon cloth, with the eumelanin fraction precipitated with the addition of 37% (v/v) HCl of a series of proprietary steps. The procedure is then concluded with lyophilization to obtain salt-free, water-soluble, sub-micrometres particles of BSF-EuM.

In this work two types of keratins are investigated. The first type of keratin used in this work is extracted from organic waste feathers samples, but adopting the steam explosion extraction technique, which we labeled as KerST. In this process the biomass is treated with hot steam (180 °C–240 °C) under pressure (1–3.5 MPa) followed by an explosive decompression, resulting in a breakage of the rigid structure of the fibers [59, 60]. Feathers for the process were prepared as follows: a first wash with cold water and common soap followed by drying at 60 °C in a forced-air oven. The second wash is then with ethanol at 50 °C for 2 h to remove surface fats and waxes. The defatted feathers were then removed from the ethanol solvent and ethanol residue removed after incubation for 3 h in a forced-air oven at 60 °C. The feathers were then soaked in demineralized water, at a ratio of 1:1 feather to water. This mixture is then pretreated using steam explosion using an ENEA 10 l Staketech batch digester at 200 °C for 10 min

Table 1. List of mixtures investigated in this study. * Filtered by a 0.45 μm membrane before the measurement.

Suspensions	Mel:Ker	Items code	SAXS (mg ml^{-1})	BDS/TEM (mg ml^{-1})
BSF-EuMF*	1:0	S0F	—	10
BSF-EuMUF	1:0	S0UF	4.0	10
KerST	0:1	S10	17.5	10
KerBS	0:1	S20	7.5	10
BSF-EuM:KerST 15*	1:4	S15	10	10
BSF-EuM: KerST 16*	1:9	S16	—	10
BSF-EuM: KerST 17*	4:1	S17	—	10
BSF-EuM : KerST 18*	9:1	S18	—	10
BSF-EuM :KerBS 21*	1:4	S21	10	10
BSF-EuM :KerBS 22*	1:9	S22	—	10
BSF-EuM :KerBS 23*	4:1	S23	—	10
BSF-EuM :KerBS 24*	9:1	S24	—	10

under a pressure of 15 bar. After 10 min of each pre-treatment with saturated steam, the biomass was rapidly transitioned to atmospheric pressure by opening an electronic valve, promoting further breakdown. The impregnation process favors the deconstruction of the biomass within the reactor [61]. The steam explosion process was carried out in duplicate and from the process we obtained keratin in water solution at a concentration of 45 mg ml^{-1}. To obtain powder samples useful for measurement, KerST was subjected to a lyophilization process. This process removes the water by freezing the material, then lowering the pressure and applying heat, causing the frozen water to sublimate directly from solid to vapor [62]. For lyophilization we employed a FreeZone Freeze Dryer (LABCONCO), subjecting the samples to 0.02 mbar in vacuum at 20 °C for about 5 d.

The second keratin system was extracted from the same organic waste feathers (KerBS) as the KerST using the chemical process, as described in Mattiello *et al* [63], consisting of a metabisulfite extraction method. This process was selected as it provides sufficient persistence of the secondary structure of the protein. In addition, the procedure is effective, easily applicable to the raw material, requires lower amounts of chemicals and has a lower toxicity compared to other methods such as the mercaptoethanol method [64, 65].

2.2. Suspensions preparation

The solutions and concentration shown in this work are shown in table 1. For SAXS measurements the concentration in single component suspension was regulated to reduce the interactions between the chains and study the fine structure. In mixed suspensions the final concentration was still 10 mg ml^{-1} keeping the same mass ratio and concentration adopted for BDS/TEM measures. The measurement was focused on the 1:4 mass ratio in both keratin types.

In BDS/TEM measurements the suspensions were made by dissolving the powders of the biopolymers, whether single or mixed, in deionized water (H2O conductivity $\sigma = 1.0$ μS cm^{-1}). The total concentration of the biopolymer was 10 mg ml^{-1}, with the ratio between BSF-EuM and Keratin varied by mass.

In all the characterizations, the various suspensions were filtered by a 0.45 μm filter membranes, a procedure that enabled the selection of particles with similar dimensions and, in BSF-EuM the removal of residual protein in BSF-Eumel.

2.3. Transmission electron microscopy (TEM)

For TEM analysis, a drop (20 μl) of a solution was applied to a carbon-coated copper/rhodium grid (400 mesh) (TAAB Laboratories Equipment Ltd, Aldermaston, Berks, ENGLAND). The coated grid was floated for 2 min on the drop, rinsed with 200 μl of double distilled water and then stained by a negative staining solution (200 μl of 0.5% w/v UA-Zero EM stain, Agar-Scientific Ltd, Stansted, UK). After draining off the excess staining solution by means of dabbing it with filter paper, the specimen was then transferred to the electron microscope for examination, using a Philips Morgagni 282D transmission electron microscope, operating at 80 kV. Electron micrographs of negatively stained samples were photographed on Kodak electron microscope film 4489 (Kodak Company, New York, USA). The negative staining procedure is employed to take advantage of increased electron scattering from higher density materials. Consequently, electrons being scattered from the negative staining solution exhibit brighter signals in the resulting images. In non-homogenous items, the final images is shown in grayscale; the bright region means 100% materials, the black absence of material.

2.4. Fourier transform infrared spectroscopy (FT-IR)

FT-IR spectra were recorded from 4000 to 600 cm^{-1} with a PerkinElmer Spectrum 100 FT-IR instrument (Waltham, MA, USA) by total reflectance utilizing a CdSe crystal. The FT-IR spectra were collected on KerBS and BSF-EuM in powder form.

2.5. Small-angle x-ray scattering (SAXS)

SAXS experiments were performed using a Xeuss 2.0 Q Xoom system (Xenocs SA, Grenoble, France) equipped with a microfocus Genix 3D x-ray Cu source ($\lambda = 0.1542$ nm) and a

two-dimensional Pilatus3 R 300 K detector placed at variable distance from the sample (Dectris Ltd, Baden, Switzerland). Measurements were made on liquid solutions obtained by dissolving powder samples in distilled water (DI) at different concentrations as listed in table 1.

The samples were loaded into disposable borosilicate capillaries with nominal thick-ness 1.5 mm and sealed with hot glue. Two capillaries, one loaded with the deionized water used as dispersant and an empty one, were used for background subtraction.

The measurements were performed at room temperature and at reduced pressure (∼0.2 mbar), with two different sample-detector distances to access a scattering vector modulus (q) range between 0.045 and 13 nm^{-1}, where $q = \frac{4\pi \sin(\theta)}{\lambda}$, 2θ is the scattering angle and λ is the x-ray wavelength of light. The two-dimensional scattering patterns were subtracted for the 'dark' counts, and then masked, azimuthally averaged, and normalized for transmitted beam intensity, exposure time, and subtended solid angle per pixel, by using the FoxTrot software developed at SOLEIL. The one-dimensional intensity vs. q profiles were subtracted for the contributions of the solvent and empty capillary and reported in intensity units of macroscopic scattering cross-section (cm^{-1}) by dividing by the capillary thickness estimated from the alignment scans. Pair distance distributions were obtained by indirect Fourier inversion of the $I(q)$ profiles, or $I(q)\cdot q$ in case of the cross-section of elongated objects. These distributions were obtained with the software BayesApp [66]. Model intensities to help data interpretation were calculated using the software SASfit [67].

2.6. Electrical measurements configuration and experimental apparatus

The electrical measurements of the suspensions were done by using a disposable standard 8 well arrays (Applied Biophysics, maximum volume well 600 μl, figure 1) provided with interdigitated Au electrodes (IDE) at the bottom side. The IDE structure consists of a comb structure composed of nine couples of Au electrode fingers, 0.8 cm long, placed at 50 μm.

The sampling of the suspension was kept constant by using only 200 μl, whereas the IDE configuration ensured a consistent electrode geometry, thus eliminating variation from geometrical effects. The electrical data of the suspensions were measured using Electrical Impedance Spectroscopy (EIS), where the complex impedance of the suspension Z is obtained from scanning several frequencies of sinusoidal, alternating current-voltage measurements.

The EIS measurements were obtained by a NOVOCONTROL Impedance Analyzer. The AC voltage signal amplitude (V_{AC}) was fixed at 300.0 mV, DC offset was 0.0 V, and the frequency (f) range scan was between 0.1 Hz to 10.0 MHz, 8 pts/decade, with a total of 56 points and a recording time of around three minutes.

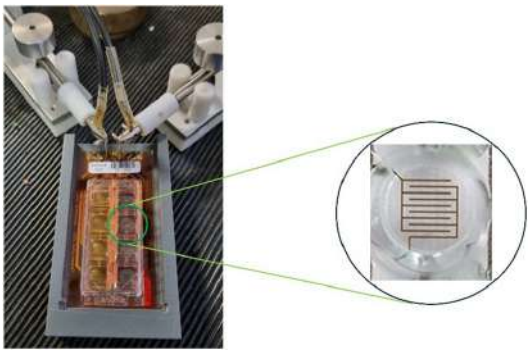

Figure 1. Representative disposable 8 well arrays provided by IDE at the bottom side (left, Applied BioPhysics) and probe connection to the measurement apparatus adopted for the electrical measurements on suspensions. The enlarged view of the IDE on the bottom of the well is shown on the right.

2.7. Electric data analysis and modeling

The EIS data were analyzed within the broadband dielectric spectroscopy (BDS) approach, utilizing two representations: the first is the complex dielectric permittivity ε^* spectra; the second is the complex AC conductivity spectra, σ^*.

The permittivity ε^* is related to the real (ε') and imaginary (ε'') components as:

$$\varepsilon^* = \varepsilon' - j\varepsilon''. \tag{1}$$

Each component is calculated from the complex impedance by [56, 68] by the following equation

$$\varepsilon' = \frac{-\mathrm{Im}\,[Z]}{2\pi f |Z|^2 C_0}; \text{and } \varepsilon'' = \frac{-\mathrm{Re}\,[Z]}{2\pi f |Z|^2 C_0} \tag{2}$$

with C_0 representing the equivalent vacuum cell capacitance, $|Z|$ the modulus of the impedance Z and f the frequency. In the present case, since it is difficult to estimate the geometrical parameters, we obtained C_0 by directly measuring the impedance vs. frequency on the empty cell and taking the value at the highest frequency, which is related to the dielectric constant and geometrical parameter of the cell [69]. We obtained a value of $C_0 = (1.0 \pm 0.1) \times 10^{-13}$ F cm^{-1}.

Additionally, the loss factor $\tan\delta$ is derived via:

$$\tan\delta = \frac{\varepsilon''}{\varepsilon'}. \tag{3}$$

We adopt the Trukhan model to estimate the diffusion coefficient D_{ion} of free ionic charge carriers where [57, 70]:

$$D_{\mathrm{ion}} = \frac{\omega_{\max} L^2}{9 \times 32 \left(\tan\delta_{\max}\right)^3} \tag{4}$$

that has been rescaled with respect two known parameters, i.e. the number of finger couples (9) and finger distance

($L = 50\ \mu$m). The 'max' subscription indicates the radial frequency position and corresponding value of the maximum of the loss factor

The free ionic concentration n is then determined from the Nerst equation by

$$n = \frac{\sigma'_{DC}}{e^2}\frac{k_B T}{D} \tag{5}$$

where e is the fundamental charge and $\sigma'_{\mathrm{DC}}$is the real part of the conductivity at $\omega_{\max}$, i.e. the conductivity corresponding to the plateau value in the real AC conductivity spectrum, $k_B T$ is as normal Boltzmann's constant and temperature multiplied, which for room temperature and our measurements is 0.025 eV. Also, the Debye lengths are calculated as:

$$L_D = \frac{L}{8(\tan\delta_{\max})^2}. \tag{6}$$

Since the as calculated ε' spectra also includes the DC conductivity contribution, it is useful to remove it by representing a particular ε' derivative (Kramers-Kronig relationship) with respect to lnω where ($\omega = 2\pi$f) is the radial frequency [56, 71]:

$$D_{\ln\omega}\varepsilon'(\omega) = -\frac{\pi}{2}\frac{\partial\varepsilon'}{\partial\ln\omega} \approx \varepsilon''_{\mathrm{rel}}. \tag{7}$$

Here we adopt the *'D'* notation for the derivative. $\varepsilon''_{\mathrm{rel}}$ is the dissipation of the complex dielectric function, but which excludes the conductive components of the dissipation, leaving only the polarizing components. This feature enables the better resolution of polarization relaxation peaks, especially peaks at lower frequencies assigned to α and β relaxations [71, 72]. This is justified since we are examining the AC response of protein-derived systems [56].

Considering the equivalence of the derivative in expr. 7 with $\varepsilon''_{\mathrm{rel}}$, it comes out that the relaxation processes will be featured by the same parameters as $\varepsilon'_{\mathrm{rel}}$. Therefore, we can apply the Havriliak-Negami (HN) formalism, which is used to model relaxation peaks, but without the conductivity term [56, 71]. This means that we examine the derivative of the real part of the dielectric permittivity via:

$$D_{\ln\omega}\varepsilon'(\omega) = \sum_{i=1}^{K}\left[\frac{\Delta\varepsilon_i}{\left(1+(j\omega\tau_{HNi}^{a_i})^{b_i}\right)}\right]. \tag{8}$$

The superposition of up to three ($K = 3$) dielectric relaxation functions enabled to achieve the best fit of the spectra. Each HN function is featured by a relaxation time distribution peak at a specific relaxation time (τ_{HNi}), with characteristic parameters $\Delta\varepsilon_i$, termed as the dielectric strength and coefficients a_i and b_i. The former coefficient is assigned to the broadening and the latter to the symmetry of the time relaxation peak [73–75].

The frequency of the peak $f_{\mathrm{MAX,HNi}}$ for each relaxation (α, β, EP, see below for further definition) is determined from the τ_{HNi} values by using [76]:

$$f_{\mathrm{MAX,HNi}} = \frac{\omega_{\mathrm{MAX,HNi}}}{2\pi} = \left(\frac{\sin\left(\frac{\pi a_{\mathrm{HNi}}}{2(b_{\mathrm{HNi}}+1)}\right)}{\sin\left(\frac{\pi b a_{\mathrm{HN}}}{2(b_{\mathrm{HNi}}+1)}\right)}\right)^{a^{-1}}\tau_{\mathrm{HNi}}^{-1},$$

$$\mathrm{HNi} = \alpha, \beta, EP\,. \tag{9}$$

From now on we will use $f_{\alpha/\beta/\mathrm{EP}}$ and $\omega_{\alpha/\beta/\mathrm{EP}}$ referring to the values determined via expr. 9.

A consolidated picture considers the dielectric relaxations observed in polyelectrolyte in aqueous solutions as due to counterion polarizability, balancing the ionic groups in the polymer backbone [77]. The peculiar chemical structure of eumelanin and keratin let to assigned both to the class of (poly)electrolyte [17, 78] where proton ions (H_3O^+) acts as the counterions.

Within a polyelectrolyte system a phenomenon of counter ion condensation in water is highly probable. This situation is when the charge density of a linear polyelectrolyte chains exceeds a critical value that is then neutralized by counterions in solution; 'Free' counterions 'condense' in the vicinity of the chain such that the Coulomb repulsion energy of two adjacent charged groups on the chain decreases below kT [79].

This condensation condition is reached when the separation, d, of monovalent charges along the polymer chain is less than the Bjerrum length l_B where $l_B = \mathrm{e}^2/(4\pi\varepsilon_r\varepsilon_0\mathrm{kT})$. This condition is generally satisfied for polyelectrolytes in water since $\varepsilon_r(H_2O) = 80$, which yields an $l_B = 7$ Å while $d < 7$ Å [77].

This condensation manifests itself in the dielectric response as a feature at low frequency f_α (α -relaxation) with polarization along the longitudinal direction of the polymeric chain. Whereas the β-relaxation frequency, f_β, represents the free counterions still available and is seen at higher frequencies and polarization along the radial along the radial direction [77].

Given that these frequencies relate also to the linear l_α and radial l_β dimension of the polymeric aggregates, one can determine these effective lengths via the diffusion coefficients of the condensed $D_{\mathrm{ion},\alpha}$ and free counterions $D_{\mathrm{ion},\beta}$ [77, 80–82]:

$$f_{\mathrm{MAX}(\alpha/\beta)} \sim \frac{6D_{\mathrm{ion}(\alpha/\beta)}}{l^2_{\alpha/\beta}} \quad \text{and} \quad \omega_{\mathrm{MAX}(\alpha/\beta)} = 2\pi f_{\mathrm{MAX}(\alpha/\beta)} \tag{10}$$

where $D_{\mathrm{ion}_{(\alpha/\beta)}}$ are the Nerst diffusion coefficient (expr. 4) corresponding to the conductivity values at f_α and f_β. As a first approximation we will use the free ionic charge density n as calculated via the Trukhan Model in expr. 5 to estimate the corresponding counterion density either in the calculation of both D_{ion_α} or D_{ion_β}.

3. Results and discussion

3.1. Transmission microscopy results

The BSF-EuM morphology in the filtered suspension (BSF-EuMF) as observed by TEM (figure 2) was characterized by

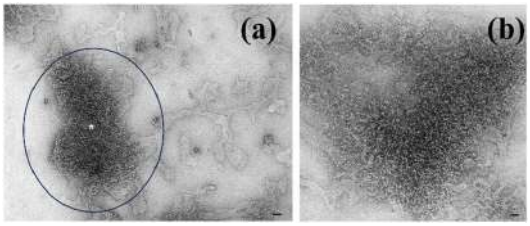

Figure 2. (a) TEM images of the BSF-EuMF structure; magnification 30.000X, bar = 100 nm. The bright region refers to high particle density continuously dispersed and the gray/black zone refers to a low particle density region both assuming a sheet like structure (b) Magnified image of the region indicated via the asterisk and circle, (magnification 150.000X, bar = 30nm), evidencing a low-density region of the sheet constituted by a discrete aggregation of nanoparticles ø = 5 nm.

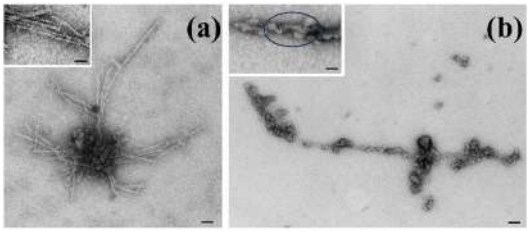

Figure 3. TEM images of the (a) KerST, left and (b) KerBS, right structure; in both cases the magnification 80.000X, bar = 40 nm and for the inset 150.000X, bar = 25 nm. In (a) KerST: Star-like aggregation and tubular filamentary structure (the inset in figure 3(a) is a magnification of the tubular structure). In (b) KerBS: Linear aggregation in a bent-like structure; the inset displays a magnified view highlighting the presence of a helix- like bent structure.

a non-homogeneous distribution of submicrometric colloidal particles represented by the bright region of figure 2(a) that contours, and a high density of small colloidal particle aggregation represented by the gray/black region (on the left side of figure 2(a) and magnified in figure 2(b)). The estimated dimension of the particles has been measured between 4 and 10 nm in size (modal value ∼7 nm) in agreement with other previous observations [9].

The KerST and KerBS structures (figures 3(a) and (b) respectively) resulted immersed in a colloidal suspension, (bright region) made up of dispersed particles. Notably, their size has been found non uniform in KerST and highly homogenous in KerBS. Moreover, KerST displayed starlight aggregation featured by tubular filamentary structure (see inset in figure 3(a)), whereas KerBS displayed a linear belt structure. Furthermore, the magnification of the KerBS structure (see inset in figure 3(b)) evidence the presence of a helix-like substructure. The TEM morphological analysis (figures 4(a)–(d)) in BSF-EuM: KerBS and KerST mixed suspensions still evidenced a colloidal background (bright scale) of dispersed particles where the two components cannot be clearly distinguished. However, the radial structure of KerST and of KerBS are greatly modified in the 1:4 case (a-e) and 4:1 (b-f) where the aggregation region exhibits similar features.

In both the 1:9 and 9:1 system the particle aggregation is modified by becoming more linearized, driven by the Keratin structure. Some peculiar arrangement of the 1:9 and 9:1 BSF-EuM:KerBS (figures 4(g) and (h)) have been observed with the internalization of the eumelanin in between the keratin filaments in the former and the external arrangements in the latter.

3.2. FT-IR results

In figure 5, the FT-IR taken on one component compares those already published on BSF-EuMel [57] and KerBS [63] with the data collected for the first time on KerST. This because the steam explosion method is not usually adopted for protein extraction and to verify that the process did not degrade the protein. On mixed component suspensions, the FT-IR of keratin spectrum always dominated the melanin one, notwithstanding the relative concentration ratios with no observable and relevant new spectral features. As a matter of example we add the comparison between FT-IR in mixed BSF-Eum: KerBS and BSF-EuM:KerST at a ratio of 1:4 (see figure in ESI) (see figure S1 in ESI).

The spectrum of BSF-EuM is characterized by several vibration bands, indicated in the figure 5 with the stars. A wide band in zone of 3200 cm^{-1} can be observed, corresponding to links vibration of the functional groups −OH and −NH2, 2918 cm^{-1} corresponding to the N–H stretching [83–87]. Specific eumelanin stretches were observed also between 1500–1400 cm^{-1}, which were attributed to the bending vibration of N–H and the stretching vibration of C–N (secondary amine) of an indolic [88]. The strong infrared band in the range of 1380–1240 cm^{-1} indicated the presence of a pyran ring [89]. Several eumelanin spectra have also included absorption bands between 1250–1180 cm^{-1}, caused by the stretching vibration of phenolic –OH groups [88]. The spectrum confirms that the extracted eumelanin is a eumelanin.

The spectra for KerST and KerBS exhibit the characteristics protein bands of Keratin. The absorption band at approximately 3300 cm^{-1}, is attributed to the stretching vibrations of N–H and O–H bonds and is associated with amide A [90]. Stretching vibrations of the C=O bonds, appearing between 1600 and 1700 cm^{-1}, are characteristic of the amide I band, which is linked to the secondary structure of keratin [91]. The bending vibration of N–H at 1520 cm^{-1} corresponds to amide II [92]. The stretching vibrations of C–N and C–H, along with the bending vibrations of N–H and C=O, occurring around 1220–1300 cm^{-1}, are related to amide III [93]. A notable difference between the two spectra is the sizeable reduction of the amide III signal components (1220–1300 cm^{-1}) and the vibrations present in the region between 700 and 1100 cm^{-1} visible in the KerBS sample. This range is highly sensitive to the presence of sulfur derivatives, suggesting that an increasing number of disulfide bonds have been reduced to form cysteic

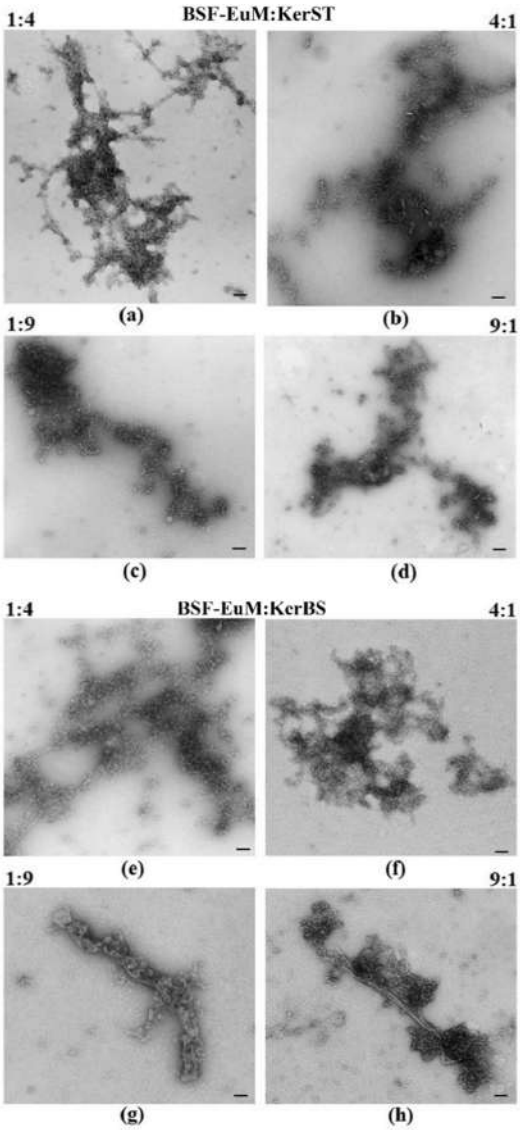

Figure 4. TEM micrographs of BSF-EuM:KerST (a)-(d) and BSF-EuM:KerBS (e)-(h) in different ratios. (Magnification 80.000 X, bar = 50nm). In figure 4(c) the different positioning of BSF-EuM around the KerBS ribbon is evidenced, showing the BSF-EuM internalization in KerBS in the former.

acid [91], which is related to the use of the metabisulfite method. From the above, the FT-IR analysis confirms that the underlying structure of keratin has been conserved and not destroyed by the extraction methods, though in the case of KerST less Sulphur groups are present.

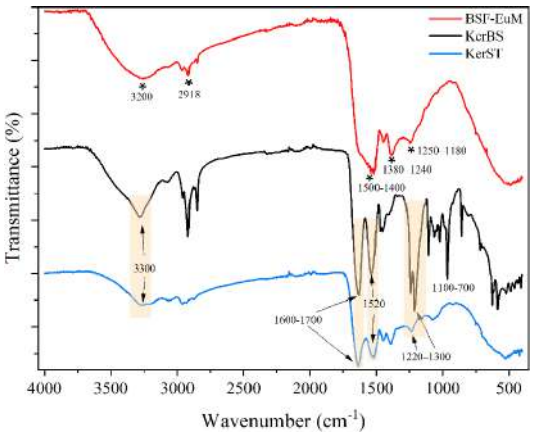

Figure 5. Comparison of FT-IR spectra for one component KerBS, KerST and BSF-EuM in powder form. The yellow boxes highlight the principal protein bands, while stars indicate the principal eumelanin vibration bands. The wavenumber corresponding to the vibration are also reported.

3.3. SAXS results

The profile collected for BSF-EuM (figure 6(a)) shows both an initial slope ($q < 0.1$ nm^{-1}) and a final slope ($1 < q < 3$ nm^{-1}) close to q^{-2}. suggesting them to fall within the case of an approximately planar geometry of both the overall dispersed aggregates and the individual particles [94]. In the intermediate q range (0.5–0.8 nm^{-1}) a knee is visible that corresponds to inhomogeneities in the dimension of particles with a radius of gyration of ∼2.5 nm, as assessed by an indirect Fourier transform in the range of 0.18–4 nm^{-1} to obtain a pair distance distribution function (p(r), inset of figure 6(a)). The model that provides an overall curve fit corresponds to a form factor of thin disks with diameter of 5.2 ± 0.1 nm and average thickness of 0.6 ± 0.3 nm, correlated by a mass fractal structure factor with fractal dimension of 2.9 and overall aggregate size above the limit imposed by the available angular range (>100 nm).

These dimensions for BSF-EuM are noteworthy. In previous x-ray diffraction literature from Cheng *et al* [95, 96], powdered eumelanin was also modeled to a similar disklike structure with lateral dimensions of 4–8 units of eumelanin, with 4 layers of stacking and a repeating dimension of ∼1.5 nm. In our results, it should be noted that the thickness of approximately 1 nm is poorly determined and with a high uncertainty due to the signal of the sample (being a 4 mg ml^{-1} diluted suspension in water rather than a powdered solid) reaching the water background level for $q > 5$ nm^{-1}. However, if a thickness equal or greater than 1.5 nm is imposed, the model visibly deviates from the data, and this suggests that the disks should be made by less than 5 layers of π-π/pancake bonded stacking structure [97].

In addition, our most probable modeled disk diameter (4 nm) is much wider than Cheng *et al*'s, suggesting that the BSF-EuM particles are extended 'floppy' sheets of material.

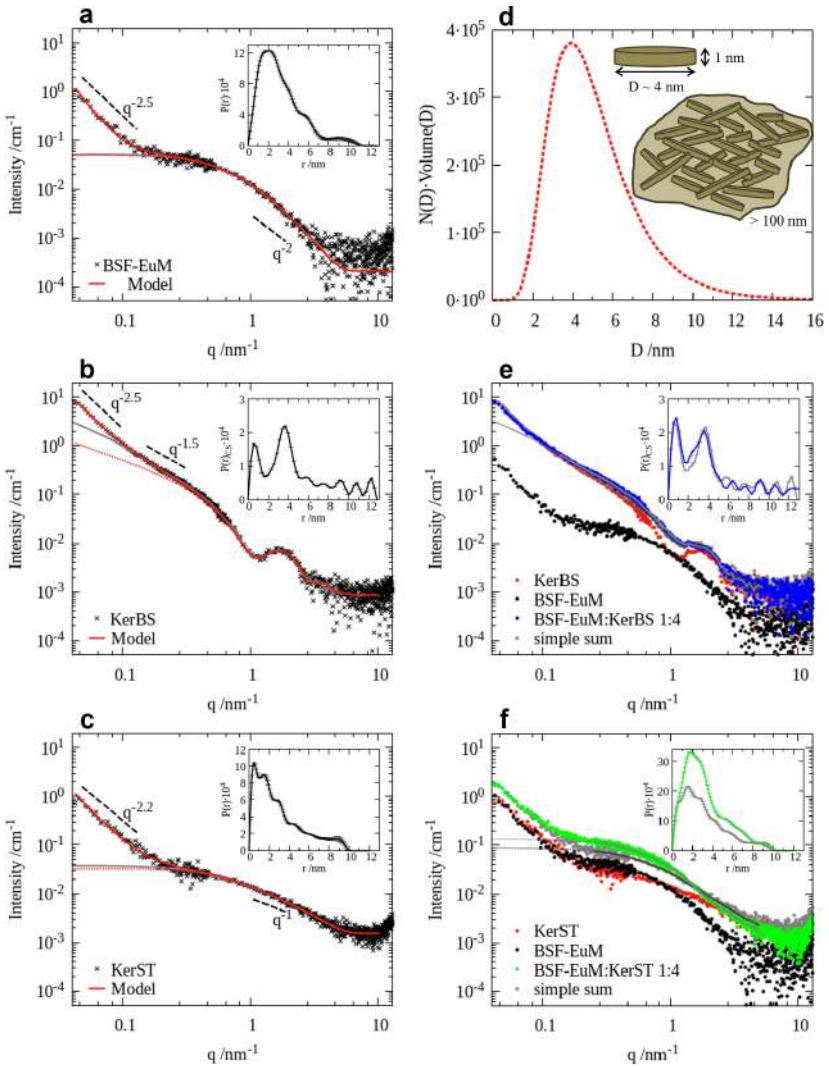

Figure 6. SAXS scattering curves of pure components (the black crosses represent raw data, the red line represent the calculated model curve, with the dotted portion only showing the form factor without structure factor): (a) BSF-EuM at 4 mg ml^{-1} concentration in water solution and (d) BSF-EuM size distribution of disk diameter that fits the data keeping fixed the disk thickness to 1 nm, is shown, together with a sketch of the model; (b) KerBS at 7.5 mg ml^{-1} concentration in water solution (c) KerST with a concentration of 17.5 mg ml^{-1} in water solution. (e) and (f) Superimposition on absolute units of the SAXS data of eumelanin (black dots), keratin (red dots) and their mixtures (blue or green dots), compared to simulated data obtained as a simple sum of the two components (grey dots): (e) eumelanin (BSF-EuM), sulphitolysis keratin (KerBS) and their mixture obtained in the BSF-EuM: KerBS 1:4 proportion; (f) eumelanin (BSF-EuM), steam explosion keratin (KerST) and their mixture obtained in the BSF-EuM: KerST 1:4 proportion. In all panels the insets show the pair distance distribution functions of the overall data ($P(r)$) or of the cross-section for elongated objects ($P_{CS}(r)$), and the corresponding fits to the data by indirect Fourier inversion are shown as solid grey lines in the main plots.

When inspecting Cheng *et al*'s data though, it should be noted that their data was obtained on dried eumelanin, both natural and synthetic, but at higher q ranges (10–100 nm^{-1}) where they also saw additional peaks, corresponding to much smaller characteristic distances, below 0.5 nm.

A better comparison to our data set would be the work of Gallas *et al* [98] and Littrell *et al* [99] where the authors did a SAXS study on various synthetic eumelanin, where similar concentrations and q ranges were employed. These works exhibit SAXS data with similar knee features as those reported here (figure 6(a)). What is interesting is that these authors determined stacked particles of thicknesses of ∼1 nm (3–4 layers), with disklike structures showing diameters of 5 nm. In this regard, the extent of the particles contained in the BSF-EuM sample correspond well with this synthetic eumelanin dispersed in water.

As a second pristine material to consider is the KerBS keratin from metabisulphite extraction [63]. In this case the best model for the data in figure 6(b), indicate a core-shell cylinder model, whose overall length extends above the limit imposed by the minimum scattering momentum detected (>100 nm). Additionally, there is a lower electron density of the core and higher electron density of the shell, compatibly with the higher sulphur content occurring on the keratin protofilament surface. The core radius assumes values from 1.2 nm to 3.3 nm according to a decaying size distribution that can accommodate a possible small number of bundled individual filaments within fibrils (<7), while the shell thickness is of the order of 0.8 nm. The deviation in the low q regime ($q < 0.15$ nm^{-1}) from the power law expected for rigid rods (close to $q^{-2.5}$ rather than q^{-1}) can be due to flexibility of individual fibrils or a degree of inter-fibril correlation. Such deviation can be reproduced by considering a mass fractal structure factor with dimensionality 2, characteristic object size of 13 nm and cut-off distance of 100 nm. Such a model is like what is observed in [94], which shows long ribbons with cross-sectional units of about 3 × 3 nm^2, hinting a possible preservation of the keratin protofilament structure by the extraction method.

Differently from KerBS, the scattering profile collected for KerST (figure 6(c)), does not show the features of a fibrillar structure, but has two characteristic slopes (close to q^{-1} for $q > 1.5$ nm and close to q^{-2} for q <0.2 nm^{-1}), and a knee in the intermediate range that would correspond to characteristic sizes of the order of 2 nm. A possible model used to represent the SAXS data is consisting of a form factor of a swollen coil, with radius of gyration of 1.8 nm and a self-avoiding behavior with Flory exponent close to 0.6 (rather than 0.5 for random walk), in conjunction with a fractal structure factor in which the individual object size is around 7.5 nm and the dimensionality is 2.5. Alternatively, the high q data is preferably interpreted in terms of compact particles rather than chain structures. The best fit was obtained with a spheroid model, which implies a pronouncedly prolate geometry (with axes 1.1 nm × 1.1 nm × 9 nm) rather than oblate and flat-like. In any case, the average size of individual scatterers is significantly smaller compared to the KerBS structure, probably due to the mechanical action of the extraction process and the fragmentation in elementary sections and unfolded peptide chains.

In these two latter cases of keratin a different power law was observed in the intermediate q range (around 0.1 nm^{-1}, approximately a length scale of 30 nm), corresponding to a transition from a preferentially 1D system (KerBS) to a 2–3D one (KerST).

For the mixed sample involving KerBS (BSF-EuM:KerBS (1:4), figure 6(e)) we find that the scattering profile of the mixture closely resembles the signal observed for KerBS, indicating that the fibrillar structure of the keratin is substantially preserved after interaction with eumelanin.

In this case, comparing the mixture data with simulated data as a simple sum of the two components, a small deviation can be appreciated in the q range 0.7–1.5 nm^{-1}. Observing the calculated pair distance distribution functions of the cross section, the deviation can be related to a change of the internal fibril electron density contrast (distances <5 nm), suggesting that the small eumelanin disks can be partially incorporated into the fibril structure. For the mixed sample involving KerST (BSF-EuM:KerST (1:4), figure 6(f)) no large structural transition of the eumelanin is detected, but the significantly higher scattering intensity of the mixture compared to a simple sum of the profiles of pure keratin and eumelanin samples suggests enhanced co-aggregation of the keratin extracted components within the eumelanin clusters, whose individual units preserve sizes of 5–6 nm.

3.4. Broadband dielectric spectroscopy

The BDS is recognized as a technique highly sensitive to dipolar interaction of water molecules (proton ions) on a wide set of materials [56, 77, 79] Among the others, its application has been widely used to provide deep insight on water-biopolymer and protein interaction, the former including BSF-Eumelanin as well [57]. In the first case, the examination was exclusively performed between water vapor molecule and BSF-EuM layer providing detailed information on the evolution of the dielectric response vs. hydration [57]. Water-protein interaction [56] has been also the subject of several studies adopting BDS. Since keratin belongs to the class of protein, BDS can be considered a suitable technique for studying its interaction with water. The structural information gained by TEM evidenced the formation of a homogenous colloidal suspension and regions where peculiar aggregation structures are observed. SAXS suggested enhanced co-aggregation of the keratin extracted components within the eumelanin clusters. The structural picture gathered via TEM and SAXS will take advantage of the BDS, suitable in providing more information on the effect of those structures via the dielectric relaxation and, much more, in a solvent dipolar system like water. In fact, the feasibility of spanning a wide range of frequency via BDS offers detailed insights into the AC response of a biopolymer mixture. In this framework, the BDS is intended to be the superposition of regions that respond to the frequency of the AC signal depending on their

extension and resulting in final relaxation observed in the spectra. As stated above, the slower relaxation depends on the linear extension of the aggregates the faster on the radial extension. (expr.10) Both regulate the dynamic of the ionic charges (counterions) leading to slow (condensed counterions) or fast (free counterion) ion charge dynamics. Therefore, these measurements are guided by dielectric polarization mechanisms, thus the 'geometrical' dimensions determined by using this approach may differ from those seen in SAXS and TEM.

The BDS results is particularly suitable in detecting the AC response of a biopolymer mixture in a solvent dipolar system like water. The ε' spectra, as seen on a linear y-axis scale (figure 7), show that each single component biomaterial suspension decreases their dielectric constant at a characteristic radial frequency, $\omega_{EP,}$ which signals the cut-off frequency of the electrode polarization (EP) effect [57, 100]. The EP attribution is justified by the criterion adopted consisting in the comparison between the real and imaginary part of the dielectric permittivity (ε', ε'') and conductivity (σ', σ'') (figure 8) where the corresponding peaks in the imaginary part of the dielectric constant (ε'') and conductivity (σ'') signals the full development of the EP [100] (figure 8).

Thus, these lower frequency ranges capture the behavior of the electrode and its influence on the material under investigation. These effects are electrode-material specific and is not intrinsic to the biopolymer per se, which make low frequency features less useful for interrogation [100, 101]. However, in our study we use the same set of electrodes and geometry, allowing us to make an accounting of the electrode effects and talk intelligibly about the material behavior in the sub-EP region. We note that the variation in ω_{EP} depends on the biopolymer and suggest a different extension (range) of the electrostatic forces acting on the ionic charge distribution, which regulates the screening length termed as Debye length [100, 102].

We also note that at high frequency the real component of the dielectric constant saturates to a value of ∼80 for all the suspensions, which is close to the background solvent of water [103].

It is noteworthy that qualitatively the unfiltered BSF-EuMUF and KerST and the filtered BSF-EuMF and KerBS are similar. Specifically, dispersion of KerST and unfiltered BSF-EuME reveals two visible relaxation peaks (figure 7(b)). The first one we attribute to a β-relaxation. Utilizing the elicited AC conductivity data alongside the permittivity leads us to attribute the second peak to the relaxation frequency of the electrode polarization (see figure 8) [100, 104]. In contrast, the spectra of filtered BSF-EuM and KerBS seems to exhibit only a single dominant relaxation process.

However, it is essential to recognize that the DC conductivity contribution to the relaxation processes is superimposed on the as received permittivity data, which may obscure the true dielectric dispersion and prevent complete resolution of relaxation processes [56].

Therefore, to gain accurate insights into the relaxation processes, we employ the $D_{\ln\omega}\varepsilon'(\omega) \approx \varepsilon''_{rel}$ representation to eliminate the DC contribution (figure 7(c)). Each spectrum exhibits unique features, although similarities emerge due to the same derivation of the dissolved/suspended components.

With the corrected data set, we employ a best fit approach adopting the HN formalism to $D_{\ln\omega}\varepsilon'(\omega) \approx \varepsilon''_{rel}$ with the fits shown in figure 9 and fitting parameters summarized in table S1. We clearly distinguish three HN distributions: HN_α, HN_β & HN_{EP} corresponding to three distinct relaxation processes, α, β & EP. These are now better resolved compared to their somewhat hindered representation in ε' or ε''. In the low-frequency region (0.1–10 Hz), the increase in $D_{\ln\omega}\varepsilon'(\omega) \approx \varepsilon''_{rel}$ evidence the tail of a slower α-relaxation with the frequency of the peak displaced close to the lower of the measurement range (see f_α values in table 2). This relaxation is representative of the slow motion in the solvent of larger aggregates and can be furthermore associated to the system viscosity [81, 106, 107]. The magnitude of the corresponding dielectric strengths increases in BSF-EuMF with respect to BSF-EuMUF, whereas in KerBS it is higher than in KerST.

The second component, which is in the medium-frequency range, is assigned as a β relaxation and is associated with the polymer local conduction via ionic charge hopping mechanisms [77, 80, 104]. In this specific case the hopping is water mediated and depends on the hydration [55]. Notably, β relaxation magnitudes and peak positions are the same in KerST and BSF-EuMUF, highlighting similar features in the hydration-mediated processes. This may be the result in both cases of the presence of residual impurities as recently evidenced by 13 C CP/Mas NMR spectra of BSF-MelEuM where an intense signal is present in the aliphatic region of BSF eumelanin [108, 109]. Inspecting the keratin data reveals that in KerBS the contribution of the β relaxation is smaller than either the EP or α relaxation. Additionally, the β relaxation has a broader frequency distribution. The lower relative effect of the β relaxation with respect to EP can be a consequence of the more hydrophobic nature of KerBS, which was observed to be less soluble in water. Again, this may be due to a higher presence of sulfur functionalization, leading to a more hydrophobic property.

Finally, the third component represents the EP, whose magnitude may be regarded as an index of the strength of the screening charge effect. Following what is declared in the TEM analysis, if we regard the suspensions as a colloidal one, these values estimate the extension of the ionic charge distribution from around the suspended particles to the medium, i.e. the Debye length L_D [102, 110]. In the present case, the calculation of L_D via expr. 6 returned values between 0.27 nm to 2.03 nm corresponding to free ionic charge concentrations of approximated 10^{20} cm^{-3} in BSF-EuMF to 10^{18} cm^{-3} in all the other systems (see table 2).

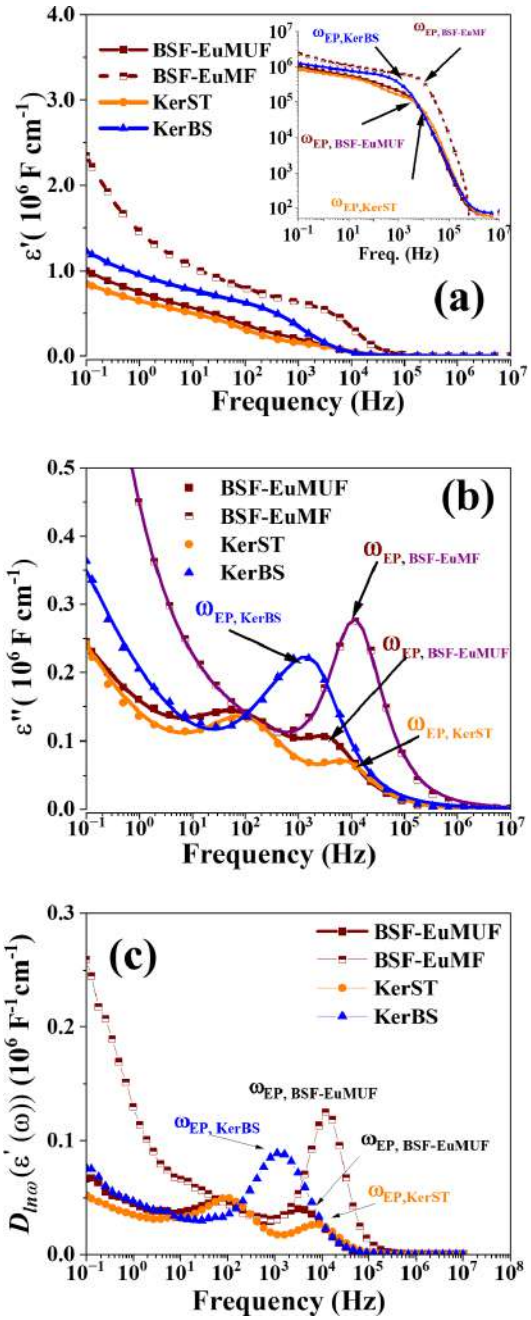

Figure 7. Linear scale representation of the dielectric permittivity dispersion relations of the single component suspension (conc. 10.0 mg ml^{-1}). Spectra include: (a) the real part of the dielectric permittivity ε' (inset shows log scale representation and radial frequency EP position; (b) the imaginary component ε''; $D_{\ln\omega}\varepsilon'(\omega) \approx \varepsilon''_{\rm rel}(\omega)$. In the inset of (a) the log ε' vs. f show the radial frequency $\omega_{\rm EP}$ corresponding to the drop of the ε' curve. We also indicate by $\omega_{\rm EP,\ BSF\text{-}EuMUF}$ and $\omega_{\rm EP,\ BSF\text{-}EuMF}$ the radial frequency position in unfiltered and filtered BSF-EuM suspensions. The radial frequency positions relate to that shown on the f-axis as $\omega = 2\pi f$.

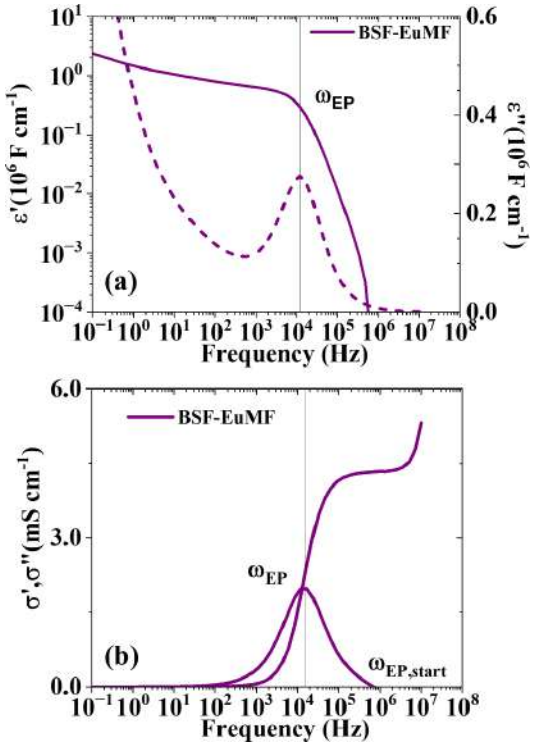

Figure 8. Representative example of the localization of the radial frequency $\omega_{EP} = 2\,\pi\,f_{EP}$ corresponding to the full development of the EP via the comparison between the real and imaginary part of the dielectric permittivity (8a, ε', ε'') and conductivity (8b, σ', σ''). The plateau in ε' is due to the charge accumulation at the electrodes and may mask possible other relaxations (see main text). The radial frequency of the frequency referred to the EP in ε'', and σ'' correspond to the drop in permittivity and to the onset in the σ' towards the plateau. In σ'' the radial frequency of the start of the EP has been indicated. The data refers to BSF-EuMF suspension (10 mg ml^{-1}) [104, 105].

The as calculated dielectric permittivity spectra for the two component suspensions are shown in figure S2, where substantial differences in the behaviors are manifested as compared to the single component spectra in figure 7.

More specifically, the changes revealed much relevant modification in the shape with respect to the single component, hinting furthermore a superposition of the contribution of relaxation of both components. Notably, the impact of the co-presence of the two polymers is evidenced by the shape modification becoming much more evident when increasing the eumelanin content. This is more noticeable in KerST mixed suspension (see 4:1 and 9:1, figure 10(c)) whereas in the case of KerBS mixed suspensions, this is noticeable in the 9:1 ratio (figure 11(d)). These behaviors agree with the SAXS results describing a higher co-aggregation in the case of KerST, that could be also the reasoning behind the behavior seen via BDS, furthermore evidencing the dependence vs. the increase of the melanin :keratin ratio.

To gain clarity, we again utilize the $D_{\ln\omega}\varepsilon'(\omega) \approx \varepsilon''_{\text{rel}}$ formalism to subtract the DC conductivity, with the corrected spectra shown in figures 10 and 11.

The significant alteration of the derivatives spectra $D_{\ln\omega}\varepsilon'(\omega) \approx \varepsilon''_{\text{rel}}$ can be related to the values calculated from the best fit dielectric parameters extracted vi the HN approach. These results (table 2) indicate that this is due to shifts in the peak frequencies, $f_{\alpha,\beta}$ (and correspondingly of the $\omega_{\alpha,\beta}$) of the α and β relaxations along with variations in the dielectric strength ($\Delta\varepsilon_{\alpha,\beta}$) parameters. These distributions are also influenced by changes in the a_i and b_i parameters (see values in table S1 and figure 12).

The behavior of the radial frequencies ω_α and ω_β of the relaxation peaks (symbols) vs. BSF-EuM:KerST(BS) ratio (figures 12(a) and (b)) suggests changes in the ion chain dynamics, ω_α, and local motion compared to those in the single component (straight lines) and more vs. the keratin ones. Specifically, a general increase is observed in ω_α (figure 12(a)) hinting the changes (i.e. reduced length) in the polymer chain dimension possibly due to the melanin introduction and/or a cooperative effect between both components. Conversely, the modification of the dynamics of the local motion, represented by the ω_β (figure 12(b)), is notable in the case of KerBS -based mixtures.

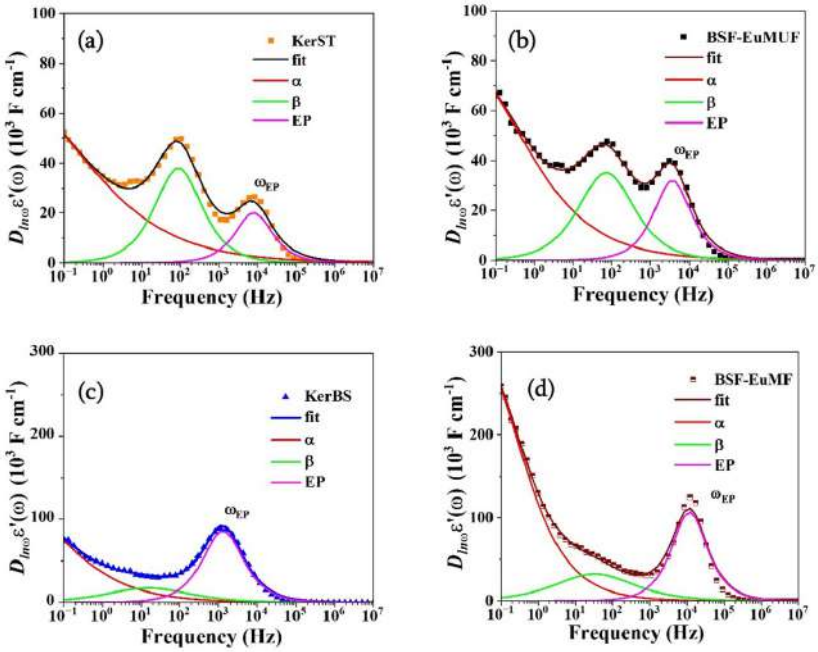

Figure 9. HN fits to the $D_{\ln\omega}\varepsilon'(\omega)$ representation of the single material/solvent suspensions (10.0 mg ml^{-1}). (a) KerST spectra; (b) KerBS spectra; (c) BSF-EuMUF spectra; (d) BSF-EuMF spectra. The three relaxations are represented in distinct colors: red for α-relaxation, green for β relaxation and magenta for EP relaxation. The corresponding HN parameters are listed in table S1).

The ω_{EP} in mixed suspensions display values generally lowering vs the BSF-EuM:KerST(BS) ratio (figure 12(c)). This effect together with the lowering of the $\Delta\varepsilon_{EP}$ implies a lower strength of the electrode polarization effect and lower ionic charge density (n in table 2) manifesting itself by the increase in the Debye length L_D particularly evident with respect to BSF-EuMF dipolar relaxation [106].

Inspecting the peak frequency positions and calculating l_α and l_β through the diffusivities of the 'condensed' $D_{ion,\alpha}$ and free counterion density $D_{ion,\beta}$ provided further insight on the interaction in one and mixed component with water. In single component suspensions, the two keratin systems show similar ω_α (f_α) values whereas variation have been observed in ω_β (f_β). These returned similar dimensions of the particle aggregates l_α, and different radial dimension i.e. ion charge hopping distance, l_β (table 2) [80, 81].

The former can be explained as due to the similar extension/length of the keratin rod-like aggregates and polymer chain motion features; the latter being related to ionic charge local motion can be due to the more hydrophobic properties of KerBS in water due to the local presence of a higher Sulphur functionalized surface with respect to KerST as also evidenced by FTIR results.

The lower values of l_α and the corresponding values of $D_{ion,\alpha}$ in almost all mixed suspensions vs. keratin suggest that the dielectric response modifies in water due to reciprocal effect of eumelanin on the structure of the keratin aggregate. Furthermore, this let to hypothesize the increase of the 'condensed' proton counterion density binding with the ionic dipoles on keratin backbone, thus explaining the blue shift of the radial frequencies ω_α [111]. Also, l_α being related to the α-relaxation, this let to argue that the variation may affect suspension viscosity [106, 112].

Moreover, we observe the increase l_β i.e. hopping distance, vs. the increase of the relative eumelanin content with respect to keratin, meaning that the hopping is slowed down.

The analysis of the dielectric strengths values shows an overall strong reduction of the $\Delta\varepsilon_\alpha$ (from 10^6 to 10^5 F cm^{-1}) and $\Delta\varepsilon_{EP}$ (from 10^5 to 10^4 F cm^{-1} with respect to the single component one (see table S1), whereas the magnitude of $\Delta\varepsilon_\beta$ is much less affected. The lower values of $\Delta\varepsilon_\alpha$, further underlining the reciprocal effect of the two biopolymers in affecting the cooperative motion and the dipolar relaxation of each single component [106].

Finally, although the measured AC conductivities fall in the range 10^{-5} S cm$^{-1} \div 10^{-3}$ S cm^{-1} in all suspensions, either in one component and mixed ones, (figure 13) a lowering of the values of the DC values (value at the plateau in the real component σ') has been found in mixed suspension especially with respect to BSF-EuMF. This suggest that keratin insertion is the main component limiting, via proton counterion condensation the free ionic charge transport. The lowering of the DC conductivity, combined with the changes in l_α, hints possible keratin-vehiculated plasticizing effect [113].

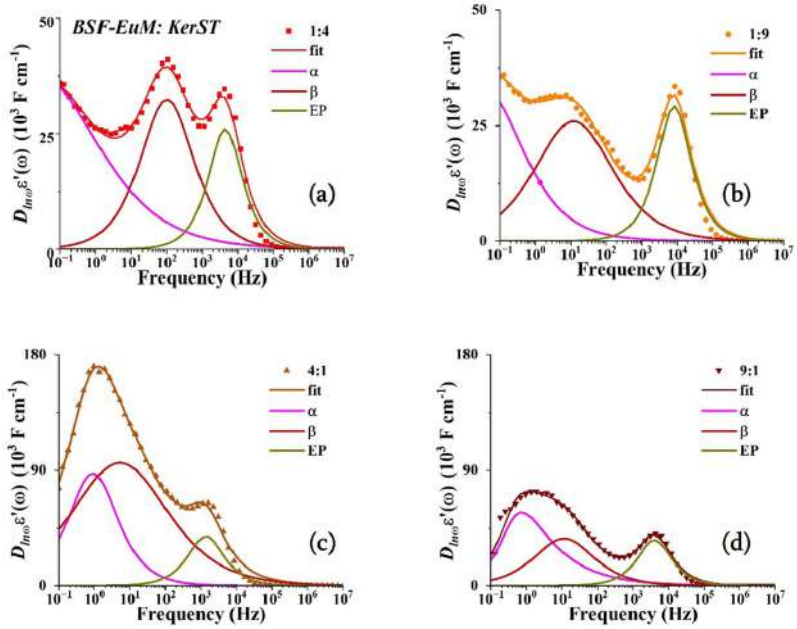

Figure 10. The $D_{\ln\omega}\varepsilon'(\omega)$ spectra with associated HN fits for the two component suspensions of BSF-EuM and KerST for different ratios: (a) 1:4, (b) 1:9, (c) 4:1, (d) 9:1. The three relaxations peaks are represented by distinct colors: magenta—α-relaxation, wine—β relaxation, dark yellow—EP relaxation. The corresponding HN parameters are reported in table S1.

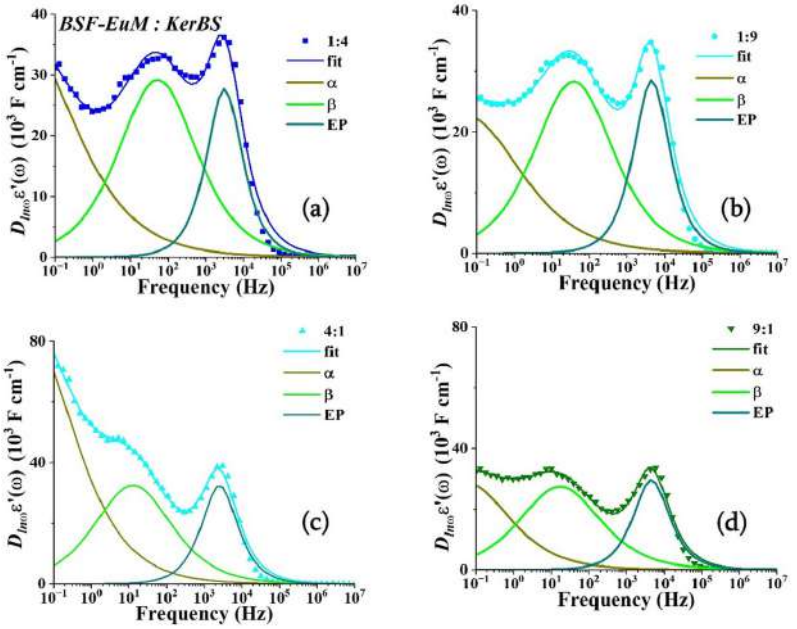

Figure 11. The $D_{\ln\omega}\varepsilon'(\omega)$ spectra with associated HN fits for the two component suspensions of BSF-EuM and KerBS for different ratios; (a) 1:4, (b) 1:9, (c) 4:1, (d) 9:1. The three relaxations peaks are represented by distinct colors: dark yellow—α-relaxation, green—β relaxation, dark cyan—EP relaxation. The corresponding HN parameters are reported in table S1

Table 2. Free ionic charge concentrations, n, and Debye lengths, L_D, of one the component and mixed suspensions calculated via expr. 5 and 6; values of diffusivity of condensed $D_{ion\alpha}$ and free $D_{ion\beta}$ counterion diffusivity together with the estimated rod length l_α and hopping/radial distance l_β.* BSF-EuM:KerST mass ratio.

Suspensions	n (10^{18}cm^{-3})	L_D (nm)	ω_{EP} (rad s^{-1})	ω_α (rad s^{-1})	ω_β (rad s^{-1})	$D_{ion\alpha}$ (10^{-10} cm^{2}s^{-1})	$D_{ion\beta}$ (10^{-8} cm^{2}s^{-1})	Ratio*	l_α (μm)	l_β (μm)
BSF-EuMUF	1.27	1.92	23 364	0.09	457	1.67	7.6	—	2.60	0.79
BSF-EuMF	164	0.27	73 529	0.21	205	0.05	0.03	—	0.30	0.08
KerST	0.96	2.12	52 910	0.01	633	2.19	13	—	9.00	0.88
KerBS	1.51	2.03	14 285	0.01	2994	2.09	46	.	8.00	0.76
BSF-EuM:KerST										
	1.04	2.35	51546	0.23	76	0.96	0.84	0.11	1.26	0.64
S16 1:9	1.00	2.63	27 778	0.15	667	1.20	10.9	0.25	1.75	0.78
S15 1:4	2.46	2.31	8696	5.62	33	3.13	0.91	4.00	0.45	1.04
S17 4:1	1.13	2.66	25 189	3.05	48	19.0	1.35	9.00	1.58	1.03
S18 9:1					—					
BSF-EuM:KerBS										
	1.23	2.57	28571	0.33	240	0.80	2.20	0.11	0.95	0.58
S22 1:9	1.01	2.98	19 724	0.06	680	0.82	9.70	0.25	2.30	0.73
S21 1:4	1.03	2.49	16 077	0.12	80	2.26	1.20	4.00	2.60	0.77
S23 4:1	1.60	1.64	28 902	0.37	107	0.98	2.30	9.00	1.00	0.90
S24 9:1										

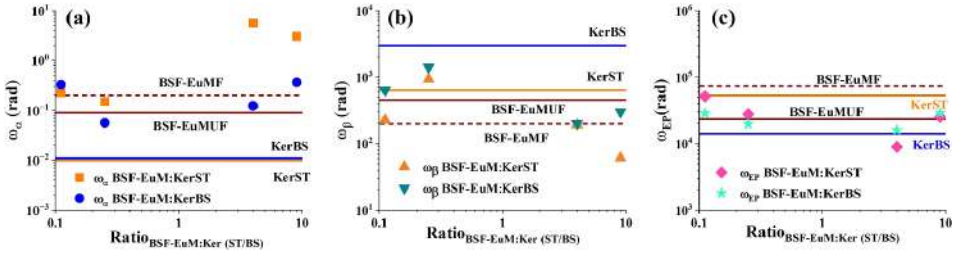

Figure 12. Comparison between the relaxation frequencies determined by expr. 9a in single component (straight line) and mixed suspensions (symbols).

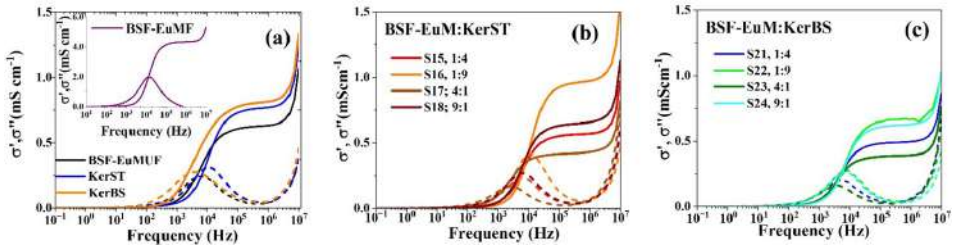

Figure 13. Real (σ') and imaginary (σ'') parts of the AC conductivity of one component (a) and mixed suspension of BSF:EuMF :KerST (b) and BSF:EuMF :KerBS (c). The inset of (a) shows the AC conductivity of BSF:EuM. The mixed suspensions are labeled following table 1.

4. Conclusions

The chemical, structural and dielectric properties of powders and water-based suspensions of eumelanin and two types of keratins derived from organic waste via sustainable processes are discussed. The examined suspensions included both single component and their mix at selected BSF-Mel: Ker mass ratios. FTIR on biopolymer powders together with SAXS, TEM and BDS on suspensions provided comprehensive insight of their properties and correlation between chemistry, structure and dielectric properties.

As a whole, the study discussed the fundamental properties of water-based suspensions made up of one and mixed Eumelanin-Keratin biopolymer and extends the one(s) on BSF-EuM [57] and related devices all derived in the framework of the CE approach [19].

The adopted techniques enabled to evidence specific features of the suspensions under different observation points. In one component suspensions

- SAXS modeling returned BSF-EuM aggregation confirm the π-π/pancake structure [97]. In KerST and KerBS the derived geometrical extension returned a 2-dimensional structure in KerST opposed to a more linear structure of KerBS.
- TEM results were in line with SAXS i.e. aggregation of nanoparticles in BSF-EuM, a planar star-like structure in KerST and a linear one in KerBS
- BDS responses differ in each biopolymer, with some similarities between unfiltered and filtered BSF-EuM with KerST and KerBS, due to residual proteins. The values of l_α and l_β confirms TEM and SAXS results.

In the two-component suspensions:

- the SAXS modeling evidenced a superposition of independent contributes, with higher coaggregation in the case of KerST
- TEM confirms the superposition seen via SAXS modeling with BSF-EuM eumelanin surrounding KerST loosing the star light features; in BSF-EuM:KerBS mixtures 1:9 and 9:1 eumelanin internalization (1:9) or surrounding the KerBS bent (9:1) are found.
- TEM in line with SAXS suggests biopolymers aggregate in a different geometry when are both in water, thus explaining the carrier hopping lengths l_α and radial distances l_β extracted from BDS data.
- BDS spectra evidence a cooperative effects via a substantial different behavior respect to the one component, that is more expressed when increasing the eumelanin content (i.e. BSF-EuM:KerST (4:1) and (9:1)).
- The DC conductivities hint a keratin vehiculated plasticizing effect.

Finally, the production of disposable or medium-long time working devices by adopting deposition techniques from such aqueous liquid phase suspensions is already in progress, with promising results that will be the subject of our future research papers

Data availability statement

All data that support the findings of this study are included within the article (and any supplementary files).

Acknowledgments

M A and P F A acknowledge the Italian Ministry of University and Research (MUR) PONa3_00369 SISTEMA.

D A thanks Italian National Recovery and Resilience Plan (NRRP), funded by the European Union—NextGenerationEU (Mission 4, Component 2, Investment 3.1—Area ESFRI Energy—Call for tender No. 3264 of 28-12-2021 of Italian University and Research Ministry (MUR), Project ID IR0000007 'NEFERTARI—', MUR Concession Decree No. 243 del 04/08/2022, CUP B53C22003070006,). Views and opinions expressed are however those of the author(s) only and do not necessarily reflect those of the European Union or the European Commission. Neither the European Union nor the European Commission can be held responsible for them.

A B M aknowledges the support by the UKRI Research Partnerships Investment Fund through the Centre for Integrative Semiconductor Materials'.

Author contributions

Conceptualization, M A, S M, A B M and R G;
Methodology, M A, S M, J W P, R G, A D G, D A A D S, A G, S M,F L,C L
Software, M A, S M,A D S, P F:A;
Validation M A, A B M, R G;
Formal analysis, A B M, M A,A D G;
Investigation, M A, S M,
Resources, M A, J W P, G L, F L,C L, P F A, A D S, R,G;
Data curation: M A.,A B M, A D G,S M;
Writing—**O**riginal draft preparation: M A; A B M;
Writing—**R**eview and **E**diting, M A,A B M;
Visualization, M A, P F A, S M; supervision, M A, A B M; **P**
Project administration, M A, P F A, A B M, R G;
Funding acquisition, M A, P F A, A B M, R G
All authors have read and agreed to the published version of the manuscript.

Fundings

For R G and S M: this work is funded by European Union—NextGenerationEU under the Italian Ministry of University and Research (MUR) National Innovation Ecosystem grant ECS00000041—VITALITY—Spoke 9.

For A B M: this work was also supported by the UKRI Research Partnerships Investment Fund through the Centre for Integrative Semiconductor Materials.'

For P.F.A and D.A.: this work was supported by Regione Puglia, Riparti—POC PUGLIA FESRT-FSE 2014/2020.

Conflict of interest

'The authors declare no conflicts of interest'.

ORCID iDs

Marianna Ambrico https://orcid.org/0000-0002-0568-6860
Sara Mattiello https://orcid.org/0009-0000-9601-4703
Albertus Bernardus Mostert https://orcid.org/0000-0002-9590-2124
Jun Wei Phua https://orcid.org/0009-0002-1763-0861
Domenico Aceto https://orcid.org/0000-0002-5748-8962
Paolo F Ambrico https://orcid.org/0000-0002-2455-6949
Alessandro Guzzini https://orcid.org/0009-0006-2166-7391
Angelo De Stradis https://orcid.org/0000-0003-1624-2365
Federico Liuzzi https://orcid.org/0000-0001-9890-8014
Carlo Santulli https://orcid.org/0000-0002-1686-4271
Giulio Lupidi https://orcid.org/0000-0001-9452-0741
Alessandra Del Giudice https://orcid.org/0000-0002-1916-8300
Roberto Gunnella https://orcid.org/0000-0003-4739-6375

References

[1] United Nations Development Programm-Climate Promise 2023 What is Circular Economy and why does it matter? (available at: https://climatepromise.undp.org/news-and-stories/what-is-circular-economy-and-how-it-helps-fight-climate-change)
[2] Jane G *et al* (European Compost Network ECN e.V.) 2022 Compost and digestate for a circular bioeconomy *ECN Data Report 2022 Compost and Digestate for a Circular Bioeconomy*
[3] Baldé C P, Forti V, Gray V, Kuehr R and Stegmann P 2017 *The Global E-waste Monitor 2017: Quantities, Flows, and Resources* (United Nations University (UNU), International Telecommunication Union (ITU) & International Solid Waste Association (ISWA))
[4] Garam B *et al* (WEF (World Economic Forum) and PACE (Platfor for accelerating Circular Economi)) 2019 *A New Circular Vision for Electronics Time for a Global Reboot* United Nation E-Waste Coalition
[5] Mozhiarasi V and Natarajan T S 2022 Slaughterhouse and poultry wastes: management practices, feedstocks for renewable energy production, and recovery of value added products *Biomass Convers. Biorefin* **12** 1–24
[6] Malviya R and Sundram S 2023 *Engineering Materials Engineered Biomaterials Synthesis and Applications* ed R Malviya and S Sundram (Springer)
[7] Paulin J V, Albano L G S, Camargo D H S, Pereira M P, Bregadiolli B A, Graeff C F O and Bufon C C B 2022 Eumelanin-based multisensory platform: a case of study for photolithographic patterning *Appl. Mater. Today* **28** 101525
[8] Migliaccio L, Aprano S, Iannuzzi L, Maglione M G, Tassini P, Minarini C, Manini P and Pezzella A 2017 Eumelanin–PEDOT:PSS complementing En Route to mammalian-pigment-based electrodes: design and fabrication of an ITO-Free organic light-emitting device *Adv. Electron. Mater.* **3** 1600342

[9] D'Amora U *et al* 2022 Eumelanin from the black soldier fly as sustainable biomaterial: characterisation and functional benefits in tissue-engineered composite scaffolds *Biomedicines* **10** 2945
[10] Placone J K, Navarro J, Laslo G W, Lerman M J, Gabard A R, Herendeen G J, Falco E E, Tomblyn S, Burnett L and Fisher J P 2017 Development and characterization of a 3D printed, keratin-based hydrogel *Ann. Biomed. Eng.* **45** 237–48
[11] Patil A B *et al* 2020 Tailoring the meso-structure of gold nanoparticles in keratin-based activated carbon toward high-performance flexible sensor *Nanomicro Lett.* **12** 1–11
[12] Shen B, Zhang D, Wei Y, Zhao Z, Ma X, Zhao X, Wang S and Yang W 2019 Preparation of Ag doped keratin/PA6 nanofiber membrane with enhanced air filtration and antimicrobial properties *Polymers* **11** 1–13
[13] Lazarus B S, Chadha C, Velasco-Hogan A, Barbosa J D V, Jasiuk I and Meyers M A 2021 Engineering with keratin: a functional material and a source of bioinspiration *iScience* **24** 102798
[14] Feroz S, Muhammad N, Ranayake J and Dias G 2020 Keratin—Based materials for biomedical applications *Bioact. Mater.* **5** 496–509
[15] Hamouche H, Makhlouf S, Chaouchi A and Laghrouche M 2018 Humidity sensor based on keratin bio polymer film *Sens. Actuators* A **282** 132–41
[16] Nowogrodski C, Simon I, Magdassi S and Shoseyov O 2020 Fabrication of second skin from keratin and melanin *Polymers* **12** 1–13
[17] Lin Q, Hao S, Hu W, Wang M, Zang Z, Zhu L, Du J and Tang X 2019 Human hair keratin for physically transient resistive switching memory devices *J. Mater. Chem.* C **7** 3315–21
[18] Pan J, Xia Z, Deng N, Chen L, Zhang H, Lu Y, Liu Y and Gao H 2023 Eumelanin-inspired nanomaterials in electrochemical energy storage devices: a review *Chem. Eng. J.* **452** 138607
[19] Krebsbach P, Rincón-Iglesias M, Pietsch M, Henel C, Lanceros-Mendez S, Phua J W, Ambrico M and Hernandez-Sosa G 2024 Inkjet-printed bio-based melanin composite humidity sensor for sustainable electronics *ACS Appl. Mater. Interfaces* **16** 42555–65
[20] Ischia M, Wakamatsu K, Briganti S, Kovacs D, Meredith P, Pezzella A, Sarna T, Simon J D and Ito S 2013 Melanins and melanogenesis: methods, standards, protocols *Pigment Cell Melanoma Res.* **26** 616–33
[21] Zucca F A *et al* 2004 The neuromelanin of human substantia nigra: physiological and pathogenic aspects *Pigment Cell Res.* **17** 610–7
[22] Bush W D, Garguilo J, Zucca F A, Albertini A, Zecca L, Edwards G S, Nemanich R J and Simon J D 2006 The surface oxidation potential of human neuromelanin reveals a spherical architecture with a pheomelanin core and a eumelanin surface *Proc. Natl Acad. Sci.* **103** 14785–9
[23] Meredith P, Powell B J, Riesz J, Nighswander-Rempel S P, Pederson M R and Moore E G 2006 Towards structure-property-function relationships for eumelanin *Soft Matter* **2** 37–44
[24] Solano F 2014 Melanins: skin pigments and much more—types, structural models, biological functions, and formation routes *New J. Sci.* **2014** 1–28
[25] Paulin J V, Coleone A P, Batagin-Neto A, Burwell G, Meredith P, Graeff C F O and Mostert A B 2021 Melanin thin-films: a perspective on optical and electrical properties *J. Mater. Chem.* C **9** 8345–58
[26] Felix C C, Hyde J S, Sarna T and Sealy R C 1978 Interactions of melanin with metal ions. Electron spin resonance evidence for chelate complexes of metal ions with free radicals *J. Am. Chem. Soc.* **100** 3922–6
[27] Al Khatib M, Costa J, Baratto M C, Basosi R and Pogni R 2020 Paramagnetism and relaxation dynamics in melanin biomaterials *J. Phys. Chem.* B **124** 2110–5
[28] Vasileiou T and Summerer L 2021 Vasileiou T and Summerer Erratum: a biomimetic approach to shielding from ionizing radiation: the case of melanized fungi *PLoS One* **16** e0257068
[29] Vasileiou T and Summerer L 2020 A biomimetic approach to shielding from ionizing radiation: the case of melanized fungi *PLoS One* **15** e0229921
[30] Mostert A B 2022 The importance of water content on the conductivity of biomaterials and bioelectronic devices *J. Mater. Chem.* B **10** 7108–21
[31] Sheliakina M, Mostert A B and Meredith P 2018 An all-solid-state biocompatible ion-to-electron transducer for bioelectronics *Mater. Horiz.* **5** 256–63
[32] Abramov P A, Zhukov S S, Savinov M, Mostert A B and Motovilov K A 2023 The influence of copper ions on the transport and relaxation properties of hydrated eumelanin *Phys. Chem. Chem. Phys.* **25** 11601–12
[33] Mostert A B, Rienecker S B, Sheliakina M, Zierep P, Hanson G R, Harmer J R, Schenk G and Meredith P 2020 Engineering proton conductivity in melanin using metal doping *J. Mater. Chem.* B **8** 8050–60
[34] Nozella N L, Lima J V M, de Oliveira R F and de Oliveira Graeff C F 2023 Melanin/PEDOT:PSS blend as organic mixed ionic electronic conductor (OMIEC) for sustainable electronics *Mater. Adv.* **4** 4732–43
[35] Xu R, Gouda A, Caso M F, Soavi F and Santato C 2019 Melanin: a greener route to enhance energy storage under solar light *ACS Omega* **4** 12244–51
[36] Kumar P, Di Mauro E, Zhang S, Pezzella A, Soavi F, Santato C and Cicoira F 2016 Melanin-based flexible supercapacitors *J. Mater. Chem.* C **4** 9516–25
[37] Kim Y J, Wu W, Chun S E, Whitacre J F and Bettinger C J 2013 Biologically derived melanin electrodes in aqueous sodium-ion energy storage devices *Proc. Natl Acad. Sci. USA* **110** 20912–7
[38] Paulin J V, Fernandes S L and Graeff C F O 2021 Solid-state electrochemical energy storage based on soluble melanin *Electrochem* **2** 264–73
[39] Ambrico M, Ambrico P F, Ligonzo T, Cardone A, Cicco S R, Lavizzera A, Augelli V and Farinola G M 2012 Memory-like behavior as a feature of electrical signal transmission in melanin-like bio-polymers *Appl. Phys. Lett.* **100** 253702
[40] Ambrico M, Cardone A, Ligonzo T, Augelli V, Ambrico P F, Cicco S, Farinola G M, Filannino M, Perna G and Capozzi V 2010 Hysteresis-type current–voltage characteristics in Au/eumelanin/ITO/glass structure: towards melanin based memory devices *Org. Electron.* **11** 1809–14
[41] Wahab A, Gogurla N, Park J Y and Kim S 2022 Architecting silk protein and melanin for photoresponsive and self-healable optoelectronic skins *Adv. Mater. Technol.* **7** 2101271
[42] Nam H J, Cha J, Lee S H, Yoo W J and Jung D Y 2014 A new mussel-inspired polydopamine phototransistor with high photosensitivity: signal amplification and light-controlled switching properties *Chem. Commun.* **50** 1458–61
[43] Xiao M, Li Y, Zhao J, Wang Z, Gao M, Gianneschi N C, Dhinojwala A and Shawkey M D 2016 Stimuli-responsive structurally colored films from bioinspired synthetic melanin nanoparticles *Chem. Mater.* **28** 5516–21
[44] Wu T F, Wee B H and Hong J D 2015 An ultrasensitive and fast moisture sensor based on self-assembled

dopamine-melanin thin films *Adv. Mater. Interfaces* **2** 1500203
[45] Silva M P D, Fernandes J C, De Figueiredo N B, Congiu M, Mulato M and Graeff C F D O 2014 Melanin as an active layer in biosensors *AIP Adv.* **4** 127149
[46] Tehrani Z, Whelan S P, Mostert A B, Paulin J V, Ali M M, Ahmadi E D, Graeff C F O, Guy O J and Gethin D T 2020 Printable and flexible graphene pH sensors utilising thin film melanin for physiological applications *2D Mater.* **7** 024008
[47] Whelan S P, Tehrani Z, Peacock M, Paulin J V, Guy O and Gethin D 2022 Investigation into the suitability of screen printed graphene-melanin pH sensors for use in bacterial culturing applications *J. Electroanal. Chem.* **904** 115868
[48] Di Mauro E, Rho D and Santato C 2021 Biodegradation of bio-sourced and synthetic organic electronic materials towards green organic electronics *Nat. Commun.* **12** 1–10
[49] Wang B, Yang W, McKittrick J and Meyers M A 2016 Keratin: structure, mechanical properties, occurrence in biological organisms, and efforts at bioinspiration *Prog. Mater. Sci.* **76** 229–318
[50] Shavandi A, Silva T H, Bekhit A A and Bekhit A E D A 2017 Keratin: dissolution, extraction and biomedical application *Biomater. Sci.* **5** 1699–735
[51] Hong L and Simon J D 2007 Current understanding of the binding sites, capacity, affinity, and biological significance of metals in melanin *J. Phys. Chem.* B **111** 7938–47
[52] Bento-Lopes L, Cabaço L C, Charneca J, Neto M V, Seabra M C and Barral D C 2023 Melanin's journey from melanocytes to keratinocytes: uncovering the molecular mechanisms of melanin transfer and processing *Int. J. Mol. Sci.* **24** 11289
[53] Amdursky N, Głowacki E D and Meredith P 2019 Macroscale biomolecular electronics and ionics *Adv. Mater.* **31** 1802221
[54] Shim J S, Rogers J A and Kang S K 2021 Physically transient electronic materials and devices *Mater. Sci. Eng.* R **145** 100624
[55] Schwan H P 1957 Electrical properties of tissue and cell suspensions *Adv. Biol. Med. Phys.* **5** 147–209
[56] Nakanishi M and Sokolov A P 2015 Protein dynamics in a broad frequency range: dielectric spectroscopy studies *J. Non– Cryst. Solids* **407** 478–85
[57] Ambrico M, Mostert A B, Ambrico P F, Phua J, Mattiello S and Gunnella R 2024 Exploring ion mobility mechanisms in poly indolequinone polymers: a case study on black soldier fly melanin *J. Phys. D: Appl. Phys.* **57** 265303
[58] Phua J W and Ottenheim C J H 2021 A method for obtaining melanin from invertebrate biomass and the product obtained therefrom US20230127563A1
[59] Shen Q, Ma Y, Qin X, Guo Y and Zhang C 2024 Steam explosion as a green method to treat animal waste: a mini-review *Process. Saf. Environ. Prot.* **181** 43–52
[60] Caporusso A, De Bari I, Liuzzi F, Albergo R, Valerio V, Viola E, Pietrafesa R, Siesto G and Capece A 2023 Optimized conversion of wheat straw into single cell oils by Yarrowia lipolytica and Lipomyces tetrasporus and synthesis of advanced biofuels *Renew. Energy* **202** 184–95
[61] Tonin C, Zoccola M, Aluigi A, Varesano A, Montarsolo A, Vineis C and Zimbardi F 2006 Study on the conversion of wool keratin by steam explosion *Biomacromolecules* **7** 3499–504
[62] Kawasaki H, Shimanouchi T and Kimura Y 2019 Recent development of optimization of lyophilization process *J. Chem.* **2019** 1–14
[63] Mattiello S, Guzzini A, Del Giudice A, Santulli C, Antonini M, Lupidi G and Gunnella R 2023 Physico-chemical characterization of keratin from wool and chicken feathers extracted using refined chemical methods *Polymers* **15** 181
[64] Wang K, Li R, Ma J H, Jian Y K and Che J N 2016 Extracting keratin from wool by using l-cysteine *Green Chem.* **18** 476–81
[65] Sinkiewicz I, Śliwińska A, Staroszczyk H and Kołodziejska I 2017 Alternative methods of preparation of soluble keratin from chicken feathers *Waste Biomass Valorization* **8** 1043–8
[66] Hansen S 2012 BayesApp: a web site for indirect transformation of small-angle scattering data *J. Appl. Crystallogr.* **45** 566–7
[67] Breßler I, Kohlbrecher J and Thünemann A F 2015 SASfit: a tool for small-angle scattering data analysis using a library of analytical expressions *J. Appl. Crystallogr.* **48** 1587–98
[68] Barsoukov E and Ross Macdonald J 2005 *Impedance Spectroscopy: Theory, Experiment, and Applications* ed E Barsoukov and J R Macdonald 2nd edn (Wiley)
[69] David M, Feldman Y and Ishai P B 2023 Dielectric spectroscopy and techniques *Non-Destructive Material Characterization Methods* (Elsevier) pp 587–619
[70] Trukhan E M 1963 *Sov. Phys. Solid State* **4** 25601
[71] Wubbenhorst M and Van Turnhout J 2002 Analysis of complex dielectric spectra. I. One-dimensional derivative techniques and three-dimensional modelling *J. Non-Cryst. Solids.* **305** 40–49
[72] Steeman P A M and Van Turnhout1 J 1994 Fine structure in the parameters of dielectric and viscoelastic relaxations *Macromolecules* **27** 5421–7
[73] Cole H S and Davidson D W 1951 Dielectric relaxation in glycerol, propylene glycol *J. Chem. Phys.* **19** 1484–90
[74] Cole K S and Cole R H 1941 Dispersiona and absorption in dielectrics: I. Alternating CUrrent characteristics *J. Chem. Phys.* **9** 98–105
[75] Cole K S and Cole R H 1942 Dispersion and absorption in dielectrics: II. Direct current characteristics *J. Chem. Phys.* **10** 98–105
[76] Havriliak S and Negami S 1966 A complex plane analysis of α-dispersions in some polymer systems *J. Polym. Sci.* **14** 99–117
[77] Matos B R, Santiago E I, Rey J F Q and Fonseca F C 2014 Origin of α and β relaxations of Nafion *Phys. Rev.* E **89** 052601
[78] Guo L, Li W, Gu Z, Wang L, Guo L, Ma S, Li C, Sun J, Han B and Chang J 2023 Recent advances and progress on melanin: from source to application *Int. J. Mol. Sci.* **24** 4360
[79] Bordi F, Cametti C and Colby R H 2004 Dielectric spectroscopy and conductivity of polyelectrolyte solutions *J. Phys.* **16** R1423–63
[80] Matos B R, Politano R, Rey J F Q, Hermida-Merino D, Schade U, Puskar L and Fonseca F C 2018 Interplay of α/β-relaxation dynamics and the shape of ionomer building blocks *Sci. Rep.* **8** 13441
[81] Matos B R, Santiago E I, Rey J F Q, Scuracchio C H, Mantovani G L, Hirano L A and Fonseca F C 2015 Dc Proton conductivity at low-frequency in Nafion conductivity spectrum probed by time-resolved SAXS measurements and impedance spectroscopy *J. Polym. Sci.* B **53** 822–8
[82] Tierney N K and Register R A 2002 Ion hopping in ethylene-methacrylic acid ionomer melts as probed by rheometry and cation diffusion measurements *Macromolecules* **35** 2358–64
[83] Bedran Z V, Zhukov S S, Abramov P A, Tyurenkov I O, Gorshunov B P, Mostert B and Motovilov K A 2021 Water-activated semiquinone formation and carboxylic

Chapter3

Material Analysis for Cultural Heritage

3.1 Bronze archaeological artifacts of iron-age necropolis

Metals have played a crucial role in the development of humanity by influencing technological, socio-economic and political development. The different ages of metals have been characterized by numerous metal alloys each with specific properties, compositions and applications [1]. For this reason, metal objects found in archaeological excavations are studied using scientific methods allowing to obtain valuable information on their manufacture, use and burial context. Such studies fall within the scope of archaeometry, an interdisciplinary discipline that applies scientific methods — mainly from natural and physical sciences — to the study of archaeological materials, with the aim of providing quantitative and objective data to support archaeological interpretation, conservation and valorization of cultural heritage. [2]. For example, during the Early Bronze Age, bronze-based alloys had a relatively high As content. Later, during the Middle Bronze Age, Sn replaced As, with the final use of Sn-Pb alloys in the Late Bronze Age, and then Fe in the Iron Age [3].Due to the intrinsic and precious fragility of the work of art and archaeological objects of cultural heritage, sampling is a particularly critical and frequently discussed aspect. For this reason, it is preferable to use non-destructive or micro-destructive analytical techniques, such as X-ray fluorescence (XRF), X-ray diffractometry (XRD) and Raman spectroscopy. Alternatively, Laser-induced Breakdown Spectroscopy (LIBS) represents an in situ, rapid and sensitive methodology, capable of providing information also on light elements and allowing a stratigraphic characterization, without requiring any sample preparation [4].

The operating principle of LIBS can be summarized as illustrated in Figure 3.1a. A laser beam, appropriately focused and with a specific wavelength and energy, strikes the sample surface, producing impulsive heating that leads to the ablation and ionization of a small amount of material. Analytical information on the elemental composition of the sample is then obtained from the spectral analysis of the radiation emitted by the generated plasma. The atomic emission peaks, characteristic of the spectrum, allow the identification of the species present. The measurement spot typically has dimensions ranging from a few tens to a few hundred microns, depending on the degree of beam focusing. The ablation depth per single laser pulse depends strongly on the irradiated material: in the context of

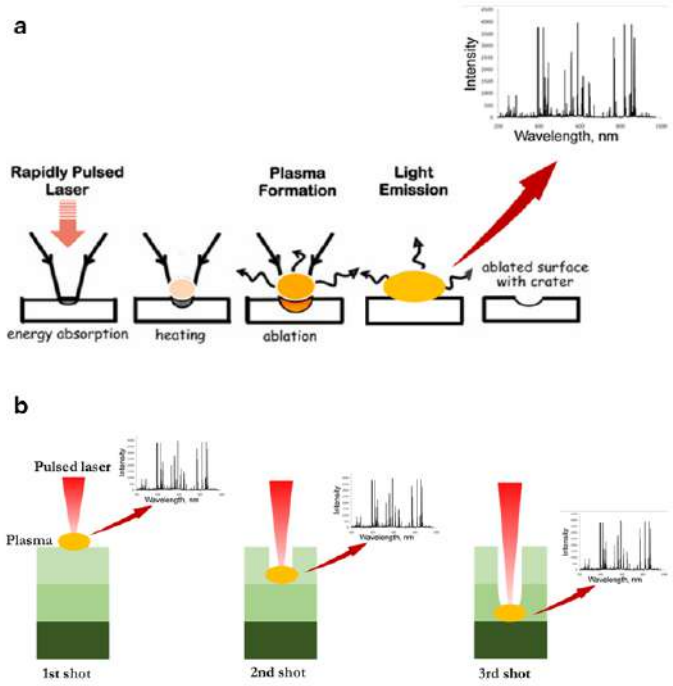

Figure 3.1: Schematic representation of: a) the working principle of LIBS the technique modified by [5] and b) LIBS depth profile analysis

cultural heritage, it generally varies from fractions of a micron up to about ten microns [6]. The technique also allows, through the application of successive pulses, the acquisition of depth profiles, reconstructing the stratigraphic succession (Figure 3.1b). This information is particularly useful in the study and conservation of cultural heritage, as it allows for comparison of surface materials with those in the bulk, distinguishing deposits due to pollutants or previous restoration interventions. Another advantage of LIBS is its ability to reveal the full spectrum of elements in the periodic table, including the light elements (H, Li, Be, B, C, N, O, F), which are difficult to detect with other techniques. For this reason, LIBS is often used as a complement to XRF, which has intrinsic limitations in the analysis of low atomic number elements (such as Si and lighter elements) due to the drastic reduction in fluorescence yield as the atomic number decreases. It is also unable to reliably identify elements such as Na and Mg, as the emitted X-rays are absorbed by the air [7]. The study of degradation phenomena in cultural heritage and, specifically, corrosion processes in metal alloys requires, given their complexity, the integrated use of different analytical methodologies.

3.1.1 Paper VI: *Application of handheld/portable spectroscopic tools to the identification, inner stratigraphy and mapping of archaeological metal artefacts*

The analysis of the variations in the composition of metal alloys over time helps to determine their production period and to classify their type, thanks to the quantitative measurement of the elements that compose them. It is essential that the techniques used in the analysis of such archaeological finds are as minimally invasive as possible, preserving the integrity

of the objects. In this context, portable instrumentation represents a valid tool to conduct archaeometric campaigns in the field, allowing to detect and quantify specific compositional elements in an efficient way. The aim of this research was to evaluate the effectiveness of the combined use of portable LIBS and ED-XRF instruments to: (a) identify and quantify in situ the elemental composition of copper-iron alloy artefacts from ancient tombs in the Minervino Murge area, Puglia, Italy; (b) assess the presence of a patina and several underlying layers by in-depth profiling, thus obtaining their internal stratigraphy; (c) map and (d) establish correlations between compositional data and technological characteristics, possibly confirming the archaeological dating of the objects. The primary elements identified by both techniques included Cu, Sn and Pb in copper and Fe alloys with small amounts of Cu and Pb in iron alloys. In addition, the elements Al, Ca, Si, Mg, Na and K, mainly came from soil contamination and the trace elements Sb, Ni and Zn were detected. The satisfactory performance of both techniques was assessed by their ability to provide reproducible data on the elemental composition. Finally, the depth profile and mapping obtained by LIBS contributed to understanding the metalworking and history of the studied objects, thus confirming that both techniques are robust analytical tools in open-air archaeology and archaeometry campaigns.

Additional details are provided in the Supplementary Information (see Appendix A.3).

References

[1] David A Scott and Roland Schwab. *Metallography in archaeology and art*. Springer, 2019. DOI: 10.1007/978-3-030-11265-3.

[2] Francesca Di Turo. "Limits and perspectives of archaeometric analysis of archaeological metals: a focus on the electrochemistry for studying ancient bronze coins". In: *Journal of Cultural Heritage* 43 (2020), pp. 271–281. DOI: 10.1016/j.culher.2019.10.006.

[3] Miljana Radivojević et al. "The provenance, use, and circulation of metals in the European Bronze Age: the state of debate". In: *Journal of archaeological research* 27 (2019), pp. 131–185. DOI: 10.1007/s10814-018-9123-9.

[4] Vincent Detalle and Xueshi Bai. "The assets of laser-induced breakdown spectroscopy (LIBS) for the future of heritage science". In: *Spectrochimica Acta Part B: Atomic Spectroscopy* 191 (2022), p. 106407. DOI: 10.1016/j.sab.2022.106407.

[5] Russell S Harmon and Giorgio S Senesi. "Laser-induced breakdown spectroscopy–a geochemical tool for the 21st century". In: *Applied Geochemistry* 128 (2021), p. 104929. DOI: 10.1016/j.apgeochem.2021.104929.

[6] David A Cremers and Leon J Radziemski. *Handbook of laser-induced breakdown spectroscopy*. John Wiley & Sons, 2013. DOI: 10.1002/9781118567371.

[7] Giorgio S Senesi, Russell S Harmon, and Richard R Hark. "Field-portable and handheld LIBS". In: *Laser-Induced Breakdown Spectroscopy* (2020), pp. 537–560. DOI: 10.1016/j.sab.2020.106013.

VI

IOP Publishing J. Phys. Photonics 6 (2024) 035005 https://doi.org/10.1088/2515-7647/ad46a7

Journal of Physics: Photonics

PAPER

Application of handheld/portable spectroscopic tools to the identification, inner stratigraphy and mapping of archaeological metal artefacts

Sara Mattiello[1,2], Olga De Pascale[1], Vincenzo Palleschi[3], Girolamo Fiorentino[4] and Giorgio S Senesi[1,*]

[1] CNR—Istituto per la Scienza e Tecnologia dei Plasmi (ISTP)—Sede di Bari, Via Amendola 122/D, 70126 Bari, Italy
[2] Physics Section, School of Science and Technology, Università di Camerino, via Madonna delle Carceri, 62032 Camerino, Italy
[3] CNR—Istituto di Chimica dei Composti Organo-Metallici (ICCOM), U.O.S. di Pisa, Pisa, 56124, Italy
[4] Laboratory of Archeobotany and Paleoecology, Department of Cultural Heritage, University of Salento, via Birago 64, 73100 Lecce, Italy
[*] Author to whom any correspondence should be addressed.

E-mail: giorgio.senesi@cnr.it

Keywords: laser-induced breakdown spectroscopy (LIBS), energy dispersive x-ray fluorescence (ED-XRF), handheld/portable instrumentation, copper and iron alloy archaeological artefacts, elemental detection and quantification, depth profiling, mapping

Supplementary material for this article is available online

OPEN ACCESS

RECEIVED
17 December 2023

REVISED
17 April 2024

ACCEPTED FOR PUBLICATION
1 May 2024

PUBLISHED
13 May 2024

Abstract

Field handheld/portable instrumentations, such as *in-situ* geochemical analyzers, have the potential to assist efficiently targeted geochemical archaeometry campaigns in detecting and quantifying specific elements. Non-destructive portable energy dispersive x-ray fluorescence and micro-destructive handheld laser-induced breakdown spectroscopy (LIBS) instrumentation were utilized to investigate the elemental composition, internal stratigraphy by depth profiling and microscale compositional mapping of five copper and two iron alloy artefacts collected from various ancient graves in the Minervino Murge area, Apulia, Italy. The primary elements identified by both techniques included Cu, Sn and Pb in copper alloys, and Fe with minor amounts of Cu and Pb in iron alloys. Furthermore, the elements Al, Ca, Si, Mg, Na and K, mostly originated from soil contamination, and the trace elements Sb, Ni and Zn were detected. The satisfactory performance of both techniques was assessed by their capacity to provide reproducible elemental composition data. Finally, the depth profile and mapping achieved by LIBS contributed to understanding the metal processing and history of the objects studied, so confirming both techniques to be robust analytical tools in outdoor archaeology and archaeometry campaigns.

1. Introduction

Throughout the last 7000–8000 years, metals have played a key role in shaping the course of human history by exerting a significant influence on the technological, socio-economic and political development. Various metal alloys with distinct properties, compositions and applications have been constructed and used during human history, which determined the beginning of the various Metal Ages and the consequent technological evolution [1]. For this reason, metal objects collected in archaeological excavations are highly appreciated for their intrinsic historical value.

The study of archaeological artefacts by archaeometric methods is instrumental to gain information on their fabrication, use and burial [2]. In particular, the evolution of metal alloys types over time has contributed to assign the production period and the classification of metal objects by measuring their quantitative elemental composition. For example, during the early bronze age, bronze-based alloys had a relatively high As content. Subsequently, during the middle bronze age, Sn replaced As with the final use of Sn-Pb alloys in the late bronze age, and then Fe in the iron age [3].

Obviously, the procedures and techniques to be used in the analysis of archaeological artefacts need to be less destructive as possible to preserve their integrity, i.e., avoid any removal of material. Typically, non-destructive analytical techniques, such as x-ray fluorescence (XRF), x-ray diffractometry and Raman spectroscopy, are the preferred ones [2]. However, the minimally destructive laser-induced breakdown spectroscopy (LIBS) features several relevant advantages, including rapidity, no sample preparation, capacity of performing multielement analysis, detection of any element of the periodic table including light elements, achievement of micro destructive compositional in-depth profile analysis, and rastering the laser beam across the sample surface in small steps to obtain a microscale compositional mapping [4, 5]. In particular, since the laser creates a tiny crater on the sample's surface, the continued firing of laser is able to penetrate below the corrosion layer, so allowing the in-depth analysis of the entire sample. This is an advantage with respect to the completely non-destructive measurements achieved by XRF, which, however, has limitations for measuring elements with low atomic number and can provide integrated information on the composition of the samples only for the entire volume. This does not allow to separate the information on the inner composition of the object from that of the surface, which in most cases is not representative of the whole object, due to effects of formation of patinas and corrosion, among others [6, 7]. Additionally, owing to variations in x-ray absorption by the elements, the effective volume of analysis is different for different elements, so that the XRF spectra frequently feature an intricate combination of fluorescence lines emitted by elements at depths extending several tens of microns beneath the surface [8].

Furthermore, recent studies have demonstrated that the mechanical cleaning typically needed before XRF analysis may produce intragranular corrosion on the surface, thus failing to provide the correct information on the original metal [9–11]. Additionally, the mechanical cleaning of historical artefacts is often prohibited, which favours the choice of LIBS analysis. Although the potential of handheld LIBS instrumentation has not yet been fully explored and its applications to archaeological metals analysis have been still sporadic [12], the application of LIBS in the sector of archaeological cultural heritage studies has been investigated and proven effective, for example in analysing glaze, the decorative layer composition of ceramics [13–15] and metallic objects [16–22].

Given the intrinsic fragility of some archaeological objects, their transport to the analytical laboratory should be avoided. Thus, movable instrumentations, such as portable energy dispersive (ED)-XRF and LIBS instruments, have emerged as very promising means for analysing archaeological artefacts both *in-situ* in field archaeological campaigns and directly in museums. A further advantage of both instruments is that they are equipped with internal protection systems that do not allow their operation if the sample is not in direct contact with the instrument, so limiting the operator's exposure to ionizing radiation for ED-XRF and avoiding the use of protective glasses for LIBS [5].

The objective of this research was to assess the feasibility of the combined use of handheld LIBS and portable ED-XRF instrumentations in: (a) identifying and quantifying *in-situ* the elemental composition of copper and iron alloy artefacts collected from various ancient graves in the Minervino Murge area, Apulia, Italy; (b) evaluating the presence of a patina and different underlying layers by in-depth profiling so achieving their inner stratigraphy; (c) mapping their surface; and (d) establishing correlations between the compositional data and the technological features, possibly confirming the archaeological dating of the objects.

2. Materials and methods

2.1. Samples

The samples investigated in this work were seven artefacts, five made of copper alloy, i.e. a belt (A), a basin (B), a fibula (C), a helm (D) and a pendant (E), and two made of iron alloy, i.e. a dagger/knife (F) and a spatula (G) (figure 1). All objects, dated by archaeological criteria, such as shape, feature and use, as belonging to the VI century B.C., were collected in an iron age necropolis located in the area of Minervino Murge, Apulia, Italy, and immediately transferred to the Soprintendenza Archeologia, Belle Arti e Paesaggio per le Province di Barletta—Andria—Trani e Foggia for conservation and restoration. The artefacts were in a relatively good preservation state and showed a thin, relatively uniform patina on the surface, but also more degraded areas. The main interest of archaeologists was to know the elemental composition of the artefacts, in order to improve the knowledge of their technical production and confirm the archaeological period.

The belt is composed of three laminas connected by nails and had the function of fastening cloths. The basin fragment features an edge worked by chisel and was used as container of water or food. The fibula was a sort of brooch and had mainly the function of stopping or closing cloths, such as cloaks and tunics. The helm fragment does not allow to identify the type of helm to which it belonged. The pendant, which had a decorative function, consists of a thin flat bronze sheet of vaguely trapezoidal shape and features a small hole positioned approximately halfway along the upper side. The dagger/knife is heavily oxidized and shows

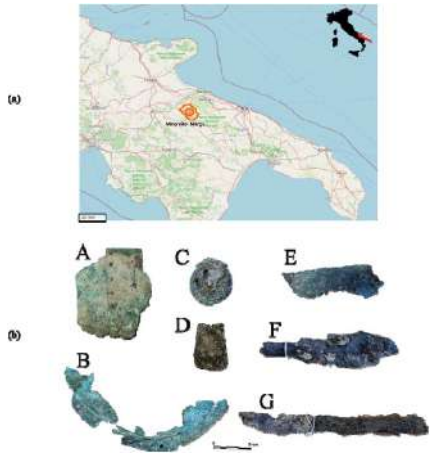

Figure 1. Location of the Minervino Murge site in the region of Apulia, Italy (a) and photos of the archaeological objects studied (b). Copper alloys: belt (A), basin (B), fibula (C), helm (D), pendant (E); iron alloys: dagger/knife (F) and spatula (G).

evident signs of solidified glue due to previous restorations. The spatula might have been used in religious contexts during ceremonies and rituals. All the artefacts appear to belong to a funeral kit.

No sample removal and neither mechanical nor solvent cleaning were performed on the objects prior to analysis. The different shapes and sizes of the objects were not a limitation for analysis, as they were placed in front of and in contact with the head of the instrument.

2.2. ED-XRF and LIBS analysis

The portable ED-XRF instrument used was a SciAps X-200 (Woburn, MA, USA) powered by an on-board rechargeable Li-ion battery and having dimensions of 18 × 27 × 11 cm and weight of 1.5 kg. The spectra were acquired in Alloy mode, which allowed the quantitative determination of elemental composition using specific reference libraries. Two measurements were used for the detection of the elements, using x-ray tube voltage of 40 kV for heavy elements and 10 kV for light ones, with an exposure time of 30 sec. The analysed area is around 8-mm of diameter.

The handheld LIBS instrument used was a SciAps Z-903 (Woburn, MA, USA) powered by an on board Li-ion battery and having dimensions of 27 × 22 × 7 cm and weight of 1.97 kg. The device uses a Class 3B 1064 nm Nd:YAG diode-pumped solid-state pulsed laser, which fires at a rate of 1–50 Hz and generates a 100 μm focused beam that provides a 5–6 mJ pulse to the sample in a 1-ns pulse. The instrument covers a spectral range from 190 to 950 nm, over which each element features at least one emission line. The spectral data were collected at a 650-nsec delay time over a 3-msec integration time. The elemental depth profiles of samples were collected at a laser firing rate of 10 Hz employing 128 successive laser shots in a single location, after one cleaning shot.

Ten measurements were acquired by both XRF and LIBS on the same points of each sample to obtain its representative average composition and mapping the variability of the bulk composition of the object. The LIBS depth profiles were measured on five points of each object. The Geochem Pro mode of the Z-903 LIBS instrument was used to identify spectral peaks and then generate the corresponding concentration microscale maps based on the relative elemental emission intensities recorded. The two-dimensional (2D) maps, commonly called 'heat maps', were obtained on six relatively flat surface areas of object A using single laser shots spaced 25 μm each other at 256 locations/points over a 16 × 16 grid covering an area of 2 mm^2.

3. Results and discussion

3.1. ED-XRF

The main elements detected with different relative intensity by ED-XRF were Cu, Sn, Pb and Fe in copper alloys and mostly Fe in iron alloys (figures 2(a) and (b)). These elements were identified based on their characteristic emission lines, i.e. Cu ($K\alpha$ at 8.04 keV and $K\beta$ at 8.9 keV), Sn ($K\alpha$ at 25.27 keV), Pb ($L\alpha$ at 10.55 keV and $L\beta$ at 12.6 keV) and Fe ($K\alpha$ 6.4 keV and $K\beta$ at 7.05 keV) [23].

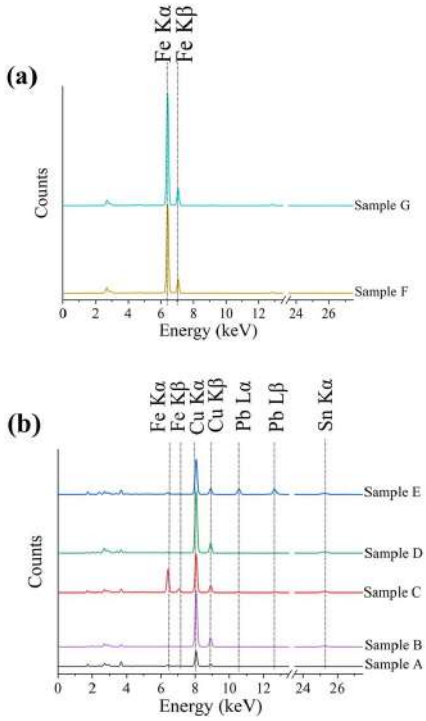

Figure 2. Representative ED-XRF spectra of iron alloy objects (a) and copper alloy objects (b), where the energy in keV is reported in the *x* axis and the counts in the *y* axis. The dashed lines indicate the main fluorescence lines of Fe, Pb, Sn and Cu.

Table 1. Average concentration (wt %) and standard deviation (SD) of the main elements identified by the portable ED-XRF instrument in the studied artefacts.

Samples	Elements							
	Fe	SD	Cu	SD	Sn	SD	Pb	SD
A (belt)	0.895	0.13	73.35	4.6	5.39	3.22	2.998	2.55
B (basin)	0.387	0.05	80.6	1.98	6.26	1.32	0.277	0.07
C (fibula)	7.288	7.07	66.74	3.43	5.82	2.92	1.478	0.51
D (helm)	0.224	0.2	82.28	4.26	6.52	2.1	0.288	0.13
E (pendant)	1.828	0.57	46.95	6.29	6.16	3.16	24.14	9.8
F (dagger)	96.94	2.03	0.225	0.12	ND	—	0.05	0.02
G (spatula)	98.28	0.78	0.22	0.13	ND	—	0.048	0.03

ND: not detected.

The quantitative elemental analysis of the alloys was referred to the reference standards included in the instrument database. The average concentration and the standard deviation (SD) of the main elements in each object, measured following the 3σ rule with 99.7% level of confidence, as reported by the instrument, are listed in table 1, whereas the complete list of element concentrations is reported in table S1 in supplementary information (SI). These values, however, should be taken with great caution because ED-XRF is a volume technique and, as such, is sensitive to the possible compositional variations below the surface of the sample, due to corrosion or depending on the technique used for their realization. In that respect, LIBS analysis would provide unique information about the in-depth variations of sample composition, so allowing to assess the reliability of ED-XRF quantitative analysis.

3.2. LIBS

The broadband LIBS spectra of iron alloy and copper alloy objects are shown, respectively, in figures S1(a) and S1(b) in the SI, whereas the emission lines of interest and their attribution based on the NIST database [24] are summarized in table 2. The main elements detected in copper alloys were Sn, Cu and Pb (figure 3)

Table 2. LIBS atomic (I) and ionic (II) emission lines used to identify elements in the studied artefacts.

Element	Wavelength (nm)
Na	588.9 (I); 589.6 (I)
Mg	279.6 (II); 280.3 (II); 285.2 (I); 448.1 (II)
Al	309.3 (I)
Si	251.6 (I); 288.2 (I)
K	766.5 (I); 769.9 (I)
Ca	393.4 (II); 396.8 (II); 422.7 (I); 430.3 (I); 445.5 (I)
Fe	259.8 (II); 259.9 (II); 274.0 (II); 275.6 (II); 364.8 (I); 372.0 (I)
Ni	338.1 (I)
Cu	224.3 (II); 224.7 (II); 324.8 (I); 327.4 (I); 465.1 (I); 510.6 (I); 515.3 (I); 521.8 (I)
Zn	202.5 (II)
Sn	190.0 (II); 283.9 (I)
Sb	217.9 (I); 247.8 (I); 252.9 (I)
Pb	261.4 (I); 283.3 (I); 364.0 (I); 368.3 (I); 405.7 (I)

and mainly Fe and minor contents of Cu and Pb in iron alloys. Other elements detected in the samples oxidation layer were Al, Ca, Si, K, Na and Mg, which originated very probably from soil contamination (figure 3(d)). Furthermore, the elements Sb, Ni and Zn were identified in trace amounts. Pyrometallurgically produced Cu contains several accidental impurities such as Sb, As, Ni, Ag and many others that may replace Cu in several minerals [1]. The amount of impurities depends on several factors, such as ore dressing, roasting, smelting and refining technologies. Anyhow, all impurities affect significantly the microstructure and properties of a Cu alloy, but the extent of their effects depend on their typology, content and solubility [1].

Copper-alloy objects showed similar emission lines with Cu being the major component, and the main difference being the variable intensity of the Sn emission. In this respect, for example, sample A showed a large variability of the intensity of the emission lines of Sn and Pb between the various points measured on the lamina. As expected, the iron-alloy objects F and G showed a predominance of Fe emission lines and minor amounts of Cu and Pb (less than 1 wt%, according to XRF analysis) (figure S1(a)). The different lines intensities of the main elements (Cu, Sn and Pb) among copper alloy samples (figure 3) may be ascribed to the different heat treatment during their manufacturing and/or to the different environmental degradation that the object has suffered over time. In particular, various environmental factors, such as variations in temperature and humidity, would have generated alterations of the structure and chemical composition of ancient metal alloys, with possible impacts on the reliability of quantitative elemental analysis [20]. The absence of As suggested that the objects were dated correctly, as the presence of As, usually between 2 and 8 wt% in copper alloys, is typical of the early Bronze Age. In particular, the presence of As allowed the alloy to be hammered without breakage and made it particularly suitable for casting. Its absence also suggested that the bronzes under analysis were not made by recycling of older objects [22].

The results of artefacts analysis by the two techniques contributed to focus on sample A, the belt, as the most interesting object studied. By visual inspection, the belt appeared composed of three different pieces of metal connected each other by small nails (figures S2(a) and (b) in SI). Furthermore, the laminas showed an inhomogeneous composition in the different points analysed. Thus, microscale LIBS mapping was performed on sample A with the purpose of identifying the most appropriate surface points where to perform a LIBS depth profile analysis.

The generation process of 2D elemental concentration maps or 'heat maps' is based on the spectral peak intensities derived from individual laser shots spaced across the sample. i.e. it involves a detailed and localized exploration of the sample elemental composition, which allows an efficient evaluation of the distribution and concentration of each element within the microscale domain. Apparently, the elemental components, i.e, Cu, Sn, Pb, Ca, Fe, Cr, P, Si, Na, K and Sb, of the three laminas on sample A surface featured a different distribution (figure S2). In particular, Sn is not detected in lamina 2, whereas this element is abundant in the back of lamina 1 (figure S2(d)). Furthermore, the presence of Cu in lamina 2 was lower than in the other two laminas probably due the thickness of the oxidation patina and the presence of soil contaminants. No differences were apparent between the composition maps of the front and back sides of the object, with the exception of Sn in lamina 1 and Ca in lamina 2, which are more abundant on the back side. Although the objects were cleaned after their collection, they show concretions on the surface due to soil deposition and oxidation patinas. The complex layered structure of patinas can be related to the use of the object (primary patina) and the chemical reactions occurred during its permanence in soil (secondary and tertiary patina) [2]. The absence of Cl in all laminas suggested good preservation conditions, whereas its

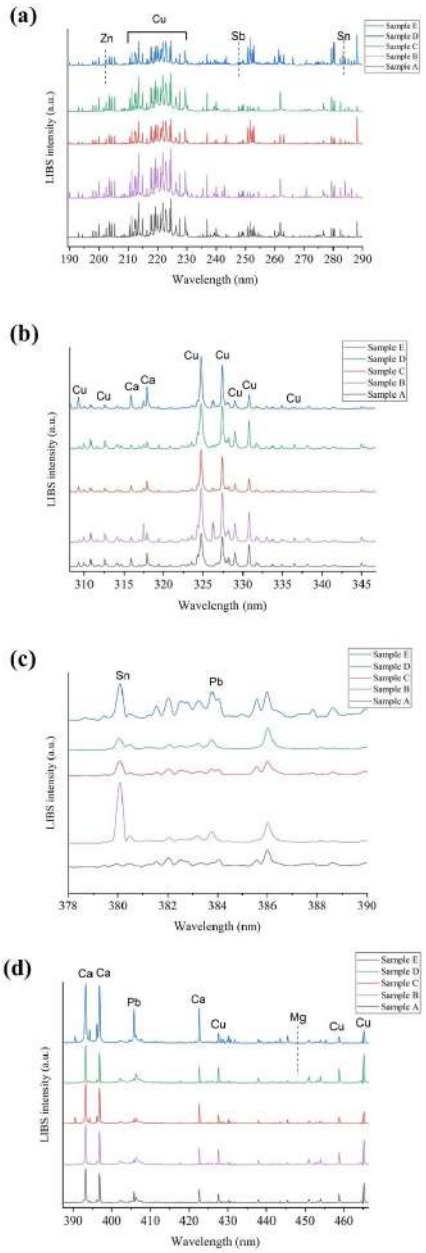

Figure 3. Detailed representative LIBS spectral ranges of copper alloy objects. (a) Spectral range from 190 to 290 nm with Zn, Cu, Sb and Sn emission lines identified; (b) spectral range from 310 to 345 nm with Ca and Cu emission lines identified; (c) spectral range from 378 to 390 nm with Sn and Pb emission lines identified, (d) spectral range from 385 to 465 nm with Ca, Pb, Cu and Mg emission lines identified.

presence would suggest the existence of the so-called 'vile' patina characterized by chloride salts that contribute to the pulverization of metals [25]. Thus, the core of the alloy under the 'noble' patina appeared to have been protected from oxidation processes.

The analysis of depth profiles can provide the composition of the alloy core below the corrosion layer, so achieving unique information on the processing technique used to construct the object. The depth profiles

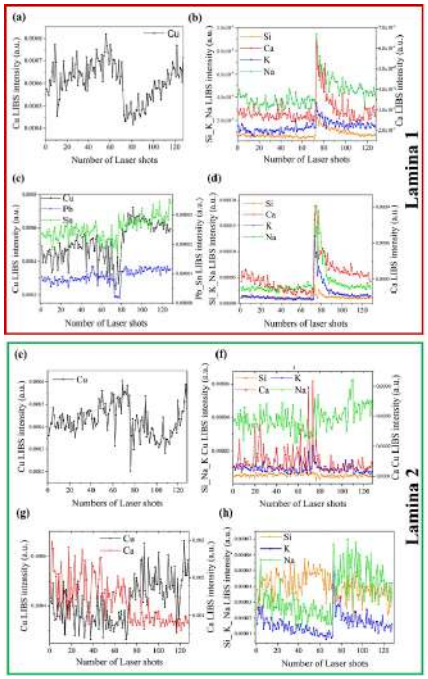

Figure 4. Depth profiles of sample A: front side (a), (b) and back side (c), (d) of lamina 1; front side (e), (f) and back side (g), (h) of lamina 2.

were achieved for the front side (a), (b) and back side (c), (d) of lamina 1 and lamina 2 (respectively, (e), (f) and (g), (h)) at depths of 10 μm for each laser shot by measuring the peak areas of the reference emission lines selected, i.e. Cu I (465.11), Sn I (283.99), Pb I (368.34), Si I (288.2), Ca I (422.7), K I (766.5) and Na I (588.9), as a function of the number of laser shots (figure 4). The LIBS signals of Pb and Sn were detected only for the back side of lamina 1 (figure 4(c)). For both front and back side of lamina 1, at the depth reached after 60–80 laser shots, a sharp change in the intensity of LIBS signals was measured (figures 4(a)–(d)). In particular, the Cu, Pb and Sn signals decreased and then increased again (figures 4(a) and (c)), whereas those of Si, K, Na and Ca increased and then decreased (figures 4(b) and (d)). These results would suggest that lamina 1 features two distinct oxidation layers. Differently, for lamina 2 after about 60–80 shots, the intensity of Cu signals decreased abruptly and then remained almost constant in the front side (figure 4(e)), whereas the opposite occurred in the back side (figure 4(g)). Only the intensity of Ca in the front side and those of K and Na in the back side of lamina 2 showed an abrupt increase after 60–80 laser shots and then returned to the previous values, whereas the intensity of the other elements due to soil contamination appeared not to change significantly as a function of increasing depth (figures 4(f) and (h)).

Based on the elemental maps and depth profiles data, it appears that the thickness of the oxidation layer(s) (600–800 μm) is much larger than the typical penetration depth of ED-XRF, which is about 100–200 μm, depending on the elements. The quantitative data reported in table 1 must be thus reconsidered, taking into account the changes in the elemental LIBS signal intensity (roughly proportional to the element concentration) under the corrosion layer. For example, the depth profiles in figure 4(c) show that the Sn and Pb signal intensities remain roughly constant down to 500 μm below the surface, while the Cu line intensity at the surface is about 20% lower than that at 500 μm depth.

Typically, a bronze alloy containing from 8 to 12 wt% Sn has a combination of hardness and plasticity that makes it easily workable at low temperatures [22]. Thus, the estimation of a Sn concentration lower than 10 wt% achieved by ED-XRF allowed to conclude that the copper alloy artefacts examined were manufactured by the cold hammer technique. If the percentage of Sn exceeds 12 wt%, the increased hardness and brittleness of the alloy make handling at low temperatures difficult and can lead to breakage of the material [26], i.e. the alloy becomes harder and requires repeated annealing cycles to be handled. However, a bronze with a Sn content above 12 wt% is more suitable for hot working.

A content of Pb lower than 3 wt% measured in all copper alloys, except sample E, might be ascribed to impurities present in the raw copper material used, e.g. smelting galena or other copper minerals containing Pb [1]. Differently, the high Pb content in sample E was likely attributable to surface enrichment phenomena due to the hammering process [27]. In particular, a content of Pb below 2 wt% supported the hypothesis of cold hammering. Differently, an amount of Pb higher than 2 wt% would indicate its intentional addition to bronze, in order to lower the melting point of the alloy and improve its casting properties [28].

Furthermore, the different concentration of the main elements in the two laminas of object A suggested that they were produced at different times and connected to each other after the object was repaired. In particular, the Sn signal was not detected in all analytical points, especially where its amount was lower than 6 wt% (as calculated by ED-XRF quantitative analysis).

4. Conclusions

The two instruments used in this study, i.e. handheld LIBS and portable ED-XRF, have been shown to be versatile, efficient and complementary for the *in-situ* analysis of archeological metal artefacts directly in the museum or in the field under ambient environmental conditions. In particular, the primary benefits of LIBS include its relatively quick and easy analytical process (few sec), the need of little or no sample preparation, the ability to analyze multiple elements at once and in specific sample regions and to achieve compositional depth profiling and surface microscale chemical mapping on a spatial scale of about 10 μm. However, in order to achieve quantitative results LIBS requires calibration using matrix-matched standards. On the other hand, the primary advantages of ED-XRF include its inherent calibration from the factory, which works well with a variety of sample types, and its ease of use for quantitative analysis in the field. The ED-XRF, however, needs a 1-to 2 min analytical time, depending on the required precision and detection limits, and is unable to measure elements with atomic numbers lower than Si.

Moreover, as the two techniques perform on very different volumes, the quantitative analysis provided by the ED-XRF technique cannot be trusted in the presence of surface corrosion layers or, in general, in-depth inhomogeneities, whereas LIBS is a tool more suitable for the analysis of patinas and corrosion layers. In particular, the area that LIBS can analyze has a diameter of around 100 μm with a depth of around 10 μm per laser pulse. Differently, ED-XRF can typically analyze a surface area of around 8 mm diameter (although it can be reduced to about 3 mm), with a depth of analysis strictly related to the x-ray attenuation that depends on energy, material and angle, but in any case of the order of several tens of microns.

In this work, the quantitative elemental composition of five copper alloy and two iron alloy archaelogical artefacts has been measured, i.e. Cu, Sn and Pb in copper alloys, and Fe with minor amounts of Cu and Pb and some trace elements Sb, Ni and Zn in iron artefacts. In particular, ED-XRF provided the quantitative estimation of the elements concentrations in the first 100–200 μm under the surface, and LIBS complemented this evaluation by measuring the in-depth variation of the sample composition. The LIBS depth profiling and mapping of the artefacts also allowed to distinguish among the different corrosion layer and hypothesize the processing technique used to construct and/or repair them. The analytical results obtained have shown that the copper alloy objects were made of bronze whose content of Sn was typical of the Iron Age, which was confirmed by the absence of As that also allowed to exclude recycling of more ancient objects. Finally, the depth profile results suggested that cold hammering was the copper alloy processing used.

In conclusion, the results of this work suggest that the instruments employed appear appropriate for the quantitative elemental analysis of archaeological metal artefacts, which is also confirmed by the good agreement with literature data regarding ancient bronze. In particular, handheld/portable instruments have shown stability in measurements over time, satisfactory reproducibility and a good balance between resolution and size, rendering them an excellent option for direct *in-situ* analysis of archaeological metal artefacts in museums, outdoor campaigns and in hardly accessible places.

Data availability statement

The data cannot be made publicly available upon publication because they are not available in a format that is sufficiently accessible or reusable by other researchers. The data that support the findings of this study are available upon reasonable request from the authors.

Acknowledgments

The authors acknowledge the financial support received under the project MIUR D D n. 2284, 29 September 2021, PRIN 'UNDERLANDSCAPE: a multi-analytic approach to the study, conservation and valorization of the underground historical environment and the surrounding landscape', Smart Ndt and SciAps for

providing us the use of X-200 portable ED-XRF instrument, and the Soprintendenza Archeologia, Belle Arti e Paesaggio per le Province di Barletta—Andria—Trani e Foggia for authorizing the analyses (M Corrente and I M Muntoni).

ORCID iDs

Sara Mattiello https://orcid.org/0009-0000-9601-4703
Olga De Pascale https://orcid.org/0000-0002-7220-1069
Vincenzo Palleschi https://orcid.org/0000-0002-6377-7656
Girolamo Fiorentino https://orcid.org/0000-0001-8480-891X
Giorgio S Senesi https://orcid.org/0000-0002-3947-6853

References

[1] Scott D A and Schwab R 2019 *Metallography in Archaeology and Art* (Springer)
[2] Di Turo F 2019 Limits and perspectives of archaeometric analysis of archaeological metals: a focus on the electrochemistry for studying ancient bronze coins *J. Cult. Herit.* **43** 271–81
[3] Radivojević M *et al* 2019 The Provenance, use, and circulation of metals in the European Bronze Age: the state of debate *J. Archaeol. Res.* **27** 131–85
[4] Detalle V and Bai X 2022 The assets of laser-induced breakdown spectroscopy (LIBS) for the future of heritage science *Spectrochim. Acta* B **191** 106407
[5] Senesi G S, Harmon R S and Hark R R 2021 Field-portable and handheld laser-induced breakdown spectroscopy: historical review, current status and future prospects *Spectrochim. Acta* B **175** 106013
[6] Frahm E and Doonan R C P 2012 The technological versus methodological revolution of portable XRF in archaeology *J. Archaeol. Sci.* **40** 1425–34
[7] Pérez-Serradilla J A, Jurado-López A and Luque de Castro M D 2007 Complementarity of XRFS and LIBS for corrosion studies *Talanta* **71** 97–102
[8] Botto A, Campanella B, Legnaioli S, Lezzerini M, Lorenzetti G, Pagnotta S, Poggialini F and Palleschi V 2019 Applications of laser-induced breakdown spectroscopy in cultural heritage and archaeology: a critical review *J. Anal. At. Spectrom.* **34** 81–103
[9] Orfanou V and Rehren T 2015 A (not so) dangerous method: pXRF vs. EPMA-WDS analyses of copper-based artefacts *Archaeol. Anthropol. Sci.* **7** 387–97
[10] Nørgaard H W 2017 Portable XRF on prehistoric bronze artefacts: limitations and use for the detection of bronze age metal workshops *Open Archaeol.* **3** 101–22
[11] Gójska A, Mišta-Jakubowska E, Banaś D, Kubala-Kukuś A and Stabrawa I 2019 Archaeological applications of spectroscopic measurements. Compatibility of analytical methods in comparative measurements of historical Polish coins *Measurement* **135** 869–74
[12] Wallace S, Smith N and Nerantzis N 2021 Handheld methods in archaeological research on large copper alloy assemblages: HH-XRF against HH-LIBS *Archaeometry* **63** 343–71
[13] Colao F, Fantoni R, Lazic V and Spizzichino V 2002 Laser-induced breakdown spectroscopy for semi-quantitative and quantitative analyses of artworks—Application on multi-layered ceramics and copper based alloys *Spectrochim. Acta* B **57** 1219–34
[14] Melessanaki K, Ferrence S C, Betancourt P P and Anglos D 2003 Application of LIBS in the analysis of archaeological objects *19th Congress Int. Commission for Optics: Optics for the Quality of Life* (SPIE) p 79
[15] Lazic V, Vadrucci M, Fantoni R, Chiari M, Mazzinghi A and Gorghinian A 2018 Applications of laser-induced breakdown spectroscopy for cultural heritage: a comparison with x-ray fluorescence and particle induced x-ray emission techniques *Spectrochim. Acta* B **149** 1–14
[16] Fortes F J, Cortés M, Simón M D, Cabalín L M and Laserna J J 2005 Chronocultural sorting of archaeological bronze objects using laser-induced breakdown spectrometry *Anal. Chim. Acta* **554** 136–43
[17] Ferretti M, Cristoforetti G, Legnaioli S, Palleschi V, Salvetti A, Tognoni E, Console E and Palaia P 2007 In situ study of the Porticello Bronzes by portable x-ray fluorescence and laser-induced breakdown spectroscopy *Spectrochim. Acta* B **62** 1512–8
[18] Arafat A, Na'es M, Kantarelou V, Haddad N, Giakoumaki A, Argyropoulos V, Anglos D and Karydas A G 2013 Combined in situ micro-XRF, LIBS and SEM-EDS analysis of base metal and corrosion products for Islamic copper alloyed artefacts from Umm Qais museum, Jordan *J. Cult. Herit.* **14** 261–9
[19] Tankova V, Malcheva G, Blagoev K and Leshtakov L 2018 Investigation of archaeological metal artefacts by laser-induced breakdown spectroscopy (LIBS) *J. Phys.: Conf. Ser.* **992** 012003
[20] Fortes F J, Cabalín L M and Laserna J J 2020 Fast and in-situ identification of archaeometallurgical collections in the museum of Malaga using laser-induced breakdown spectroscopy and a new mathematical algorithm *Heritage* **3** 1330–43
[21] Ghervase L, Dinu M, Bors C, Anghelut L M, Radvan R and Cortea I M 2020 Investigation on metal adornments from ancient Eastern Europe *Front. Mater.* **7** 600913
[22] Penkova P, Malcheva G, Grozeva M, Hristova T, Ivanov G, Alexandrov S, Blagoev K, Tankova V and Mihailov V 2023 Laser-induced breakdown spectroscopy and x-ray fluorescence analysis of bronze objects from the late bronze age baley settlement, Bulgaria *Quantum Beam Sci.* **7** 22
[23] Thompson A C *et al* 2009 *X-ray Data Booklet* (Lawrence Berkeley National Laboratory, University of California)
[24] National Institute of Standard and Technology (available at: www.nist.gov/pml/atomic-spectra-database) (Accessed 14 November 2023)
[25] Scott D A 2000 A review of copper chlorides and related salts in bronze corrosion and as painting pigments *Stud. Conserv.* **45** 39–53
[26] Leoni M 1985 Elementi di metallurgia applicata al restauro delle opere d'arte *Corrosione e Conservazione dei Manufatti Metallici (Opus Libri)*
[27] Kareem K, Sultan S and He L 2015 Fabrication, microstructure and corrosive behavior of different metallographic tin-leaded bronze alloys part II: chemical corrosive behavior and patina of tin-leaded bronze alloys *Mater. Chem. Phys.* **169** 158–72
[28] Johannsen J W 2016 Heavy metal: lead in bronze age scandinavia *J. Swed. Antiq. Res.* **111** 153–61

Chapter4

Conclusions

Knowing exactly what does a society based on knowledge receive as fruitful rewards of the study conducted above, and how they can germinate in the future generation is not trivial. For sure, common results of the research can be easily extended to similar systems and systematized to global strategies. In a way, those protocols of investigation of materials, only in appearance very different one from the other, have shown common, though important, indicators of their character and of their capacity to be transformed (or reshaped and ameliorated) to become novel materials with new properties and applications. At the centre of this process is materials science, which thanks to its interdisciplinarity and integrated approach is able to generate a significant scientific ecological and social impact.

This work addressed the mix of approaches, for pushing characterization and potential applications of biomaterials of natural origin from industrial waste, as well as the archaeometric analysis of metal manufacts, using advanced and sustainable techniques. A significant part of the research focused on the extraction and characterization of keratin from waste sources, in particular wool and chicken feathers. Using sulfitolysis and other reduction methodologies, it was possible to preserve the secondary structure of the protein, a fundamental aspect that allows to maintain its functional properties. Spectroscopic (FT-IR and Raman) and microscopic (SEM, AFM) analyses confirmed the preservation of the alpha helix structures for wool and beta sheet for feathers after extraction. SAXS data allowed to propose structural models in the liquid phase, confirming the presence of fibers with dimensions compatible with intermediate filaments. In parallel, a critical review of the biomimetic ability of feather-derived keratin was conducted, highlighting the importance of preserving secondary structures capable of self-assembly. In this direction, the analysis of the gelling properties of chicken feather-derived keratin was also carried out, with encouraging results for the use in biomedical devices. The gels obtained showed significant rheological stability, together with the ability to deliver bioactive compounds — in the case of study, curcumin — with controlled release at different physiological pH. These characteristics strengthen the potential of keratin as a component for biomedical scaffolds, drug delivery systems and functional coatings. In a further extension of the work, melanin obtained from Black Soldier Fly (*Hermetia Illucens*) was examined, a material with interesting chemical-physical properties and water solubility. Its characterization revealed

the presence of DHI and DHICA groups, partially unexpected for entomological melanins, raising relevant questions on melanogenesis. The interaction between keratin and melanin, materials studied in previous works, was explored through the preparation of colloidal suspensions, whose structure was investigated with SAXS, TEM and BDS. The mutual influence between the two components revealed phenomena of self-assembly and cooperative interaction, with important implications for the fabrication of functional composite materials through liquid phase deposition techniques. The possibility of controlling shape, aggregation and dielectric properties of these materials opens scenarios for bio-compatible and biodegradable devices, in the electronic, sensor and biomedical fields. Finally, the work included an archaeometric study, aimed at the non and micro-destructive analysis of metal finds using portable instrumentation (LIBS and ED-XRF). The results demonstrated the effectiveness of the combination of the two techniques for the in situ determination of the elemental composition, in-depth profiling, compositional mapping and correlation with technological and chronological data, confirming their reliability in excavation contexts and field analysis. The achieved results lay the foundations for future developments, both on a methodological level - through the improvement of analytical techniques - and on applicative level, in the design of advanced, sustainable and nature-inspired materials.

In summary, the case studies analysed, not only offer examples of new technical solutions, but also become awareness-raising tools on environmental issues, helping us to understand the origin of materials, the end of their life and to imagine a new beginning for them. Generating less waste, recovering waste in production processes, reducing the use of dangerous substances, replacing critical materials and using portable technologies: these approaches represent a cultural and methodological change based on good practices. A change that brings tangible benefits not only to research, but to our society as a whole.

ChapterA

Supplementary Information

A.1

Supplementary Information (SI) for Materials Advances.

Exploring the chemistry and composition of black soldier fly eumelanin, a material for a circular economy

A. B. Mostert[1]*, S. Mattiello[2,3], S. Li[4], G. Perna[5], M. Lasalvia[5], P.F. Ambrico[2], J.V. Paulin[7], J.V.M. Lima[7], C.F.O Graeff[7], J.W. Phua[8], M. Matta[4], A. J. Surman[4], R. Gunnella[3]*, M. Ambrico[2]

[1] Department of Physics and Centre for Integrative Semiconductor Materials, Swansea University Bay Campus, Fabian Way, Swansea, SA1 8EN, UK.
[2] CNR-Institute for Plasma Science and Technology, Bari Branch, Via Amendola 122/D, I-70125 Bari, Italy.
[3] School of Science and Technology University of Camerino, Via Madonna delle Carceri 9I-62032, Camerino, Italy.
[4] Department of Chemistry, King's College London, Britannia House, 7 Trinity Street, SE1 1DB London, UK.
[5] Department of Clinical and Experimental Medicine, Università degli Studi di Foggia Via Napoli 20, I-71122 Foggia, Italy
[7] São Paulo State University (UNESP), School of Sciences, Department of Physics and Meteorology, Bauru/SP, Brazil.
[8] Insectta Pte. Ltd., 8 Cleantech Loop S637145, Singapore

E-mail: a.b.mostert@swansea.ac.uk ; roberto.gunnella@unicam.it

Orcid ID:
A.B.M.: 0000-0002-9590-2124
S.M.: 0009-0000-9601-4703
S.L.: 0009-0006-3841-7364
G.P.: 0000-0001-8315-0634
M.L.: 0000-0002-8221-7849
P.F.A.: 0000-0002-2455-6949
J.V.P.: 0000-0002-2379-6203
J.V.M.L.: 0000-0001-9862-8151
C.F.O.G.: 0000-0003-0162-8273
J.W.P.: 0009-0002-1763-0861
M.M.: 0000-0002-9852-3154
A.J.S.: 0000-0002-2042-7373
R.G.: 0000-0003-4739-6375
M.A.: 0000-0002-0568-6860

UV-Vis Spectra of Various Solid-State Films

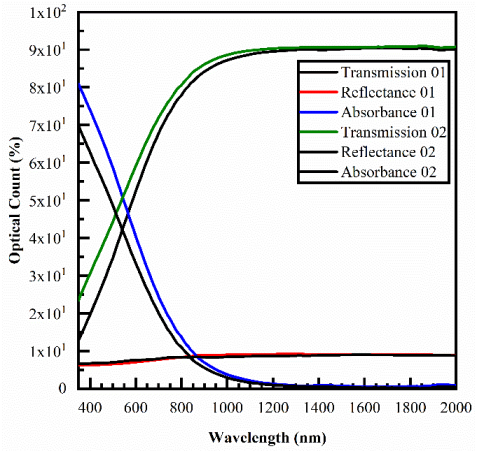

Figure S1: The optical data obtained on two films of BSF eumelanin. BSF eumelanin was filtered, and substrate ozone treated.

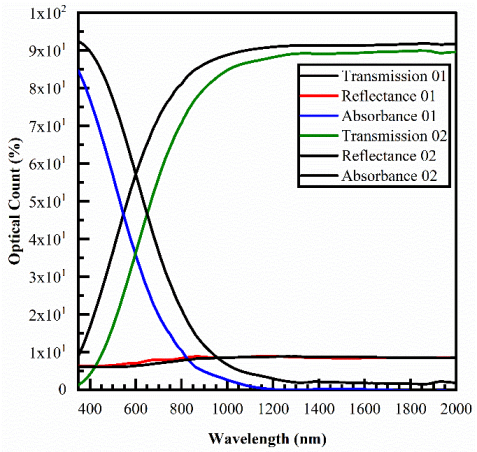

Figure S2: The optical data obtained on two films of BSF eumelanin. BSF eumelanin was filtered, and substrate was left untreated.

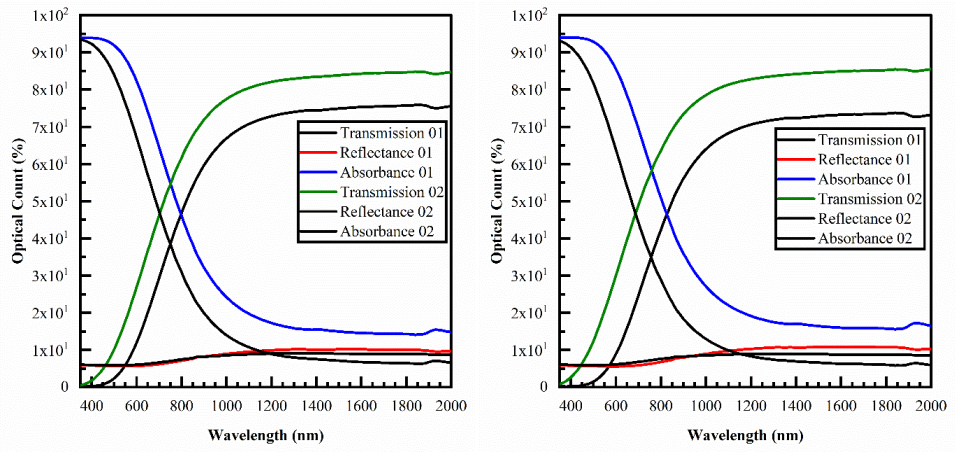

Figure S3: The optical data obtained on four films of BSF eumelanin but depicted across two sub figures for clarity. BSF eumelanin was unfiltered, and substrate was treated with ozone.

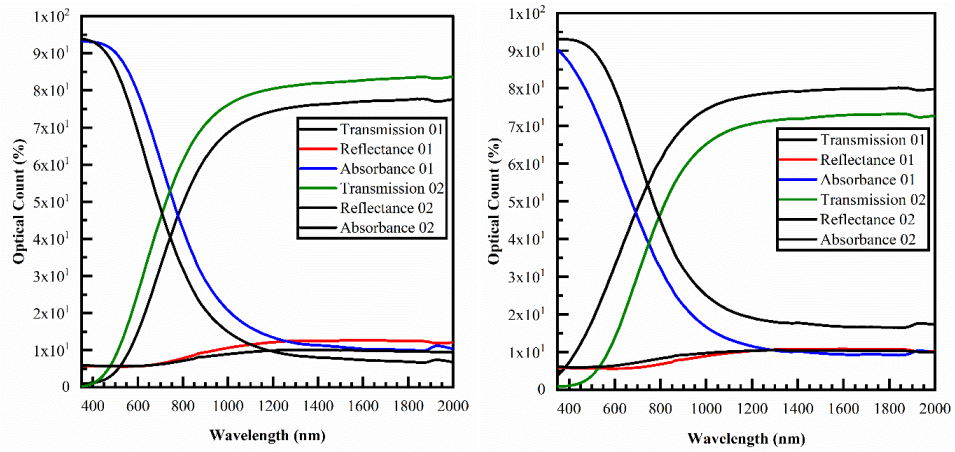

Figure S4: The optical data obtained on four films of BSF eumelanin but depicted across two sub figures for clarity. BSF eumelanin was unfiltered, and substrate was left untreated.

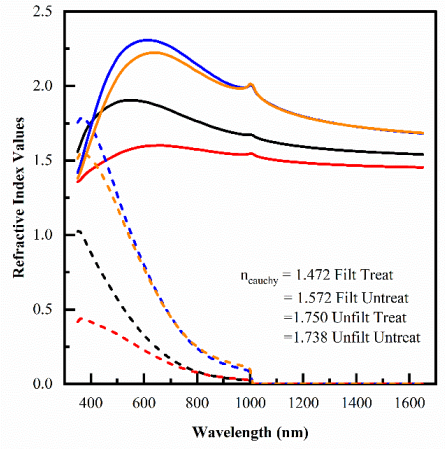

Figure S5: The overall refractive indices n (solid lines) and k (dashed lines) for films that were (blue) unfiltered BSF eumelanin on ozone treated glass, (orange) unfiltered BSF eumelanin on untreated glass, (black) filtered eumelanin on untreated glass and (red) filtered eumelanin on ozone treated glass. The Cauchy refractive index (n ($\lambda \rightarrow \infty$)) is indicated in the legend.

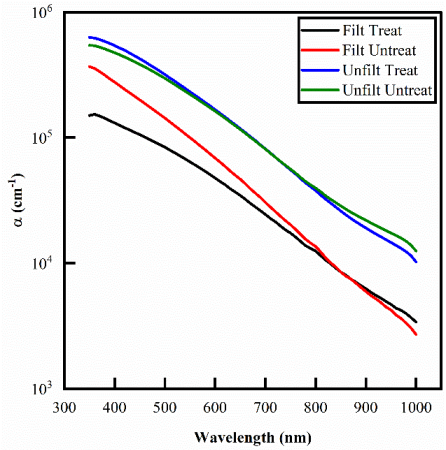

Figure S6: The absorption coefficients for the various sample types (see legend).

UV-Vis A_{650}/A_{500} ratio analysis of BSF eumelanin Solutions

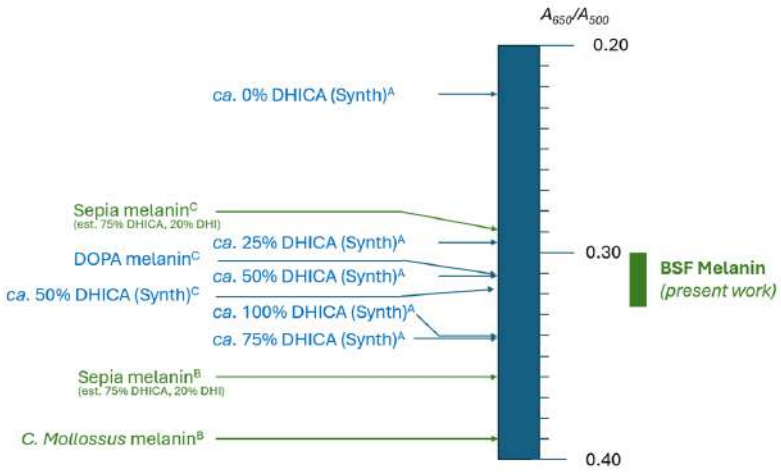

Figure S7: A_{650}/A_{500} ratios reported in the literature for synthetic (blue) and natural (green) melanins. Values are taken from: Itou *et al.* (A) where the values of %DHI 0%, 25.1%, 49.9%, 74.7%, 99.9% correspond to ratio values of 0.22, 0.30, 0.31, 0.34, 0.34;[1] Xin *et al.*[2] (B) where Sepia eumelanin from sigma was referenced as yielding a ratio of 0.36 for 75%/20% DHICA/DHI[3] and where they reported a eumelanin for *C. molossus* ratio of 0.39; Ito *et al.* (C) where Sepia eumelanin yielded a ratio of 0.29 and a synthetic eumelanin of 50%DHI/50%DHICA yielded a ratio of 0.318.[4]

The literature contains a range of reports of how A_{650}/A_{500} ratios relate to %DHI, recorded in varying conditions. For synthetic (DHI/DHICA) eumelanin of varying %DHI, a range of A_{650}/A_{500} ratios from ~0.22 (no DHI content) to 0.34 (100% DHI) was reported.[1] This dependence is not linear but monotonically increases as DHI content increases, with A_{650}/A_{500} for 80% DHI as essentially indifferentiable from 100% DHI.[1] Another report observed an A_{650}/A_{500} ratio for *Catharsius molossus L.* (dung beetles) of 0.39,[2] and for *Sepia officinalis* (cuttlefish) A_{650}/A_{500} ratio of 0.36 (noting that *Sepia* is known to have a DHICA/DHI ratio of up to 75%/20%).[3] A previous report observed an A_{650}/A_{500} ratio of 0.291 for '*Sepia* eumelanin', and 0.318 for synthetic (1:1 DHICA/DHI eumelanin).[4]

Applying this analysis to our UV-Vis spectra of solutions/suspensions of BSF eumelanin, we obtain an average result for the A_{650}/A_{500} ratio of 0.3 on unfiltered samples and 0.33 on filtered samples. Considering the literature results above together, it is not appropriate to draw quantitative conclusions of DHI/DHICA ratio from our A_{650}/A_{500} data for BSF eumelanin. However, we note that values for BSF eumelanin values fall into the range in which mixed DHI/DHICA have been reported, and therefore that our observations do not appear inconsistent with the presence of DHICA. Indeed, ca. 20% DHICA, as estimated by AHPO, would not be readily differentiated from 0% DHICA by comparing A_{650}/A_{500} ratios, following the literature.[1]

UV-Vis A_{650}/A_{500} ratio analysis of Various Solid-State Films

For various solid-state film samples, the A_{650}/A_{500} ratios obtained are shown in Table S1. What is notable is that the ratios obtained are significantly different to the suspension results obtained from the data in Figure 2. Furthermore, there are two clear categories for the solid films: data with and without treated glass slides. Clearly substrate preparation is a key determinant of the results, with glass that was treated with UV-Ozone yielding results closer to the solution/suspension data. Differences between filtered and unfiltered eumelanin was minimal, like the solution/suspension data. Still, even with cleaned substrates, the difference to Figure 2 data is substantial with almost twice the ratio values. As such, the solid-state data currently is not determinative and may indeed indicate that the solid state is not a suitable approach for ratio analysis as it is too far out of scope with what has been observed in solution based studies.

Sample Type	**Average A(650nm)/A(500nm)**	**Uncertainty A(650nm)/A(500nm)**
Filtered on treated glass	0.544	0.003
Unfiltered on treated glass	0.54	0.13
Filtered on untreated glass	0.75	0.18
Unfiltered on untreated glass	0.74	0.11

Table S1: Absorbance ratio analysis performed on thin films of BSF-eumelanin. Averages and uncertainty (range) given for various sample preparations.

Raman Spectroscopy

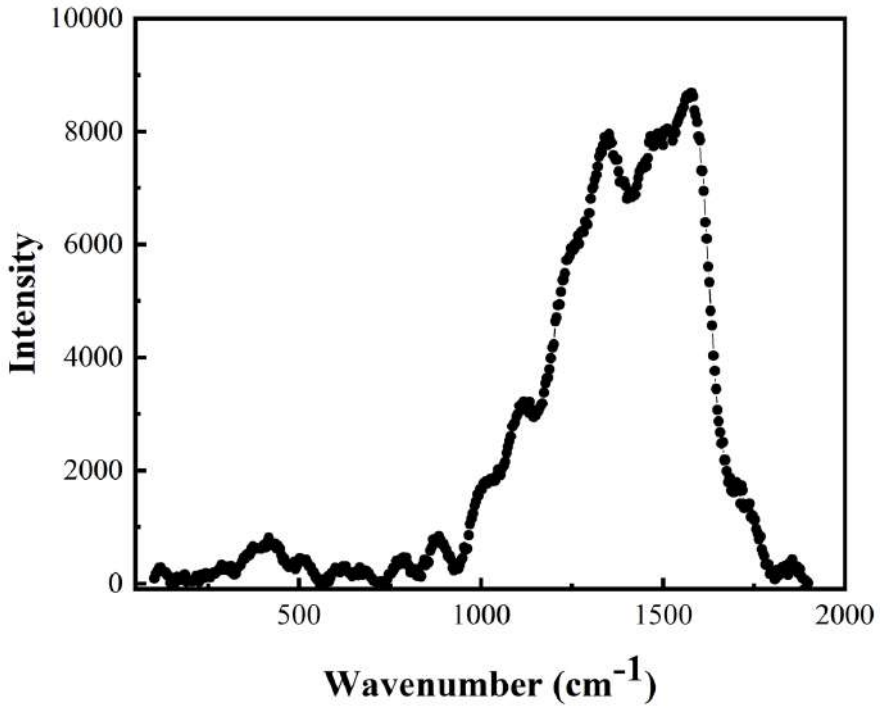

Figure S8: Full Raman spectrum of BSF-EuMel. No visible peaks are attributed to the pheomelanin.

HPLC

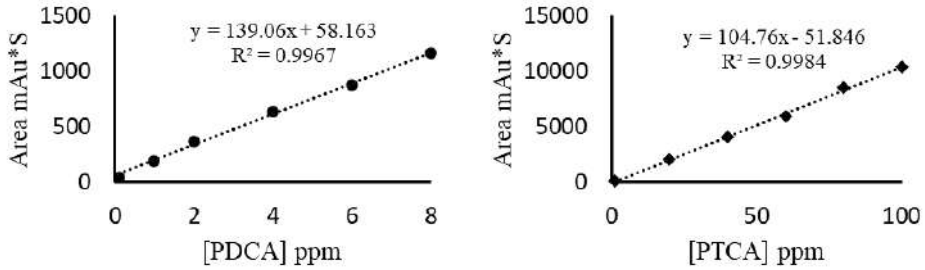

Figure S9: Standard curve of eumelanin markers PDCA and PTCA. 30 µL of standard solutions containing 0.1 to 100 µg mL^{-1} of markers, for PTCA (1, 20, 40, 60, 80, 100 µg mL^{-1}) and for PDCA (0.1 to 8 µg mL^{-1}), were injected.

Markers	**Regression Equation**	**Correlation (R^2)**	**Linearity Range (µg mL^{-1})**
PDCA	y=139.06x+58.163	0.9967	0.1-8
PTCA	y=104.76x-51.846	0.9984	1 -100

Table S2: Regression equation of eumelanin markers: pyrrole-2,3-dicarboxylic acid (PDCA) and pyrrole-2,3,5-tricarboxylic acid (PTCA).

Sample	**PDCA**	**PTCA**	**PDCA/PTCA Ratio**
Native	197.269 ± 72.98	887.942 ± 66.51	0.22
HCl-Treated	55.728 ± 12.65	475.051 ± 11.19	0.12
Filtered	309.586 ± 23.30	791.714 ± 20.26	0.39

Table S3: Content of markers in eumelanin samples (ng mg^{-1}). [values are means ± SD]

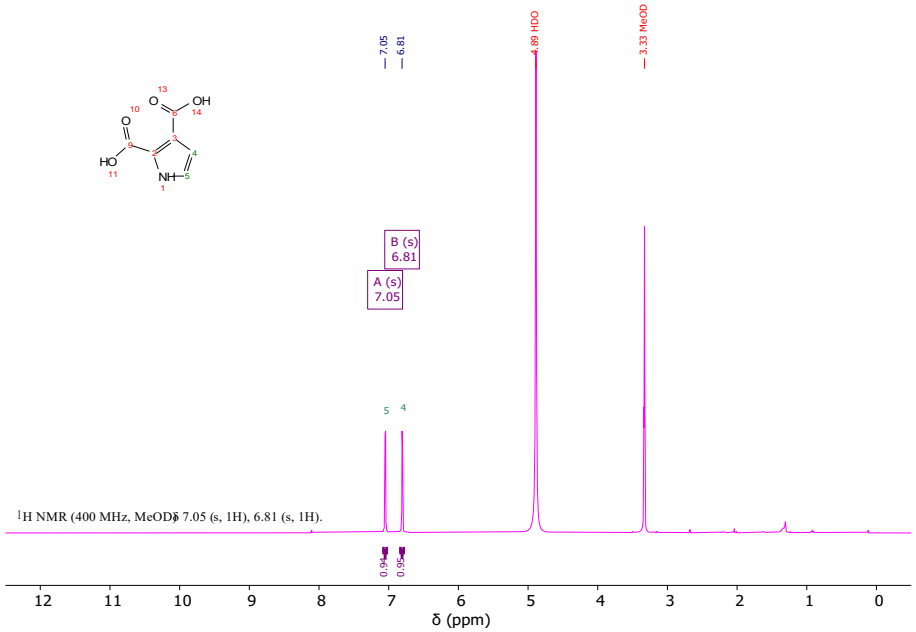

Figure S10: 1H NMR spectrum of Pyrrole-2,3-dicarboxylic acid (PDCA).

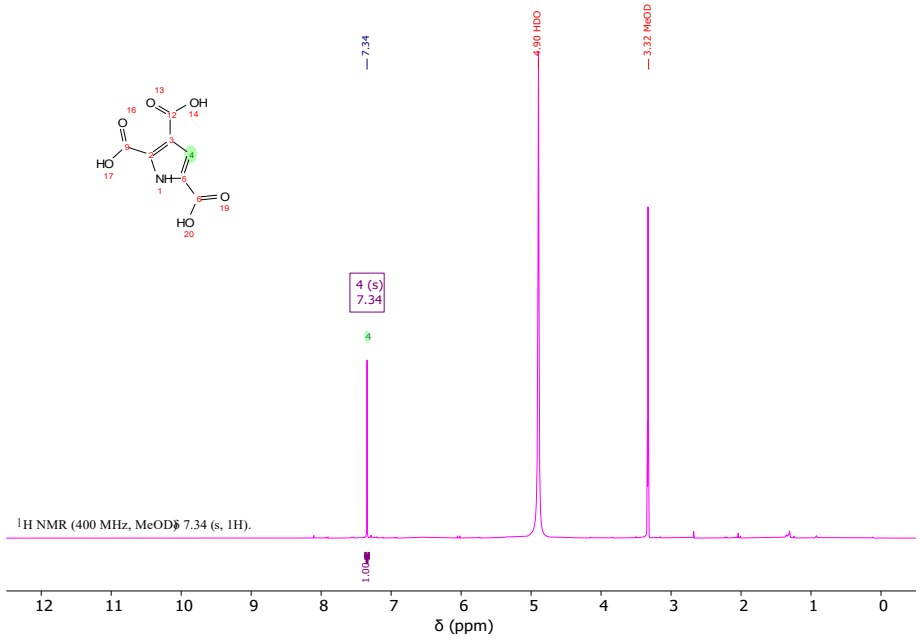

Figure S11: 1H NMR spectrum of pyrrole-2,3,5-tricarboxylic acid (PTCA).

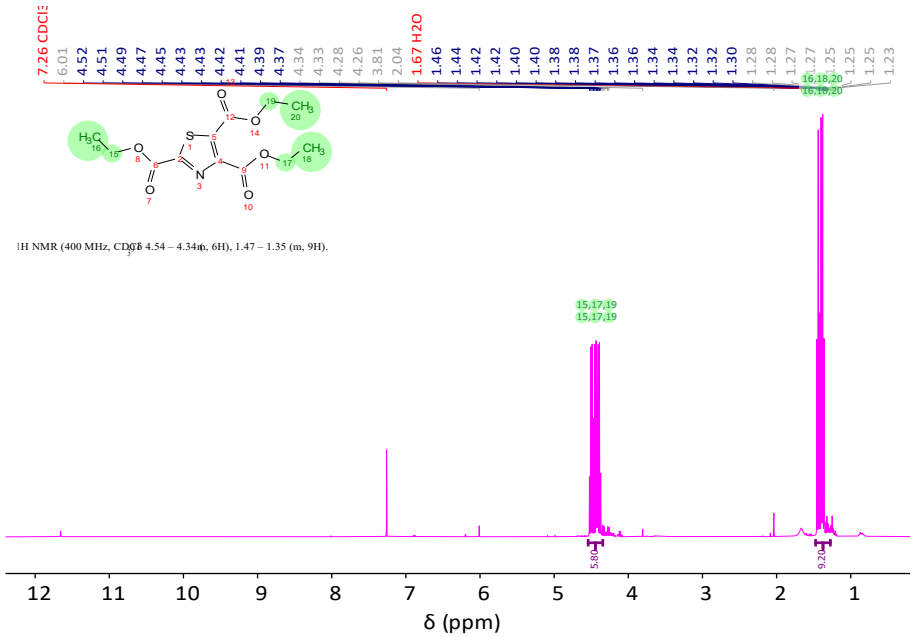

Figure S12: ^{1}H NMR of TTCA precursor: triethyl thiazole-2,4,5-tricarboxylate. ^{1}H NMR (400 MHz, $CDCl_3$) δ 4.54 – 4.34 (m, 6H), 1.47 – 1.35 (m, 9H).

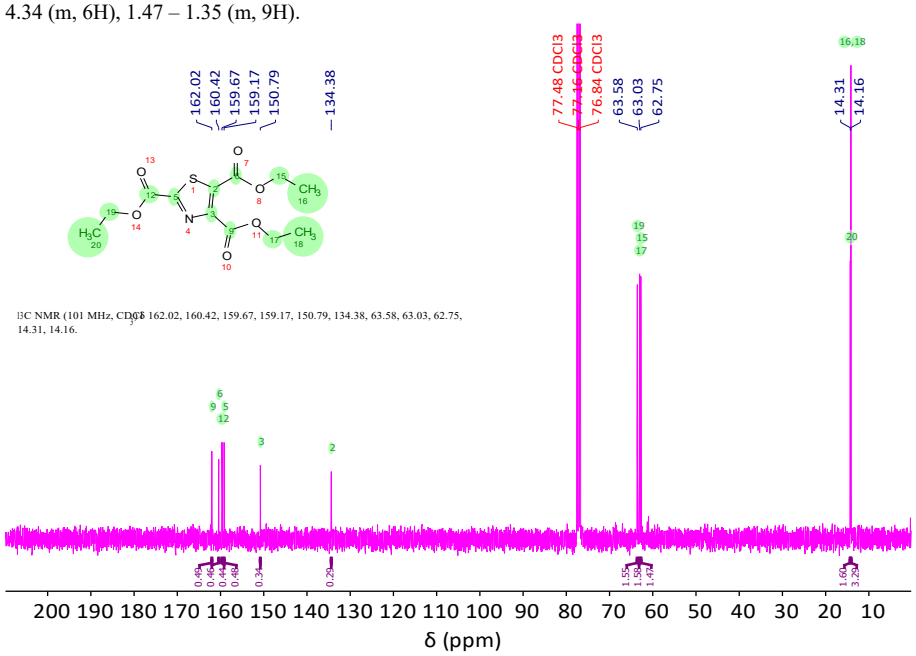

Figure S13: ^{13}C NMR of TTCA precursor: triethyl thiazole-2,4,5-tricarboxylate.^{13}C NMR (101 MHz, $CDCl_3$) δ 162.02, 160.42, 159.67, 159.17, 150.79, 134.38, 63.58, 63.03, 62.75, 14.31, 14.16. Cal. mass: 301.062 found: 302.0 [M+H^{+}].

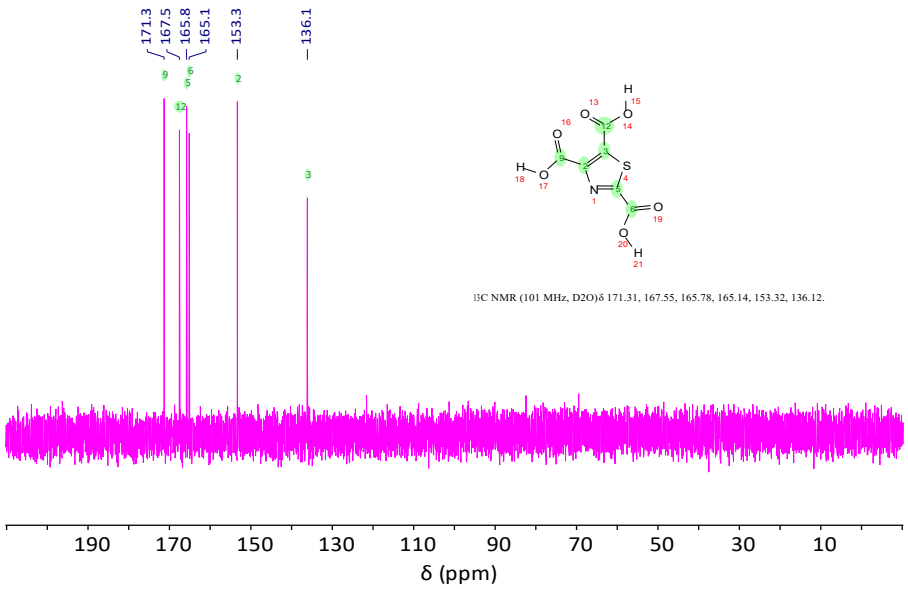

Figure S14: **^{13}C NMR of TTCA:** thiazole-2,4,5-tricarboxylic acid. ^{13}C NMR (101 MHz, D2O) δ 171.31, 167.55, 165.78, 165.14, 153.32, 136.12.

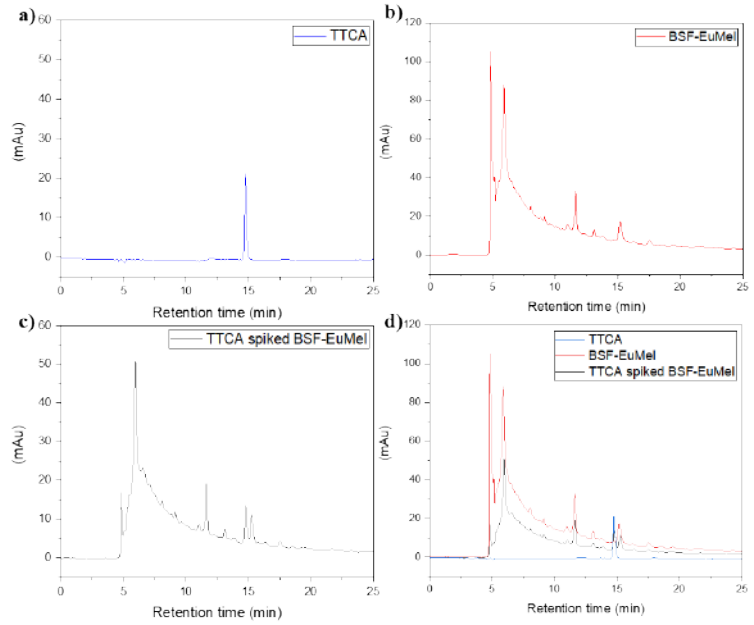

S15: HPLC analysis showing no/negligible TTCA in the BSF-EuMel sample. a) TTCA eumelanin marker. b) AHPO-digested solution of BSF-EuMel. c) AHPO-digested solution of BSF-EuMel spiked with TTCA marker. d) Superimposition of three chromatograms: no peak is observed in the AHPO-digested solution of BSF-EuMel at the retention time of TTCA.

NMR

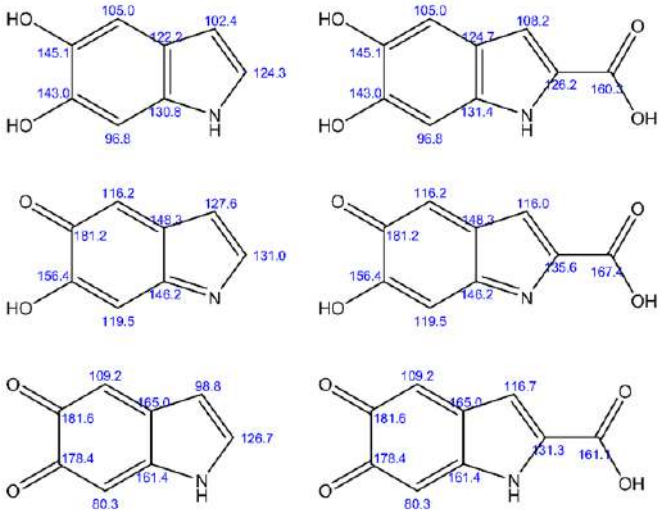

Figure S16: NMR Peak assignment for different monomer redox states of eumelanin.

Elemental Analysis

The elemental analysis on the BSF eumelanin is shown in Table S4. Sulphur was measured for, but not detected, which indicates that no significant pheomelanin is present. To demonstrate this assertion further, it should be noted that natural pheomelanin sulphur content has been quantified to be between 6 – 16% w/w.[5] If one assumes a lower limit of sulphur content to be 5%, and given that the elemental analysis has a detection limit of 0.01% w/w, then if one was able to detect sulphur at this lower limit, it would correspond with a material containing 0.2% w/w pheomelanin. As such, if pheomelanin is present in BSF eumelanin, if should be below 0.2% w/w and thus should be considered irrelevant to the rest of the analysis.

Sample ID	C%	H%	N%
QR24011	50.85	5.8	9.04
QR24007	49.3	5.52	9.08

Table S4: Content of markers in BSF eumelanin samples (ng mg^{-1}). [values are means ± SD]

References

1. T. Itou, S. Ito and K. Wakamatsu, *International Journal of Molecular Sciences*, 2019, **20**, 3739.
2. C. Xin, J.-h. Ma, C.-j. Tan, Z. Yang, F. Ye, C. Long, S. Ye and D.-b. Hou, *Journal of Bioscience and Bioengineering*, 2015, **119**, 446-454.
3. A. Pezzella, M. d'Ischia, A. Napolitano, A. Palumbo and G. Prota, *Tetrahedron*, 1997, **53**, 8281-8286.
4. S. Ito, A. Pilat, W. Gerwat, C. M. B. Skumatz, M. Ito, A. Kiyono, A. Zadlo, Y. Nakanishi, L. Kolbe, J. M. Burke, T. Sarna and K. Wakamatsu, *Pigment Cell & Melanoma Research*, 2013, **26**, 357-366.
5. W. Song, H. Yang, S. Liu, H. Yu, D. Li, P. Li and R. Xing, *Journal of Materials Chemistry B*, 2023, **11**, 7528-7543.
6. d'Ischia, M. *et al.* Melanins and melanogenesis: methods, standards, protocols. *Pigment Cell & Melanoma Research* **26**, 616–633 (2013).

A.2

Supporting Information

Eumelanin&Keratin sourced from waste: unravelling criss-cross functionalities for green electronic applications

Marianna Ambrico*[a], Sara Mattiello[b] , A. Bernardus Mostert[c] , Jun Wei Phua [d], Domenico Aceto[a], Paolo F. Ambrico[a], Alessandro Guzzini[b], Angelo De Stradis[e], Federico Liuzzi [f], Carlo Santulli[b], Giulio Lupidi[g] , Alessandra Del Giudice[h], Roberto Gunnella[b]

[a] CNR-Institute for Plasma Science and Technology, Bari Branch, Via Amendola 122/D, I-70125 Bari (Italy)
[b] School of Science and Technology University of Camerino, Via Madonna delle Carceri 9, I-62032 CAMERINO (MC) –(ITALY))
[c] Centre for Integrative Semiconductor Materials, Department of Physics, Swansea University Bay Campus, Fabian Way, Swansea, SA1 8EN UK
[d] INSECTTA Pte. Ltd., 8 Cleantech Loop, , Singapore 637145
[e] CNR-Institute for Sustainable Plant Protection, Via Amendola 165/A, I-70126 Bari (Italy)
[f] ENEA-Centro Ricerche Trisaia, S.S. 106 Ionica, 301 -75026 Rotondella (MT) (Italy)
[g] School of Pharmaceutical Sciences and Health Products , University of Camerino, Via Madonna delle Carceri 9, I-62032 Camerino (Mc)-Italy
[h] Department of Chemistry, Sapienza Università di Roma, Piazzale Aldo Moro 5, 00185 Rome, Italy

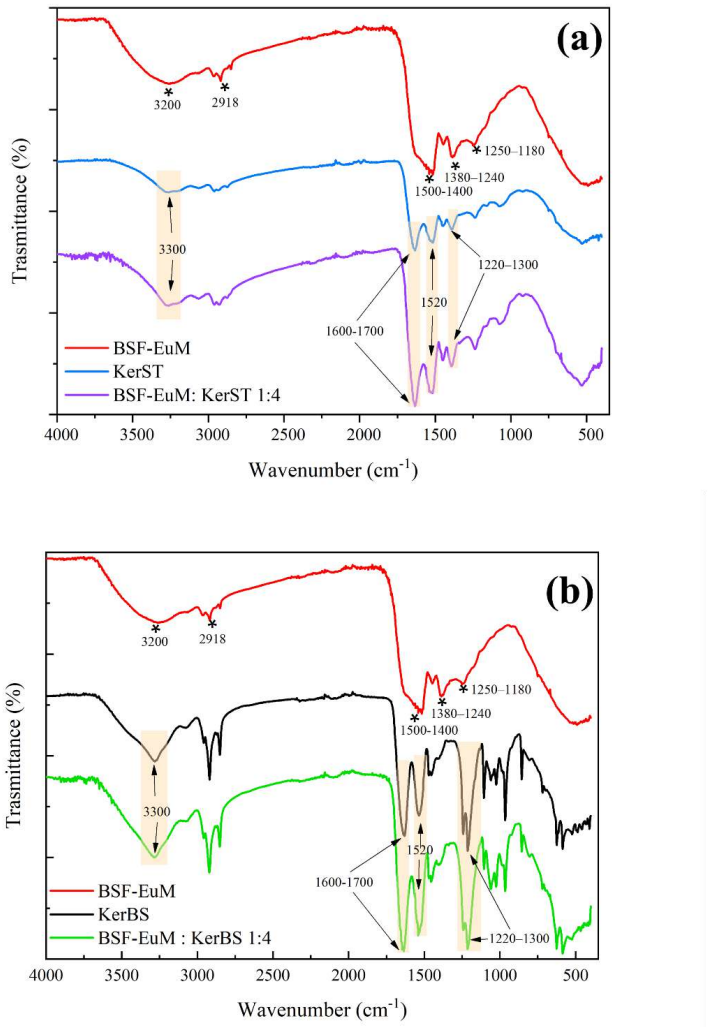

Figure S1 Comparison between FTIR spectra of one and mixed- components in powder form at the same ratio 1:4 of: (a) KerST; BSF-EuM and BSF-EuM; KerST and (b) KerBS; BSF-EuM and BSF-EuM; KerBS; The yellow boxes highlight the principal protein bands, while stars indicate the principal eumelanin vibration bands. The wavenumber corresponding to the vibration are also reported. In mixed powders, both keratin FTIR signal exceed that one of melanin.

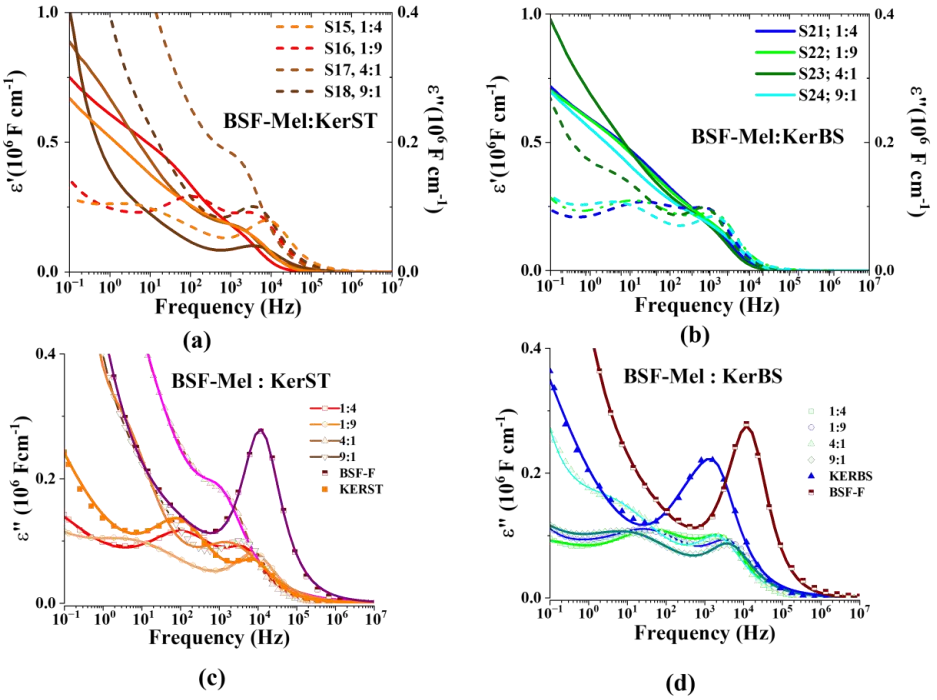

Figure S2 Dielectric permittivity spectra of the suspension of BSF-EuM:Keratin mixtures in water as calculated from the experimental Z impedance spectra (expr.2, main text) (see legends). (a) and (c) are the ε' and ε" spectra for the BSF-Mel/KerST mixtures respectively. (b) and (d) are the ε' and ε" spectra for the BSF-EuM/KerBS mixture, respectively

Items	HN	$\Delta\varepsilon_I$ Fcm^{-1}	τ_{HNi} (s)	$f_{MAX,HNi}$ (Hz)	ω_{HNi}	a	b	l_α	l_β
Mel-BSFUF	α	$4.94\ 10^5$	10.97	0.01	0.09	0.38	1.00	2.60	0.79
	β	$1.03\ 10^5$	$2.19\ 10^{-3}$	73	457	0.76	1.00		
	EP	$6.43\ 10^5$	$4.28\ 10^{-5}$	3718	23364	1.00	1.00		
Mel-BSFF	α	$1.21\ 10^6$	4.69	0.03	0.21	0.55	1.00	0.30	0.08
	β	$1.39\ 10^5$	$4.87\ 10^{-3}$	33	205	0.56	1.00		
	EP	$2.14\ 10^5$	$1.36\ 10^{-5}$	11703	73529	1.00	1.00		
KerST	α	$2.83\ 10^6$	100	0.001	0.01	0.35	1.00	9.00	0.88
	β	$3.34\ 10^5$	$1.58\ 10^{-3}$	101	633	0.71	1.00		
	EP	$1.02\ 10^5$	$1.89\ 10^{-5}$	8421	52910	1.00	1.00		
KerBS	α	$4.09\ 10^6$	90.91	0.002	0.01	0.33	1.00	8.00	0.76
	β	$3.34\ 10^5$	$3.34\ 10^{-4}$	476	2994	0.720	1.00		
	EP	$2.66\ 10^5$	$7.68\ 10^{-5}$	2274	14285	0.94	1.00		
Mel:KerST	α	$2.53\ 10^5$	6.8	0.02	0.15	0.37	0.99	1.75	0.78
1:4	β	$9.92\ 10^4$	$1.5\ 10^{-3}$	106	667	0.74	1.00		
	EP	$5.22\ 10^4$	$3.6\ 10^{-5}$	4421	27778	1.00	1.00		
	α	$1.45\ 10^5$	4.4	0.04	0.23	0.54	1.00	1.26	0.64
1:9	β	$1.14\ 10^{5.}$	$1.32\ 10^{-2}$	12	76	0.54	1.00		
	EP	$5.84\ 10^4$	$1.94\ 10^{-5}$	8204	51546	1.00	1.00		
	α	$2.48\ 10^5$	$1.80\ 10^{-1}$	0.89	5.62	0.78	0.99	0.45	1.04
4:1	β	$5.16\ 10^5$	$3.06\ 10^{-2}$	5.2	33	0.45	1.00		
	EP	$8.20\ 10^4$	$1.15\ 10^{-4}$	1384	8696	0.96	1.00		
	α	$1.01\ 10^5$	$3.28\ 10^{-1}$	0.48	3.05	1.00	1.00	1.58	1.03
9:1	β	$2.07\ 10^5$	$3.59\ 10^{-2}$	7.6	48	0.75	0.65		
	EP	$6.89\ 10^4$	$3.97\ 10^{-5}$	4009	25189	1.00	1.00		
Mel:KerBS	α	$2.25\ 10^5$	17.71	0.01	0.06	0.41	1.00	2.30	0.73
1:4	β	$1.21\ 10^5$	$3.05\ 10^{-3}$	108	680	0.57	1.00		
	EP	$5.54\ 10^4$	$5.07\ 10^{-5}$	3139	19724	1.00	1.00		
	α	$1.30\ 10^5$	3.04	0.05	0.33	0.43	1.00	0.95	0.58
1:9	β	$1.19\ 10^5$	$4.16\ 10^{-3}$	38	240	0.56	1.00		
	EP	$5.70\ 10^4$	$3.50\ 10^{-5}$	4547	28571	1.00	1.00		
	α	$4.12\ 10^5$	8.05	0.02	0.12	0.49	1.00	2.60	0.77
4:1	β	$1.34\ 10^5$	$1.25\ 10^{-2}$	13.0	80	0.57	1.00		
	EP	$6.50\ 10^4$	$6.22\ 10^{-5}$	2559	16077	1.00	1.00		
	α	$1.29\ 10^5$	2.73	0.06	0.37	0.53	1.00	1.00	0.90
9:1	β	$1.18\ 10^5$	$9.31\ 10^{-3}$	17.0	107	0.55	1.00		
	EP	$5.93\ 10^4$	$3.46\ 10^{-5}$	4600	28902	1.00	1.00		

Table S1 Best fit parameters returned by adopting the HN approach to *the* $D_{Inv}(\varepsilon')$ (expr. 8) and using the NOVOCONTROL WINFIT 2.0 software on both one-component and mixed-type suspensions. The values of the corresponding $f_{max,HNi}$ and $\omega_{max,HNi}$ have been calculated starting from τ_{HNi}, a and b values using expr.9, l_α and l_β via expr. 10 (main text)

A.3

Application of handheld/portable spectroscopic tools to the identification, inner stratigraphy and mapping of archaeological metal artefacts

Supplementary Information

Sara Mattiello[1, 2], Olga De Pascale[1], Vincenzo Palleschi[3], Girolamo Fiorentino[4], Giorgio S. Senesi[1*]

[1] CNR - Istituto per la Scienza e Tecnologia dei Plasmi (ISTP) - Sede di Bari, Via Amendola 122/D, 70126 Bari, Italy

[2] Physics Section, School of Science and Technology, Università di Camerino, via Madonna delle Carceri, 62032 Camerino, Italy

[3] CNR - Istituto di Chimica dei Composti Organo-Metallici (CNR-ICCOM), U.O.S. di Pisa, 56124 Pisa, Italy.

[4]Laboratory of Archeobotany and Paleoecology, Department of Cultural Heritage, University of Salento, via Birago 64, 73100, Lecce, Italy.

*Corresponding author: giorgio.senesi@cnr.it

ED-XRF Analysis

Table S1. Average concentration (wt %) and standard deviation (SD) of all elements identified by the portable ED-XRF instrument in the studied artefacts, as reported by the instrument software.

	A (belt)	SD	B (basin)	SD	C (fibula)	SD	D (helm)	SD	E (pendant)	SD	F (dagger)	SD	G (spatula)	SD
Si	15.068	3.484	9.796	2.088	16.298	4.460	6.932	4.799	15.238	3.608	2.416	1.696	1.163	0.666
Ti	ND	-	0.131	0.039	0.073	0.011	0.063	0.012	0.150	0.068	ND	-	ND	-
V	0.198	0.129	ND	-	0.153	0.031	ND	-	0.261	0.180	ND	-	ND	-
Fe	0.895	0.129	0.387	0.051	7.288	7.071	0.224	0.196	1.828	0.572	96.941	2.027	98.280	0.784
Ni	0.103	0.015	ND	-	ND	-	ND	-	0.070	0.004	0.056	0.019	ND	-
Cu	73.346	4.596	80.596	1.976	66.739	3.433	82.279	4.256	46.950	6.293	0.225	0.123	0.220	0.131
Mo	ND	-	ND	-	ND	-	ND	-	ND	-	0.010	0.006	0.015	0.007
Sn	5.394	3.219	6.259	1.321	5.816	2.920	6.520	2.100	6.163	3.156	ND	-	ND	-
Pb	2.998	2.545	0.277	0.072	1.478	0.510	0.288	0.133	24.143	9.797	0.050	0.021	0.048	0.031
Bi	0.085	0.019	ND	-	ND	-	ND	-	0.215	0.064	ND	-	ND	-
Sb	ND	-	ND	-	0.258	0.049	ND	-	0.425	0.123	ND	-	ND	-
P	0.525	0.222	1.006	0.193	0.618	0.200	1.216	1.166	1.372	1.189	0.143	0.151	0.055	0.041
S	ND	-	ND	-	ND	-	ND	-	ND	-	0.114	0.073	0.181	0.083

ND: not detected.

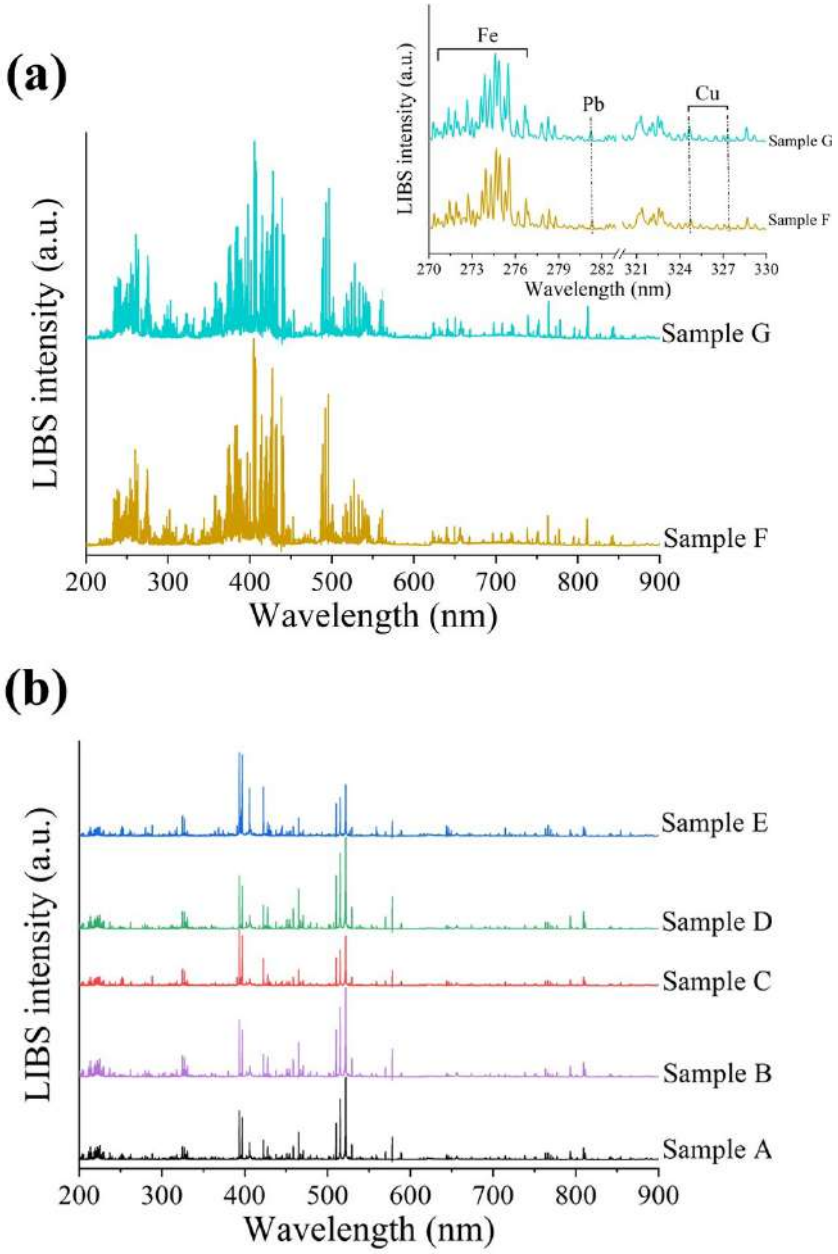

Figure S1: Representative LIBS spectra of iron alloy objects (a) and copper alloy objects (b). In the inset of (a) the detail of the spectra of iron alloy objects are shown with the indication of the Fe, Pb and Cu emission lines.

LIBS maps

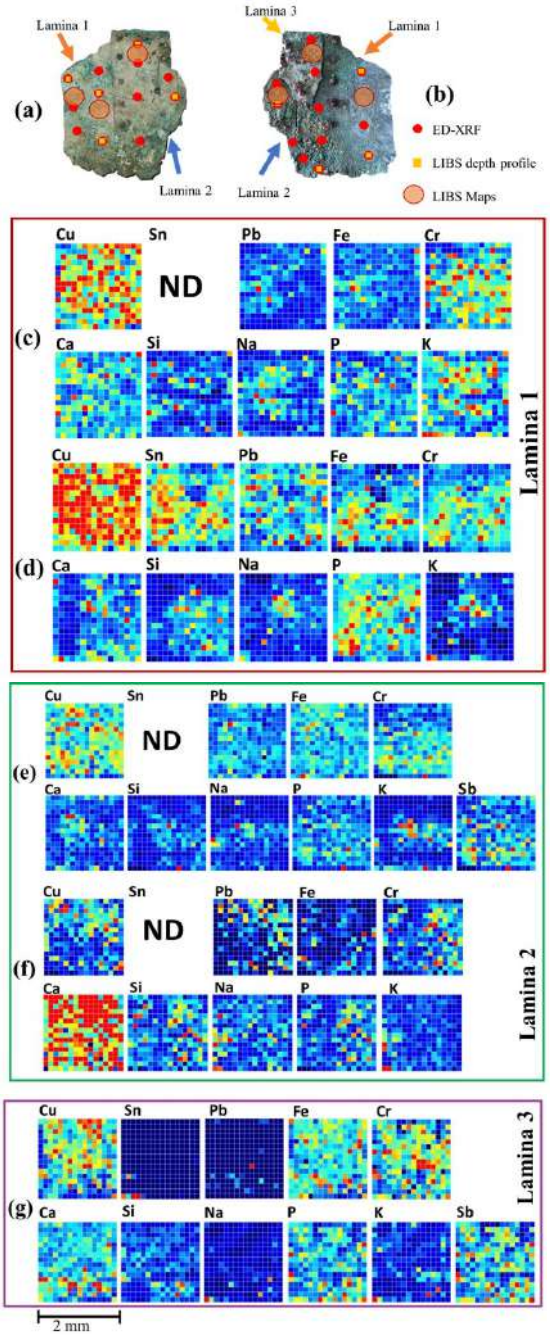

Figure S2: Front side (a) and back side (b) of laminas of sample A, the belt, on which the red circles indicate the areas where ED-XRF analysis was performed, orange circles where LIBS maps were measured and yellow squares where depth profile were determined. Elemental

distribution ‘heat maps’ obtained by LIBS scanning the surface of the front side (c) and back side (d) of lamina 1, the front side (e) and back side (f) of lamina 2, and the back side of lamina 3 (g). A color gradient that ranges from red indicating a high relative abundance to blue indicating a low relative abundance is used to show the variations in elemental emission intensity of the different elements. The spectral lines used to build the maps were: Cu=465.11 nm, Sn=317.503 nm, Pb=368.346 nm, Ca=422.673 nm, Cr=205.552 nm, P=213.62 nm, Si=251.611 nm, Na=588.995 nm, K=766.49 nm for the three laminas, Fe=273.955 nm for lamina 1 and lamina 2, and Fe=406.359 nm for lamina 3.

ChapterB

Abbreviations

AFM	Atomic Force Microscopy
BDS	Broadband Dielectric Spectroscopy
BSF-Mel	Black Soldier Fly melanin
DHI	5,6-dihydroxyindole
DHICA	5,6-dihydroxyindole-2-carboxylic acid
FT-IR	Fourier-Transform Infrared Spectroscopy
GOX	Graphene Oxide
GOXm	Graphene Oxide Micronized
KerBS	Keratin from metabisulphite extraction
KerST	Keratin from steam explosion extraction
LIBS	Laser-induced Breakdown Spectroscopy
SEM	Scanning Electron Microscopy
SAXS	Small Angle X-ray Scattering
TEM	Transmission Electron Microscopy
XPS	X-Ray Photoelectron Spectroscopy
XRF	X-ray Fluorescence

ChapterC

Publications and Conferences

Published:

1. Fragassa, C., **Mattiello**, S., Latini, M., Pesic, A., & Santulli, C. (2025). Saltwater Immersion Effects on Bio-Composites Reinforced With Seashell Powders. Applied Composite Materials, 1-23.

2. Ambrico, M.,**Mattiello**, S., Mostert, A. B., Phua, J. W., Aceto, D., Ambrico, P. F., ... & Gunnella, R. (2025). Eumelanin & keratin sourced from waste: unraveling criss-cross functionalities for green electronic applications. Journal of Physics D: Applied Physics, 58(12), 125302.

3. Fragassa, C., Pesic, A., **Mattiello**, S., Pavlovic, A., & Santulli, C. (2025). Exploring the Potential of Posidonia oceanica Fibers in Eco-Friendly Composite Materials: A Review. Journal of Marine Science and Engineering, 13(1), 177

4. **Mattiello**, S., & Santulli, C. (2025). Synthesis and Properties of Biomimetic Self-Assembling Structures from Poultry Feather Keratin. Journal of Renewable Materials, 13(1).

5. Santulli, C., Fragassa, C., Latini, M., **Mattiello**, S., & Pesic, A. (2024). Use of Adriatic Sea marine originated material in biocomposites with epoxy resin. Studia Marina, 37(2), 24–32.

6. Fragassa, C., **Mattiello**, S., Fronduti, M., Del Gobbo, J., Gagic, R., & Santulli, C. (2024). Prevention of Biofouling Due to Water Absorption of Natural Fiber Composites in the Aquatic Environment: A Critical Review. Journal of Composites Science, 8(12), 532.

7. Mostert, A. B., **Mattiello**, S., Li, S., Perna, G., Lasalvia, M., Ambrico, P. F., ... & Ambrico, M. (2024). Exploring the chemistry and composition of black soldier fly eumelanin, a material for a circular economy. Materials Advances.

8. **Mattiello**, S., Guzzini, A., Perinelli, D.R., Bonacucina, G., Gunnella, R., Lupidi, G. & Santulli, C. (2024), Keratin Gel From Chicken Feathers Waste Obtained by Mercaptoethanol Extraction. Polym Adv Technol, 35: e6605.

9. Senesi, G. S., De Pascale, O., **Mattiello**, S., Moggi Cecchi, V., Ibhi, A., Ouknine, L., & Nachit, H. (2024) Recent Advances in the Compositional and Mapping Analysis of Iron Meteorites Using a Handheld Laser-Induced Breakdown Spectroscopy Instrument. Geostandards and Geoanalytical Research.

10. **Mattiello**, S., De Pascale, O., Palleschi, V., Fiorentino, G., & Senesi, G. S. (2024). Application of handheld/portable spectroscopic tools to the identification, inner stratigraphy and mapping of archaeological metal artefacts. Journal of Physics: Photonics, 6(3), 035005.

11. Ambrico, M., Mostert, A. B., Ambrico, P. F., Phua, J., **Mattiello**, S., and Gunnella, R. (2024). Exploring ion mobility mechanisms in poly indolequinone polymers: a case study on black soldier fly melanin. Journal of Physics D: Applied Physics, 57(26), 265303.

12. Senesi G.S., **Mattiello**, S., Palleschi V., Cocciaro B., Fiorentino G. & De Pascale O. (2023). Handheld laser-induced breakdown spectroscopy, portable energy dispersive X-ray fluorescence spectroscopy and Graph Clustering applied to the identification and inner stratigraphy of archaeological metallic artifacts. Conference: 2023 IMEKO TC4 International Conference on Metrology for Archaeology and Cultural Heritage.

13. **Mattiello**, S., Guzzini, A., Del Giudice, A., Santulli, C., Antonini, M., Lupidi, G., & Gunnella, R. (2022). Physico-chemical characterization of keratin from wool and chicken feathers extracted using refined chemical methods. Polymers, 15(1), 181.

14. Parmar, R., Rezvani, S. J., de Freitas Neto, D. B., Rosolen, J. M., Kazim, S., **Mattiello**, S., ... & Gunnella, R. (2022). Structural phase stability and homogeneity enhancement of electrochemically synthesized Mn2V2O7 by nanocarbon networks. Carbon Trends, 9, 100218.

Oral presentation at Conferences:

- AdriBioPro 2024 conference, 1-4 October 2024|Kotor, Montenegro as coauthor:" Use of Adriatic Sea marine waste in biocomposites using bio-epoxy resin"

- Flash talk at "From melanogenesis to melanin technologies" Conference, 12-14 February 2024 |The view Hotel, Eastbourne, United Kingdom: "Spectroscopy characterization of melanin from soldier fly by advanced modelling"

- 2023 IMEKO international conference on Metrology for archeology and cultural heritage (MetroArcheo) 19-21 October 2023 | Roma, Italy : "Handheld laser-induced breakdown spectroscopy, portable energy dispersive x-rayfluorescence spectroscopy and graph clustering applied to the identification and inner stratigraphy of archaeological metallic artifacts"

- 16th European Conference on molecular electronics (ECME), 2-6 October 2023 | Bari, Italy as coauthor: "Mixing and matching sustainable Melanin&Keratin from waste for green electronics"

- 2023 Fall Meeting of the European Materials Research Society (E-MRS), 18-21 September 2023 | Warsaw University of Technology Poland: "Sustainable melanin and keratin waste for green electronics"

Poster for Conferences:

- "From melanogenesis to melanin technologies" Conference, 12-14 February 2024 |The view Hotel, Eastbourne, United Kingdom: "Spectroscopy characterization of melanin from soldier fly by advanced modelling".

- "From melanogenesis to melanin technologies" Conference, 12-14 February 2024 |The view Hotel, Eastbourne, United Kingdom as coauthor: "Hybrid BSF Melanin compounds with variously shaped graphene oxide nanoparticles".

- "From melanogenesis to melanin technologies" Conference, 12-14 February 2024 |The view Hotel, Eastbourne, United Kingdom as coauthor: "Mixing and matching melanin&keratin for green electronics".

- 2° Simposio Futuro in Area- Centenario CNR e Festa cittadina BAR|Code, 23-25 October 2023| Bari, Italy as coauthor: "Identification and stratigraphy of archaeological metallic artifacts by handheld laser-induced breakdown spectroscopy and portable X-ray fluorescence spectroscopy".

- CMD30 FisMat 2023, 4-8 September 2023 | Milano, Italy as coauthor: "Identification and stratigraphy of archaeological metallic artifacts by handheld laser-induced breakdown spectroscopy and portable X-ray fluorescence spectroscopy"

- Materials Today Conference, 2-5 August 2023 | Singapore Expo, Singapore as coauthor: "Black soldier fly melanin: structure, chemistry and bioelectronic properties of a new high value biomaterial"

Acknowledgment

I am grateful to the School of Science and Technology (SAS), the University of Camerino for their generous financial support throughout my Ph.D. program. In addition, I would like to express my gratitude to those who have provided various forms of support in order for me to pursue and complete my thesis.

Desidero ringraziare il mio supervisor, Prof. Roberto Gunnella, per la sua guida, la disponibilità, il prezioso supporto e la pazienza durante tutto il percorso di dottorato. Un sentito grazie va anche al gruppo di ricerca con cui ho avuto il piacere di collaborare: Prof. Carlo Santulli, Prof. Giulio Lupidi, Dott.ssa Marianna Ambrico e Alessandro Guzzini. In particolare, ringrazio Alessandro, (sì, due volte) per la collaborazione, l'amicizia e il supporto. Desidero inoltre ringraziare i ricercatori del ISTP-CNR di Bari che mi hanno ospitato e accolto durante il mio ultimo anno: Dott. Giorgio Senesi e Dott.ssa Olga De Pascale. Un ringraziamento speciale va a tutte le ragazze del dipartimento di Fisica con cui ho condiviso questa esperienza: Paola, Maryam, Nodoka, Benedetta e Laura, grazie per i caffè e le chiacchiere. Grazie a chi, pur non essendo citato qui per nome, ha lasciato un'impronta in questo percorso e tramite ogni incontro, ogni confronto, ha contribuito a rendere questo traguardo possibile. A Benedetta, Giulia, Greta e Francesco: dedico questo Gesto Forte a voi, che siete state colonne portanti del mio percorso accademico, dal primo all'ultimo giorno. Un infinito grazie va alla mia famiglia che nonostante non sappia esattamente descrivere cosa abbia fatto in questi anni, mi ha capito e supportato sempre.

E infine, grazie a te, Flavio..tu sai.🤙